# Finite Element Modelling of FRP Reinforced Concrete Beams and Comparative Analysis of Current Strength Prediction Methods

by

Ryan Barrage

A thesis
presented to the University of Waterloo
in fulfillment of the
thesis requirement for the degree of
Master of Applied Science
in
Civil Engineering

Waterloo, Ontario, Canada, 2017

# Author's Declaration

I hereby declare that I am the sole author of this thesis. This is a true copy of the thesis, including any required final revisions, as accepted by my examiners.

I understand that my thesis may be made electronically available to the public.

# Abstract

The modelling of glass fibre reinforced polymer (GFRP) reinforced, concrete beams was conducted by the author in the finite element analysis software ABAQUS. The study extended upon the work done by Joseph Stoner (2015) to calibrate the Concrete Damaged Plasticity (CDP) model, with the intent to ultimately complement laboratory testing in a research setting. Furthermore, current strength prediction methods for beams reinforced with fibre reinforced polymer (FRP) were evaluated against a database of tested beams collected from literature. The validity of the proposed ABAQUS models was assessed against selected beams from the database. Finally, a parametric study was conducted on 12 GFRP reinforced beams, over 12 slenderness ratios, to study the effects of slenderness.

The database of tested beams consisted of beams that failed in shear, as tests on slender beams reinforced with FRP are scarce. The strength prediction models were therefore evaluated on their ability to predict shear capacity. The models included in the analysis are the CSA S806-12, the ACI440.1R-15, the Japan Society of Civil Engineers (JSCE), and the Intelligent Sensing for Innovative Structures (ISIS) Canada Manual No. 3 shear models, as well as a prediction model proposed by Nehdi et al. (2007). The study concluded that Nehdi model most accurately predicts the shear capacity for beams with transverse reinforcement, with the remainder of the models providing very conservative values. For beams without shear reinforcement, all models provided good estimates for the shear capacity, with the CSA S806-12 model matching most closely to experimental data.

The ABAQUS models proposed by Stoner were evaluated against a series of 8 beams taken from literature: two beams without shear reinforcement, and six with shear reinforcement. The results validated the recommendations made by Stoner, and verified the use of 30° dilation concrete to model beams without stirrups, and 50° dilation concrete to model

beams with stirrups. Further research was deemed necessary to accurately model beams that exhibited both flexural crushing and stirrup rupture.

The results of the parametric study suggested that the beams without shear reinforcement required large shear span to depth ratios to fail in flexure, exceeding ratios of 15. The beams with shear reinforcement failed in flexure at slenderness ratios approaching 10, demonstrating the increased shear strength provided by the stirrups. The increase in slenderness ratio required to fail in flexure (compared to steel reinforced beams) is attributed to the larger tensile strength of GFRP bars. Furthermore, an investigation into the shear capacity prediction methods of CSA S806-12 yielded that the model under-predicts the stirrup contribution to shear capacity. Further investigation determined the most likely cause was the modelling of the confinement induced by the stirrups.

# Acknowledgements

I would like to first thank my supervisor, Dr. Maria Anna Polak. Dr. Polak elected to hire me as a Master's student from Physics, despite my limited knowledge in Civil Engineering. Her vast knowledge of concrete mechanics and faith in my abilities have imparted me with a solid foundation in the field, as well as the confidence to conduct meaningful research.

I would next like to thank my colleagues, for helping me make the transition to Civil Engineering almost seamless. I would like to thank Joseph Stoner, for introducing me to ABAQUS and providing me with my first tutorial; Nader Sleiman, without whom I would still be struggling to understand concrete mechanics; Graeme Milligan and Mikhail Laguta, who shared my struggles with modelling in ABAQUS, and for always being sources of advice when needed; and Piotr Wiciak, for always lending an ear when I needed to brainstorm.

Finally, I would like to thank my family for being a constant source of support. Thank you to my father, for always knowing the right thing to say to help me push forward.

# Dedication

I dedicate this thesis to my father, mother, and sister.

# Table of Contents

# List of Tables

# List of Figures

# Chapter 1

# Introduction

The use of concrete-like materials in construction can be dated back to around 6500 BC in the Levant region [27]. Since then, concrete has evolved to become one of the most widely used materials for construction. Concrete gained its popularity as a construction material due to its durability, cost-effectiveness, and sustainability. Due to its brittle nature, however, concrete as a standalone material is limited in sustaining tensile loads.

Francois Coignet, a French industrialist in the nineteenth century, constructed the first known reinforced concrete structure [67]. Coignet did not intend to add to the strength of concrete through reinforcement, but rather intended to use the reinforcement to prevent his concrete walls from overturning. He unknowingly sparked a field of study that would remain relevant for centuries.

Steel, due to its high tensile strength and cost effectiveness, has been the material of choice in reinforced concrete structures. However, due to the porous nature of concrete and its exposure to the environment, the corrosion of reinforcing steel poses a problem in the maintenance and durability of reinforced concrete structures. Several alternatives have been proposed to overcome the issue of corrosion. These alternatives include galvanized steel, stainless steel, and epoxy-coated steel, all of which have found limited success as the next viable option. Fiber reinforced polymers (FRPs), due to their high tensile strength and inability to corrode, have become an increasingly popular topic of research in the last few decades. It is becoming increasingly common to find concrete structures reinforced with FRPs as their success in durability is becoming more apparent.

To cement the use of a new material for construction, extensive testing must be conducted to ensure safety, cost-effectiveness, and overall feasibility. It is necessary to understand the behaviour of structures reinforced with the material to adequately assess its advantages and limitations. Such tests are often expensive and time consuming, and are difficult to implement at research facilities due specimen size/time required. These constraints, in addition to the need for more sustainable structures, have fuelled the need for more innovative testing methods. One such method is the use of numerical modelling techniques to virtually simulate these experiments.

The Finite Element Method (FEM) is a widely-used tool in simulating the behaviour or structures. With proper calibration, commercial FEM software can be used to accurately simulate the behaviour of new materials, and introduce a feasible, time-saving alternative to laboratory testing.

## 1.1 Research Objectives

This thesis aims to build on previous work done to calibrate the ABAQUS FEM software package for use in the testing of FRP reinforced concrete beams. The aim of the study is to conduct a comprehensive FEM analysis of FRP reinforced concrete beams, and validate the findings against experimental data, as well as design standards and codes. Specifically, this study will build on the work conducted by Joseph Stoner [66] to calibrate the ABAQUS software package, and validate the calibrated models by applying them to experimental data taken from literature.

Stoner calibrated the Concrete Damaged Plasticity Model (CDPM) within ABAQUS against test data obtained by Krall [43]. Twelve FRP reinforced, concrete beams were tested by Krall at a slenderness ratio (shear span to depth) of 2.5. This study will extend Stoner's work by conducting a parametric study to investigate the influence of slenderness on FRP reinforced beams, and the validity of current strength prediction methods for beams with higher slenderness ratios. Furthermore, current design codes will be evaluated against an experimental database of FRP reinforced beams taken from literature. A comparison between current strength prediction methods and the FEM results from ABAQUS will be drawn through analysis of the beams in the experimental database.

## 1.2 Thesis Overview

This thesis is organized into six chapters and four appendices.

Chapter 1 provides an overview of the research, and the motivations for conducting it.

Chapter 2 discusses FRP materials, their constituents, manufacturing processes, and material behaviour. Furthermore, Chapter 2 addresses previous testing done on FRP reinforced concrete beams, and current strength prediction methods. Chapter 3 focuses on modelling FRP reinforced concrete beams in ABAQUS. Chapter 4 compiles an experimental database of tested, FRP reinforced concrete beams, and compares current strength prediction methods and FEM results against the tabulated data. Chapter 5 presents a parametric study on the effects of slenderness in FRP reinforced concrete beams using the calibrated ABAQUS model. Finally, Chapter 6 delivers the conclusions of the research, and provides recommendations for future work.

Appendix A provides all the software developed during the study. This includes programs written to automate certain ABAQUS procedures, as well as all MATLAB scripts written to compute predicted shear and flexural capacities of the beams. Appendix B provides detailed drawings of the twelve beams used to calibrate the ABAQUS model. Lastly, Appendices C and D present the results of the parametric study for beams without, and with stirrups respectively.

# Chapter 2

# Background Information, Literature Review, and Strength Prediction Methods for FRP Reinforced Concrete Beams

## 2.1 Fiber Reinforced Polymers

Fiber reinforced polymer (FRP) is a composite material consisting of a polymer matrix reinforced with fibres. The most widely used fibres in FRPs are aramid, carbon, and glass fibres. FRP materials were originally developed for the aviation industry and later saw applications in the automotive, and marine industries. It was not until the 1960s that these composite materials were considered for use in construction. Interest in FRP materials stems from the desirable properties of the composite. The fibres provide most of the strength and stiffness, and carry most of the applied load. The polymer matrix bonds and protects the fibres, and acts to transfer stresses between the fibres through shear stresses [2].

FRP materials see a lot of use in civil engineering nowadays. Common applications include FRP sheets, plates, and wraps for strengthening of existing structures, as well as bars, rods, and pre-stressing tendons for use as reinforcement; some structures even see use of FRP as viable materials for structural elements. This thesis will focus on the use of FRP bars as internal reinforcement in concrete structures.

### 2.1.1 FRP Constituents and Material Behaviour

The Fibres in FRP materials provide the composite with strength, and stiffness. The most widely used fibres for structural applications are carbon, glass, and aramid fibres. Table 2.1 compares properties of interest for carbon, aramid, and glass fibres [35].

Table 2.1: Comparison of Fibre Material

| Criterion | Fiber Type | | |
|---|---|---|---|
| | Carbon | Aramid | Glass |
| Tensile Strength | Very Good | Very Good | Very Good |
| Modulus of Elasticity | Very Good | Good | Adequate |
| Long Term Behaviour | Very Good | Good | Adequate |
| Fatigue Behaviour | Excellent | Good | Adequate |
| Bulk Density | Good | Excellent | Adequate |
| Alkaline Resistance | Very Good | Good | Adequate |
| Price | Adequate | Adequate | Very Good |

Carbon fibres are made through a process called pyrolysis. Pyrolysis is an irreversible process that causes a phase change, as well as a change in chemical composition, of organic material at high temperatures (above 1000 °C) in the absence of oxygen [2]. Carbon FRP (CFRP) is desirable for its high modulus of elasticity, and good long term behaviour, making it a suitable choice in structural applications. These properties make CFRP a good option for pre-stressing tendons, as well as wraps for strengthening of concrete members.

Aramid fibres are fabricated by a process called extrusion and spinning, from aromatic polyamide [55]. This process involves extruding melted and compressed polymer granules, and then feeding them into a spinneret to produce the fibres. Aramid FRP (AFRP) exhibit low compressive strength due to their anisotropic properties. Due to their vulnerability to creep, moisture, and ultraviolet degradation, AFRP are less commonly used in structural applications.

Glass fibres are produced in a five stage process that consists of batching, melting, fiberizing, coating, and drying [25]. The melting process can be done directly, or indirectly. The indirect melting method requires melting and shaping the glass into marbles, which can then be transported and re-melted for fiberization. This method facilitates quality control, as the glass can be inspected for impurities and inconsistencies. Conversely, the direct melt method neglects the intermediary quality control step and proceeds to form the fibres directly after the first melt. This process is inexpensive, making it the primary method for producing glass fibres. The most common grade of glass fibre is E-glass due to its relatively low cost, with a modulus of elasticity ranging from 40-70GPa. Due to its high tensile strength and relatively low modulus of elasticity, glass FRP (GFRP) finds common use as rebar, pultruded structural sections, FRP wraps for seismic applications, and filament wound FRP tubes [7].

To form the composite structure, the fibres are inserted into a polymeric resin matrix. The matrix serves to coat and protect the fibres from environmental degradation, acts to transfer stresses between the fibres, and provides lateral support to prevent buckling under compressive loads [1]. Two resin types are used in the manufacturing of FRPs: thermosetting resins, and thermoplastics.

Thermosetting resins form a rigid, three-dimensional structure once cured due to cross-links formed between molecules [7]. Thermosetting resins exhibit desirable thermal and chemical resistance, making them difficult to re-shape using heat and pressure. However, these properties cause the resin to have low creep and relaxation properties in comparison to thermoplastics. Common thermosetting resins include vinylesters, epoxies, and polyesters.

Vinylesters are commonly used as rebar for concrete due to their notable resistance to strong acids and alkali. Their resistance to the alkaline environment within concrete, in addition to their low moisture absorption and shrinkage rates, makes them ideal for use as reinforcement. Epoxies are tough, high temperature resistant, and exhibit good adhesion properties. They are mainly used in FRP plates and sheets, but are more expensive and less resistant to acidic conditions than polyesters and vinylesters. Polyesters are processed in a similar manner to vinylesters, but are the cheapest of the three resins. They are the most widely used polymers as their resins cure at ambient temperatures.

Thermoplastic polymers are formed by molecules held together by weak, secondary bonds in a linear structure. Due to the weak nature of the bonds, thermoplastics can be re-shaped using heat and pressure. Unlike thermosetting resins, thermoplastics do not find common use in structural applications as they are more susceptible to heat and pressure deformations.

In addition to the fibres and resins, certain fillers and additives are required to achieve the desired mechanical properties, and facilitate processing. Fillers are inorganic compounds added to the polymer resin. They serve to dilute the resin, thereby reducing the production cost. Furthermore, fillers can improve the hardness, shrinkage, and creep performance of composites [66]. Common fillers include calcium carbonate, calcium sulphate, aluminium trihydrate, and aluminium silicate. Additives are also added to the resin to facilitate processing, and can serve to protect against ultraviolet degradation of the composite.

FRPs bars produced for use as internal reinforcement consist of unidirectional fibres, resulting in orthotropic composites. The strength and stiffness of the bars will therefore be greater in the direction of the fibres. Furthermore, FRP bars are linear elastic up to failure as they exhibit no plastic behaviour or yielding; they fail by rupturing. Due to the various methods of manufacturing FRP bars, great variability exists in the compressive strength of available bars, with compressive strengths ranging between 10% and 80% depending on the constituents used [42, 15]. For this reason, design codes typically ignore the compressive strength of FRP bars [6].

### 2.1.2 Manufacturing of FRP Reinforcing Bars

The primary methods for manufacturing FRPs used in structural applications are wet lay-up, filament winding, and pultrusion. Other manufacturing techniques exist but are omitted from this discussion as they are less common for structural applications.

Wet lay-up is a process in which a sheet of fibres is pressed into a resin-covered mold. After the resin cures, the sheet becomes bonded to the structure. To ensure adequate bonding, the resin must be pressed in a manner that completely removes any air trapped between the resin and sheet. This technique is very practical for rehabilitating existing structures as the process can be accomplished in the field. Figure 2.1 illustrates the wet lay-up process.

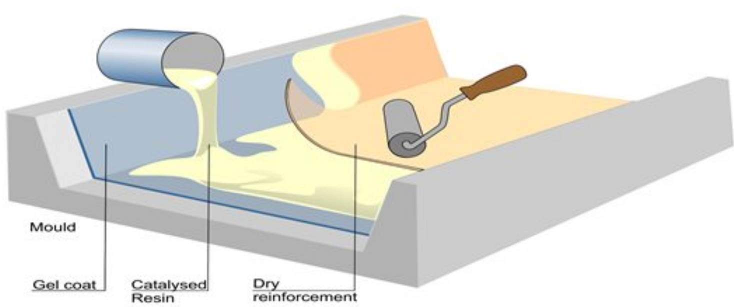


Figure 2.1: Wet Lay-Up Process [57]

Filament winding is a process in which fibres are impregnated with resin, and then wound onto a rotating mandrel [2].The process is entirely automated, allowing the fibres to be oriented with extreme precision. Once cured, the mandrel is removed. Figure 2.2 illustrates the winding process.

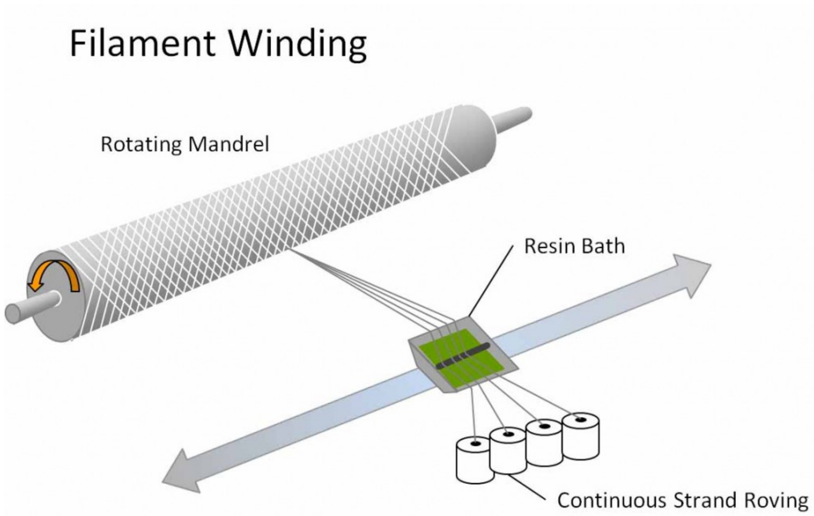


Figure 2.2: Filament Winding Process [30]

Pultrusion is the most common technique used to manufacture elements with constant cross-sections. The process is used in manufacturing bars, rods, tendons, and plates. The raw fibres are spooled into rovings which are stored in metal racks called creels. The fibres are then pulled through a resin bath for coating. After exiting the resin bath, the fibres pass through a preforming system that removes any excess resin as well as aligning the fibres. The fibres are then pulled through a heated die, in which the polymer matrix hardens to the shape of the die, producing the desired structural component. Once cured, the composite is pulled through the die in a continuous process, creating a unidirectional FRP. Furthermore, the continuous pulling of the FRP through the die allows products of any set length to be produced. The process is automated and requires very little human input, making it very cost effective. Figure 2.3 illustrates the pultrusion process.

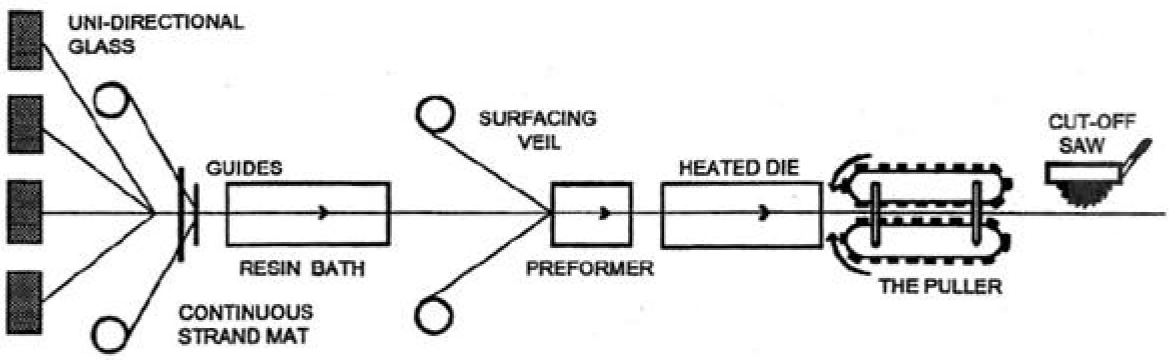


Figure 2.3: Pultrusion Process [13]

## 2.2 Tests on Concrete Beams with FRP as Internal Reinforcement

### 2.2.1 Overview of Specimens

The work done by Stoner to calibrate ABAQUS for the modelling of GFRP reinforced concrete beams is based on an experimental program run by Martin Krall at the University of Waterloo. Krall [43] tested 12 simply supported beams under three point loading, with and without shear reinforcement. The main objective of the testing was to study the influence of longitudinal and transverse reinforcement arrangements on the strength and failure mode of the beams. The 12 beams maintained a shear span to depth ratio of 2.5, making them deep beams; flexural failure of the beams was therefore not observed. Detailed drawings of the beams can be found in Appendix B. This section provides a brief overview of the experimental program, and discusses any significant results. For more detailed information regarding the testing, the reader is directed to Krall's thesis.

The beams tested contained longitudinal reinforcement with core diameters of 12,16, and

25mm, as well as closed-loop stirrups with core diameters equal to 12, and 20mm. To keep the moment capacity of the beams relatively similar, the arrangement and number of longitudinal bars in each beam were chosen as follows: 3 layers of 4 bars for beams with 12mm bars, 2 layers of 3 bars for beams with 16mm bars, 1 layer of 2 bars for beams with 25mm bars. Furthermore, all beams tested maintained a shear span to depth ratio (slenderness ratio) of 2.5, with a shear span of 675mm and a depth of 270mm. Keeping the slenderness ratio constant allowed for a more efficient test setup, as only a single pedestal configuration was required for testing. The height of the specimens varied slightly in order achieve a constant slenderness ratio, and accommodate the varying bar arrangements.

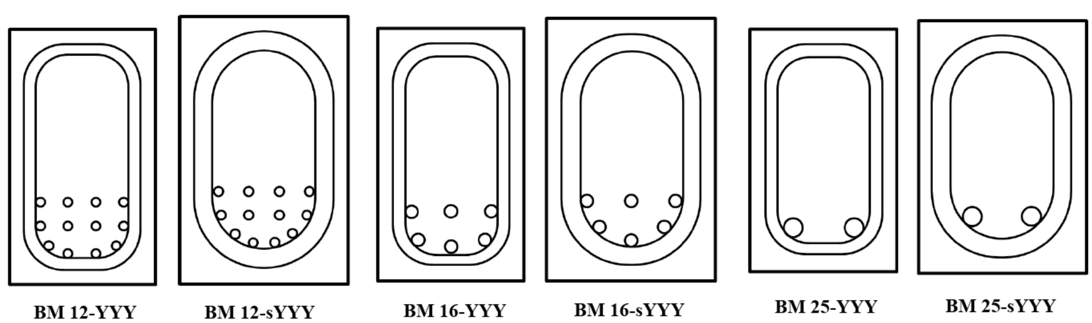


Figure 2.4: Beam Sections and Bar Configurations for Krall's Experimental Program [66]

The beams were named according to the convention BM XX-(s)YYY. XX denotes the core diameter of the longitudinal reinforcement, while the presence of 's' ahead of YYYY signifies the use of 20mm stirrups. YYY denotes the spacing of the stirrups in millimeters, and can assume the values 150,220,230, and INF (infinite spacing for beams with no stirrups). The letter 's' is only applicable to beams with 230mm stirrup spacing as it is the only case where 20mm diameter stirrups are used. To exemplify the naming convention, the beam BM 12-s230 contains 12mm longitudinal reinforcement, with 20mm diameter stirrups spaced at 230mm. Figure 2.4 illustrates the different beam sections used in the study, while Table 2.2 summarizes the material properties of the beams. The beam width, height, and depth are denoted by $b$, $h$, and $d$ respectively, while the longitudinal and transverse reinforcement ratios are denoted by $\rho_F$ and $\rho_V$ respectively. Furthermore, the compressive strength of the concrete, the modulus of elasticity of the rebar, and the modulus of elasticity of the stirrups are represented by $f'_c$, $E_F$, and $E_V$ respectively.

Table 2.2: Beam Properties

| Beam | $b$ (mm) | $h$ (mm) | $d$ (mm) | $\rho_F$ (%) | $\rho_V$ (%) | $f'_c$ (MPa) | $E_F$ (GPa) | $E_V$ (GPa) |
|---|---|---|---|---|---|---|---|---|
| 12-INF | | | | | 0.00 | 54 | | |
| 12-150 | 200 | 350 | 270 | 2.51 | 0.75 | 56.5 | 60 | 50 |
| 12-220 | | | | | 0.51 | 56.5 | | |
| 16-INF | | | | | 0.00 | 53.4 | | |
| 16-150 | 200 | 345 | 270 | 2.23 | 0.75 | 56.5 | 64 | 50 |
| 16-220 | | | | | 0.51 | 56.5 | | |
| 25-INF | | | | | 0.00 | 52 | | |
| 25-150 | 200 | 330 | 270 | 1.82 | 0.75 | 56.5 | 60 | 50 |
| 25-220 | | | | | 0.51 | 56.5 | | |
| 12-s230 | | 365 | | 2.18 | | | 60 | |
| 16-s230 | 230 | 360 | 270 | 1.94 | 1.19 | 56.5 | 64 | 50 |
| 25-s230 | | 345 | | 1.58 | | | 60 | |

At the time of testing, the maximum load supported by the testing frames at the University of Waterloo was 500KN. All beams were designed according to CSA S806-12, with the maximum testing frame load taken into account. The cover and spacing requirements set forth by CSA S806-12 were not followed rigorously to accommodate the large number of bars, while remaining within the testing frame limits. Furthermore, a highly workable concrete needed to be used to ensure the voids surrounding the bars were filled, preventing honeycombing. The concrete mix used contained 3/8 inch pea-stone aggregate, 200-250mm slump, and plasticizer to ensure workability.

### 2.2.2 Experimental Results

Strain gauges and linear variable displacement transformers (LVDTs) were used to measure the strain and displacement responses of the specimens. To measure the strains in the longitudinal reinforcement, strain gauges were placed at the midspan on the middle bars in each reinforcement layer. The strains in the stirrups were measured by placing a strain gauge at the mid-height of the stirrup on the straight portion of the bar, as well as directly above the bent portion on the opposing side. The beam displacements were measured by placing LVDTs at the mid-span as well as two quarter span locations.

The beams exhibited two modes of failure: shear-tension failure in beams without stirrups, and shear-compression failure in beams with stirrups; no stirrups ruptured during testing. Under loading, all beams initially developed flexural cracks at the midspan, which then propagated. The flexural cracking began at the stirrup locations in beams with transverse reinforcement. Shear cracks subsequently began to form at the load application point, and propagated down to the supports.

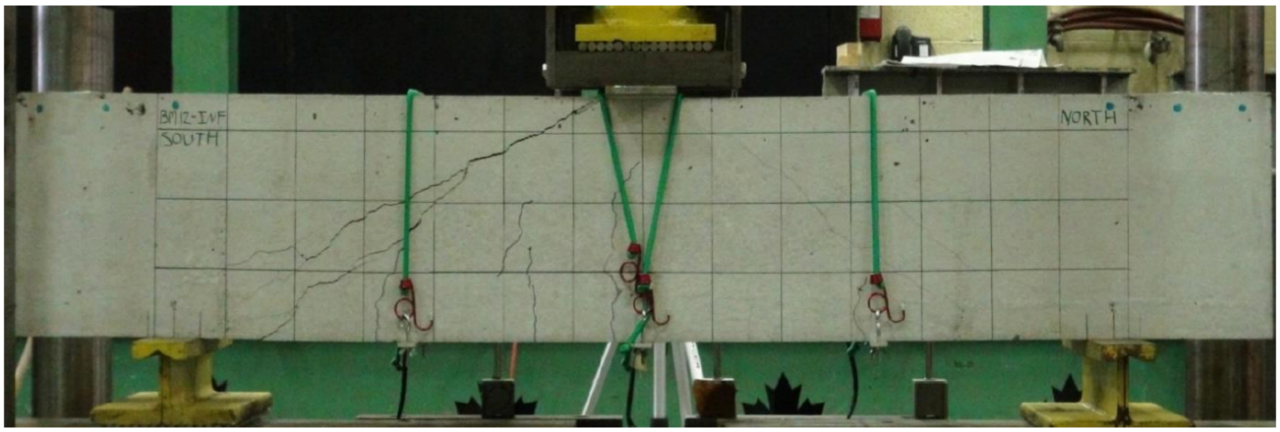


(a) Failure of BM 12-INF

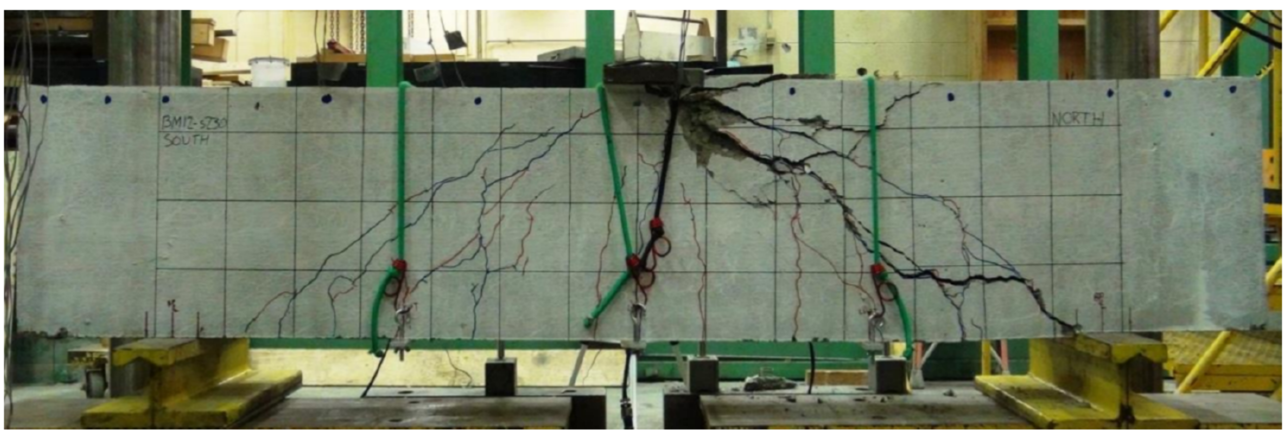


(b) Failure of BM 12-s230

Figure 2.5: Typical Failure Modes for Beams with and without Stirrups [66]

Figure 2.5a shows the typical failure mode for beams without stirrups. The cracks can be seen propagating towards the reinforcement layers, suggesting tensile-splitting. For the beams with stirrups, the concrete is visibly crushed near the load plate, suggesting a shear compression failure. The shear crack can also be seen on the right hand side of Figure 2.5b; it is noticeably larger than in beams with no transverse reinforcement.

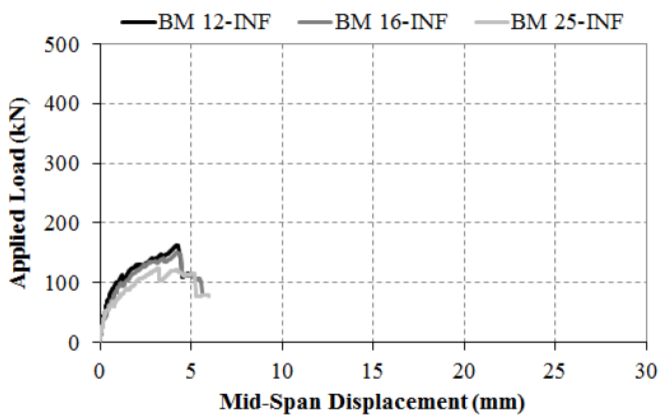


(a) Beams with no Stirrups

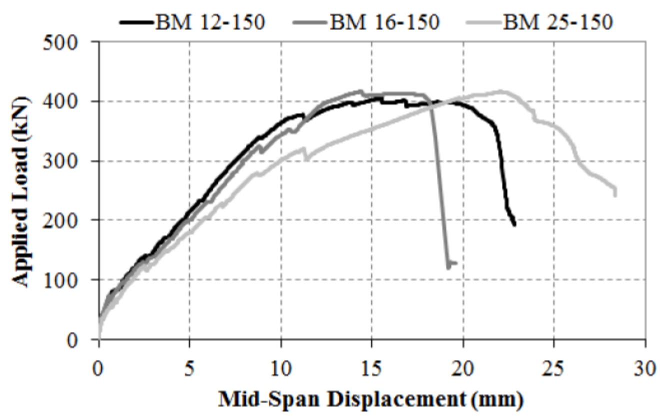


(b) Beams with Stirrups Spaced at 150mm

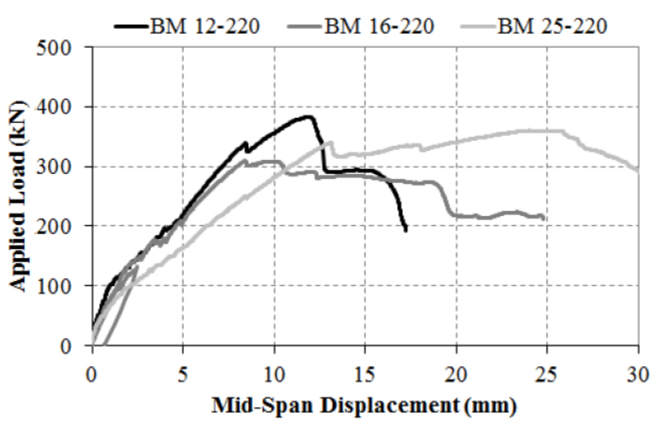


(c) Beams with Stirrups Spaced at 220mm

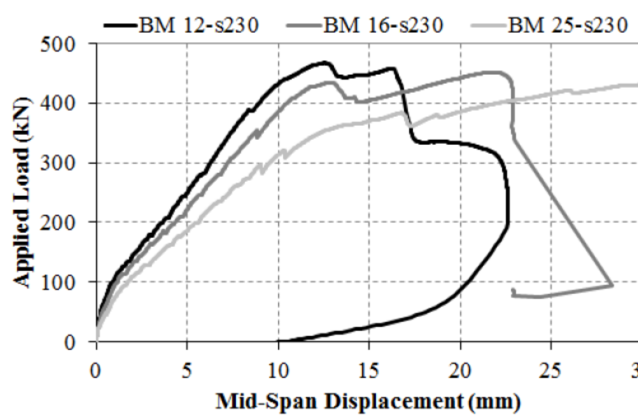


(d) Beams with Stirrups Spaced at 230mm

Figure 2.6: Load-Displacement Data for BM series [66]

Figure 2.6 displays the load-displacement data for the 12 beams. For beams without stirrups, Figure 2.6a shows that the largest response belonged to BM 12-INF, suggesting that an increase in longitudinal reinforcement ratio leads to a stiffer response. The same pattern can be observed for beams with stirrups, as the peak loads are related to the longitudinal reinforcement ratios. Figures 2.6c and 2.6d also show some post-peak ductile behaviour.

## 2.3 Strength Prediction Methods for FRP Reinforced Concrete Beams

### 2.3.1 Flexure

The CSA and ACI code provisions to determine the flexural capacity of an FRP reinforced concrete member share the following assumptions:

(i) Plane sections remain plane.

(ii) The tensile stresses in FRP are calculated using a linear relationship with strain.

(iii) Perfect bond exists between the FRP and concrete.

In calculating the flexural resistance, the following provisions also separate the calculation into two cases based on failure mode (concrete crushing, FRP rupture).

A MATLAB code to perform each calculation can be found in Appendix A.

#### CSA S806-12

The provisions set forth by CSA S806-12 [14] to determine the factored flexural resistance of a concrete section reinforced with FRP longitudinal bars uses the traditional Whitney stress block approach. The provisions for flexure can be found in Clause 8.4.1.

Furthermore, Clauses 8.4.1.2 and 8.4.1.3 state that the ultimate compressive strain in the concrete shall be 0.0035, and that the tensile stress of the concrete is to be ignored when calculating flexural capacity of reinforced/prestressed members.

Clause 8.4.1.4 assumes the compressive strain of concrete reaches the limit of 0.0035 provided that the following condition is met

$$(c/d) \geq \frac{7}{7 + 2000\epsilon_{Fu}},$$

where $\epsilon_{Fu}$ is the ultimate strain in the FRP reinforcement, c is the distance from the extreme compression fibre to the neutral axis, and d is the distance from the extreme compression fibre to the centroid of the longitudinal tension force.

Should the requirement of Clause 8.4.1.4 be satisfied, Clause 8.4.1.5 specifies that the stress in concrete should be calculated by $\alpha_1 \phi_c f'_c$, shall be uniformly distributed over the cross section, and be located at a distance $a = \beta_1 c$ from the fibre of maximum compressive strain. The clause further defines $\alpha_1$ and $\beta_1$ as

$$\alpha_1 = 0.85 - 0.0015 f'_c \geq 0.67$$
$$\beta 1 = 0.97 - 0.0025 f'_c \geq 0.67,$$

where $\phi_c$ is a safety factor applied to the concrete.

A MATLAB code to perform the calculation can be found in Appendix A. The following briefly outlines the code's algorithm.

1. Solve for stress in the FRP by calculating the tensile force in FRP (stress block) using an initial guess for FRP strength.

2. Find the strain in the FRP (using similar triangles) and use the calculated strain and Hooke's Law to find the stress in the FRP.

3. The strength is updated using a trapezoidal formulation involving the current guess and the calculated FRP stress.

4. Iterate until calculated stress match current guess.

5. Separate over-reinforced and under-reinforced cases by comparing calculated stress to $f_{Fu}$ (ultimate strength of FRP).

6. If the under-reinforced case is triggered (stress in FRP $>$ ultimate stress), $M_r$ is calculated by

$$M_r = \phi_f A_f f_f (d - \frac{\beta_1 c}{2}),$$

where $f_f$ is the calculated FRP stress, $\phi_f$ is a safety factor applied to FRP, and $A_f$ is the total area of longitudinal reinforcement.

7. If the over-reinforced case is triggered, $M_r$ is calculated using the same equation as above, however iteration is required to find the correct strain in the FRP. The parameters $\alpha_1$ and $\beta_1$ are also redefined as (for over-reinforced cases)

$$\beta_1 = (4 - \frac{\epsilon_{current}}{\epsilon_c})/(6 - 2\frac{\epsilon_{current}}{\epsilon_c})$$
$$\alpha_1 = (\frac{\epsilon_{current}}{\epsilon_c} - \frac{1}{3}(\frac{\epsilon_{current}}{\epsilon_c})^2)/\beta_1,$$

where $\epsilon_{current}$ is the current guess for strain in FRP (updated to calculated strain at each step of iteration, until they are equal), and $\epsilon_c$ is the peak strain in the Hognestad Parabola.

The failure load can also be calculated depending on the test set up for the beams. All beams used in this report follow either a three-point bend or four-point bend set up.

### ACI440.1R-15

The approach outlined in the ACI440.1R-15 [3] document to determine the flexural capacity of an FRP reinforced concrete section assumes that he tensile strength of concrete is ignored (Section 7.1.2).

ACI440 divides the calculation into two cases based on failure condition: failure by FRP rupture, and failure by concrete crushing.

The appropriate case is selected by comparing the section reinforcement ratio (1.1.2a) to the balanced ratio (1.1.2b). If the reinforcement ratio is less than the balanced ratio, FRP rupture controls. Otherwise, concrete crushing controls.

$$\rho_f = \frac{A_f}{bd} \tag{1.1.2a}$$

$$\rho_{fb} = 0.85\beta_1 \frac{f'_c}{f_{fu}} \frac{E_f \epsilon_{cu}}{E_f \epsilon_{cu} + f_{fu}}, \tag{1.1.2b}$$

where $A_f$ is the total area of longitudinal reinforcement, b is the beam width, d is the distance from the extreme compression fibre to the centroid of the longitudinal tension reinforcement, $\beta_1$ is the Whitney stress block parameter, $f_{fu}$ is the ultimate tensile strength of the FRP, $\epsilon_{cu}$ is the ultimate strain in concrete, and $E_f$ is the modulus of elasticity of the FRP.

Unlike the CSA, the ACI does not require an iterative procedure to determine the flexural capacity, but rather derives the required equations from equilibrium of forces and strain compatibility.

The required equations for the concrete crushing mode of failure are

$$M_n = \rho_f f_f \left(1 - 0.59\frac{\rho_f f_f}{f_c'}\right) bd^2, \quad \text{where}$$

$$f_f = \left(\sqrt{\frac{(E_f \epsilon_{cu})^2}{4} + \frac{0.85\beta_1 f_c'}{\rho_f} E_f \epsilon_{cu}} - 0.5 E_f \epsilon_{cu}\right) \leq f_{fu}$$

If the controlling limit state is FRP rupture, the required equation to compute the flexural capacity is given by

$$M_n = A_f f_{fu}(d - \frac{\beta_1 c}{2}),$$

where $\beta_1$ and c are obtained by following the procedures listed for steel reinforcement in ACI318.

A safety factor is to be applied to the final calculated value and is determined by the following.

$$\phi = \begin{cases} 0.55 & \text{for } \rho_f \leq \rho_{fb} \\ 0.3 + 0.25\frac{\rho_f}{\rho_{fb}} & \text{for } \rho_{fb} < \rho_f < 1.4\rho_{fb} \\ 0.65 & \text{for } \rho_f \geq 1.4\rho_{fb} \end{cases}$$

### 2.3.2 Shear

The following provisions calculate the shear capacity of an FRP reinforced member by summing the contributions from the concrete, and stirrups separately.

$$V_r = V_{concrete} + V_{stirrups},$$

A MATLAB code to perform each calculation can be found in Appendix A.

#### CSA S806-12

The total factored shear capacity of a beam is outlined in Clause 8.4.4 [14] and is defined by

$$V_r = V_c + V_{sF},$$

where $V_c$ is the factored resistance provided by the concrete, and $V_{sF}$ is the factored shear resistance provided by the FRP stirrups. Clause 8.4.4.4 requires that the ultimate shear resistance not exceed (for non-prestressed members)

$$V_r \leq V_{r,max} = 0.22\phi_c f'_c b_w d_v,$$

where $\phi_c$ is the safety factor for concrete, $b_w$ is the beam width, $f'_c$ is the compressive strength of the concrete, and $d_v$ is the effective shear depth.

The effective shear depth $d_v$ is taken to be the larger of $0.9d$ or $0.72h$, where d is the distance from the extreme compression fibre to the centroid of the longitudinal tension force, and h is the height of the member.

The concrete contribution to the shear capacity is outlined in Clause 8.4.4.5 and states that for members with an effective depth less than 300mm, and $f'_c$ less than 60MPa

$$V_c = 0.005\lambda\phi_c k_m k_r (f'_c)^{\frac{1}{3}} b_w d_v,$$

where $\lambda$ is a factor that accounts for concrete density (taken as 1 for normal density concrete), $k_m$ is a factor that accounts for the influence of bending moment, and $k_r$ is a factor that accounts for the influence of the reinforcement's rigidity. $k_m$ and $k_r$ are calculated by

$$k_m = \sqrt{\frac{V_f d}{M_f}} \leq 1.0$$

$$k_r = 1 + (E_f \rho_{Fw})^{\frac{1}{3}},$$

where $V_f$ and $M_f$ are the factored shear force and bending moment at the chosen section, and $\rho_{Fw}$ is the longitudinal reinforcement ratio.

Furthermore, Clause 8.4.4.5 imposes upper and lower bounds on the value of $V_c$, given by

$$V_c < 0.22\phi_c\sqrt{f'_c} b_w d_v,$$

$$V_c > 0.11\phi_c\sqrt{f'_c} b_w d_v,$$

Clause 8.4.4.6 defines the shear modification factor $k_a$. This factor accounts for arch effect and is applicable to sections located within a distance of $2.5d$ from the face of a support that causes compression parallel to the direction of shear in the beam. $k_a$ is given by

$$k_a = \frac{2.5}{\frac{M_f}{V_f d}},$$

$$1.0 \leq k_a \leq 2.5$$

Clause 8.4.4.7 specifies a modification factor $k_s$ (applied to $V_c$) for members with an effective depth greater than 300mm and less transverse shear reinforcement than required by Clause 8.4.5.2. $k_s$ is given by

$$k_s = \frac{750}{450 + d} \leq 1.0,$$

and is taken to be 1.0 in cases where the effective depth is greater than 300mm but adequate transverse shear reinforcement is provided.

Clause 8.4.4.9 provides the equations to calculate the shear reinforcement's contribution to the factored shear capacity. The clause defines $V_{sF}$ (for members whose transverse reinforcement is perpendicular to the longitudinal axis) to be

$$V_{sF} = \frac{0.4\phi_F A_{Fv} f_{Fu} d_v}{s} cot\theta,$$

where $\phi_F$ is the safety factor for the FRP, $A_{Fv}$ is the area of transverse shear reinforcement, $f_{Fu}$ is the ultimate tensile strength of the FRP (straight portion) and shall not exceed $0.005E_F$, $s$ is the spacing of the transverse reinforcement, and theta is given by

$$\theta = 30^\circ + 7000\epsilon_l,$$

where $\epsilon_l$ is the longitudinal strain at mid-depth, and is calculated by

$$\epsilon_l = \frac{\frac{M_f}{d_v} + (V_f - V_p) + 0.5N_f - A_p f_{po}}{2(E_F A_F + E_p A_p)} \geq 0,$$

where $V_p$ is the component of the prestressing force in the direction of applied shear, $N_f$ is the factored axial load normal to the cross section, $A_p$ is the area of the prestressing tendons, $f_{po}$ is the stress in prestressing tendon when strain in the surrounding concrete is zero, $A_F$ is the total area of the FRP longitudinal reinforcement, and $E_p$ is the elastic modulus of the prestressing tendons. Furthermore, $V_f$ and $M_f$ must be positive and Mf shall not be taken less than $(V_f - V_p)d_v$.

Clause 8.4.4.9 also states that $\epsilon_l$ can also be calculated at a distance of $d$ from the support if the section of interest is closer than $d$ from the face of the support. Lastly, the value of $\theta$ is bounded by

$$30^\circ \leq \theta \leq 60^\circ$$

If $M_f$ and $V_f$ are not given, it is possible to write them in terms of the applied load and implement an iteration scheme over the applied load until it matches the calculated shear capacity $V_r$.

### ACI440.1R-15

The ACI [3] provides a similar approach for calculating the factored shear capacity of FRP reinforced beams as for steel reinforced beams. The procedure is outlined in Chapter 8 of the ACI440 document. The ultimate shear resistance is given by

$$V_u = V_c + V_f,$$

The concrete contribution to the shear capacity is given by

$$V_c = 5\sqrt{f_c'} b_w(kd) \quad \text{(Imperial)},$$
$$V_c = \frac{2}{5}\sqrt{f_c'} b_w(kd) \quad \text{(SI)},$$

where $f_c'$ is the compressive strength of the concrete, $b_w$ is the width of the beam, $d$ is the distance from the extreme compression fibre to the centroid of the longitudinal tension force, and k is given by

$$k = \sqrt{2\rho_f n_f + (\rho_f n_f)^2} - \rho_f n_f,$$

where

$$n_f = \frac{E_f}{E_c},$$

where $E_f$ is the modulus of elasticity of the longitudinal FRP reinforcement, and $E_c$ is the modulus of elasticity of the concrete.

The transverse reinforcement's contribution to the shear capacity is given by

$$V_f = \frac{A_{fv} f_{fv} d}{s},$$

where $A_{fv}$ is the area of transverse shear reinforcement perpendicular to the member's axis, $s$ is the spacing of the transverse reinforcement, and $f_{fv}$ is given by

$$f_{fv} = 0.004 E_f \leq f_{fb},$$

where $E_f$ is the modulus of elasticity of the FRP stirrup, and $f_{fb}$ is the tensile strength of the bent portion of the FRP stirrup.

**Nehdi et al., 2007**

The model proposed by Nehdi et al. [53] uses a genetic algorithm to solve for coefficients to be used in the shear equations. The genetic algorithm is a global optimization technique used to minimize the difference between an experimental database and the predicted values for the shear capacity, and is mostly used for complex and non-linear problems. Nehdi et al. obtained their optimized coefficients by feeding a database of 168 FRP reinforced beams through the algorithm, 68 of which had no transverse reinforcement. The total shear capacity is given by

$$V_r = V_{cf} + V_{fv},$$

The concrete contribution to the shear capacity was found to depend on the slenderness ratio of the beams (a/d), where a is the shear span of the beam, and d is the distance from the extreme compression fibre to the centroid of the longitudinal tension force. The optimized concrete contribution is given by

$$V_{cf} = \begin{cases} 2.1 \left(\frac{f'_c \rho_{fl} d}{a} \frac{E_{fl}}{E_s}\right)^{0.23} b_w d & \text{for } \frac{a}{d} > 2.5 \\ 2.1 \left(\frac{f'_c \rho_{fl} d}{a} \frac{E_{fl}}{E_s}\right)^{0.23} b_w d \left(\frac{2.5d}{a}\right) & \text{for } \frac{a}{d} < 2.5, \end{cases}$$

where $f'_c$ is the compressive strength of the concrete, $\rho_{fl}$ is the longitudinal reinforcement ratio, $E_{fl}$ is the modulus of elasticity of the longitudinal reinforcement, $E_s$ is the modulus of elasticity of steel (usually taken as 200GPa), and $b_w$ is the width of the beam.

The transverse shear reinforcement's contribution to the shear capacity is given by

$$V_{fv} = 0.74(\rho_{fv} f_{fv})^{0.51} b_w d,$$

where $\rho_{fv}$ is the transverse reinforcement ratio, and $f_{fv}$ is the ultimate tensile strength of the transverse shear reinforcement.

**Japan Society of Civil Engineers (JSCE)**

The Japan Society of Civil Engineers [40] define the total shear capacity of a member to be

$$V_{ud} = V_{cd} + V_{sd},$$

where $V_{ud}$ is the design shear capacity of the member, $V_{cd}$ is the concrete contribution to shear capacity, and $V_{sd}$ is the transverse shear reinforcement's contribution to the shear capacity. $V_{cd}$ is given by

$$V_{cd} = \frac{\beta_d \beta_p \beta_n f_{vcd} b_w d}{\gamma_b},$$

where

$$f_{vcd} = \sqrt[3]{f'_{cd}} \leq 0.72,$$
$$\beta_d = \sqrt[4]{\frac{1}{d}} \leq 1.5,$$
$$\beta_p = \sqrt[3]{\frac{100\rho_w E_{fu}}{E_0}} \leq 1.5,$$
$$\beta_n = \begin{cases} 1 + \frac{M_0}{M_d} & \text{for } N'_d \geq 0 \\ 1 + 2\frac{M_0}{M_d} & \text{for } N'_d < 0, \end{cases}$$
$$0 \leq \beta_n \leq 2,$$

where $f'_{cd} = f'_c/\gamma_c$ ($\gamma_c$ is a safety factor for concrete, and $f'_c$ is the compressive strength of concrete), $b_w$ is the width of the member section, d is the distance from the extreme compression fibre to the centroid of longitudinal tension force, $E_{fu}$ is the modulus of elasticity of the longitudinal tensile reinforcement, $E_0$ is the reference modulus of elasticity (steel, 200GPa), $M_0$ is the bending moment required to cancel out stresses set up by axial forces in the tensioned edge, relative to design bending moment $M_d$, $N'_d$ is the design axial compressive force, $\gamma_b$ is a material factor generally taken as 1.3, and $\rho_w$ is the longitudinal reinforcement ratio given by

$$\rho_w = \frac{A_f}{b_w d},$$

where $A_f$ is the total cross-sectional area of the longitudinal reinforcement.

The transverse shear reinforcement's contribution to the shear capacity (for non-prestressed members) is given by

$$V_{cd} = \left( \frac{A_w E_w \epsilon_{fwd} (sin\alpha_s + cos\alpha_s)}{s_s} \right) \frac{z}{\gamma_b},$$

where $A_w$ is the total area of shear reinforcement, $E_w$ is the modulus of elasticity of the shear reinforcement, $\alpha_s$ is the angle between the shear reinforcement and the member axis, $s_s$ is the spacing of the shear reinforcement, $z$ is the distance from the point of action of the compressive stress resultant force (generally taken as $\frac{d}{1.15}$), and $\epsilon_{fwd}$ is given by

$$\epsilon_{fwd} = \sqrt{f'_{mcd}\frac{\rho_w E_{fu}}{\rho_{web} E_w}}\left[1 + 2\left(\frac{\sigma'_N}{f'_{mcd}}\right)\right] * 10^{-4},$$
$$\sigma'_N = \frac{N'_d}{A_g} \leq 0.4 f'_{mcd},$$
$$f'_{mcd} = \left(\frac{h}{0.3}\right)^{\frac{-1}{10}} f'_{cd},$$

where $A_g$ is the gross area of the section, and $h$ is the height of the member.

### Intelligent Sensing for Innovative Structures (ISIS) Canada Manual No.3

The design manual set forth by ISIS Canada's [37] group of researchers defines the shear capacity of a member to be

$$V = V_c + V_{FRP},$$

where $V_c$ is the concrete contribution to shear capacity, and $V_{FRP}$ is the transverse shear reinforcement's contribution to the shear capacity. $V_c$ is given as

$$V_c = 0.2\lambda\phi_c\sqrt{f'_c} b_w d\sqrt{\frac{E_{frp}}{E_s}},$$

for sections with $d < 300mm$ or containing at least the minimum transverse reinforcement, and

$$V_c = \left(\frac{260}{1000 + d}\right)\lambda\phi_c\sqrt{f'_c} b_w d\sqrt{\frac{E_{frp}}{E_s}} \geq V_{c,min},$$
$$V_{c,min} = 0.1\lambda\phi_c\sqrt{f'_c} b_w d\sqrt{\frac{E_{frp}}{E_s}},$$

for sections with $d > 300mm$ and not containing at least the minimum transverse reinforcement, where $\lambda$ is the concrete density factor, $\phi_c$ is the safety factor for concrete, $f'_c$ is the compressive strength of the concrete, $b_w$ is the width of the section, d is the distance from the extreme compression fibre to the centroid of longitudinal tension force, $E_{frp}$ is the modulus of elasticity of the flexural reinforcement, and $E_s$ is the modulus of elasticity of steel (200GPa).

The transverse reinforcement's contribution to the shear capacity is based on the criteria given in the Canadian Highway Bridge Design Code (CHBDC 2006) and is given by

$$V_{FRP} = \phi_{frp} \frac{A_{frpv} \sigma_v d_v cot\theta}{s},$$

where $\phi_{frp}$ is the material safety factor for the FRP (taken as 1 in all subsequent calculations), $A_{frpv}$ is the area of the transverse shear reinforcement, $d_v$ is the effective shear depth taken to be $0.9d$, $s$ is the spacing of the transverse reinforcement, $\theta$ is calculated in the same manner (requires iteration) as outlined in the CSA code, and $\sigma_v$ is the effective tensile capacity of stirrups given by

$$\sigma_v = \frac{(0.05 \frac{r_b}{d_s} + 0.3) f_{frpv}}{1.5},$$

where $r_b$ is the bend radius of the stirrups, $d_s$ is the diameter of the stirrups, and $f_{frpv}$ is the ultimate tensile capacity of the transverse reinforcement.

### 2.3.3 Summary of Strength Prediction Methods

Table 2.3: Summary of Strength Prediction Methods

| Code | Flexure | Shear |
|---|---|---|
| **CSA S806-12** | $M_r = \phi_f A_f f_f (d - \frac{\beta_1 c}{2})$ | $V_r = V_c + V_{sF} \leq 0.22\phi_c f_c' b_w d_v$,<br>$V_c = 0.005\lambda\phi_c k_m k_r (f_c')^{\frac{1}{3}} b_w d_v$,<br>$V_c \geq 0.22\phi_c \sqrt{f_c'} b_w d_v$,<br>$V_c \leq 0.11\phi_c \sqrt{f_c'} b_w d_v$,<br>$k_m = \sqrt{\frac{V_f d}{M_f}} \leq 1.0$,<br>$k_r = 1 + (E_f \rho_{Fw})^{\frac{1}{3}}$,<br>$1.0 \leq k_a = \frac{2.5}{\frac{M_f}{V_f d}} \leq 2.5$,<br>$k_s = \frac{750}{450+d} \leq 1.0$,<br>$V_{sF} = \frac{0.4\phi_F A_{Fv} f_{Fu} d_v}{s} cot\theta$,<br>$\theta = 30° + 7000\epsilon_l$,<br>$30° \leq \theta \leq 60°$,<br>$\epsilon_l = \frac{\frac{M_f}{d_v} + (V_f - V_p) + 0.5N_f - A_p f_{po}}{2(E_F A_F + E_p A_p)} \geq 0$ |
| **ACI440.1R-15** | $\rho_f = \frac{A_f}{bd}$,<br>$\rho_{fb} = 0.85\beta_1 \frac{f_c'}{f_{fu}} \frac{E_f \epsilon_{cu}}{E_f \epsilon_{cu} + f_{fu}}$,<br>Concrete Crushing:<br>$M_n = \rho_f f_f \left(1 - 0.59\frac{\rho_f f_f}{f_c'}\right) bd^2$,<br>$f_f = \left(\sqrt{\frac{(E_f \epsilon_{cu})^2}{4} + \frac{0.85\beta_1 f_c'}{\rho_f} E_f \epsilon_{cu}} - 0.5 E_f \epsilon_{cu}\right)$,<br>$f_f \leq f_{fu}$,<br>FRP Rupture:<br>$M_n = A_f f_{fu} (d - \frac{\beta_1 c}{2})$ | $V_u = V_c + V_f$,<br>$V_c = \frac{2}{5}\sqrt{f_c'} b_w (kd)$,<br>$k = \sqrt{2\rho_f n_f + (\rho_f n_f)^2} - \rho_f n_f$,<br>$n_f = \frac{E_f}{E_c}$,<br>$V_f = \frac{A_{fv} f_{fv} d}{s}$,<br>$f_{fv} = 0.004 E_f \leq f_{fb}$ |
| **Nehdi et al. (2007)** | - | $V_r = V_{cf} + V_{fv}$,<br>$V_{cf} = \begin{cases} 2.1\left(\frac{f_c' \rho_{fl} d}{a} \frac{E_{fl}}{E_s}\right)^{0.23} b_w d \text{ for } \frac{a}{d} > 2.5 \\ 2.1\left(\frac{f_c' \rho_{fl} d}{a} \frac{E_{fl}}{E_s}\right)^{0.23} b_w d \left(\frac{2.5d}{a}\right) \text{ for } \frac{a}{d} < 2.5 \end{cases}$,<br>$V_{fv} = 0.74(\rho_{fv} f_{fv})^{0.51} b_w d$ |

| | | |
|---|---|---|
| **JSCE (1997)** | - | $V_{ud} = V_{cd} + V_{sd}$,<br>$V_{cd} = \frac{\beta_d \beta_p \beta_n f_{vcd} b_w d}{\gamma_b}$,<br>$f_{vcd} = \sqrt[3]{f'_{cd}} \leq 0.72$,<br>$\beta_d = \sqrt[4]{\frac{1}{d}} \leq 1.5$,<br>$\beta_p = \sqrt[3]{\frac{100 \rho_w E_{fu}}{E_0}} \leq 1.5$,<br>$\beta_n = \begin{cases} 1 + \frac{M_0}{M_d} & \text{for } N'_d \geq 0 \\ 1 + 2\frac{M_0}{M_d} & \text{for } N'_d < 0, \end{cases}$<br>$0 \leq \beta_n \leq 2$,<br>$f'_{cd} = f'_c/\gamma_c$,<br>$\rho_w = \frac{A_f}{b_w d}$,<br>$V_{cd} = \left(\frac{A_w E_w \epsilon_{fwd}(sin\alpha_s + cos\alpha_s)}{s_s}\right) \frac{z}{\gamma_b}$,<br>$\epsilon_{fwd} = \sqrt{f'_{mcd} \frac{\rho_w E_{fu}}{\rho_{web} E_w}} \left[1 + 2\left(\frac{\sigma'_N}{f'_{mcd}}\right)\right] * 10^{-4}$,<br>$\sigma'_N = \frac{N'_d}{A_g} \leq 0.4 f'_{mcd}$,<br>$f'_{mcd} = \left(\frac{h}{0.3}\right)^{\frac{-1}{10}} f'_{cd}$ |
| **ISIS Canada Manual No. 3** | Same as CSA S806-12 | $V = V_c + V_{FRP}$,<br>$V_{FRP} = \phi_{frp} \frac{A_{frpv} \sigma_v d_v cot\theta}{s}$,<br>$\sigma_v = \frac{(0.05\frac{r_b}{d_s} + 0.3) f_{frpv}}{1.5}$,<br>For $d < 300mm$/adequate reinforcement:<br>$V_c = 0.2\lambda\phi_c\sqrt{f'_c} b_w d \sqrt{\frac{E_{frp}}{E_s}}$,<br>For $d > 300mm$/inadequate reinforcement:<br>$V_c = \left(\frac{260}{1000+d}\right)\lambda\phi_c\sqrt{f'_c} b_w d \sqrt{\frac{E_{frp}}{E_s}} \geq V_{c,min}$,<br>$V_{c,min} = 0.1\lambda\phi_c\sqrt{f'_c} b_w d \sqrt{\frac{E_{frp}}{E_s}}$ |

# Chapter 3

# Finite Element Modelling of FRP Reinforced Beams in ABAQUS

Chapter 2 discussed the work conducted by Joseph Stoner to test FRP reinforced concrete beams. Stoner's thesis focused on the calibration of the Concrete Damaged Plasticity Model (CDPM) in ABAQUS by evaluating it against experimental data. Stoner calibrated the model by running simulations on 12 different beams, studying the effects of dilation angle, reinforcement modelling, slenderness, and material modelling.

This chapter explains the process by which Stoner modelled the beams in ABAQUS, as well as the steps taken for this thesis to automate the simulations for bulk analysis. All methods discussed in this chapter were developed by Stoner, with the exception of the Python code used to automate the process.

The beams studied follow the naming convention BM XX-(s)YYY, where XX denotes the diameter of the longitudinal reinforcement used, YYY denotes the stirrup spacing, and the presence of the letter 's' signifies the use of 20 mm stirrups (12 mm otherwise). The longitudinal bar diameters included in this study are 12mm, 16mm, and 25mm. The stirrup spacings studied are 150mm, 220mm, 230mm, and none (no stirrups, denoted INF). Table 3.1 illustrates the beam dimensions and reinforcement ratios used in the study.

Table 3.1: Beam Specimen Details

| Beam | $b$ (mm) | $h$ (mm) | $d$ (mm) | $\rho_F$ (%) | $\rho_V$ (%) |
|---|---|---|---|---|---|
| 12-INF | | | | | 0.00 |
| 12-150 | 200 | 350 | 270 | 2.51 | 0.75 |
| 12-220 | | | | | 0.51 |
| 16-INF | | | | | 0.00 |
| 16-150 | 200 | 345 | 270 | 2.23 | 0.75 |
| 16-220 | | | | | 0.51 |
| 25-INF | | | | | 0.00 |
| 25-150 | 200 | 330 | 270 | 1.82 | 0.75 |
| 25-220 | | | | | 0.51 |
| 12-s230 | | 365 | | 2.18 | |
| 16-s230 | 230 | 360 | 270 | 1.94 | 1.19 |
| 25-s230 | | 345 | | 1.58 | |

## 3.1 Modelling in ABAQUS

A total of 12 beams were modelled for this study with the slenderness ratio, and dilation angle, of the specimens being the varied parameters. The beams shown in Table 3.1 were analyzed at $a/d$ ratios ranging from 1.5 to 12.5, at concrete dilation angles of 30° and 50°.

This section discusses the parameters used in the modelling of the beams, as well as the methodology for running the analyses. The following modelling process summarizes the work done by Stoner, and the extensions made for this thesis.

### 3.1.1 Parts Created

The beams and reinforcement were modelled as separate components rather than one continuous, partitioned medium for practical purposes. Automation of the analyses, as well as organization of the different components were the deciding factors in choosing to model the components individually.

The components were separated to simplify the process of altering them from a programming perspective. The ABAQUS package contains several Python modules that can be used to automate pre, and post processing procedures. Some of these procedures will be discussed in the context of the study in Section 3.1.5.

The specimens are comprised of three distinct components: the beam, the longitudinal reinforcement, and the transverse reinforcement.

Modelling a part in ABAQUS is a three step procedure. First, the geometry for the part must be created. Next, the material properties for the part must be assigned. To accomplish this, a material must be created and assigned all the relevant properties (elastic, plastic, thermal). Once the material has been created, a section can be created. Sections contain information about the material to be used, as well as the cross sectional area and body type (solid, composite, membrane). The section is then assigned to the part, which can then be assembled with the other parts to form the complete structure.

The beam is modelled as a three-dimensional deformable solid. A deformable solid assignment is selected to allow the part to deform under mechanical, thermal, and electrical loading. The part is created by first sketching a rectangular section, and then extruding it to the required length. A homogeneous, solid section is assigned to the beam to ensure uniformity in material properties throughout the part.

The longitudinal reinforcement is modelled as a deformable, wire part; the wire assignment is used to model objects whose thicknesses are notably smaller than their lengths. The parameters of interest in the modelling the longitudinal reinforcement are the axial stiffness, and cross sectional area. These parameters are best represented by truss sections. The cross sectional areas of the reinforcing bars used are presented in Table 3.2.

Table 3.2: Reinforcement Geometry

| **Longitudinal Reinforcement** | |
|---|---|
| Bar Diameter ($mm$) | Cross-Sectional Area ($mm^2$) |
| 12 | 113 |
| 16 | 201 |
| 25 | 491 |
| **Transverse Reinforcement** | |
| Bar Diameter ($mm$) | Cross-Sectional Area of Two Legs ($mm^2$) |
| 12 | 226 |
| 20 | 628 |

Stoner investigated the modelling of the transverse reinforcement and concluded that a smeared membrane approach was more successful than using a truss section. The stirrups are modelled as smeared membranes with cross sections equal to those of the beams. The stirrups used are two-legged, closed stirrups with diameters equal to 12 mm, and 20 mm (for BM-XX-s230).

### 3.1.2 Material Modelling

Extensive work was conducted by Stoner [66] to model the material properties of the concrete used in this study. Stoner used the CDP model to represent the behaviour of concrete.

His study concluded that the Hognestad Parabola most accurately represented the compressive behaviour of low and normal strength, while the modified Hognestad Parabola best represented higher strength concrete.

A fracture mechanics approach was used to model the post-cracking tensile properties, utilizing a bilinear stress-displacement formulation with $G_f = 90N/m$.

All beams were analyzed using the same concrete, with $f_c^{'}$ equal to 56.5 MPa, a modulus of elasticity equal to $37,583$ MPa, dilation angles of 30° and 50°, and a cracking stress equal to 22.6 MPa. Table 3.4 in section 3.1.6 summarizes the parameters used for modelling.

Because GFRP exhibits brittle failure (rupture), and is thus linear elastic until failure, extensive modelling was not required. Only the tensile modulus of elasticity and ultimate FRP stress were required. Furthermore, testing of the stirrups did not result in rupture, allowing for a simplification in modelling of the bent portion; reduced strength at the bend was not considered. Table 3.3 summarizes the bar material properties used in the analyses.

Table 3.3: Reinforcement Properties

| Longitudinal Reinforcement | | | | Transverse Reinforcement | | | | |
|---|---|---|---|---|---|---|---|---|
| Beam | $f_{fu,straight}$ $(MPa)$ | $E_f$ $(GPa)$ | $A_f$ $(mm^2)$ | $f_{fu,straight}$ $(MPa)$ | $f_{fu,bent}$ $(MPa)$ | $r_{bend}$ $(mm)$ | $E_f$ $(GPa)$ | $A_f$ $(mm^2)$ |
| 12-INF | | | 113 | | | | | |
| 16-INF | 1000 | 63.5 | 201 | - | - | - | - | - |
| 25-INF | | | 491 | | | | | |
| 12-150 | | | 113 | | | | | |
| 16-150 | 1000 | 63.5 | 201 | 1000 | 700 | 42 | 50 | 113 |
| 25-150 | | | 491 | | | | | |
| 12-220 | | | 113 | | | | | |
| 16-220 | 1000 | 63.5 | 201 | 1000 | 700 | 42 | 50 | 113 |
| 25-220 | | | 491 | | | | | |
| 12-s230 | | | 113 | | | | | |
| 16-s230 | 1000 | 63.5 | 201 | 900 | 550 | 70 | 50 | 314 |
| 25-s230 | | | 491 | | | | | |

### 3.1.3 Assembly and Boundary Conditions

To adequately discuss the boundary conditions, the coordinate axes used in the models must be clarified. The coordinate directions x,y, and z will henceforth refer to the directions along the beam's width, height, and length respectively.

All beams that were analyzed in this study were simulated under 3 point loading. Due to the symmetry of the problem, only half beams were modelled, making use of the symmetry boundary condition in ABAQUS/CAE. The beams were divided at the midspan, such that one support, and one shear span was analyzed. To maintain continuity, the face of the midspan was restrained from moving in the z direction, as well as rotating about the x axis.

The simple support was modelled using a line segment with boundary conditions imposed to restrict movement. Movement along the beam's width was restricted by defining a 3 node set around the support line (shown in Figure 3.1) and setting its movement along the x axis to 0. Motion in the vertical direction was restricted by setting the support line's movement in the y-direction to 0.

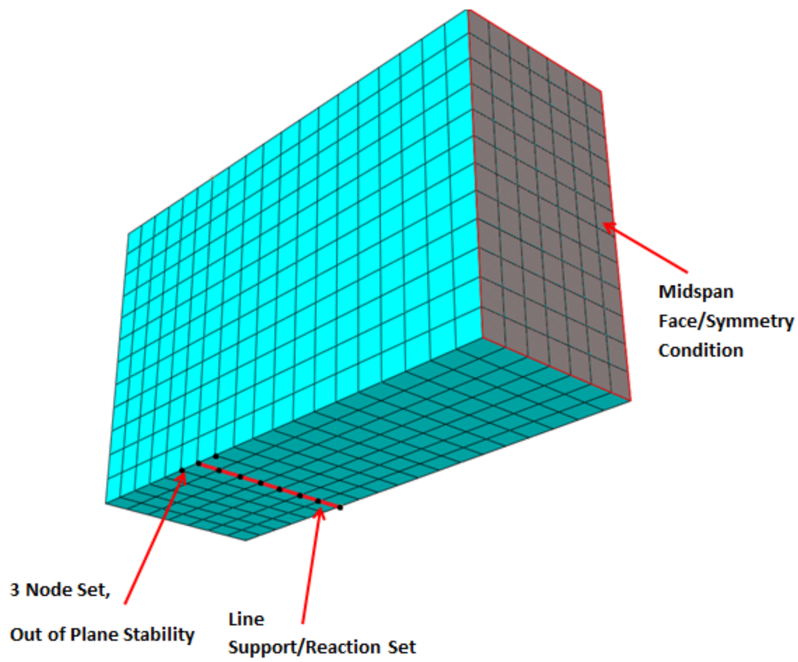


Figure 3.1: BM 12-150, Meshed, with Boundary Conditions

The assembly consisted of the concrete half beam, with the longitudinal and transverse reinforcement embedded using the Embedded Region constraint. The Embedded Region constraints, in addition to introducing Normal Contact behaviour served to simulate perfect bond between the reinforcement and concrete. Figure 3.2 illustrates the final assembly for the beam.

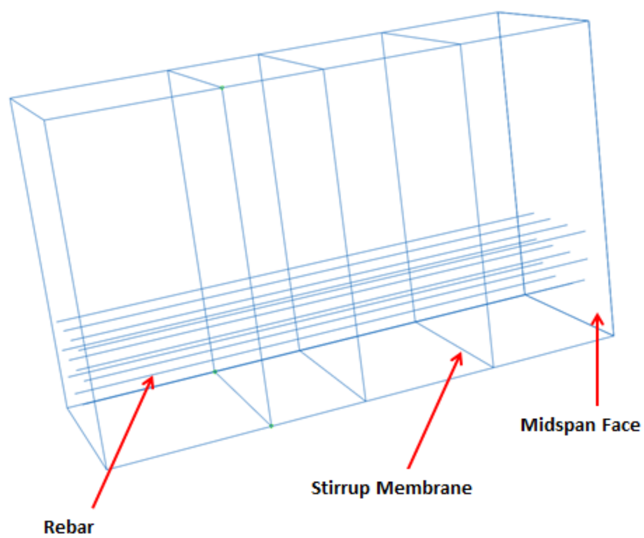


Figure 3.2: BM 12-150, Final Assembly

The beams were loaded using an imposed displacement at the midspan rather than a force/pressure. The purpose of loading through displacement was to study the post-peak response and facilitate the post processing. In addition, Stoner concluded that more consistent results were achieved when loading through displacement, as opposed to applying a direct load.

To apply the displacement loading, a two element deep layer was created along the face of the midspan. A boundary condition was then created to impose the desired vertical displacement on the layer.

### 3.1.4 Meshing

Due to the large number of simulations that were conducted, a mesh sensitivity analysis was not conducted on each specimen. However, an investigation into the optimal element size for the smallest beams was conducted. The results, in addition to the convergence studies conducted by Stoner, provided an optimal element size of 30 mm. All meshes were generated using element sizes of 30 mm, resulting in finer meshes as the beam size increased. The uniformity of the beam sections, in addition to the consistent element size, also facilitated the collection and processing of nodal data.

The concrete was meshed using hexahedral, first-order, continuum C3D8R elements. These elements are three-dimensional, 8 noded, linear bricks with reduced integration. Reduced integration was used to avoid shear-locking, and improve computational efficiency. One disadvantage of using reduced integration is that it can lead to hourglassing effects; hourglassing can lead to unwanted mesh distortions. To account for this, ABAQUS provides elements with hourglass control options to reduce these effects.

The longitudinal reinforcement was meshed using first-order, truss T3D2 elements, while the transverse reinforcement was meshed using 4-noded, quadrilateral, membrane M3D4R elements. The T3D2 (three-dimensional, 2 noded, linear) elements were deemed adequate in capturing the reinforcing bars' strain distributions. For the stirrups, the M3D4R 4 noded, three-dimensional membrane elements were used, with reduced integration, and hourglass control. Figure 3.1 shows the final mesh for BM 12-150, for a slenderness ratio of 1.5.

### 3.1.5 Simulation and Post Processing

To adequately represent the results, 3 data requests were required from ABAQUS: the vertical deflection of the midspan, the magnitude of the plastic strains, and the vertical reaction of the beam support.

Since the imposed displacement was uniform along the face of the midspan, selecting any node along the face provided the required deflection data.

The crack patterns were collected by requesting the magnitude of plastic strain at each integration point. Plotting the contour of this data at failure provided a visual representation of the crack patterns.

To determine the applied load on the beam, the reactions were measured at the modelled support. Since the beams were studied under 3 point loading, the applied load was calculated by multiplying the recorded reactions by 2.

To record the vertical support reaction, a node set was created along the line support. The vertical force was polled at each node in the set at each time increment, and then summed to provide the net support reaction. Since only two beam widths were analyzed in this study (200 mm, 230 mm), and meshing was consistent across all beams, automation of this process was achievable.

All beams with widths of 200 mm had reaction sets consisting of 8 nodes, while beams with widths of 230 mm had reaction sets consisting 9 nodes. Using the built in Python modules in ABAQUS, it was possible to automate the entire post-processing procedure. A copy of the code used in included in Appendix A.

The following algorithm summarizes the mentioned Python code.

1. Create .INP file

2. Run job, wait for completion
3. Open .ODB file
4. Create XY data for midspan deflection and nodal reaction forces
5. Create and open Excel file
6. Sum nodal reactions at each time increment, multiply by 2 to obtain load (3 point loading), store in first column of Excel file. Iteratively calculate the max load as data is being stored, noting the index position of the time increment.
7. Store absolute values of midspan deflection at each time increment in second column of Excel file
8. Compute moment at each time increment using load data and beam length. The depth and slenderness ratio are used to calculate beam length
9. Select the PEMAG contours to be plotted in the viewport on the undeformed shape
10. Set the current frame to noted index position of the max load. This will plot the crack patterns at failure
11. Center the view to obtain a presentable screen capture of the beam and save capture as .PNG file
12. Loop over desired beams and slenderness ratios

### 3.1.6 Summary of Modelling Parameters

Table 3.4 summarizes the primary modelling parameters used.

Table 3.4: Summary of ABAQUS Modelling Parameters Used

| | |
|---|---|
| **Concrete** | |
| Damage Model: | Concrete Damaged Plasticity (Tension, Compression) |
| Compression Model: | Modified Hognestad Parabola |
| Tension Model: | Bilinear Stress-Displacement |
| Fracture Energy ($G_f$): | 90 N/m |
| Dilation Angle: | 30°, 50° |
| $E_c$: | 37583 MPa |
| Poisson's Ratio ($\nu$): | 0.2 |
| $\sigma_{bo}/\sigma_{co}$: | 1.16 |
| Eccentricity ($\epsilon$): | 0.1 |
| $K_c$: | 2/3 |
| Viscosity ($\mu$): | 0.0001 |
| Element Type: | C3D8R |
| Element Size: | 30 mm |
| **Longitudinal Reinforcement** | |
| $E_f$: | 63500 MPa |
| Poisson's Ratio ($\nu$): | 0.3 |
| Element Type: | T3D2 |
| Element Size: | 30 mm |
| **Transverse Reinforcement** | |
| $E_{f,v}$: | 50000 MPa |
| Poisson's Ratio ($\nu$): | 0.3 |
| Element Type: | M3D4R |
| Element Size: | 30 mm |

# Chapter 4

# Comparison of Strength Predictions and ABAQUS Models to Experimental Database of FRP Reinforced Beams

This chapter focuses on the collection of test data from literature on FRP reinforced concrete beams, and the evaluation of current strength prediction models against the experiments. Furthermore, the ABAQUS models developed by Stoner are evaluated against selected beams from the experimental database to determine their efficacy. Final recommendations for the modelling parameters in ABAQUS will be made and will be implemented in a parametric study in Chapter 5.

The database consists of CFRP and GFRP reinforced beams tested under 3 point and 4 point loading conditions, for varying concrete strengths and reinforcing ratios. A total of 57 beams are analyzed, 45 beams without stirrups, and 12 with stirrups.

Section 4.1 evaluates current strength prediction models against the experimental data from each paper, while Section 4.2 evaluates the efficacy of Stoner's ABAQUS model against beams tested by Johnson and Sheikh [39].

## 4.1 Strength Predictions for Experimental Database of FRP Reinforced Beams

The collated data is presented in three tables. The first table provides the specimen names, as well as the relevant material properties. The second table provides data on the geometry of the beams, the loading condition, as well as the required reinforcement details. Finally, the last table compares the experimentally obtained peak loads to the current prediction models.

### 4.1.1 Duranovic, N., Pilakoutas, K. and Waldron, P. (1997)

Duranovic et al. [20] tested 6 beams reinforced with GFRP. The beams contained both longitudinal and transverse reinforcement, with the transverse reinforcement consisting of closed stirrups of rectangular cross-section. All beams were tested under 4 point loading, and had a maximum slenderness ratio of 3.5. Table 4.1 presents the ultimate strengths and elastic moduli of the concrete and reinforcement.

Table 4.1: Material Properties, Duranovic et al.

| Beam | Reinforcing Material | $f'_c$ (MPa) | $E_c$ (GPa) | $E_{fl}$ (GPa) | $E_{fv}$ (GPa) | $f_{fu}$ (MPa) |
|---|---|---|---|---|---|---|
| GB5 | GFRP | 31.2 | 26.25 | 45 | 45 | 1000 |
| GB9 | GFRP | 39.8 | 29.65 | 45 | 45 | 1000 |
| GB10 | GFRP | 39.8 | 29.65 | 45 | 45 | 1000 |
| GB11 | GFRP | 39.8 | 29.65 | 45 | 45 | 1000 |
| GB12 | GFRP | 39.8 | 29.65 | 45 | 45 | 1000 |
| GB13 | GFRP | 43.4 | 30.96 | 45 | 45 | 1000 |

Table 4.2 presents the geometry of the beams, as well as the reinforcement ratios and spacing of the transverse reinforcement. All beams except for GB12 had a slenderness ratio of 3.5, while GB12 had a ratio of 2.34. The parameters of interest in this study were the longitudinal and transverse reinforcement ratios, as well as the spacing of the transverse reinforcement.

Table 4.2: Beam Properties, Duranovic et al.

| Beam | Test Set Up | $b_w$ (mm) | $d$ (mm) | $\frac{a}{d}$ | $h$ (mm) | $L$ (m) | $\rho_f$ (%) | $\rho_v$ (%) | s (mm) |
|---|---|---|---|---|---|---|---|---|---|
| GB5 | 4 Point Loading | 150 | 219.25 | 3.5 | 250 | 2.3 | 1.31 | 1.52 | 35 |
| GB9 | 4 Point Loading | 150 | 219.25 | 3.5 | 250 | 2.3 | 1.31 | 0.7 | 76.7 |
| GB10 | 4 Point Loading | 150 | 219.25 | 3.5 | 250 | 2.3 | 1.31 | 0.7 | 76.7 |
| GB11 | 4 Point Loading | 150 | 219.25 | 3.5 | 250 | 2.3 | 1.31 | 0.35 | 153 |
| GB12 | 4 Point Loading | 150 | 219.25 | 2.34 | 250 | 2.3 | 1.31 | 0.35 | 153 |
| GB13 | 4 Point Loading | 150 | 219.25 | 3.5 | 250 | 2.3 | 0.87 | 0.7 | 76.7 |

Table 4.3 compares the experimentally obtained peak loads to predictions by current prediction models. The presented beams had relatively low slenderness ratios, suggesting

shear failure.

Table 4.3: Comparison of Ultimate Loads (KN), Duranovic et al.

| Beam | Test | CSA S806-12 (Flexure) | ACI440.1R-15 (Flexure) | CSA S806-12 (Shear) | ACI440.1R-15 (Shear) | Nehdi et al. (2007) (Shear) | JSCE (Shear) | ISIS Canada (Shear) |
|---|---|---|---|---|---|---|---|---|
| GB5 | 105.1 | 48.48 | 69.84 | 35.09 | 29.56 | 127.4 | 25.27 | 45.64 |
| GB9 | 103.6 | 55.2 | 50.79 | 30.69 | 35.56 | 97.28 | 25.74 | 32.56 |
| GB10 | 103 | 55.2 | 50.79 | 30.69 | 35.56 | 97.28 | 25.74 | 32.56 |
| GB11 | 97.95 | 55.2 | 50.79 | 28.03 | 25.3 | 77.73 | 24.6 | 26.14 |
| GB12 | 133.1 | 82.69 | 75.97 | 35.8 | 25.3 | 83.17 | 24.6 | 26.14 |
| GB13 | 90.6 | 49.05 | 44.5 | 28.46 | 33.31 | 95.02 | 22.93 | 33.43 |

Both the CSA S806-12 and ACI440.1R-15 models predicted a shear driven failure which agrees with the expected behaviour (due to low slenderness ratio). The Nehdi model matched most closely to the experimentally obtained peak loads, slightly over-predicting failure in the GB5, and GB13 specimens. All other models vastly under-predicted the failure load, suggesting a conservative approach to strength prediction. The current code provisions were developed using a combination of empirically obtained data and mechanics, while the Nehdi model utilizes a genetic optimization algorithm to determine the influence of key parameters on the strength, and formulate a relationship between them. The fitting approach presented by Nehdi is evident from the closely matching values for the peak loads.

### 4.1.2 Matta, F., El-Sayed, A.K., Nanni, A., Benmokrane, B. (2013)

Matta et al. [48] tested 7 beams reinforced with GFRP. The beams contained no transverse reinforcement and were tested under 4 point loading. The beams had a maximum slenderness ratio of 3.13. Table 4.4 presents the ultimate strengths and elastic moduli of the concrete and reinforcement.

Table 4.4: Material Properties, Matta et al.

| Beam | Reinforcing Material | $f'_c$ (MPa) | $E_c$ (GPa) | $E_{fl}$ (GPa) | $E_{fv}$ (GPa) | $f_{fu}$ (MPa) |
|---|---|---|---|---|---|---|
| S1-0.12-1A | GFRP | 29.5 | 26.25 | 41 | N/A | 476 |
| S1-0.12-2B | GFRP | 29.6 | 29.65 | 41 | N/A | 483 |
| S3-0.12-1A | GFRP | 32.1 | 29.65 | 43.2 | N/A | 849 |
| S3-0.12-2A | GFRP | 32.1 | 29.65 | 43.2 | N/A | 849 |
| S6-0.12-1A | GFRP | 59.7 | 29.65 | 43.2 | N/A | 849 |
| S6-0.12-2A | GFRP | 32.1 | 30.96 | 43.2 | N/A | 849 |
| S6-0.12-3A | GFRP | 32.1 | 30.96 | 43.2 | N/A | 849 |

Table 4.5 presents the geometry of the beams, as well as the reinforcement ratios. The varied parameters in this study were the strength of the concrete used, as well as the section geometry. The aim was to observe the influence of maintaining the same slenderness ratio while varying the section geometry. All specimens were tested with normal strength concrete except for S6-0.12-1A (higher strength concrete, 59.7 MPa).

Table 4.5: Beam Properties, Matta et al.

| Beam | Test Set Up | $b_w$ (mm) | $d$ (mm) | $\frac{a}{d}$ | $h$ (mm) | $L$ (m) | $\rho_f$ (%) | $\rho_v$ (%) | s (mm) |
|---|---|---|---|---|---|---|---|---|---|
| S1-0.12-1A | 4 Point Loading | 457 | 883 | 3.11 | 978 | 0.914 | 0.6 | N/A | N/A |
| S1-0.12-2B | 4 Point Loading | 457 | 883 | 3.11 | 978 | 0.914 | 0.6 | N/A | N/A |
| S3-0.12-1A | 4 Point Loading | 114 | 292 | 3.13 | 330 | 0.61 | 0.6 | N/A | N/A |
| S3-0.12-2A | 4 Point Loading | 114 | 292 | 3.13 | 330 | 0.61 | 0.6 | N/A | N/A |
| S6-0.12-1A | 4 Point Loading | 229 | 146 | 3.13 | 178 | 0.61 | 0.6 | N/A | N/A |
| S6-0.12-2A | 4 Point Loading | 229 | 146 | 3.13 | 178 | 0.61 | 0.6 | N/A | N/A |
| S6-0.12-3A | 4 Point Loading | 229 | 146 | 3.13 | 178 | 0.61 | 0.6 | N/A | N/A |

Table 4.6 compares the experimentally obtained peak loads to predictions by current prediction models. The presented beams had relatively low slenderness ratios, suggesting shear failure.

Table 4.6: Comparison of Ultimate Loads (KN), Matta et al.

| Beam | Test | CSA S806-12 (Flexure) | ACI440.1R-15 (Flexure) | CSA S806-12 (Shear) | ACI440.1R-15 (Shear) | Nehdi et al. (2007) (Shear) | JSCE (Shear) | ISIS Canada (Shear) |
|---|---|---|---|---|---|---|---|---|
| S1-0.12-1A | 154.1 | 377.58 | 236.92 | 231.17 | 113.55 | 304.44 | 127.94 | 137.02 |
| S1-0.12-2B | 151.4 | 383.21 | 242.71 | 231.43 | 113.66 | 304.44 | 128.08 | 137.25 |
| S3-0.12-1A | 19.2 | 40.39 | 36.44 | 19.85 | 9.82 | 25.88 | 14.57 | 17.53 |
| S3-0.12-2A | 17.9 | 40.39 | 36.44 | 19.85 | 9.82 | 25.88 | 14.57 | 17.53 |
| S6-0.12-1A | 28.6 | 55.38 | 54.78 | 25.57 | 11.63 | 29.98 | 18.72 | 24.01 |
| S6-0.12-2A | 36.9 | 40.57 | 36.71 | 19.93 | 9.86 | 25.99 | 16.13 | 17.61 |
| S6-0.12-3A | 26.3 | 40.57 | 40.96 | 19.93 | 9.86 | 25.99 | 16.13 | 17.61 |

Once more, Table 4.6 shows that the CSA S806-12 and ACI440.1R-15 predict shear failure, in agreement with the expected behaviour. For specimens S1-0.12-1A and S1-0.12-1A, which had the largest sections, the CSA and Nehdi models greatly over-predict failure, suggesting the models may have difficulty in predicting the failure of larger sections. The JSCE and ISIS Canada models matched closest to the observed failure loads, closely under-predicting the experimental data.

Observing the comparisons for the JSCE and ISIS Canada models from the Duranovic et al., and Matta et al. papers, one might infer that the discrepancy in prediction occurs due to the presence of stirrups. Both models predict failure more accurately in the absence of stirrups.

### 4.1.3 Razaqpur, A. G., Isgor, B. O., Greenaway, S., and Selley, A. (2004)

Razaqpur et al. [62] tested 6 beams reinforced with CFRP. The beams contained no transverse reinforcement and were tested under 4 point loading. The beams had slenderness ratios ranging from 2.67 to 4.22. Table 4.7 presents the ultimate strengths and elastic moduli of the concrete and reinforcement.

Table 4.7: Material Properties, Razaqpur et al.

| Beam | Reinforcing Material | $f'_c$ (MPa) | $E_c$ (GPa) | $E_{fl}$ (GPa) | $E_{fv}$ (GPa) | $f_{fu}$ (MPa) |
|---|---|---|---|---|---|---|
| BR1 | CFRP | 40.5 | 29.91 | 145 | N/A | 2250 |
| BR2 | CFRP | 49 | 32.9 | 145 | N/A | 2250 |
| BR3 | CFRP | 40.5 | 29.91 | 145 | N/A | 2250 |
| BR4 | CFRP | 40.5 | 29.91 | 145 | N/A | 2250 |
| BA3 | CFRP | 40.5 | 29.91 | 145 | N/A | 2250 |
| BA4 | CFRP | 40.5 | 29.91 | 145 | N/A | 2250 |

Table 4.8 presents the geometry of the beams, as well as the reinforcement ratios. The parameters of interest in this study were the longitudinal reinforcement ratio and the slenderness of the beams. A constant section geometry was used for all beams.

Table 4.8: Beam Properties, Razaqpur et al.

| Beam | Test Set Up | $b_w$ (mm) | $d$ (mm) | $\frac{a}{d}$ | $h$ (mm) | $L$ (m) | $\rho_f$ (%) | $\rho_v$ (%) | s (mm) |
|---|---|---|---|---|---|---|---|---|---|
| BR1 | 4 Point Loading | 200 | 225 | 2.67 | 250 | 2 | 0.25 | N/A | N/A |
| BR2 | 4 Point Loading | 200 | 225 | 2.67 | 250 | 2 | 0.5 | N/A | N/A |
| BR3 | 4 Point Loading | 200 | 225 | 2.67 | 250 | 2 | 0.63 | N/A | N/A |
| BR4 | 4 Point Loading | 200 | 225 | 2.67 | 250 | 2 | 0.88 | N/A | N/A |
| BA3 | 4 Point Loading | 200 | 225 | 3.56 | 250 | 2 | 0.5 | N/A | N/A |
| BA4 | 4 Point Loading | 200 | 225 | 4.22 | 250 | 2 | 0.5 | N/A | N/A |

Table 4.9 compares the experimentally obtained peak loads to predictions by current prediction models. The presented beams had relatively low slenderness ratios, suggesting shear failure.

Table 4.9: Comparison of Ultimate Loads (KN), Razaqpur et al.

| Beam | Test | CSA S806-12 (Flexure) | ACI440.1R-15 (Flexure) | CSA S806-12 (Shear) | ACI440.1R-15 (Shear) | Nehdi et al. (2007) (Shear) | JSCE (Shear) | ISIS Canada (Shear) |
|---|---|---|---|---|---|---|---|---|
| BR1 | 36.1 | 82.51 | 70.26 | 34.6 | 16.5 | 41.35 | 25.4 | 48.77 |
| BR2 | 47 | 119 | 106.93 | 45.27 | 23.8 | 50.67 | 33.54 | 53.64 |
| BR3 | 47.2 | 117.6 | 108.49 | 45.55 | 25.03 | 51.14 | 34.56 | 48.77 |
| BR4 | 42.7 | 131.99 | 122.4 | 50.41 | 28.93 | 55.23 | 38.63 | 48.77 |
| BA3 | 49.7 | 81.06 | 74.57 | 36.8 | 22.6 | 45.39 | 32 | 48.77 |
| BA4 | 38.5 | 68.26 | 62.91 | 33.8 | 22.6 | 43.65 | 32 | 48.77 |

As expected, the CSA S806-12 and ACI440.1R-15 confirmed the expected shear failure, with the CSA S806-12 shear model matching most closely to the observed peak loads. The ACI440.1R-15 shear model consistently under-predicted the measured peak loads, showing no difference in capacity between the specimens BA3 and BA4. The only difference between the two specimens is the slenderness of the beams (3.56 and 4.22 respectively). This suggests a conservative approach by the ACI, electing to neglect slenderness effects by providing a conservative value for failure.

The Nehdi and JSCE models are consistent in matching closely with the experimental values. The effects of a higher elastic modulus for the reinforcement, as well as the varying longitudinal reinforcement ratios have negligible impact on the accuracy of the model predictions.

The ISIS Canada shear model predicts the same peak load for all specimens that varied the longitudinal reinforcement ratio, and slenderness. Tables 4.8 and 4.9 suggest that the strength of the concrete used has the greatest influence on the strength prediction for the ISIS Canada shear model. Further research is required on larger specimens to determine the efficacy of the model in dealing with slenderness effects.

### 4.1.4 Yost, J. R., Gross, S. P., and Dinehart, D. W. (2001)

Yost et al. [73] tested 18 beams reinforced with GFRP. The beams contained no transverse reinforcement and were tested under 4 point loading. The beams all had slenderness ratios of approximately 4. Table 4.10 presents the ultimate strengths and elastic moduli of the concrete and reinforcement.

Table 4.10: Material Properties, Yost et al.

| Beam | Reinforcing Material | $f'_c$ (MPa) | $E_c$ (GPa) | $E_{fl}$ (GPa) | $E_{fv}$ (GPa) | $f_{fu}$ (MPa) |
|---|---|---|---|---|---|---|
| 1FRPa | GFRP | 36.3 | 39.9 | 40.3 | N/A | 690 |
| 1FRPb | GFRP | 36.3 | 39.9 | 40.3 | N/A | 690 |
| 1FRPc | GFRP | 36.3 | 39.9 | 40.3 | N/A | 690 |
| 2FRPa | GFRP | 36.3 | 39.9 | 40.3 | N/A | 690 |
| 2FRPb | GFRP | 36.3 | 39.9 | 40.3 | N/A | 690 |
| 2FRPc | GFRP | 36.3 | 39.9 | 40.3 | N/A | 690 |
| 3FRPa | GFRP | 36.3 | 39.9 | 40.3 | N/A | 690 |
| 3FRPb | GFRP | 36.3 | 39.9 | 40.3 | N/A | 690 |
| 3FRPc | GFRP | 36.3 | 39.9 | 40.3 | N/A | 690 |
| 4FRPa | GFRP | 36.3 | 39.9 | 40.3 | N/A | 690 |
| 4FRPb | GFRP | 36.3 | 39.9 | 40.3 | N/A | 690 |
| 4FRPc | GFRP | 36.3 | 39.9 | 40.3 | N/A | 690 |
| 5FRPa | GFRP | 36.3 | 39.9 | 40.3 | N/A | 690 |
| 5FRPb | GFRP | 36.3 | 39.9 | 40.3 | N/A | 690 |
| 5FRPc | GFRP | 36.3 | 39.9 | 40.3 | N/A | 690 |
| 6FRPa | GFRP | 36.3 | 39.9 | 40.3 | N/A | 690 |
| 6FRPb | GFRP | 36.3 | 39.9 | 40.3 | N/A | 690 |
| 6FRPc | GFRP | 36.3 | 39.9 | 40.3 | N/A | 690 |

Table 4.14 presents the geometry of the beams, as well as the reinforcement ratios. The

parameters of interest in this study were the longitudinal reinforcement ratio and the width of the beams. A constant slenderness ratio was used for all specimens.

Table 4.11: Beam Properties, Yost et al.

| Beam | Test Set Up | $b_w$ (mm) | $d$ (mm) | $\frac{a}{d}$ | $h$ (mm) | $L$ (m) | $\rho_f$ (%) | $\rho_v$ (%) | s (mm) |
|---|---|---|---|---|---|---|---|---|---|
| 1FRPa | 4 Point Loading | 229 | 225 | 4.06 | 286 | 2.13 | 1.1 | N/A | N/A |
| 1FRPa | 4 Point Loading | 229 | 225 | 4.06 | 286 | 2.13 | 1.1 | N/A | N/A |
| 1FRPa | 4 Point Loading | 229 | 225 | 4.06 | 286 | 2.13 | 1.1 | N/A | N/A |
| 2FRPa | 4 Point Loading | 178 | 225 | 4.06 | 286 | 2.13 | 1.42 | N/A | N/A |
| 2FRPa | 4 Point Loading | 178 | 225 | 4.06 | 286 | 2.13 | 1.42 | N/A | N/A |
| 2FRPa | 4 Point Loading | 178 | 225 | 4.06 | 286 | 2.13 | 1.42 | N/A | N/A |
| 3FRPa | 4 Point Loading | 229 | 225 | 4.06 | 286 | 2.13 | 1.65 | N/A | N/A |
| 3FRPa | 4 Point Loading | 229 | 225 | 4.06 | 286 | 2.13 | 1.65 | N/A | N/A |
| 3FRPa | 4 Point Loading | 229 | 225 | 4.06 | 286 | 2.13 | 1.65 | N/A | N/A |
| 4FRPa | 4 Point Loading | 279 | 225 | 4.06 | 286 | 2.13 | 1.81 | N/A | N/A |
| 4FRPa | 4 Point Loading | 279 | 225 | 4.06 | 286 | 2.13 | 1.81 | N/A | N/A |
| 4FRPa | 4 Point Loading | 279 | 225 | 4.06 | 286 | 2.13 | 1.81 | N/A | N/A |
| 5FRPa | 4 Point Loading | 254 | 224 | 4.08 | 286 | 2.13 | 2 | N/A | N/A |
| 5FRPa | 4 Point Loading | 254 | 224 | 4.08 | 286 | 2.13 | 2 | N/A | N/A |
| 5FRPa | 4 Point Loading | 254 | 224 | 4.08 | 286 | 2.13 | 2 | N/A | N/A |
| 6FRPa | 4 Point Loading | 229 | 224 | 4.08 | 286 | 2.13 | 2.22 | N/A | N/A |
| 6FRPa | 4 Point Loading | 229 | 224 | 4.08 | 286 | 2.13 | 2.22 | N/A | N/A |
| 6FRPa | 4 Point Loading | 229 | 224 | 4.08 | 286 | 2.13 | 2.22 | N/A | N/A |

Table 4.12 compares the experimentally obtained peak loads to predictions by current models. The presented beams had relatively low slenderness ratios, suggesting shear failure.

Table 4.12: Comparison of Ultimate Loads (KN), Yost et al.

| Beam | Test | CSA S806-12 (Flexure) | ACI440.1R-15 (Flexure) | CSA S806-12 (Shear) | ACI440.1R-15 (Shear) | Nehdi et al. (2007) (Shear) | JSCE (Shear) | ISIS Canada (Shear) |
|---|---|---|---|---|---|---|---|---|
| 1FRPa | 39.1 | 63.4 | 71.64 | 33.42 | 17.18 | 43.91 | 29.98 | 27.87 |
| 1FRPb | 38.5 | 63.4 | 71.64 | 33.42 | 17.18 | 43.91 | 29.98 | 27.87 |
| 1FRPc | 36.8 | 63.4 | 71.64 | 33.42 | 17.18 | 43.91 | 29.98 | 27.87 |
| 2FRPa | 28.1 | 54.59 | 50.67 | 28.01 | 15.02 | 36.2 | 25.38 | 21.66 |
| 2FRPb | 35 | 54.59 | 50.67 | 28.01 | 15.02 | 36.2 | 25.38 | 21.66 |
| 2FRPc | 32.1 | 54.59 | 50.67 | 28.01 | 15.02 | 36.2 | 25.38 | 21.66 |
| 3FRPa | 40 | 74.22 | 69.07 | 37.69 | 20.7 | 48.2 | 34.32 | 27.87 |
| 3FRPb | 48.6 | 74.22 | 69.07 | 37.69 | 20.7 | 48.2 | 34.32 | 27.87 |
| 3FRPc | 44.7 | 74.22 | 69.07 | 37.69 | 20.7 | 48.2 | 34.32 | 27.87 |
| 4FRPa | 43.8 | 93.57 | 87.16 | 47.21 | 26.29 | 59.99 | 43.12 | 33.96 |
| 4FRPb | 45.9 | 93.57 | 87.16 | 47.21 | 26.29 | 59.99 | 43.12 | 33.96 |
| 4FRPc | 46.1 | 93.57 | 87.16 | 47.21 | 26.29 | 59.99 | 43.12 | 33.96 |
| 5FRPa | 37.7 | 87.61 | 81.62 | 44.18 | 24.93 | 55.57 | 40.45 | 30.78 |
| 5FRPb | 51 | 87.61 | 81.62 | 44.18 | 24.93 | 55.57 | 40.45 | 30.78 |
| 5FRPc | 46.6 | 87.61 | 81.62 | 44.18 | 24.93 | 55.57 | 40.45 | 30.78 |
| 6FRPa | 43.5 | 81.97 | 76.48 | 41.11 | 23.55 | 51.32 | 37.76 | 27.75 |
| 6FRPb | 41.8 | 81.97 | 76.48 | 41.11 | 23.55 | 51.32 | 37.76 | 27.75 |
| 6FRPc | 41.3 | 81.97 | 76.48 | 41.11 | 23.55 | 51.32 | 37.76 | 27.75 |

6 distinct specimens were tested in this study, with each test conducted 3 times to ensure validity of the results. All specimens were named per the format XY-ZZ, where X denotes the specimen class, Y denotes the test, and ZZ is another test case identifier. The distinct tests were separated by the X identifier with values ranging from 1 to 6, while each iteration of the distinct test was distinguished by the Y identifier taking values a,b, and c.

All beams failed in shear, which agrees with the predictions made by the CSA and ACI models.

The CSA shear model value matched the experimental results most closely, suggesting model robustness under varying longitudinal reinforcement ratios.

The ACI shear model greatly under-predicts failure for all beams, showing consistent results for their conservative approach.

The Nehdi shear model is consistent in matching very closely to the observed values, slightly over-predicting the failure load. All other models matched closely, under-predicting the failure load on average.

### 4.1.5 Gross, S. P., Yost, J. R., Dinehart, D. W., Svensen, E., and Liu, N. (2003)

Yost et al. [28] furthered their experimental program by testing 12 beams reinforced with GFRP. The beams contained no transverse reinforcement and were tested under 4 point loading. The beams all had slenderness ratios of approximately 4. Table 4.13 presents the ultimate strengths and elastic moduli of the concrete and reinforcement.

Table 4.13: Material Properties, Gross et al.

| Beam | Reinforcing Material | $f'_c$ (MPa) | $E_c$ (GPa) | $E_{fl}$ (GPa) | $E_{fv}$ (GPa) | $f_{fu}$ (MPa) |
|---|---|---|---|---|---|---|
| 1a-26 | GFRP | 79.6 | 36.3 | 40.3 | N/A | 690 |
| 1b-26 | GFRP | 79.6 | 36.3 | 40.3 | N/A | 690 |
| 1c-26 | GFRP | 79.6 | 36.3 | 40.3 | N/A | 690 |
| 2a-26 | GFRP | 79.6 | 36.3 | 40.3 | N/A | 690 |
| 2b-26 | GFRP | 79.6 | 36.3 | 40.3 | N/A | 690 |
| 2c-26 | GFRP | 79.6 | 36.3 | 40.3 | N/A | 690 |
| 3a-27 | GFRP | 79.6 | 36.3 | 40.3 | N/A | 690 |
| 3b-27 | GFRP | 79.6 | 36.3 | 40.3 | N/A | 690 |
| 3c-27 | GFRP | 79.6 | 36.3 | 40.3 | N/A | 690 |
| 4a-37 | GFRP | 79.6 | 36.3 | 40.3 | N/A | 690 |
| 4b-37 | GFRP | 79.6 | 36.3 | 40.3 | N/A | 690 |
| 4c-37 | GFRP | 79.6 | 36.3 | 40.3 | N/A | 690 |

Table 4.14 presents the geometry of the beams, as well as the reinforcement ratios. Following their previous experimental program, Yost et al. conducted tests on similar beams, with higher strength concrete. The influence of concrete strength on shear capacity was the focus of this study.

Table 4.14: Beam Properties, Gross et al.

| Beam | Test Set Up | $b_w$ (mm) | $d$ (mm) | $\frac{a}{d}$ | $h$ (mm) | $L$ (m) | $\rho_f$ (%) | $\rho_v$ (%) | s (mm) |
|---|---|---|---|---|---|---|---|---|---|
| 1a-26 | 4 Point Loading | 203 | 225 | 4.06 | 286 | 2.13 | 1.25 | N/A | N/A |
| 1b-26 | 4 Point Loading | 203 | 225 | 4.06 | 286 | 2.13 | 1.25 | N/A | N/A |
| 1c-26 | 4 Point Loading | 203 | 225 | 4.06 | 286 | 2.13 | 1.25 | N/A | N/A |
| 2a-26 | 4 Point Loading | 152 | 225 | 4.06 | 286 | 2.13 | 1.66 | N/A | N/A |
| 2b-26 | 4 Point Loading | 152 | 225 | 4.06 | 286 | 2.13 | 1.66 | N/A | N/A |
| 2c-26 | 4 Point Loading | 152 | 225 | 4.06 | 286 | 2.13 | 1.66 | N/A | N/A |
| 3a-27 | 4 Point Loading | 165 | 224 | 4.08 | 286 | 2.13 | 2.1 | N/A | N/A |
| 3b-27 | 4 Point Loading | 165 | 224 | 4.08 | 286 | 2.13 | 2.1 | N/A | N/A |
| 3c-27 | 4 Point Loading | 165 | 224 | 4.08 | 286 | 2.13 | 2.1 | N/A | N/A |
| 4a-37 | 4 Point Loading | 203 | 224 | 4.08 | 286 | 2.13 | 2.56 | N/A | N/A |
| 4b-37 | 4 Point Loading | 203 | 224 | 4.08 | 286 | 2.13 | 2.56 | N/A | N/A |
| 4c-37 | 4 Point Loading | 203 | 224 | 4.08 | 286 | 2.13 | 2.56 | N/A | N/A |

Table 4.15 compares the experimentally obtained peak loads to predictions by current prediction models. The presented beams had relatively low slenderness ratios, suggesting shear failure.

Table 4.15: Comparison of Ultimate Loads (KN), Gross et al.

| Beam | Test | CSA S806-12 (Flexure) | ACI440.1R-15 (Flexure) | CSA S806-12 (Shear) | ACI440.1R-15 (Shear) | Nehdi et al. (2007) (Shear) | JSCE (Shear) | ISIS Canada (Shear) |
|---|---|---|---|---|---|---|---|---|
| 1a-26 | 41.6 | 82.27 | 73.1 | 41.02 | 24.99 | 48.02 | 30.16 | 36.59 |
| 1b-26 | 30.4 | 82.27 | 73.1 | 41.02 | 24.99 | 48.02 | 30.16 | 36.59 |
| 1c-26 | 42.1 | 82.27 | 73.1 | 41.02 | 24.99 | 48.02 | 30.16 | 36.59 |
| 2a-26 | 31 | 70.94 | 72.72 | 32.56 | 21.29 | 38.38 | 24.82 | 27.39 |
| 2b-26 | 33.1 | 70.94 | 72.72 | 32.56 | 21.29 | 38.38 | 24.82 | 27.39 |
| 2c-26 | 33.5 | 70.94 | 72.72 | 32.56 | 21.29 | 38.38 | 24.82 | 27.39 |
| 3a-27 | 38.4 | 83.84 | 79.02 | 37.84 | 25.57 | 43.73 | 29.04 | 29.6 |
| 3b-27 | 32.2 | 83.84 | 79.02 | 37.84 | 25.57 | 43.73 | 29.04 | 29.6 |
| 3c-27 | 36.8 | 83.84 | 79.02 | 37.84 | 25.57 | 43.73 | 29.04 | 29.6 |
| 4a-37 | 48.3 | 111.44 | 105.31 | 49.43 | 34.35 | 56.31 | 38.17 | 36.42 |
| 4b-37 | 45.7 | 111.44 | 105.31 | 49.43 | 34.35 | 56.31 | 38.17 | 36.42 |
| 4c-37 | 45.2 | 111.44 | 105.31 | 49.43 | 34.35 | 56.31 | 38.17 | 36.42 |

The beams tested by Yost et al. in this study followed the same naming convention as their previous program. Each test was repeated, resulting in a total of 3 repetitions per specimen.

All beams failed in shear, which agrees with the predictions made by the CSA and ACI models. The results obtained Yost et al. are consistent with their previous findings, with the CSA shear model matching most closely to the measured values. This study demonstrates that high strength concrete does not impact the efficacy of the models in predicting shear capacity.

### 4.1.6 Johnson, D. T., & Sheikh, S. A. (2016)

Johnson and Sheikh [39] tested 8 beams reinforced with GFRP. Their experimental program consisted of 2 beams without shear reinforcement, and 6 beams with shear reinforcement. They used 3 different concrete strengths, varied the reinforcement properties, varied stirrup spacing, and tested all beams under 3 point loading. Table 4.16 presents the ultimate strengths and elastic moduli of the concrete and reinforcement.

Table 4.16: Material Properties, Johnson and Sheikh

| Beam | Reinforcing Material | $f'_c$ (MPa) | $E_c$ (GPa) | $E_{fl}$ (GPa) | $E_{fv}$ (GPa) | $f_{fu}$ (MPa) |
|---|---|---|---|---|---|---|
| JSC32-NT | GFRP | 32 | 26.59 | 61.2 | N/A | 1204 |
| JSC32-22B | GFRP | 34 | 27.41 | 61.2 | 57.5 | 1204 |
| JSC32-40B | GFRP | 34 | 27.41 | 61.2 | 57.5 | 1204 |
| JSC32-50B | GFRP | 34 | 27.41 | 61.2 | 57.5 | 1204 |
| JSV40-NT | GFRP | 40 | 29.73 | 71.2 | N/A | 1264 |
| JSV40-22B | GFRP | 40 | 29.73 | 71.2 | 41.5 | 1264 |
| JSV40-40B | GFRP | 40 | 29.73 | 71.2 | 41.5 | 1264 |
| JSV40-50B | GFRP | 40 | 29.73 | 71.2 | 41.5 | 1264 |

Table 4.17 presents the geometry of the beams, as well as the reinforcement ratios. This study investigated the effects of concrete strength, stirrup spacing, and reinforcement material properties. All beams maintained a constant slenderness ratio of 2.92.

Table 4.17: Beam Properties, Johnson and Sheikh

| Beam | Test Set Up | $b_w$ (mm) | $d$ (mm) | $\frac{a}{d}$ | $h$ (mm) | $L$ (m) | $\rho_f$ (%) | $\rho_v$ (%) | s (mm) |
|---|---|---|---|---|---|---|---|---|---|
| JSC32-NT | 3 Point Loading | 400 | 575 | 2.92 | 650 | 3.64 | 1.05 | N/A | N/A |
| JSC32-22B | 3 Point Loading | 400 | 575 | 2.92 | 650 | 3.64 | 1.22 | 200 | 200 |
| JSC32-40B | 3 Point Loading | 400 | 575 | 2.92 | 650 | 3.64 | 1.22 | 150 | 150 |
| JSC32-50B | 3 Point Loading | 400 | 575 | 2.92 | 650 | 3.64 | 1.22 | 112 | 112 |
| JSV40-NT | 3 Point Loading | 400 | 575 | 2.92 | 650 | 3.64 | 1.05 | N/A | N/A |
| JSV40-22B | 3 Point Loading | 400 | 575 | 2.92 | 650 | 3.64 | 1.22 | 200 | 200 |
| JSV40-40B | 3 Point Loading | 400 | 575 | 2.92 | 650 | 3.64 | 1.22 | 150 | 150 |
| JSV40-50B | 3 Point Loading | 400 | 575 | 2.92 | 650 | 3.64 | 1.22 | 112 | 112 |

Table 4.18 compares the experimentally obtained peak loads to predictions by current prediction models. The presented beams had relatively low slenderness ratios, suggesting shear failure.

Table 4.18: Comparison of Ultimate Loads (KN), Johnson and Sheikh

| Beam | Test | CSA S806-12 (Flexure) | ACI440.1R-15 (Flexure) | CSA S806-12 (Shear) | ACI440.1R-15 (Shear) | Nehdi et al. (2007) (Shear) | JSCE (Shear) | ISIS Canada (Shear) |
|---|---|---|---|---|---|---|---|---|
| JSC32-NT | 308 | 850.26 | 796.44 | 372 | 236 | 447.42 | 229.73 | 237.62 |
| JSC32-22B | 775 | 928.24 | 868.54 | 548 | 518 | 1102.3 | 324.25 | 572.81 |
| JSC32-40B | 901 | 928.24 | 868.54 | 632 | 704 | 1198.9 | 336.69 | 637.89 |
| JSC32-50B | 1095 | 928.24 | 868.54 | 692 | 864 | 1320 | 350.41 | 724.57 |
| JSV40-NT | 327 | 1014.2 | 929.59 | 414 | 252 | 487.66 | 260.28 | 286.55 |
| JSV40-22B | 749 | 1070.06 | 895.38 | 608 | 434 | 1199 | 355.65 | 670.85 |
| JSV40-40B | 895 | 1070.06 | 895.38 | 702 | 558 | 1302.3 | 369.08 | 746.41 |
| JSV40-50B | 1067 | 1070.06 | 895.38 | 770 | 660 | 1436.7 | 383.38 | 857.53 |

All beams failed in shear, confirming the predictions made by the CSA and ACI models. The predictions by all models matched closely with the experimental values for the beams without transverse reinforcement (JSC32-NT,JSV40-NT). This pattern is consistent across all beams in examined in this chapter, suggesting consistency in the models' prediction capabilities for beams without stirrups.

For beams with transverse reinforcement, the Nehdi model is consistent in over-predicting the failure of the beams. The error for the predicted values is shown to be related to the stirrup spacing, with the error becoming smaller as the stirrup spacing decreases. This suggests that the Nehdi model considers the confining effects of the stirrups, as the model becomes more accurate when the stirrup spacing is decreased. However, for beams with the largest stirrup spacing, specimens JSC32-22B and JSV40-22B, the large errors (42.2%,60.1% respectively) suggest that confinement is considered even when the effects are not prominent. This pattern is consistent with the results obtained by Duranovic et al. (Section 4.1.1) for beams GB11 and GB10.

All other models provide very conservative values for failure, greatly under-predicting the observed failure loads. These predictions agree with the findings in Section 4.1.1, suggesting a very conservative approach by all provisions when computing the stirrup contribution to the shear strength of the beams. Further research is recommended to determine the confining effects of transverse reinforcement on the shear strength of FRP reinforced beams.

### 4.1.7 Summary of Results - Strength Predictions

Analysis of the various strength prediction methods yielded that the CSA S806 shear prediction model displayed robustness to changes in longitudinal reinforcement ratios and concrete strengths. However, the accuracy of the model decreases when stirrups are present. The ACI 440 method of calculating the shear capacity presented a conservative approach, neglecting the effects of slenderness and under-predicting the contribution of the stirrups to the shear capacity. Moreover, the JSCE and ISIS Canada predictions for shear capacity matched closely with experimental data for beams without stirrups, but failed to accurately predict the capacity with the inclusion of transverse reinforcement. Lastly, the model proposed by Nehdi et al. followed the experimental data closely, slightly over-predicting failure in all cases. The model captured the contribution of the stirrups to strength better than all other models, but overcompensated for the confining effects of the stirrups.

## 4.2 Verification of ABAQUS Models Against Experimental Data

The beams analyzed in Section 4.1.6 were modelled in ABAQUS using the calibrated Concrete Damaged Plasticity (CDP) model. To verify the accuracy of the results, both the load-deflection curves and crack patterns determined by ABAQUS were compared to the experimentally determined plots. Furthermore, the observed behaviour at failure was compared to the conclusions drawn from the ABAQUS simulations.

The beams were analyzed using dilation angles of 30° and 50° to study the effects of confinement on the model's accuracy.

### 4.2.1 Beams without Stirrups

#### 30° Dilation

#### JSC32-NT

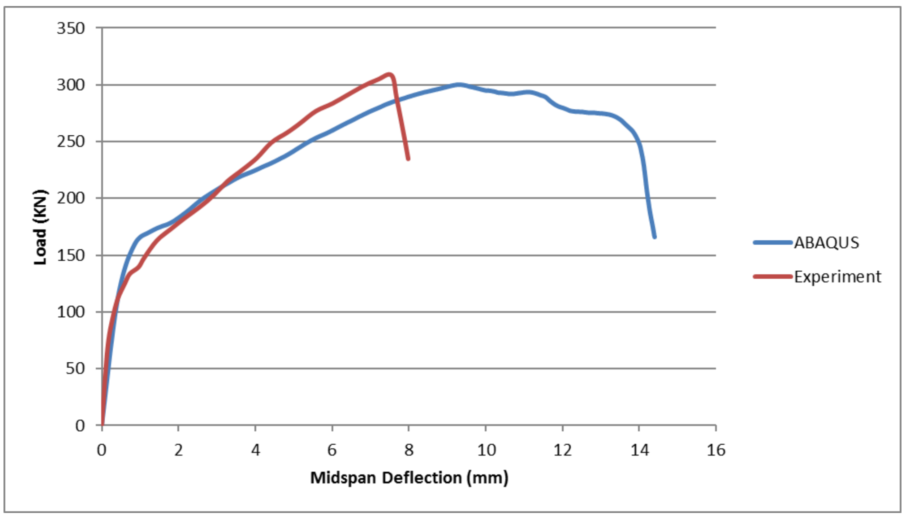


Figure 4.1: Load-Deflection Graphs for JSC32-NT, 30° Dilation

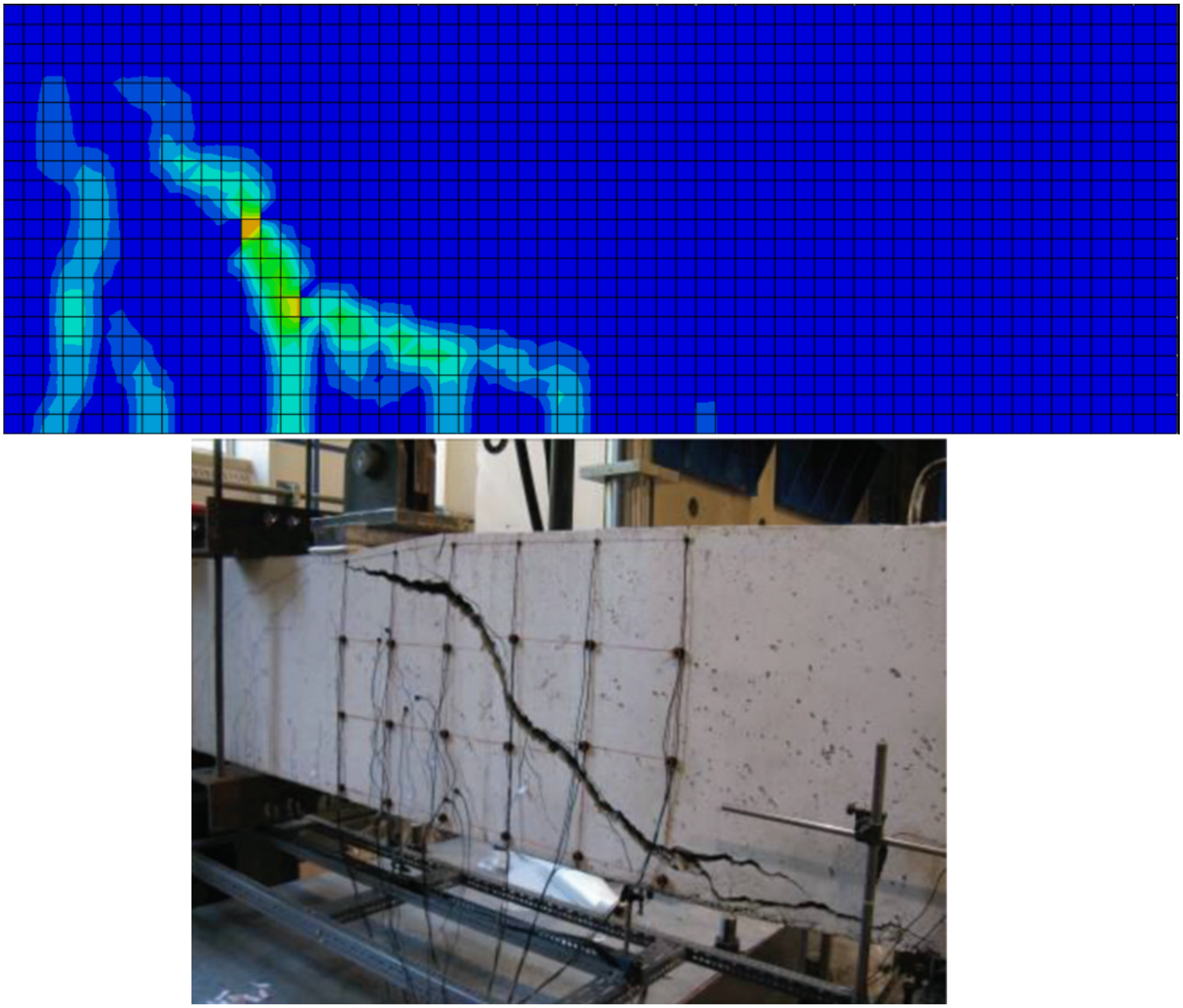

Figure 4.2: Simulated (Top) vs. Experiment (Bottom) [39] Crack Pattern for JSC32-NT, 30° Dilation

Figure 4.1 compares the experimentally determined load-deflection curve to the one generated by ABAQUS for specimen JSC32-NT. The peak loads for both curves match closely, suggesting the model to be a good approximation for the observed behaviour. The authors selected to end the experiment prior to the peak load, as the plot ends abruptly, prior to an inflection point.

The crack patterns displayed in Figure 4.2 are consistent with one another, with the model results showing a similar diagonal shear crack and no crushing at the load application point.

## JSV40-NT

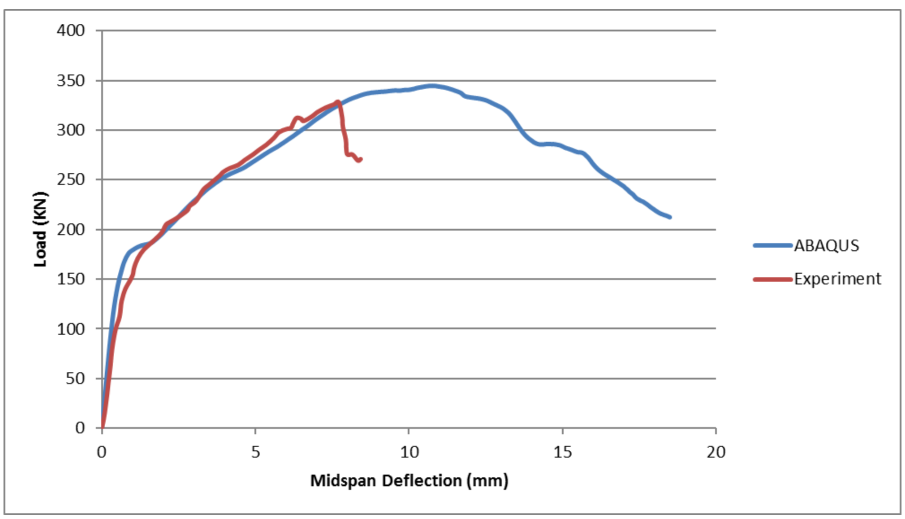


Figure 4.3: Load-Deflection Graphs for JSV40-NT, 30° Dilation

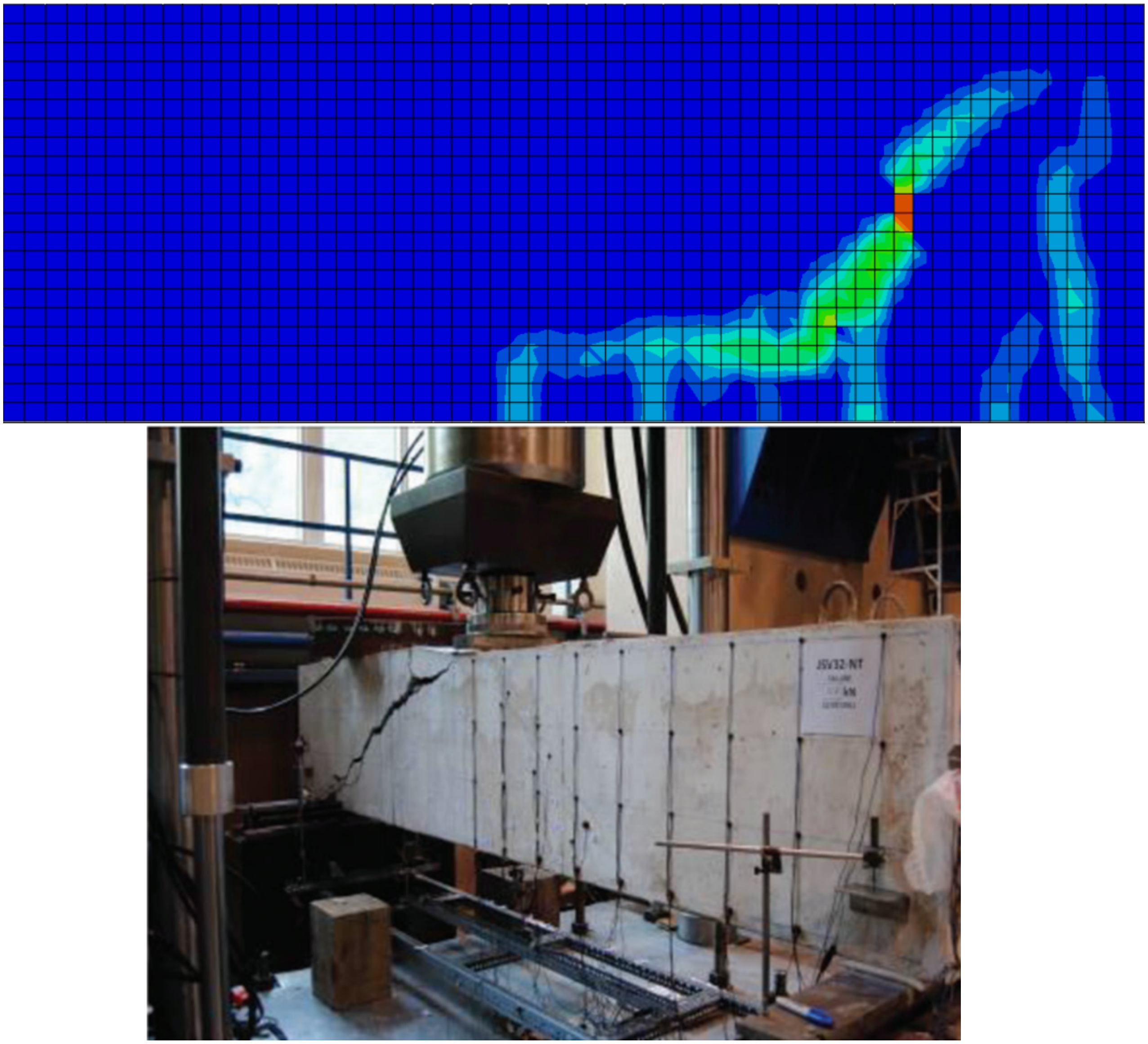


Figure 4.4: Simulated (Top) vs. Experiment (Bottom) [39] Crack Pattern for JSV40-NT, 30° Dilation

Figure 4.3 shows the cracking loads and slopes of the load-deflection curves matching very closely, suggesting an accurate response from ABAQUS.

The crack patterns displayed in Figure 4.4 are consistent with a shear failure. The simulated pattern shows the same diagonal shear crack at failure.

## 50° Dilation

## JSC32-NT

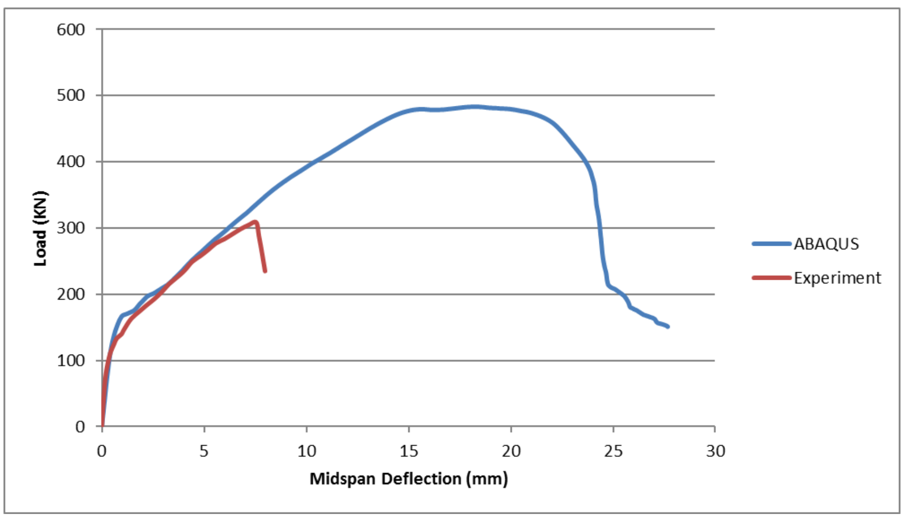


Figure 4.5: Load-Deflection Graphs for JSC32-NT, 50° Dilation

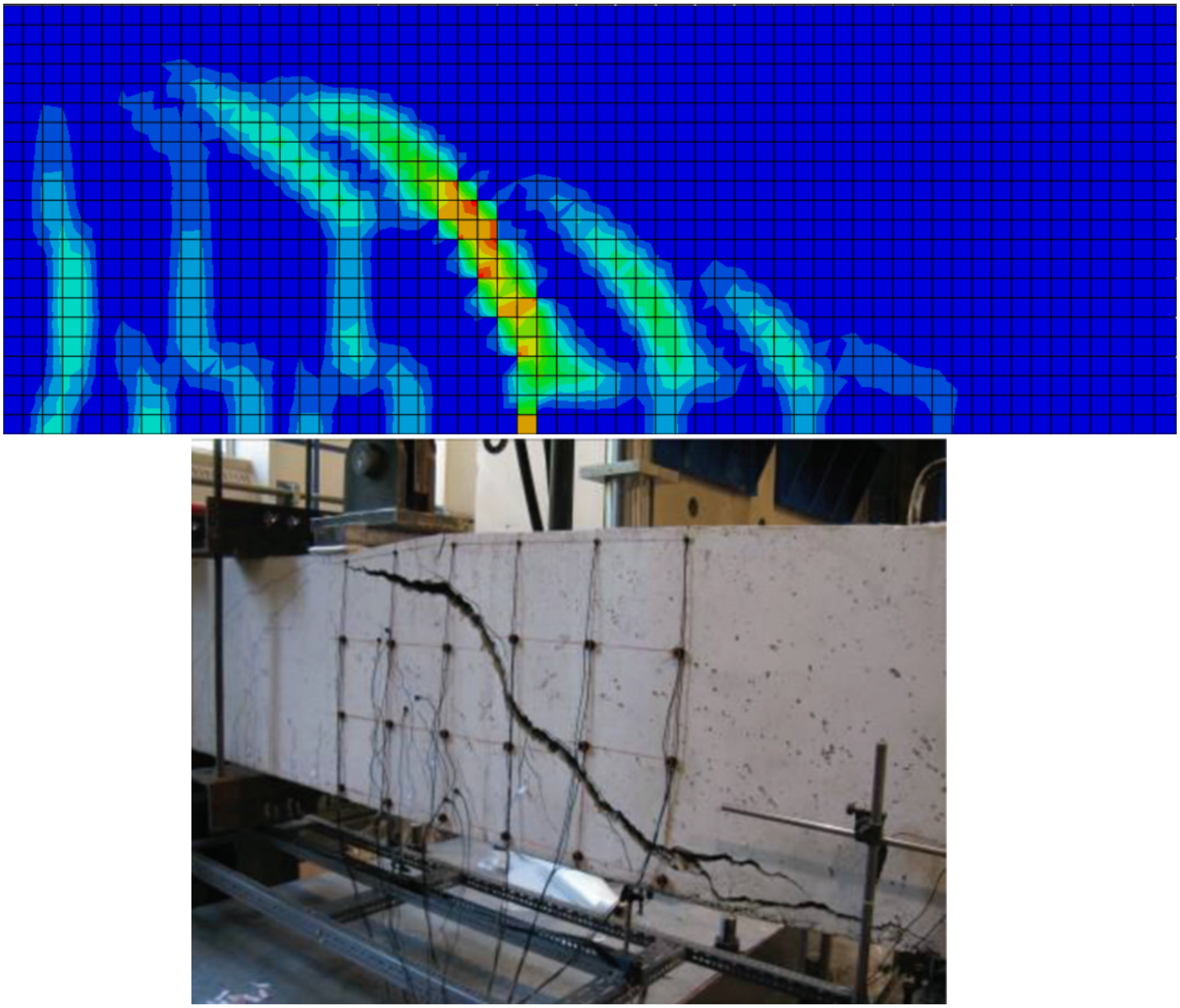

Figure 4.6: Simulated (Top) vs. Experiment (Bottom) [39] Crack Pattern for JSC32-NT, 50° Dilation

The slope of the load-deflection curves shown in Figure 4.5 suggest that the ABAQUS model will over-predict the peak load for beam JSC32-NT. The drop in load in the experimental load-deflection curve can be attributed to the authors ending the experiment, however the slope suggests further load capacity. A higher load is obtained from ABAQUS due to the extra stiffness provided by the increased dilation angle.

The crack patterns from Figure 4.6 are consistent with the mode of failure observed in the experiment, as the diagonal shear crack can be observed in the simulated crack pattern.

## JSV40-NT

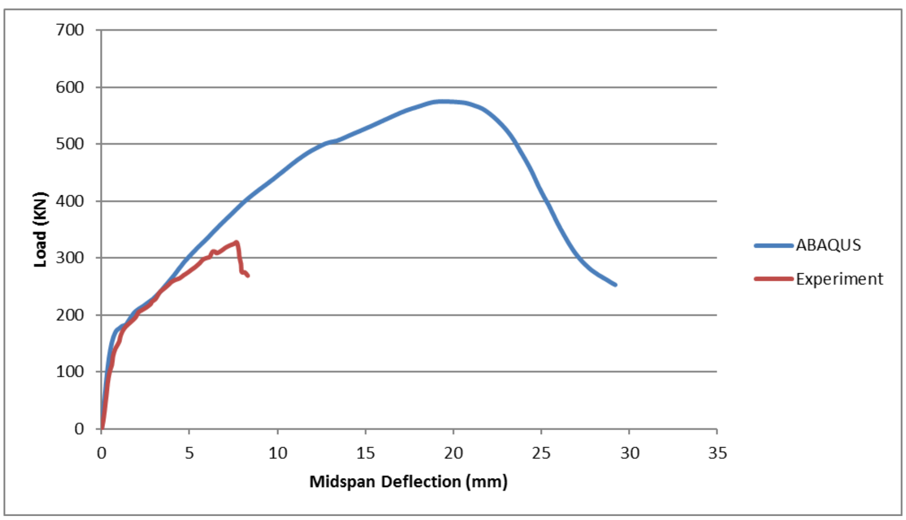


Figure 4.7: Load-Deflection Graphs for JSV40-NT, 50° Dilation

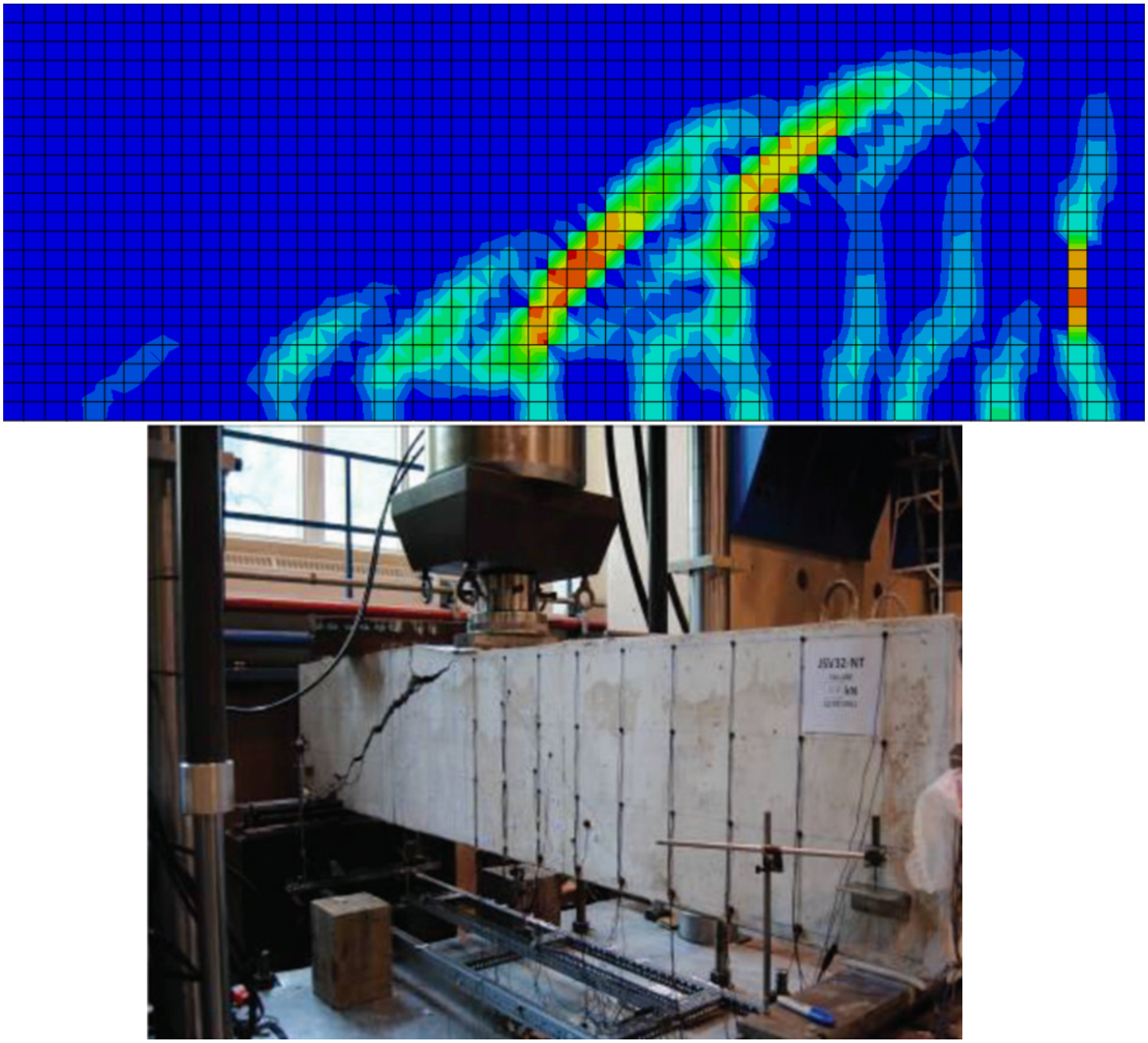


Figure 4.8: Simulated (Top) vs. Experiment (Bottom) [39] Crack Pattern for JSV40-NT, 50° Dilation

Similar to the results observed for specimen JSC32-NT, the model results closely match the observed behaviour, with the results for 30° dilation concrete presenting a more accurate depiction. This thesis therefore confirms Stoner's recommendation that 30° dilation concrete be used to model beams without stirrups.

### 4.2.2 Beams with Stirrups

#### 30° Dilation

#### JSC32-22B

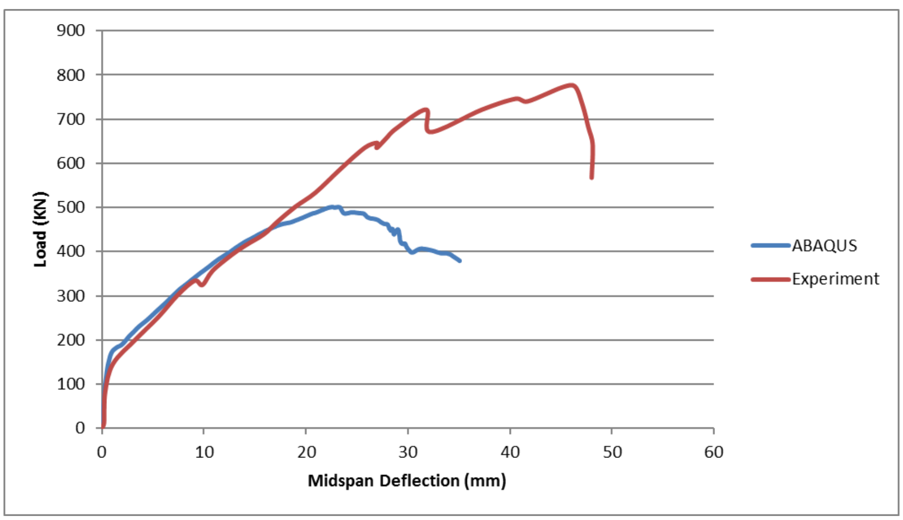


Figure 4.9: Load-Deflection Graphs for JSC32-22B, 30° Dilation

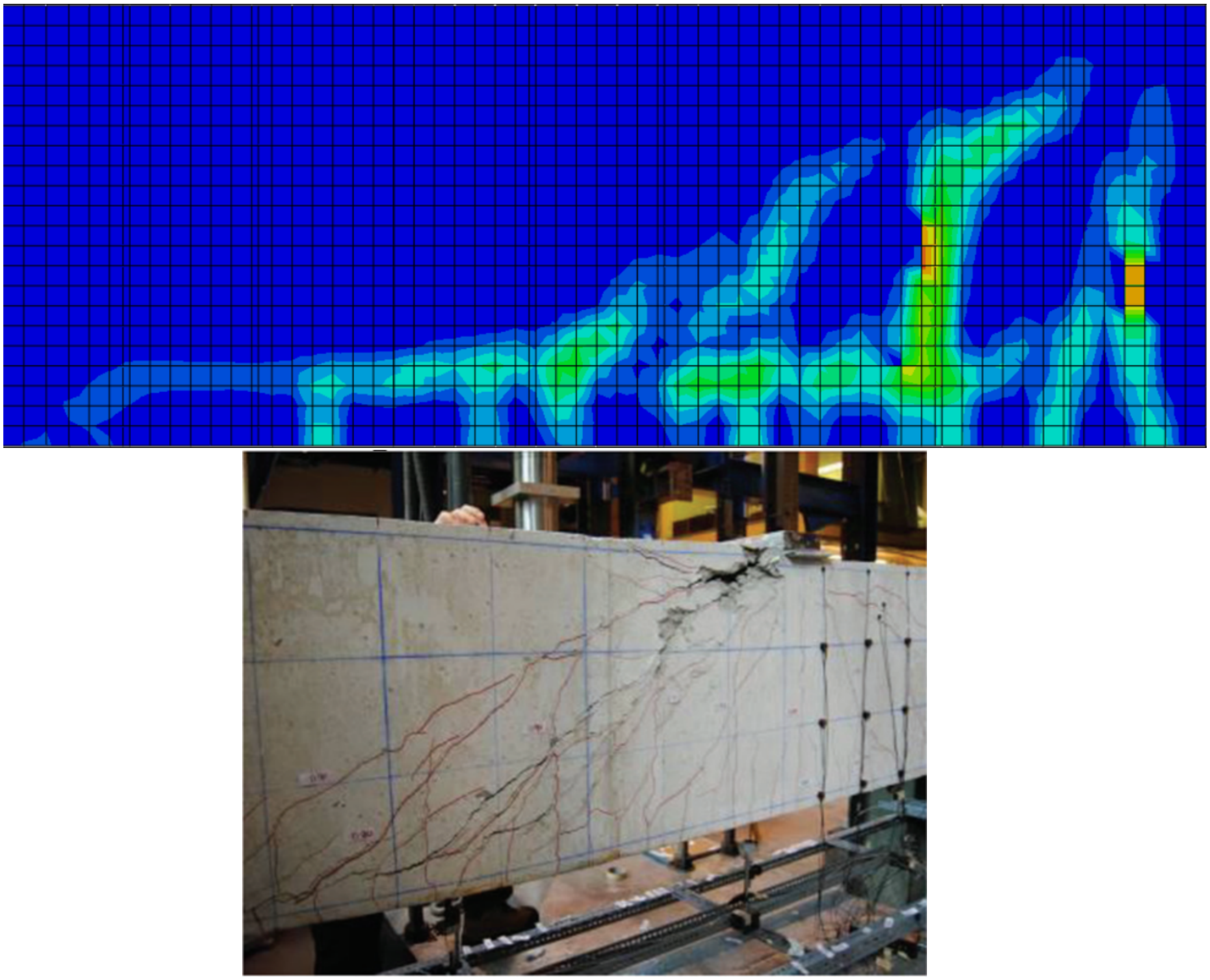

Figure 4.10: Simulated (Top) vs. Experiment (Bottom) [39] Crack Pattern for JSC32-22B, 30° Dilation

The load-deflection curves shown is Figure 4.9 suggest that the ABAQUS model under-predicted the failure load for specimen JSC32-22B. The simulated cracks from Figure 4.10 also depict a shear failure but the strains in the stirrups shown (orange) do not capture the observed stirrup rupture.

## JSC32-40B

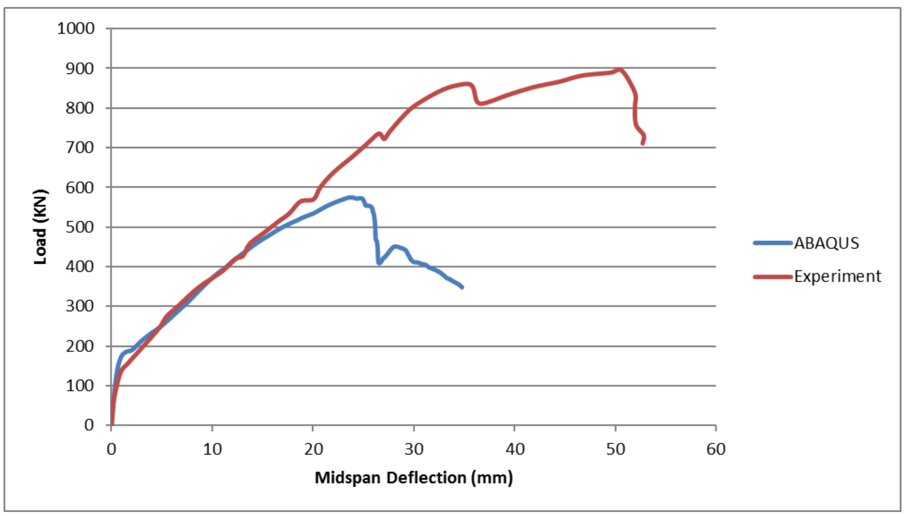


Figure 4.11: Load-Deflection Graphs for JSC32-40B, 30° Dilation

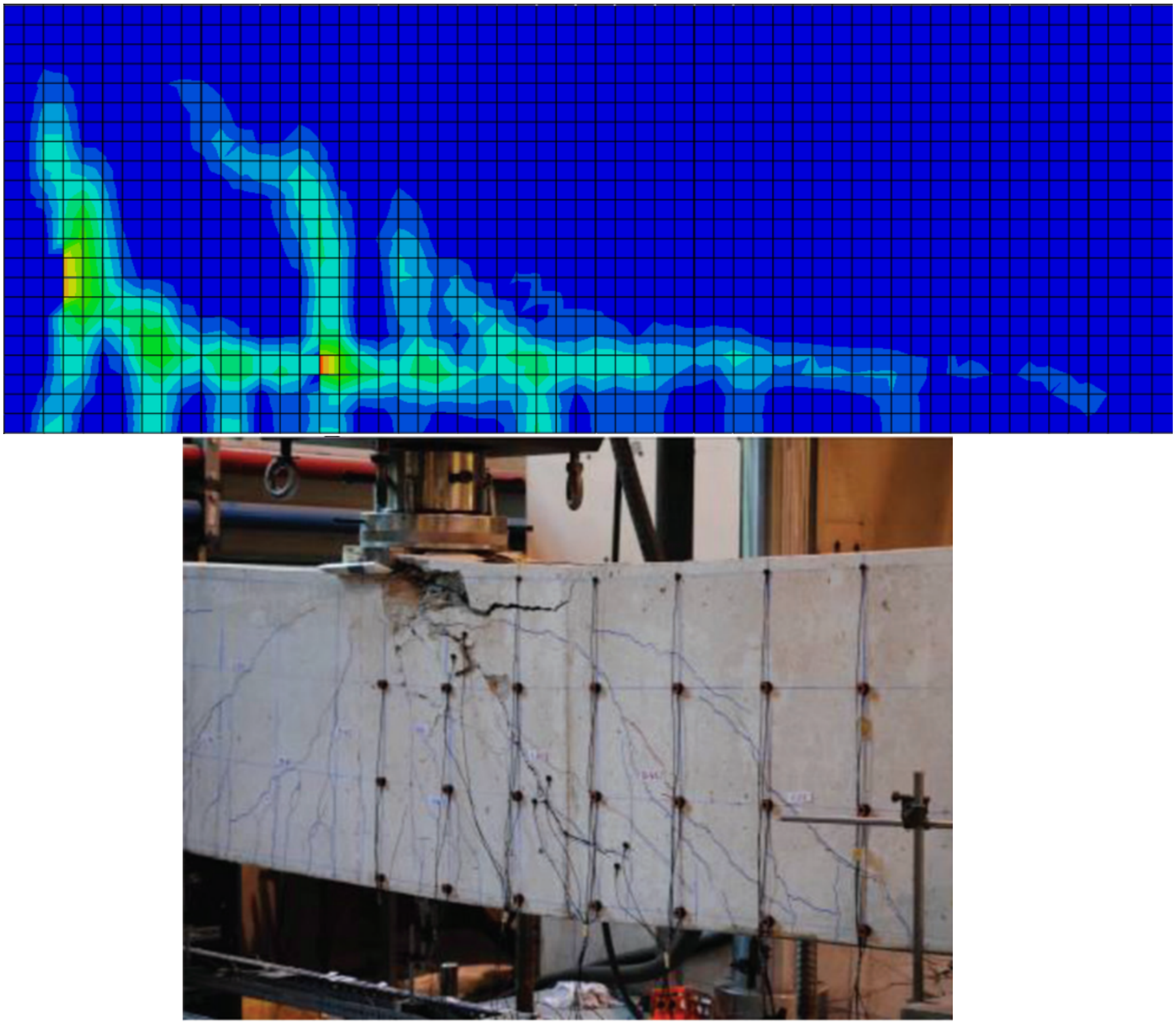

Figure 4.12: Simulated (Top) vs. Experiment (Bottom) [39] Crack Pattern for JSC32-40B, 30° Dilation

Specimen JSC32-40B exhibited concrete crushing at the load application point, which continued down to the core concrete enclosed by the stirrups. The load then stabilized and began to slowly increase with increased displacement. The strains in the stirrups then increased as the concrete delaminated from the surface of the stirrups, resulting in rupture; shear failure was ultimately observed.

The load-deflection curves and crack patterns shown in Figures 4.11 and 4.12 respectively yield the same results as specimen JSC32-22B. The model under-predicts the failure load of the specimen and crack pattern does not depict the crushing of concrete at the load application point.

## JSC32-50B

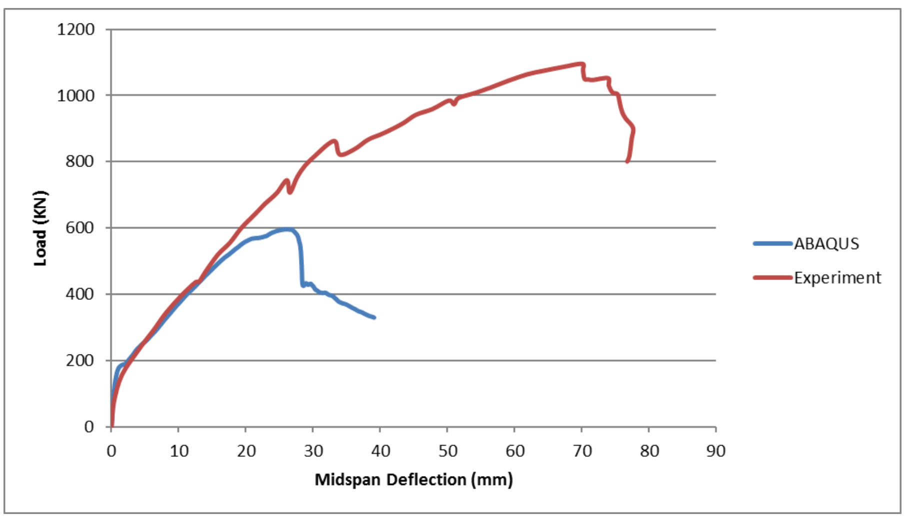


Figure 4.13: Load-Deflection Graphs for JSC32-50B, 30° Dilation

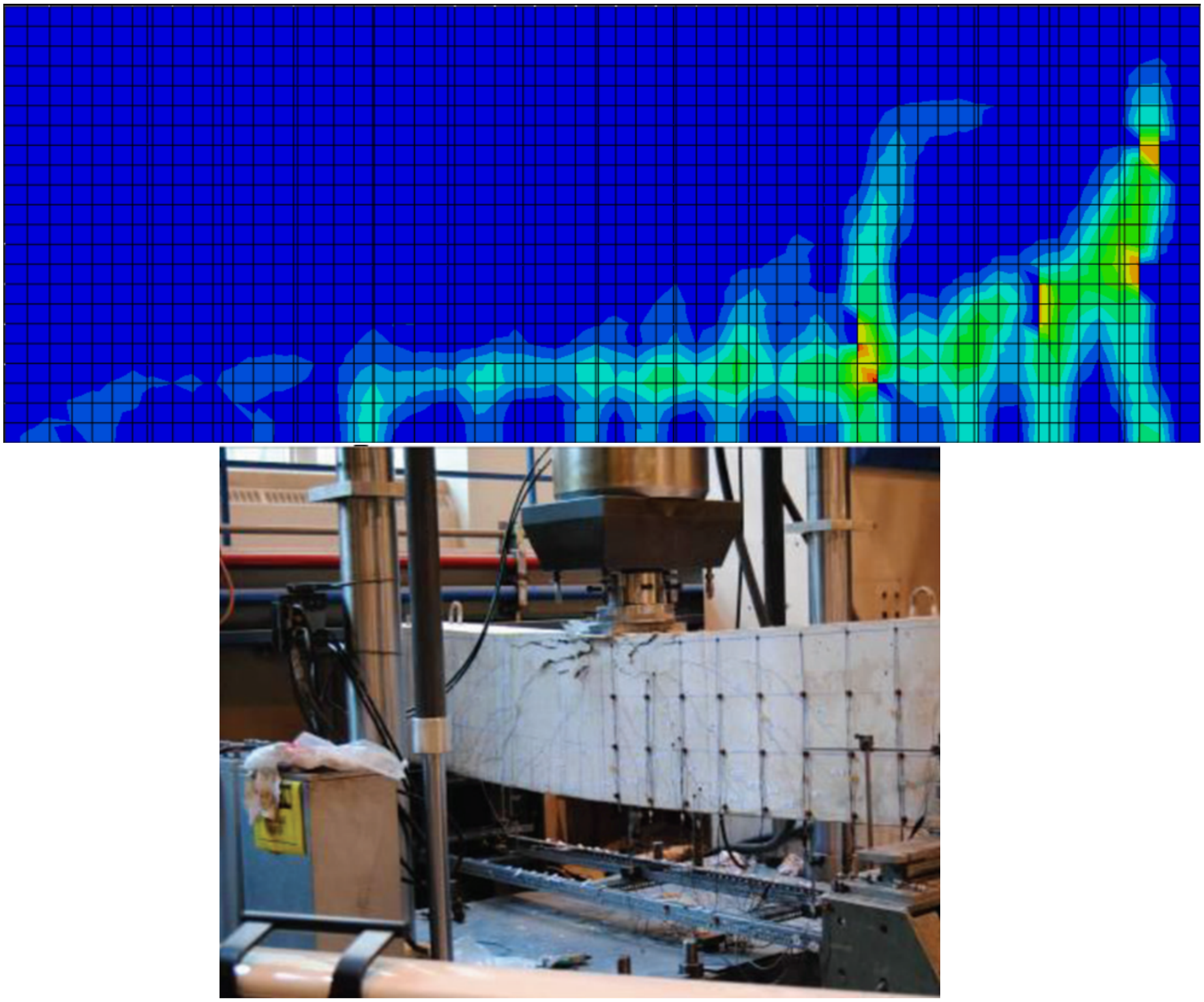

Figure 4.14: Simulated (Top) vs. Experiment (Bottom) [39] Crack Pattern for JSC32-50B, 30° Dilation

Specimen JSC32-50B failed in a similar manner to specimen JC32-40B, with a higher peak load as a result of reduced stirrup spacing. Crushing of the concrete began at the load application point, followed by shear failure due rupture of the stirrups. The model once again under-predicts failure, and the crushing of the concrete is not event from the simulated crack patterns.

## JSV40-22B

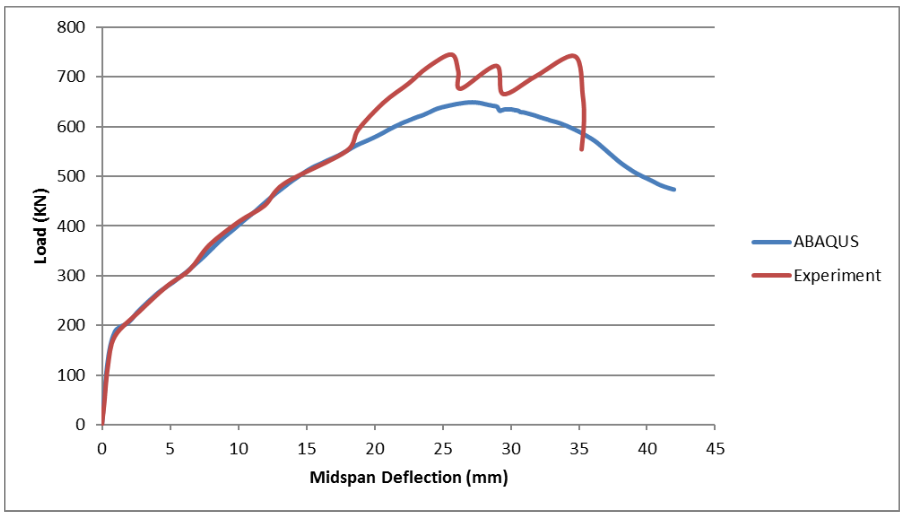


Figure 4.15: Load-Deflection Graphs for JSV40-22B, 30° Dilation

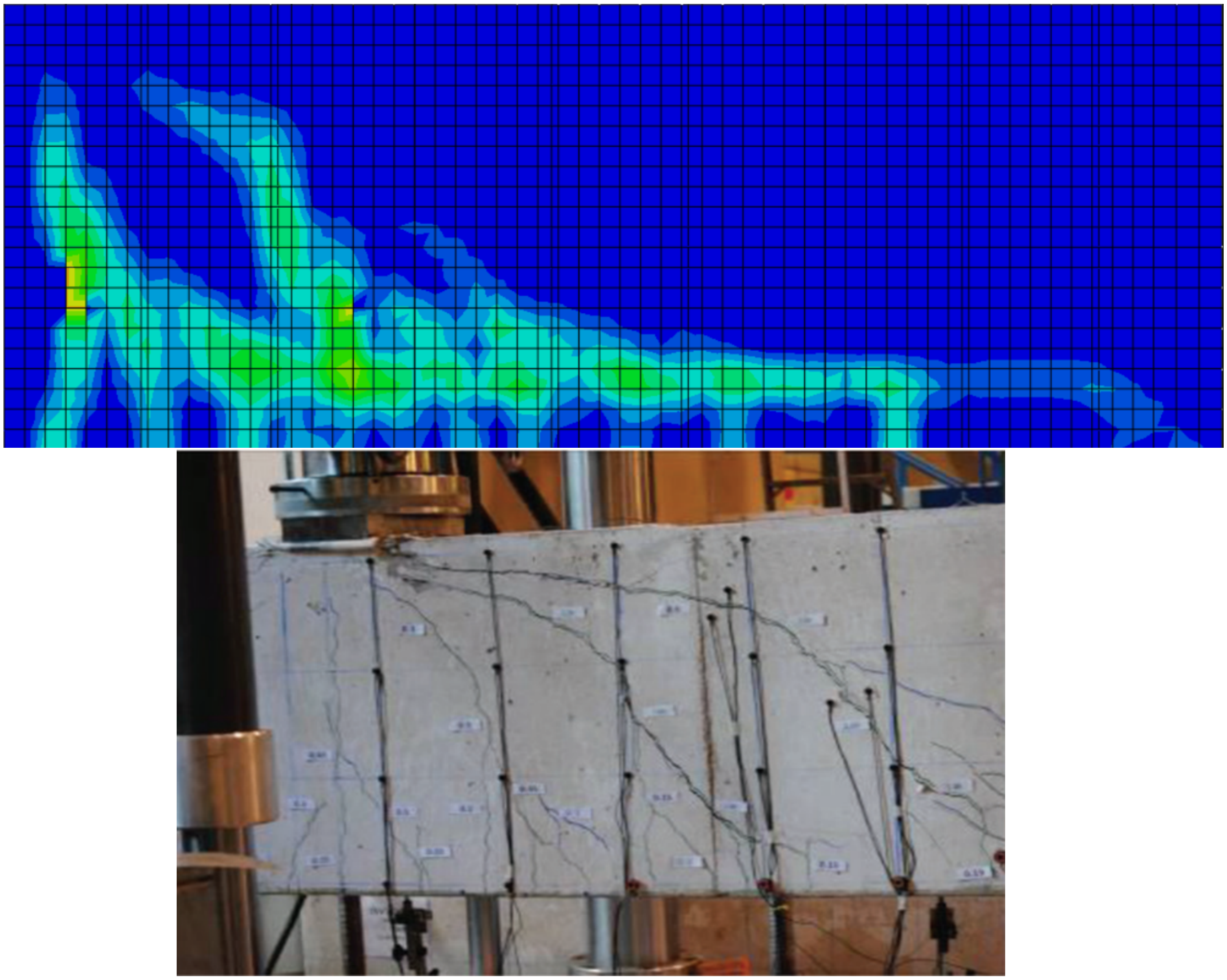

Figure 4.16: Simulated (Top) vs. Experiment (Bottom) [39] Crack Pattern for JSV40-22B, 30° Dilation

Specimen JSV40-22B failed in shear due to rupturing of the stirrups. The shear failure was preceded by widening shear cracks as observed in Figure 4.16. The simulated crack pattern fails to adequately capture the rupturing of the stirrups, as suggested by the intensity of the contours in Figure 4.16.

## JSV40-40B

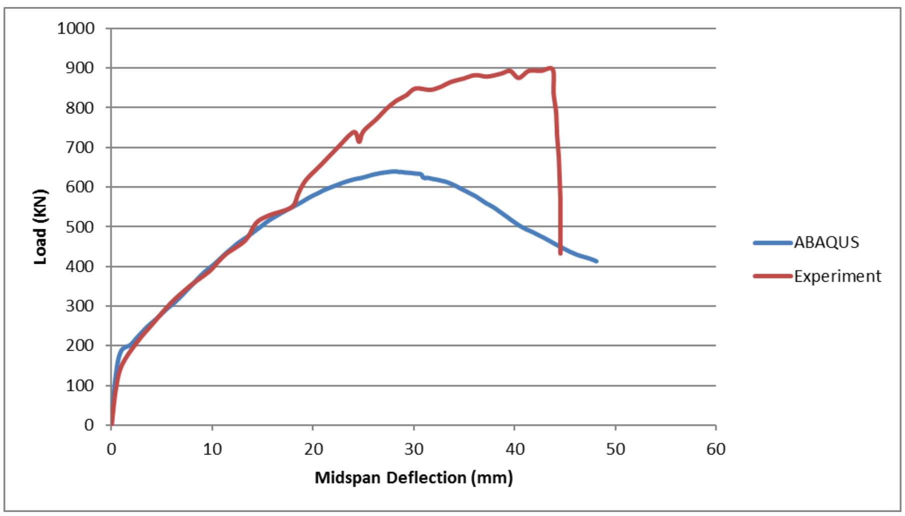


Figure 4.17: Load-Deflection Graphs for JSV40-40B, 30° Dilation

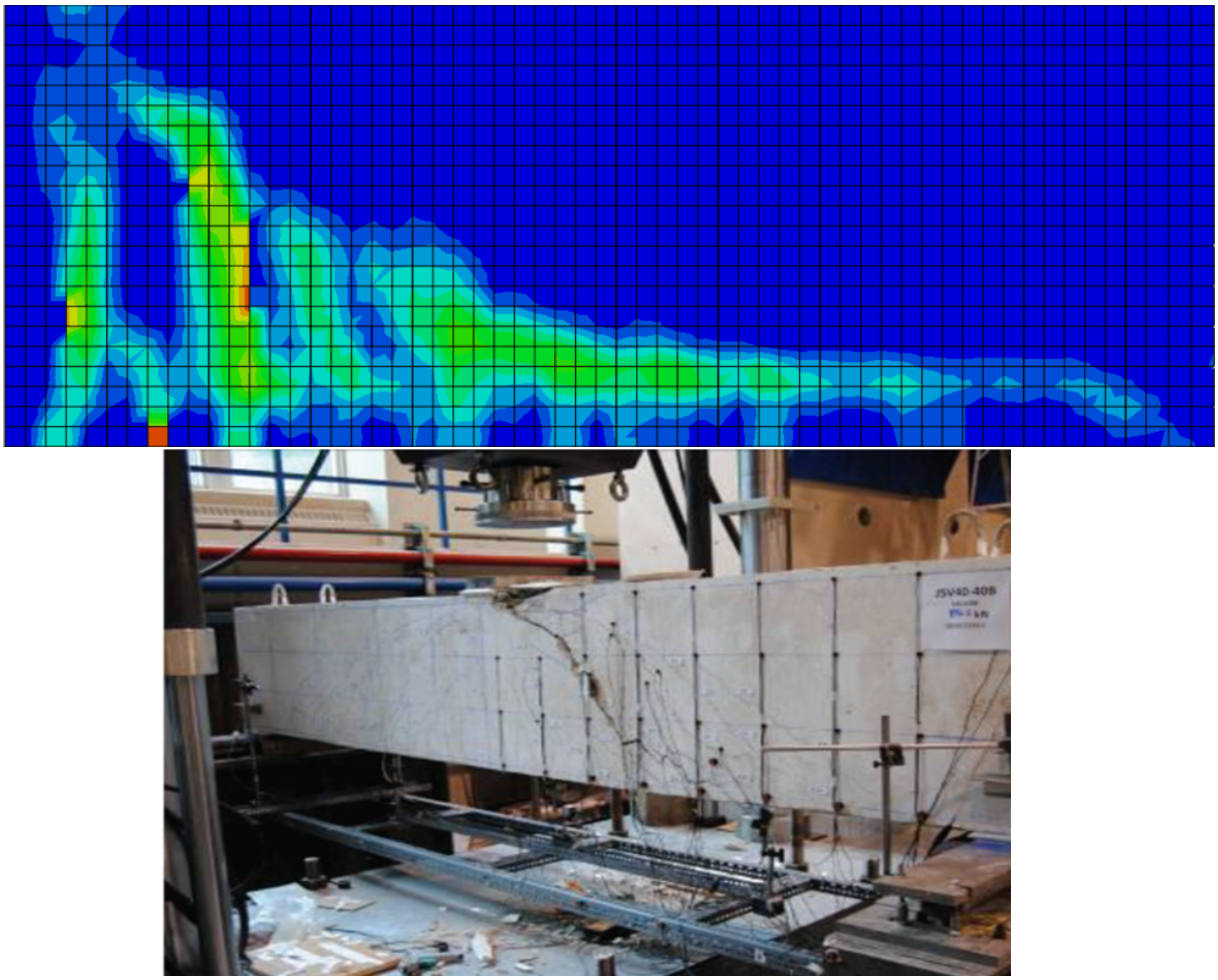


Figure 4.18: Simulated (Top) vs. Experiment (Bottom) [39] Crack Pattern for JSV40-40B, 30° Dilation

Specimen JSV40-50B also failed due to widening shear cracks leading to stirrup rupture. Like specimen JSV40-22B, the peak load is under-predicted by the model. However, the strain intensity in crack pattern shown in Figure 4.18 better reflects a rupture failure than in specimen JSV40-22B.

## JSV40-50B

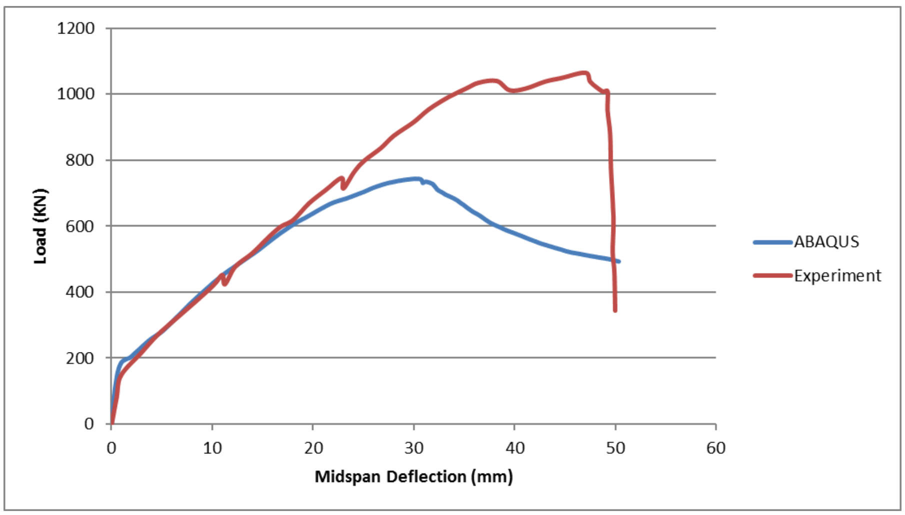


Figure 4.19: Load-Deflection Graphs for JSV40-50B, 30° Dilation

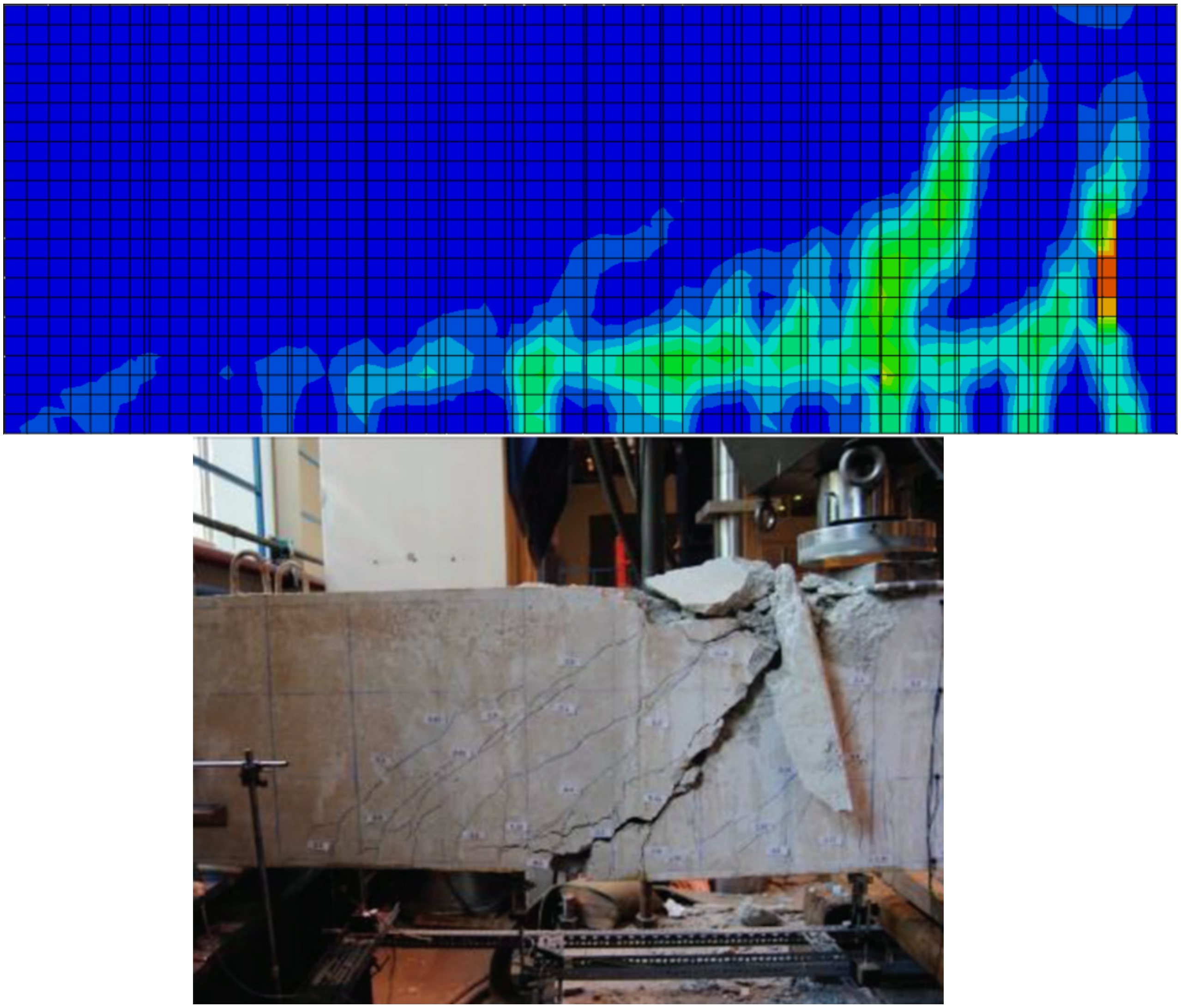

Figure 4.20: Simulated (Top) vs. Experiment (Bottom) [39] Crack Pattern for JSV40-50B, 30° Dilation

Similar to specimen JSC32-40B and JSC32-50B, specimen JSV40-50B exhibited concrete crushing at the load application point, followed by an eventual rupturing of the stirrups. The shear failure can be observed in the simulated crack patterns shown in Figure 4.20, however the contours fail to adequately depict the crushing of concrete at the load application point. Furthermore, the model follows the pattern of under-predicting the failure, suggesting stiffer concrete may be required.

## 50° Dilation

## JSC32-22B

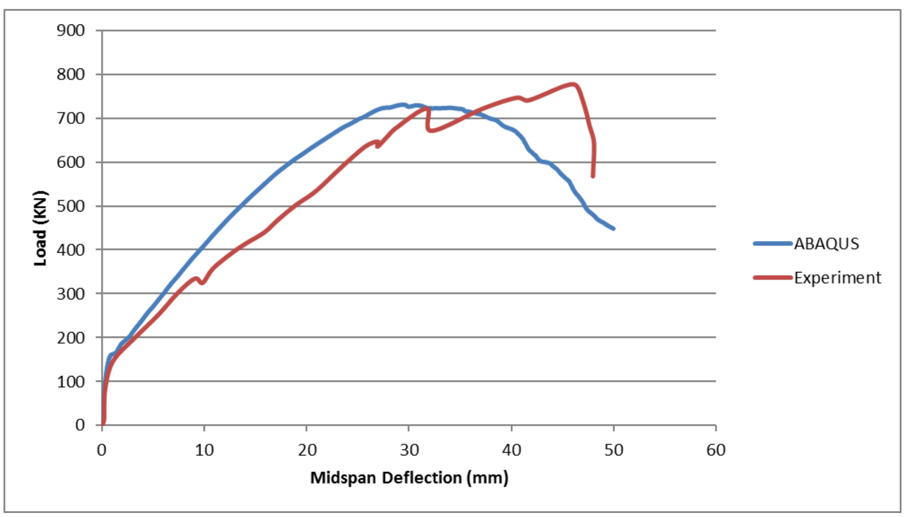


Figure 4.21: Load-Deflection Graphs for JSC32-22B, 50° Dilation

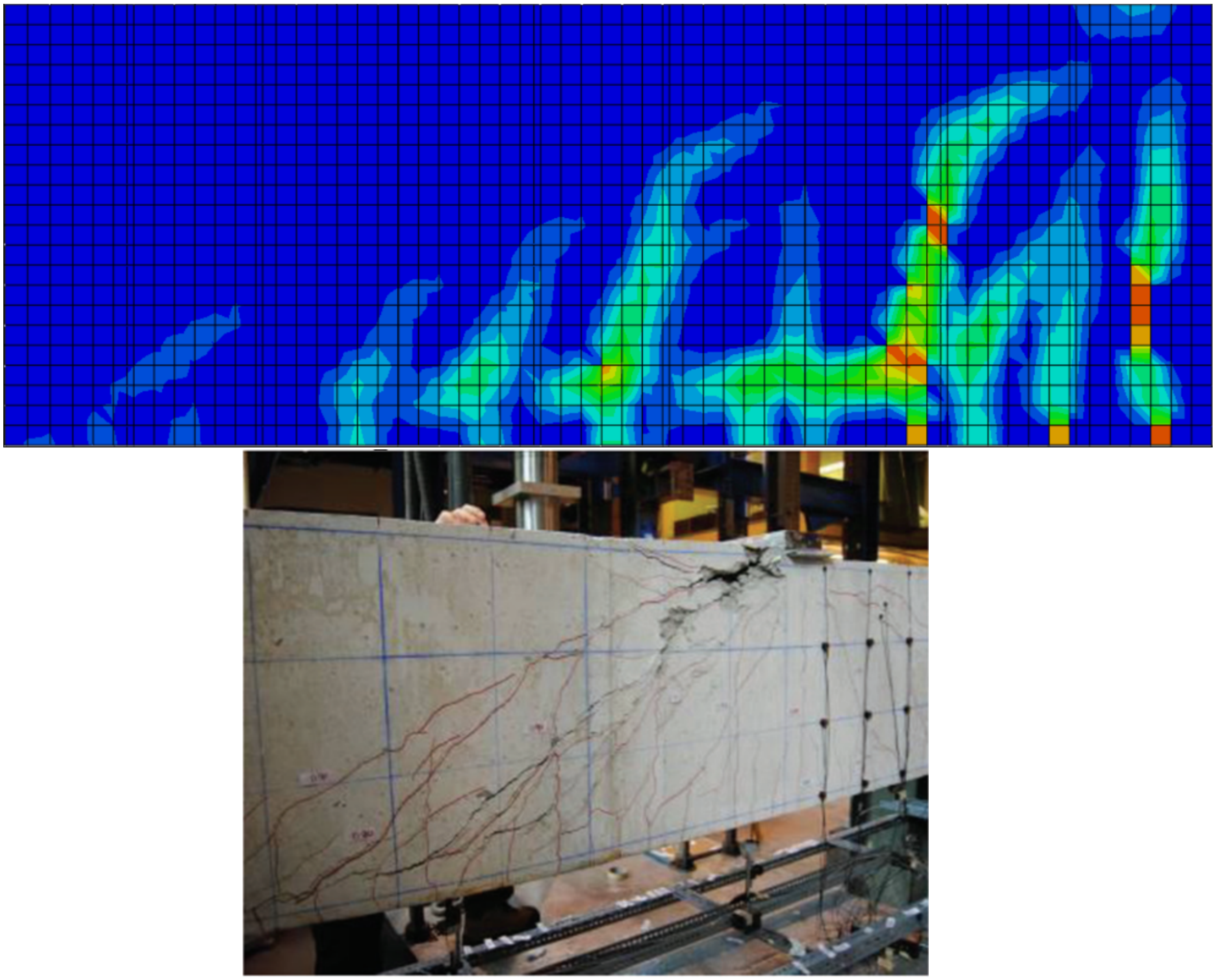

Figure 4.22: Simulated (Top) vs. Experiment (Bottom) [39] Crack Pattern for JSC32-22B, 50° Dilation

The load-deflection curves shown in Figure 4.21 suggest a more accurate prediction than 30° dilation model. The model does not capture the reduction in strength after the concrete crushing occurs, but the increased stiffness from raising the dilation angle resulted in a more accurate peak load prediction. Furthermore, the rupture of the stirrups is more evident in Figure 4.22, as the contours show larger strains in the vertical planes where the stirrups lie.

## JSC32-40B

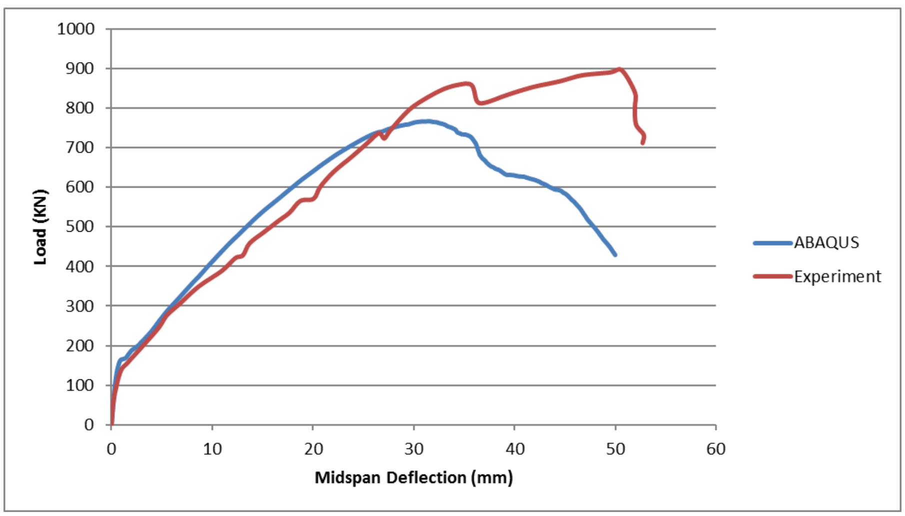


Figure 4.23: Load-Deflection Graphs for JSC32-40B, 50° Dilation

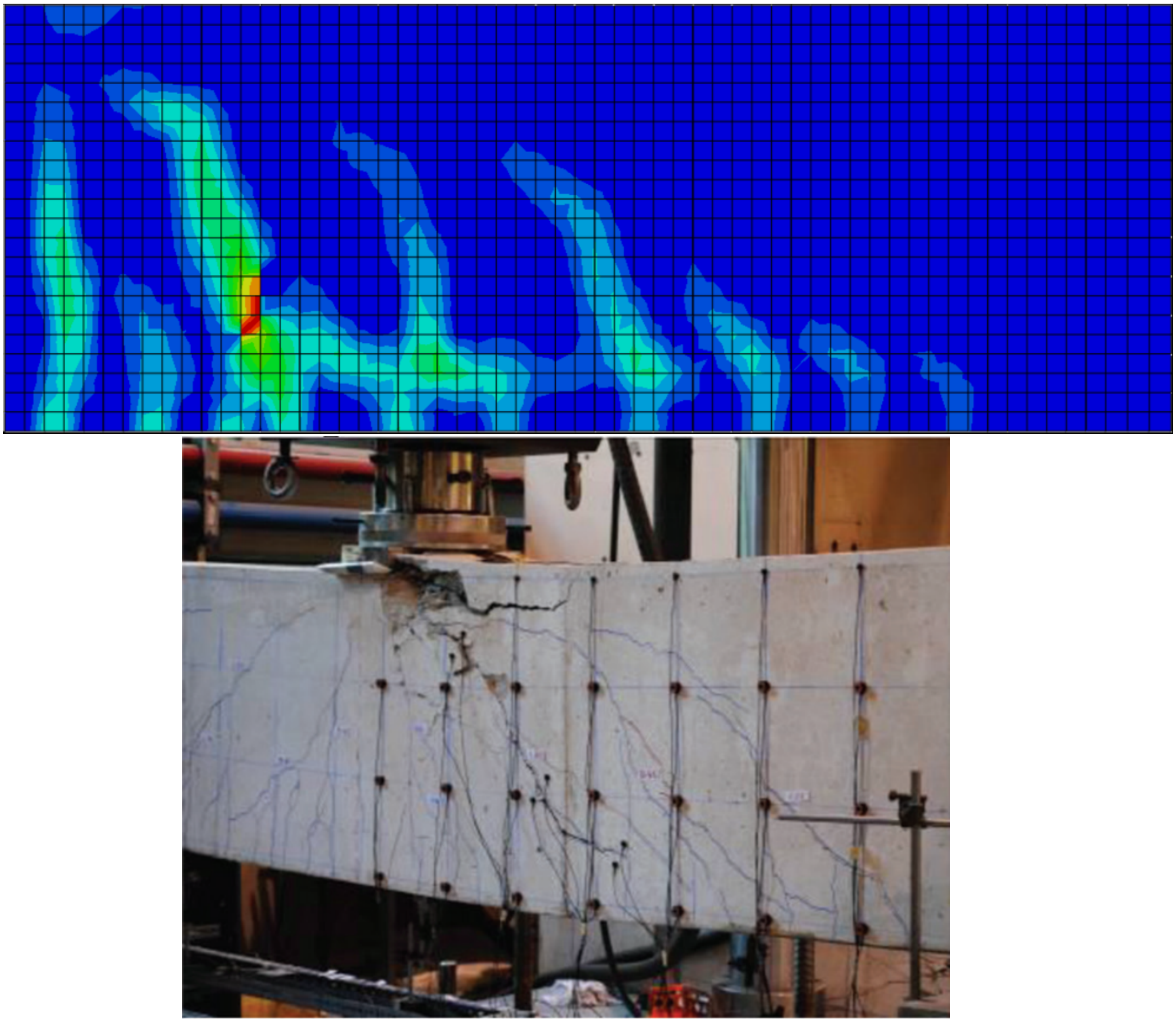

Figure 4.24: Simulated (Top) vs. Experiment (Bottom) [39] Crack Pattern for JSC32-40B, 50° Dilation

Specimen JSC32-40B exhibited a similar response to the influence of dilation angle as specimen JSC32-22B, as Figure 4.23 suggests a more closely matching peak load. The rupture of the stirrups is also more evident in Figure 4.24, as the large strains in the stirrups are more apparent. Furthermore, the 50° dilation model displays the strains indicative of concrete crushing at the load application point; these strains were not apparent in the 30° model.

## JSC32-50B

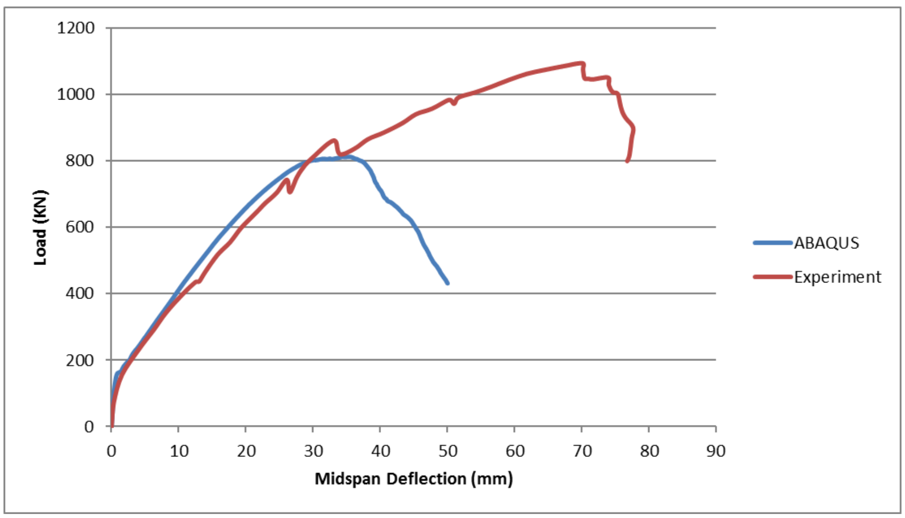


Figure 4.25: Load-Deflection Graphs for JSC32-50B, 50° Dilation

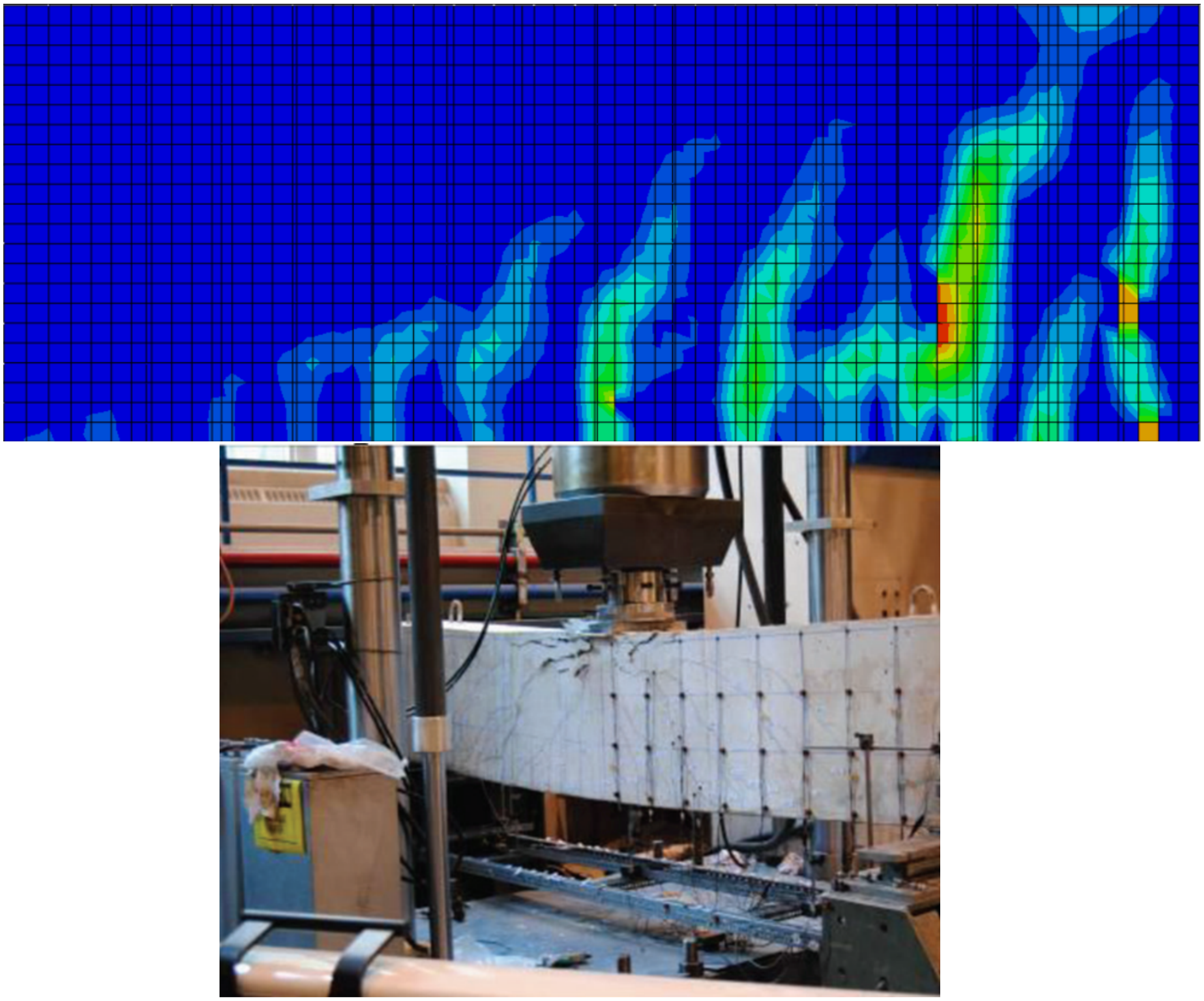

Figure 4.26: Simulated (Top) vs. Experiment (Bottom) [39] Crack Pattern for JSC32-50B, 50° Dilation

The results for the 50° dilation model remain consistent with the previously discussed beams, showing a more accurate depiction of the load capacity of beams with stirrups. Figure 4.25 shows the ultimate load predicted by ABAQUS to coincide the with the point of concrete crushing from the experiment. The model does not capture the increase in load past the crushing at the application point. This pattern is consistent with the results for specimen JSC32-40B, suggesting that ABAQUS considers the ultimate failure of the specimen to occur at the first determined failure (crushing). Further calibration of the ABAQUS model may be required to capture the complete behaviour.

## JSV40-22B

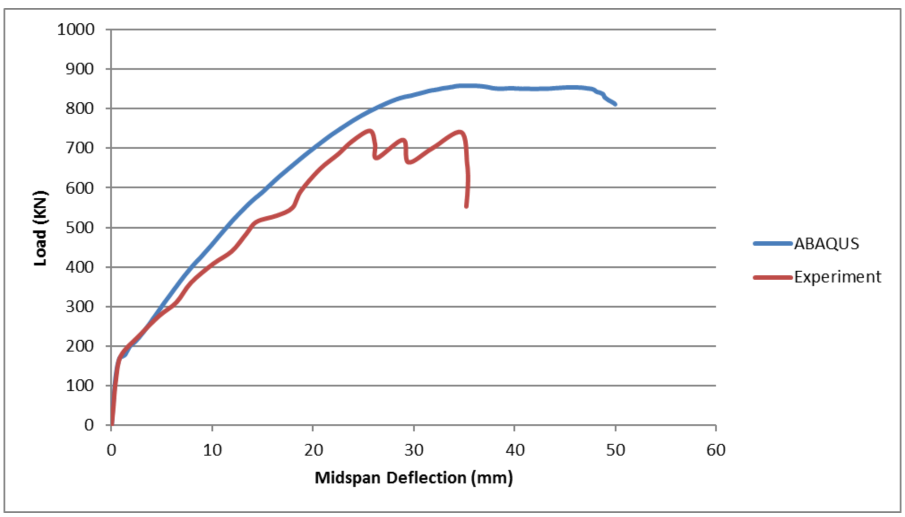


Figure 4.27: Load-Deflection Graphs for JSV40-22B, 50° Dilation

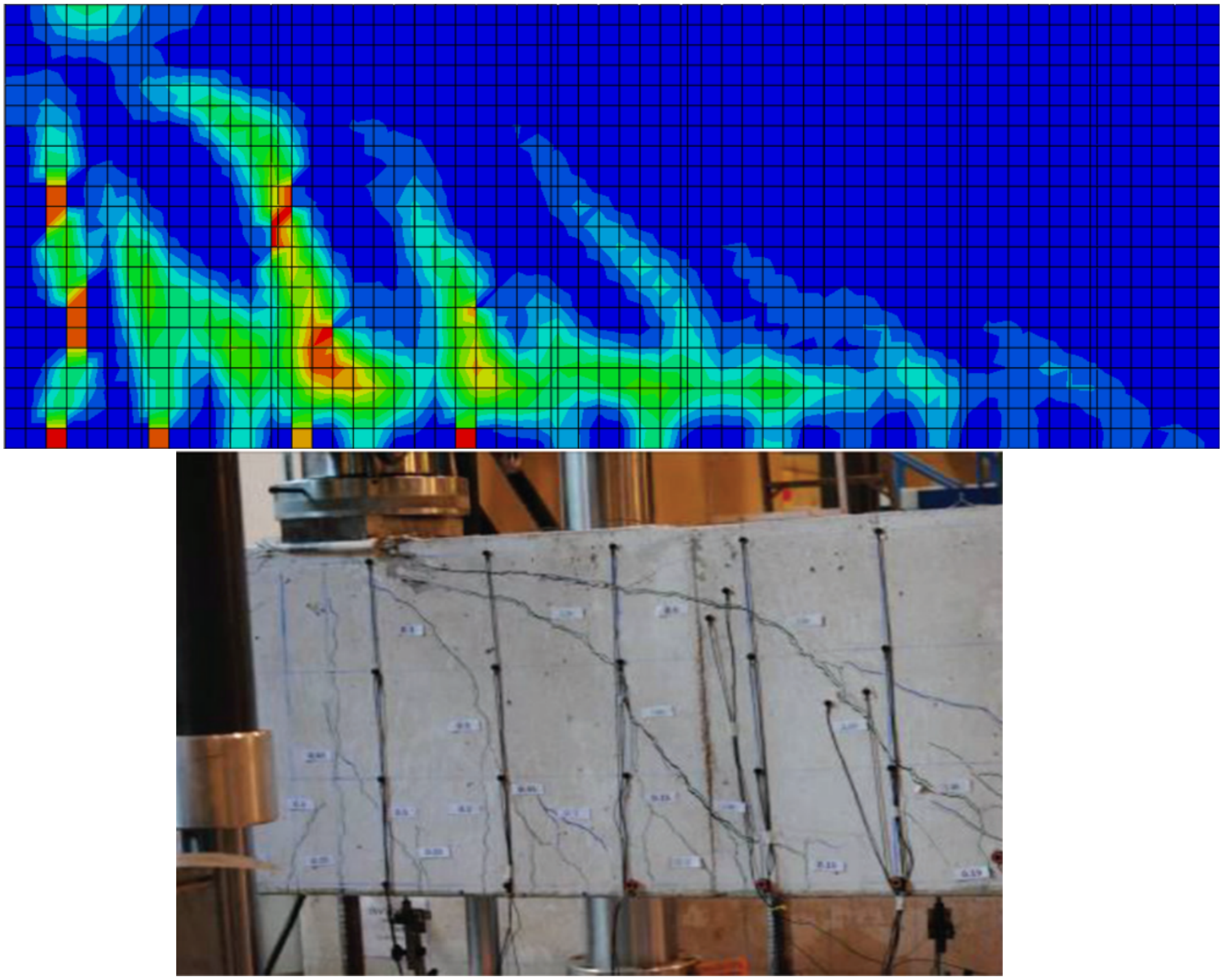

Figure 4.28: Simulated (Top) vs. Experiment (Bottom) [39] Crack Pattern for JSV40-22B, 50° Dilation

Figure 4.27 shows the predicted load capacity to match more closely than the 30° model. The successive peaks shown on the experimental curve illustrate the successive stirrup ruptures. The model curve does not capture this behaviour, but rather considers the first rupture to coincide with the peak load. This behaviour is consistent with specimens JSC32-40B and JSC32-50B, where behaviour past the flexural crushing was not captured. Furthermore, the simulated cracks shown in Figure 4.28 better demonstrate the rupturing of the stirrups, as can be seen by the vertical segments of concentrated strains.

## JSV40-40B

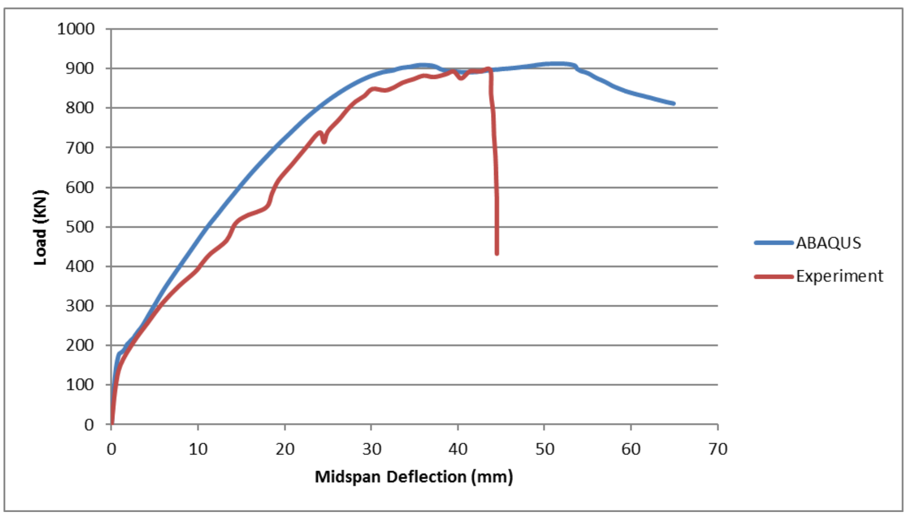


Figure 4.29: Load-Deflection Graphs for JSV40-40B, 50° Dilation

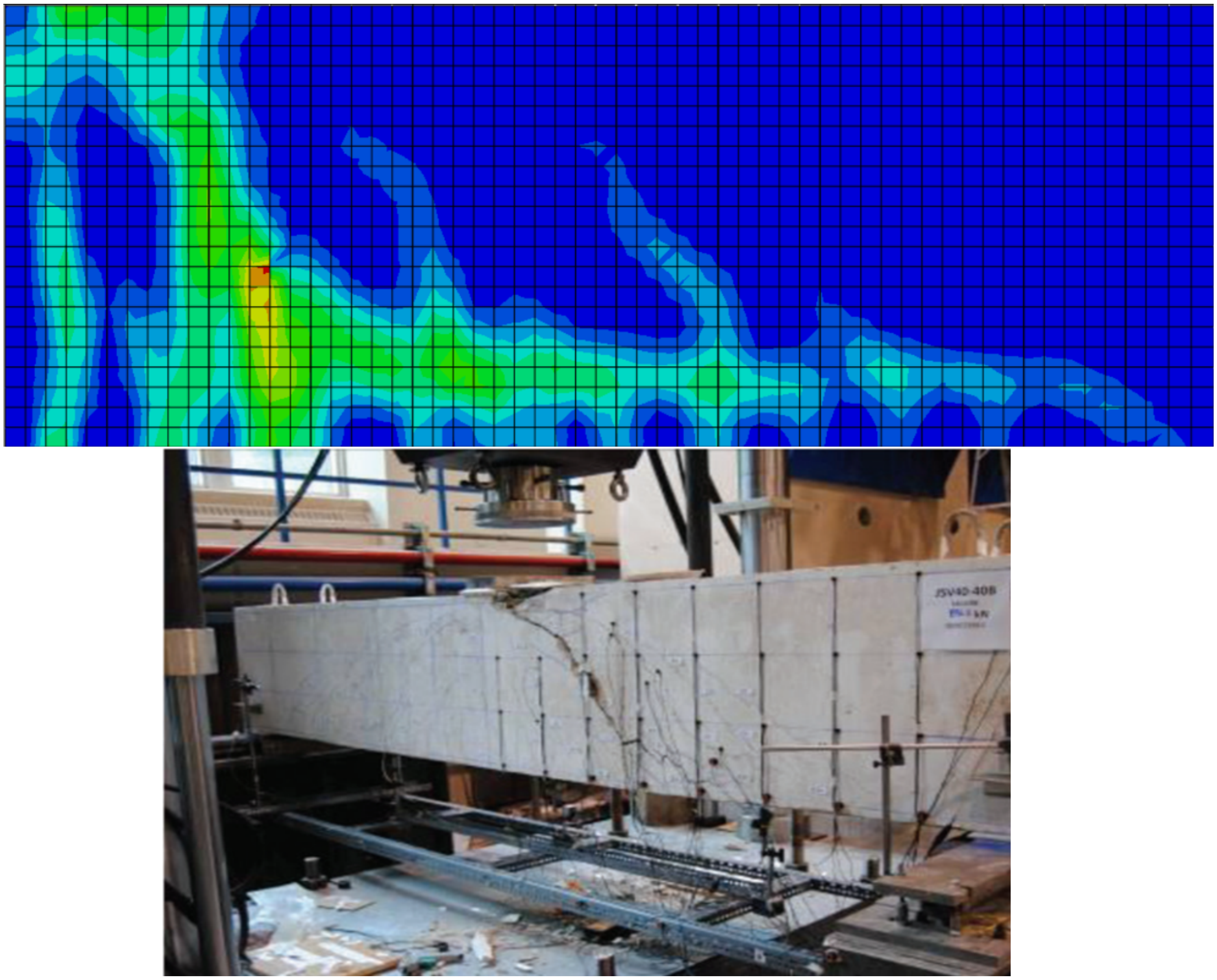


Figure 4.30: Simulated (Top) vs. Experiment (Bottom) [39] Crack Pattern for JSV40-40B, 50° Dilation

The load-deflection graphs shown in Figure 4.29 suggest a better response from the 50° model than the 30° model, as the curves match more closely. The slope of the experimental curve near the peak shows a plateau in the load, matching the model results; the authors ended the experiment at a deflection of 43 mm. The model crack patterns shown in Figure 4.30 accurately capture the primary diagonal crack, also displaying the increased strain at mid-height seen in the experiment (Figure 4.30, bottom).

## JSV40-50B

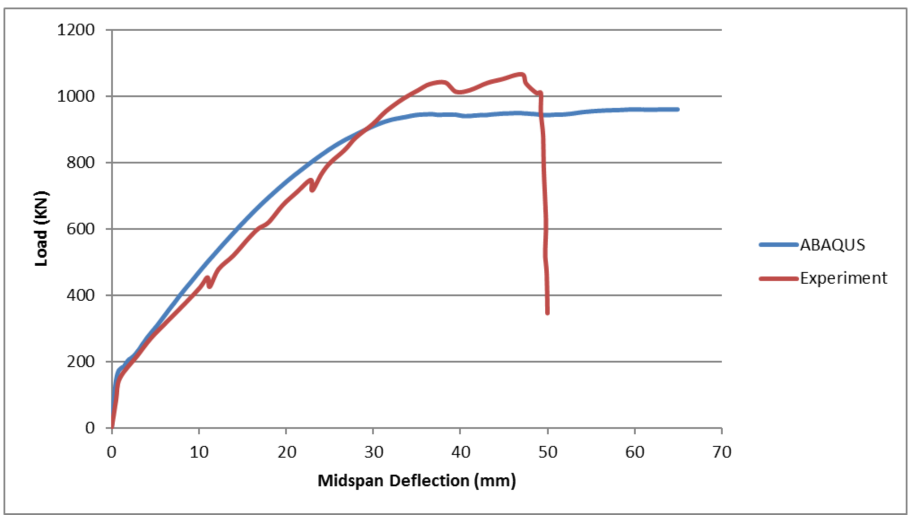


Figure 4.31: Load-Deflection Graphs for JSV40-50B, 50° Dilation

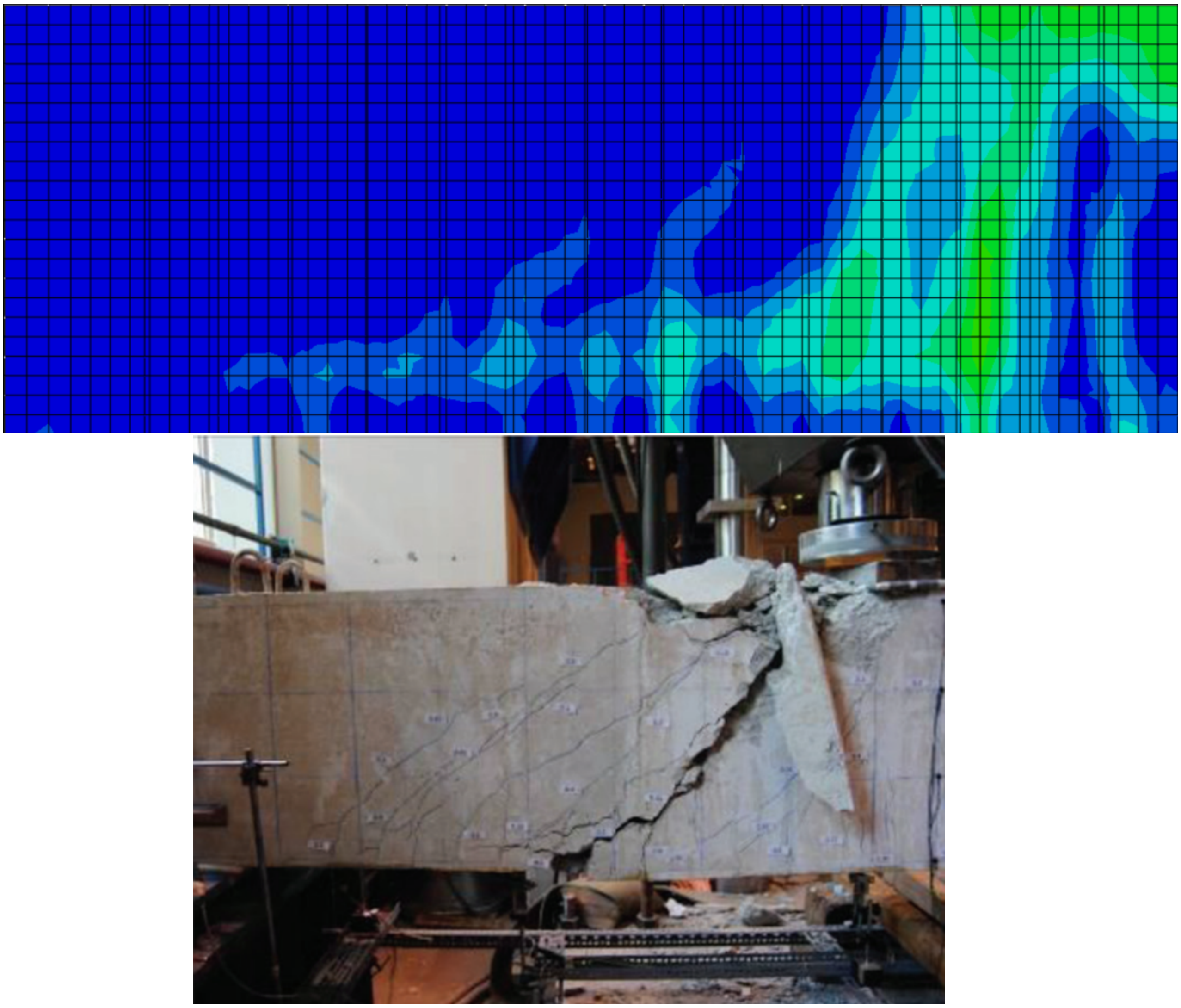

Figure 4.32: Simulated (Top) vs. Experiment (Bottom) [39] Crack Pattern for JSV40-50B, 50° Dilation

Much like specimens JSC32-40B and JSC32-50B, the model response shown in Figure 4.31 does not capture the increase in load past the flexural failure, as ABAQUS considers the crushing to simulate the peak load. The peak load however matches more closely than the 30° model. The simulated crack patterns in Figure 4.32 also illustrate the large shear crack seen in the experiment, as well as the flexural crushing that occurs near the load application point.

### 4.2.3 Summary of Results - Model Validation

The load-deflection responses generated by ABAQUS followed the same trends for all specimens, with the concrete for beams without stirrups being best modelled using a dilation angle of 30°. For beams with stirrups, the results were most accurate when a dilation angle of 50° was used to model the concrete. These results validate the recommendations by Stoner to model the confining effects of stirrups with an increased dilation angle.

For beams with stirrups, primarily specimens JSC32-40B and JSC32-50B, the results exemplified the model's inability to accurately represent behaviour past the first failure point(usually concrete crushing). The two specimens exhibited flexural crushing, followed by an increase in stirrups strains, ultimately leading to rupture and shear failure. The model determined the load at flexural crushing to be the peak load, not accounting for the increase leading up to the stirrup rupture.

# Chapter 5

# Parametric Study on Slender GFRP Reinforced Beams in ABAQUS

This chapter describes the extension of the slenderness study conducted by Stoner [66] to investigate the behaviour of very slender FRP reinforced beams. The beams were modelled in ABAQUS using the models that were developed by Stoner [66] and evaluated in Chapter 4. Stoner calibrated the material models using test data from Krall [43].

Beams with 12 different cross-sections were tested in ABAQUS under 3 point loading, with slenderness ratios ranging from 1.5 to 12.5, as well as dilation angles of 30°, and 50°. Chapter 4 verified the use of 30° to model the dilation angle for concrete beams without stirrups, while an angle of 50° was found suitable to model beams with stirrups. A dilation angle of 50° was used to model the increased strength of concrete due to confining effects from the stirrups. A total of 288 model simulations were conducted for this parametric study. Due to the symmetric nature of the problem, only half models for the beams were considered. The results are collated in the form of moment-deflection and load-deflection graphs, as well as crack patterns. The failure loads are also compared to strength predictions provided by current codes and literature.

The scope of the parametric study is to extend the work done by Stoner [66] to higher slenderness ratios. The goal of the investigation is to study the governing failure modes of the beams, and the accuracy of code predictions (ACI, CSA) at higher slenderness ratios.

The chapter is divided into two sections. The first section discusses the investigation of flexural failure in slender GFRP reinforced beams, while the second section analyzes the prediction capabilities of the ACI and CSA against slender beams.

Since all beam series follow the same trends, only the results for representative beams will be discussed. The results for all beams analyzed are presented in Appendices C and D.

Table 5.1 presents properties of the beams analyzed in this chapter, while Figure 5.1 illustrates typical cross sections for the BM XX-(s)YYY series. Note that beams BM XX-s230 have wider sections than the other beams, and use 20 mm diameter stirrups, rather than the 12 mm diameter stirrups used in all other beams.

Table 5.1: Beam Properties

| Beam | $b$ (mm) | $h$ (mm) | $d$ (mm) | $\rho_F$ (%) | $\rho_V$ (%) | $f'_c$ (MPa) | $E_F$ (GPa) | $E_V$ (GPa) |
|---|---|---|---|---|---|---|---|---|
| 12-INF | | | | | 0.00 | | | |
| 12-150 | 200 | 350 | 270 | 2.51 | 0.75 | 56.5 | 63.5 | 50 |
| 12-220 | | | | | 0.51 | | | |
| 16-INF | | | | | 0.00 | | | |
| 16-150 | 200 | 345 | 270 | 2.23 | 0.75 | 56.5 | 63.5 | 50 |
| 16-220 | | | | | 0.51 | | | |
| 25-INF | | | | | 0.00 | | | |
| 25-150 | 200 | 330 | 270 | 1.82 | 0.75 | 56.5 | 63.5 | 50 |
| 25-220 | | | | | 0.51 | | | |
| 12-s230 | | 365 | | 2.18 | | | | |
| 16-s230 | 230 | 360 | 270 | 1.94 | 1.19 | 56.5 | 63.5 | 50 |
| 25-s230 | | 345 | | 1.58 | | | | |

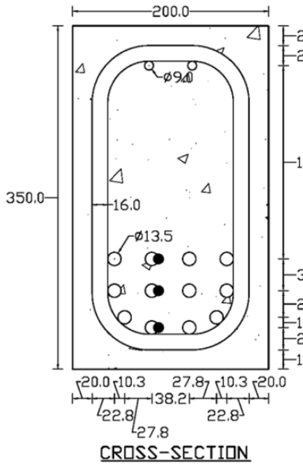


(a) BM 12-YYY

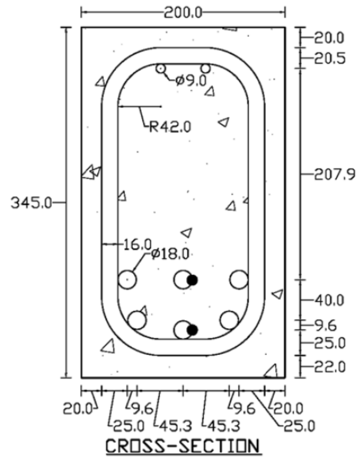


(b) BM 16-YYY

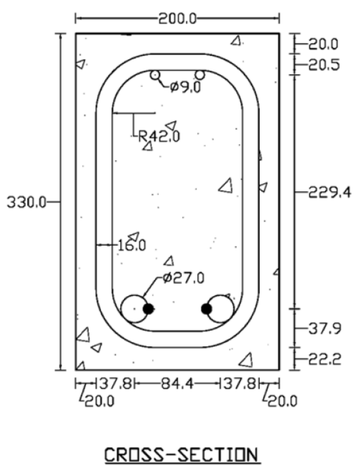


(c) BM 25-YYY

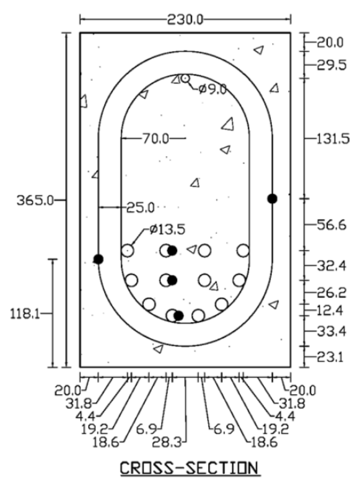


(d) BM 12-s230

Figure 5.1: Section Geometry for BM Series

## 5.1 Investigation into Flexural Failure of Slender GFRP Reinforced Beams using Finite Element Analysis

### 5.1.1 Beams without Stirrups

#### BM 12-INF

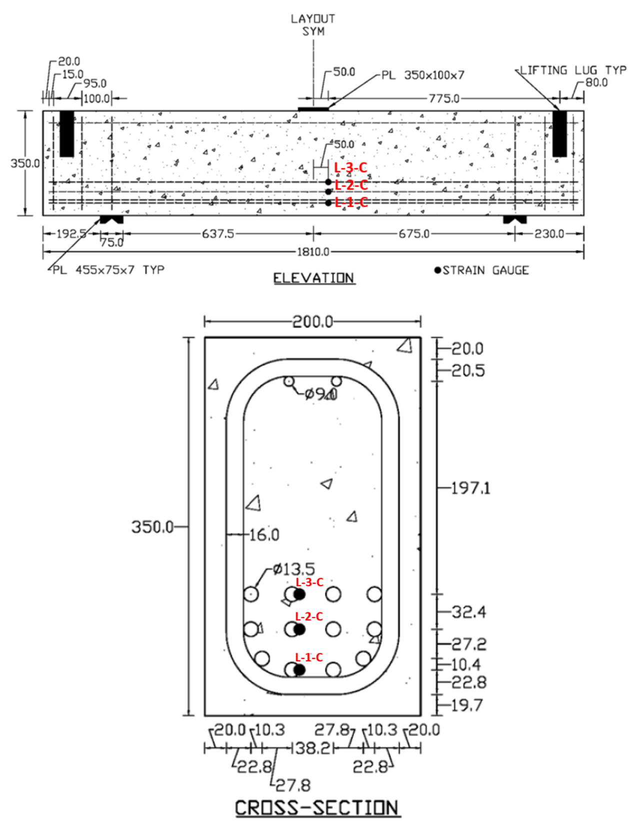


Figure 5.2: Beam Drawings and Strain Gauge Locations BM 12-INF

Figure 5.2 illustrates the geometry of BM 12-INF, tested by Krall [43]. Strain gauges were placed at the midspan of the middle bar in each layer of longitudinal reinforcement.

To ensure the accuracy of the models in simulating Krall's [43] beams, model strain and load-deflection data was compared to experimental values obtained for a/d = 2.5.

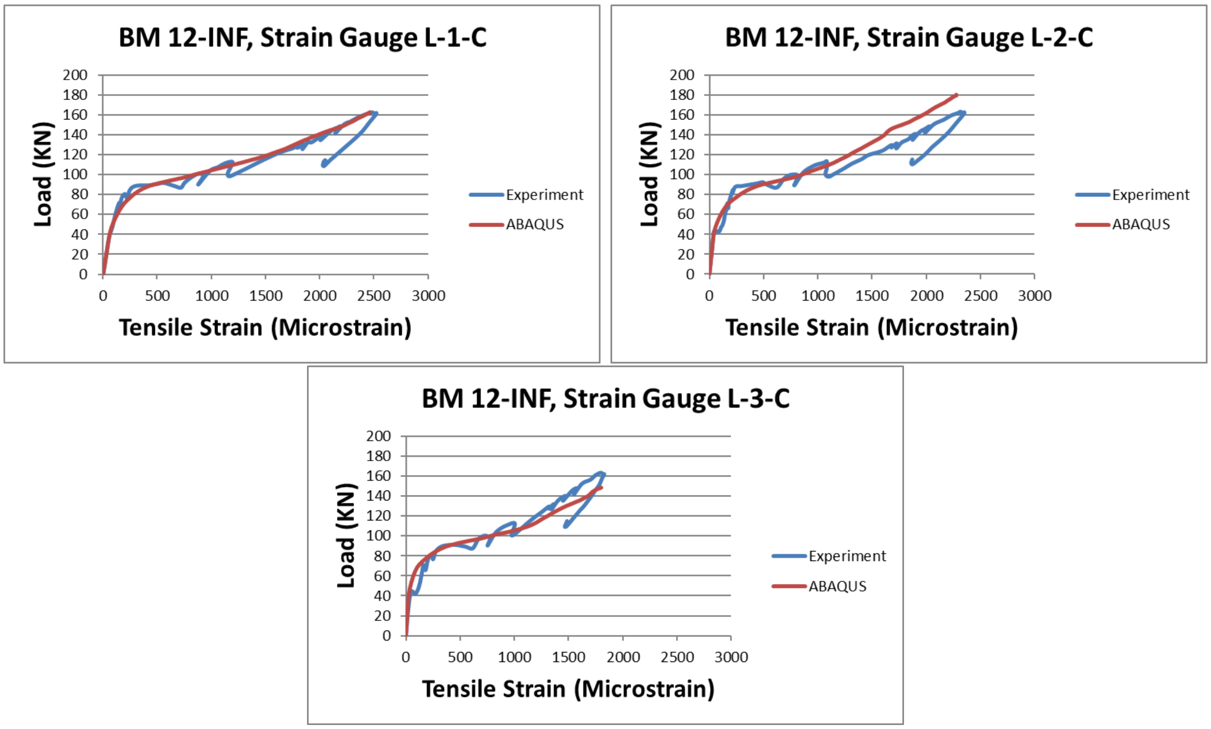


Figure 5.3: Longitudinal Reinforcement Strains - BM 12-INF

Figure 5.3 compares the experimentally obtained strains for strain gauges L-1-C, L-2-C, and L-3-C to the values obtained from the ABAQUS model. The strains obtained from the ABAQUS model correlate strongly with experimental values, confirming the accuracy of the adopted material model.

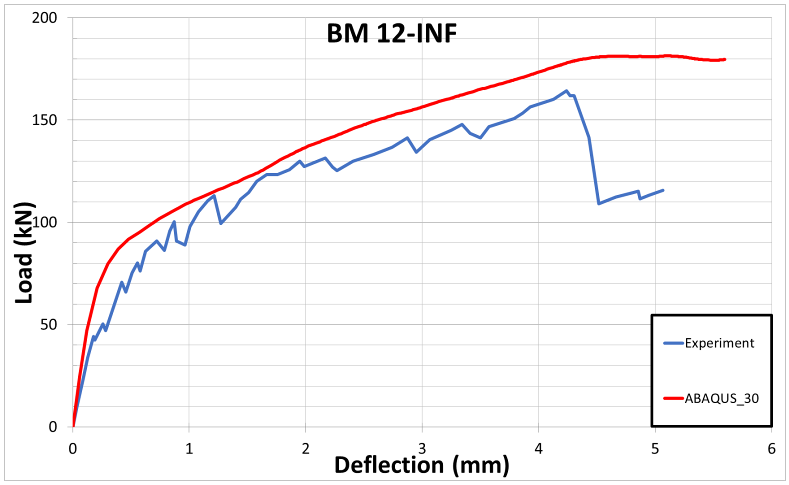


Figure 5.4: ABAQUS Load-Deflection Data vs Experiment for BM 12-INF, a/d = 2.5, 30° Dilation

Furthermore, the load-deflection responses plotted in Figure 5.4 show similar trends, with the peak loads occurring at approximately the same midspan deflection. The abrupt drop in load in the experimental response signifies the end of the experiment. The calibrated models were then used to study the load-deflection and moment-deflection responses for BM 12-INF, over slenderness ratios ranging from 1.5 to 12.5.

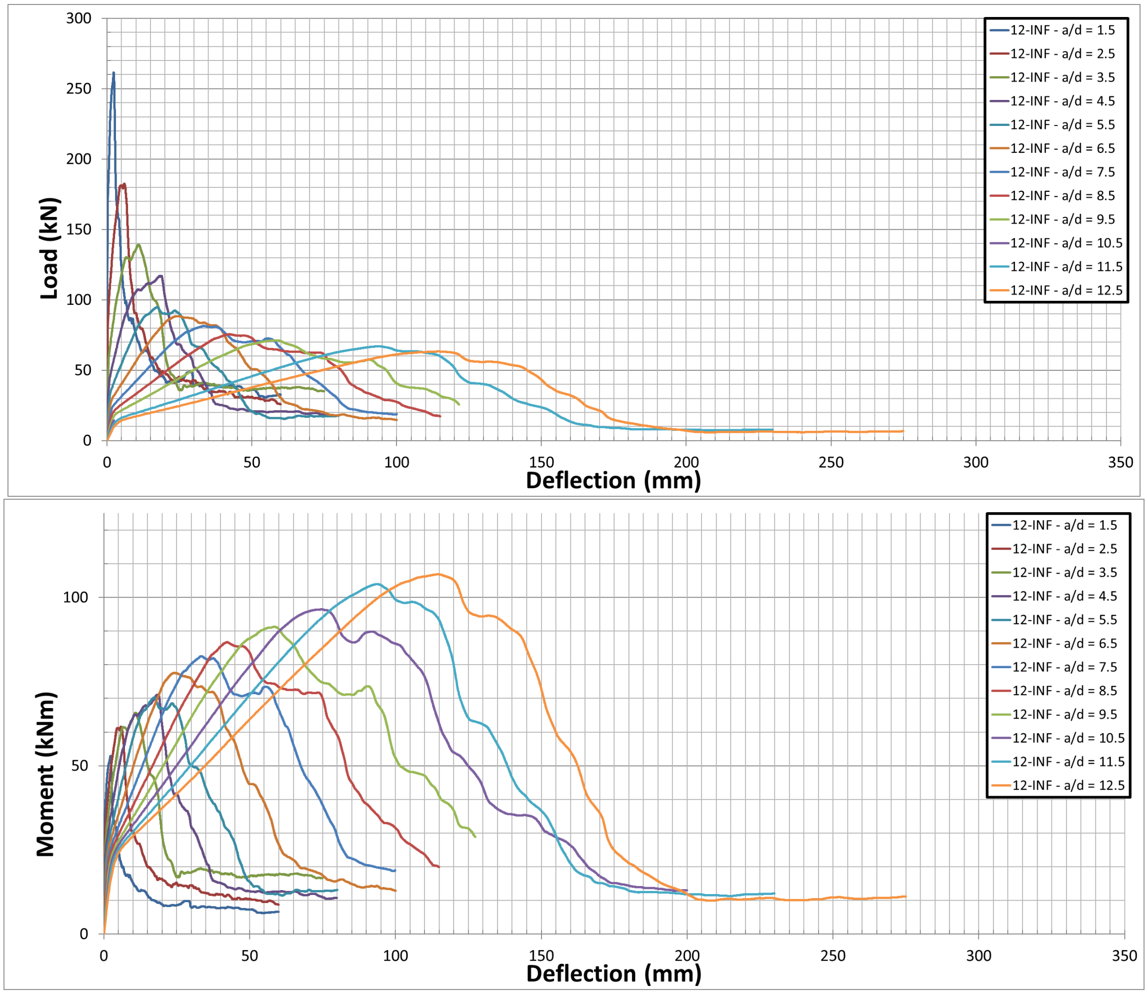


Figure 5.5: Influence of Slenderness Ratio for BM 12-INF, 30° Dilation

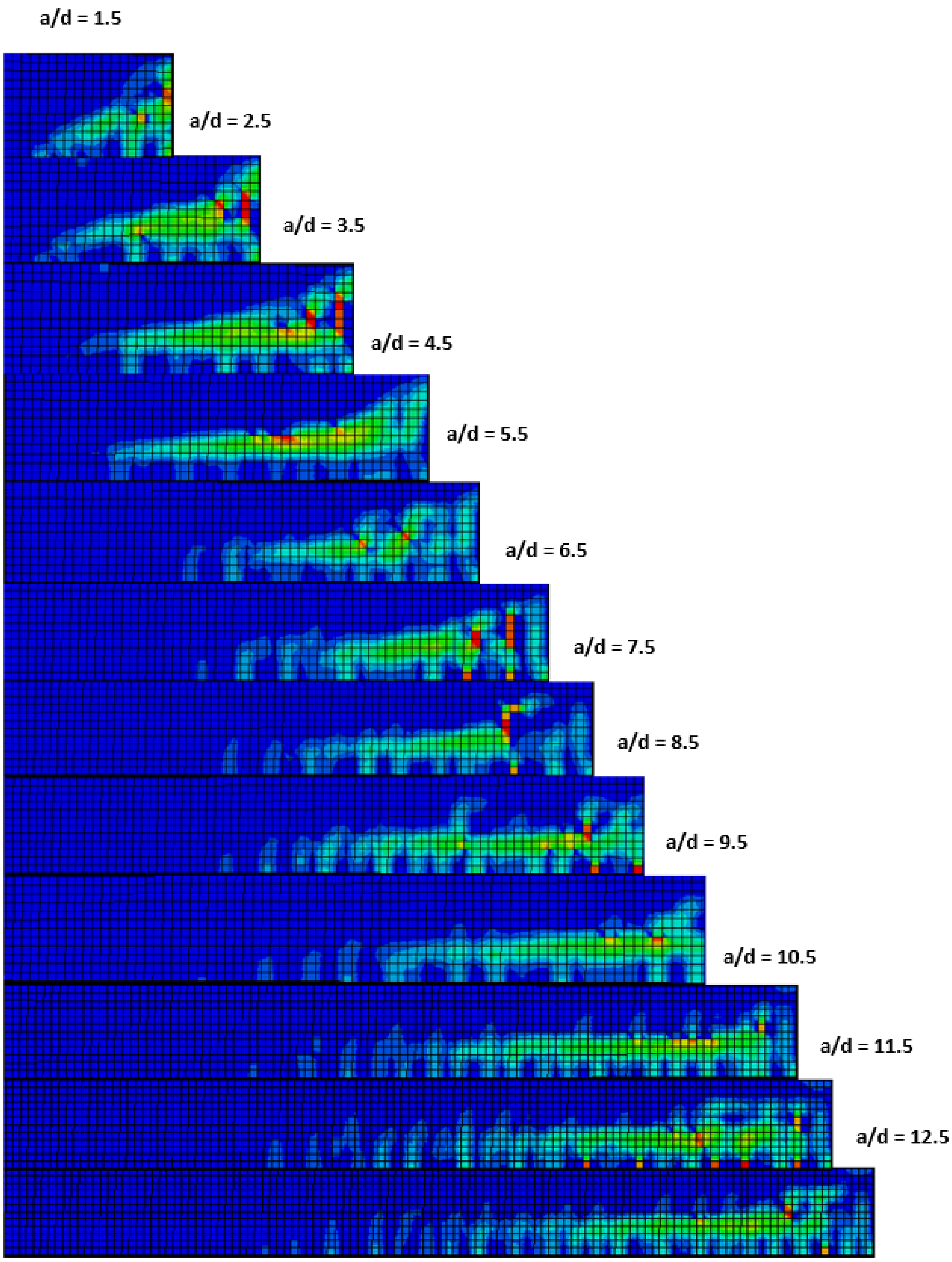


Figure 5.6: Influence of Slenderness Ratio for BM 12-INF - Crack Patterns, 30° Dilation

The moment-deflection responses shown in Figure 5.5 display increasing failure moments. The failure moments never plateau, suggesting shear to be the governing mode of failure. The same conclusion can be drawn from the crack patterns illustrated in Figure 5.6. Diagonal shear cracks propagating from the load application points down to the supports can be observed for slenderness ratios 1.5 through 10.5. Shear cracks can still be observed for slenderness ratios 11.5 and 12.5, however flexural cracks become more distinct, suggesting a transition from shear driven failure towards flexural failure. An analysis of the failure loads (compared to code predictions) was conducted to further investigate the observed behaviour.

Table 5.2 compares the ultimate loads obtained from ABAQUS for BM 12-INF with flexural strength predictions from CSA S806-12 (CSA Flexure), and ACI440.1R-15 (ACI Flexure). The failure moments obtained from the ABAQUS model continue to increase with slenderness, never reaching the capacities predicted by both the CSA and ACI flexure models. The continually increasing failure moments indicate that the flexural capacity of the beam has not been reached, suggesting shear driven failure.

Table 5.2: Comparison of Ultimate Loads to Flexure Models for BM 12-INF

| $a/d$ | ABAQUS (30°, KN) | ABAQUS (30°, KNm) | CSA (Flexure, KNm) | CSA (Flexure, KN) | ACI (Flexure, KNm) | ACI (Flexure, KN) |
|---|---|---|---|---|---|---|
| 1.5 | 261 | 53 | 147 | 724 | 132 | 653 |
| 2.5 | 182 | 62 | 147 | 435 | 132 | 392 |
| 3.5 | 139 | 66 | 147 | 311 | 132 | 280 |
| 4.5 | 117 | 71 | 147 | 242 | 132 | 218 |
| 5.5 | 95 | 70 | 147 | 198 | 132 | 178 |
| 6.5 | 88 | 78 | 147 | 167 | 132 | 151 |
| 7.5 | 81 | 82 | 147 | 145 | 132 | 131 |
| 8.5 | 76 | 87 | 147 | 128 | 132 | 115 |
| 9.5 | 71 | 91 | 147 | 114 | 132 | 103 |
| 10.5 | 68 | 96 | 147 | 104 | 132 | 93 |
| 11.5 | 67 | 104 | 147 | 95 | 132 | 85 |
| 12.5 | 63 | 107 | 147 | 87 | 132 | 78 |

Table 5.3 compares the ultimate loads obtained from ABAQUS for BM 12-INF with shear strength predictions from CSA S806-12 (CSA Shear), and ACI440.1R-15 (ACI Shear). The CSA models predict that flexural failure will begin to govern at slenderness ratios higher than 12.5, as the predicted shear capacity for the most slender beam was 83 KN, while the ultimate load based on the CSA flexure model was 87 KN. The ACI models however predict flexural failure to begin governing at a slenderness ratio of 12.5, with predicted shear and flexural capacities of 82 KN and 78 KN respectively. Further investigation into higher slenderness ratios was required to confidently identify the transition to flexure governed failure. The parametric study for beams without stirrups was therefore extended to observe flexural failure, but was limited to BM 12-INF due to time constraints.

Table 5.3: Comparison of Ultimate Loads to Shear Models for BM 12-INF

| $a/d$ | ABAQUS (30°, KN) | CSA (Shear, KN) | ACI (Shear, KN) |
|---|---|---|---|
| 1.5 | 261 | 167 | 82 |
| 2.5 | 182 | 155 | 82 |
| 3.5 | 139 | 131 | 82 |
| 4.5 | 117 | 115 | 82 |
| 5.5 | 95 | 105 | 82 |
| 6.5 | 88 | 96 | 82 |
| 7.5 | 81 | 90 | 82 |
| 8.5 | 76 | 84 | 82 |
| 9.5 | 71 | 83 | 82 |
| 10.5 | 68 | 83 | 82 |
| 11.5 | 67 | 83 | 82 |
| 12.5 | 63 | 83 | 82 |

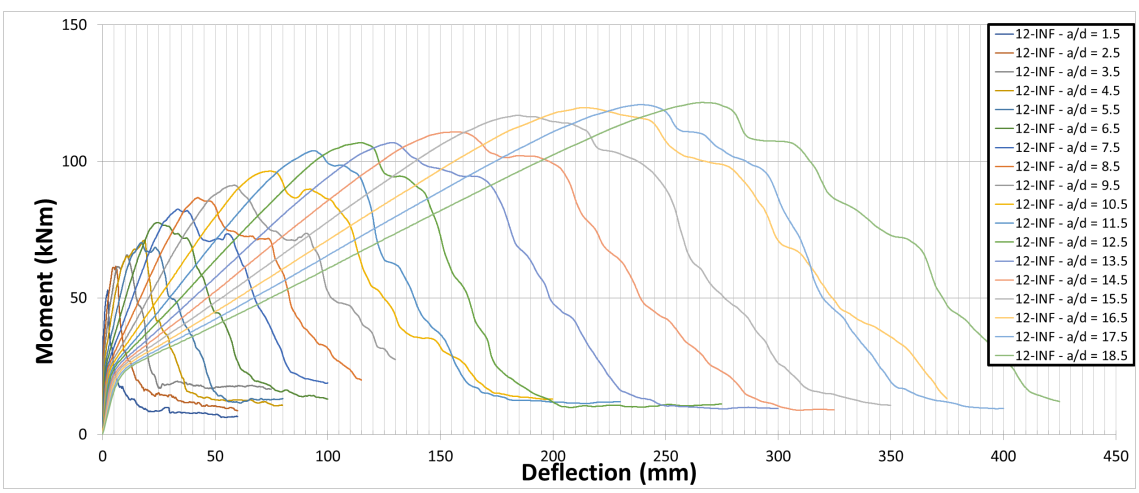


Figure 5.7: Influence of Slenderness Ratio on Flexural Failure of BM 12-INF, 30° Dilation

The moment capacities shown in Figure 5.7 display the expected plateau for slenderness ratios higher than 16.5. Furthermore, Table 5.4 shows near identical failure moments for slenderness ratios 16.5, 17.5, and 18.5, suggesting flexure to be the governing mode of failure. The CSA models predict flexural failure to occur at a slenderness ratio of 13.5 (Table 5.4). Both the ACI and CSA models predict the change in failure mode to occur sooner than the ABAQUS model.

Table 5.4: Comparison of Ultimate Loads to Prediction Models for BM 12-INF

| $a/d$ | ABAQUS (30°, KN) | ABAQUS (30°, KNm) | CSA Flexure (KN) | CSA Shear (KN) | ACI Flexure (KN) | ACI Shear (KN) |
|---|---|---|---|---|---|---|
| 10.5 | 68 | 96 | 104 | 83 | 93 | 82 |
| 11.5 | 67 | 104 | 95 | 83 | 85 | 82 |
| 12.5 | 63 | 107 | 87 | 83 | 78 | 82 |
| 13.5 | 59 | 108 | 81 | 83 | 73 | 82 |
| 14.5 | 57 | 111 | 75 | 83 | 68 | 82 |
| 15.5 | 56 | 117 | 70 | 83 | 63 | 82 |
| 16.5 | 54 | 120 | 66 | 83 | 59 | 82 |
| 17.5 | 51 | 121 | 62 | 83 | 56 | 82 |
| 18.5 | 49 | 122 | 59 | 83 | 53 | 82 |

## 5.1.2 Beams with Stirrups

### BM 12-150

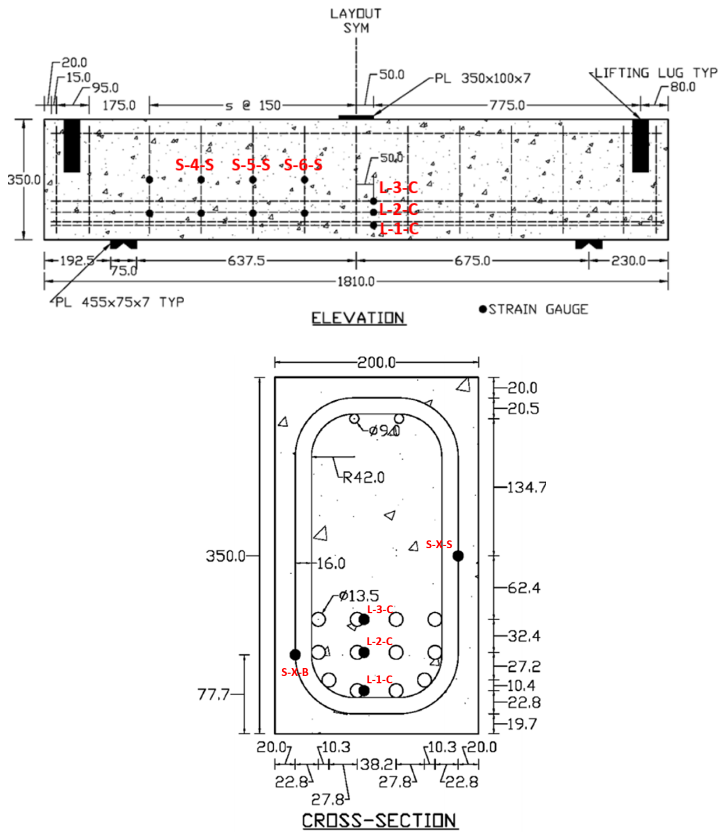


Figure 5.8: Beam Drawings and Strain Gauge Locations BM 12-150

Figure 5.8 illustrates the geometry of BM 12-150, tested by Krall [43]. Strain gauges were placed at the midspan of the middle bar in each layer of longitudinal reinforcement. Three additional gauges were placed at mid-height on the first 3 stirrups to the left of midspan. To ensure the accuracy of the models in simulating beams with transverse reinforcement, model strain, and load-deflection, data was compared to experimental values obtained for a/d = 2.5.

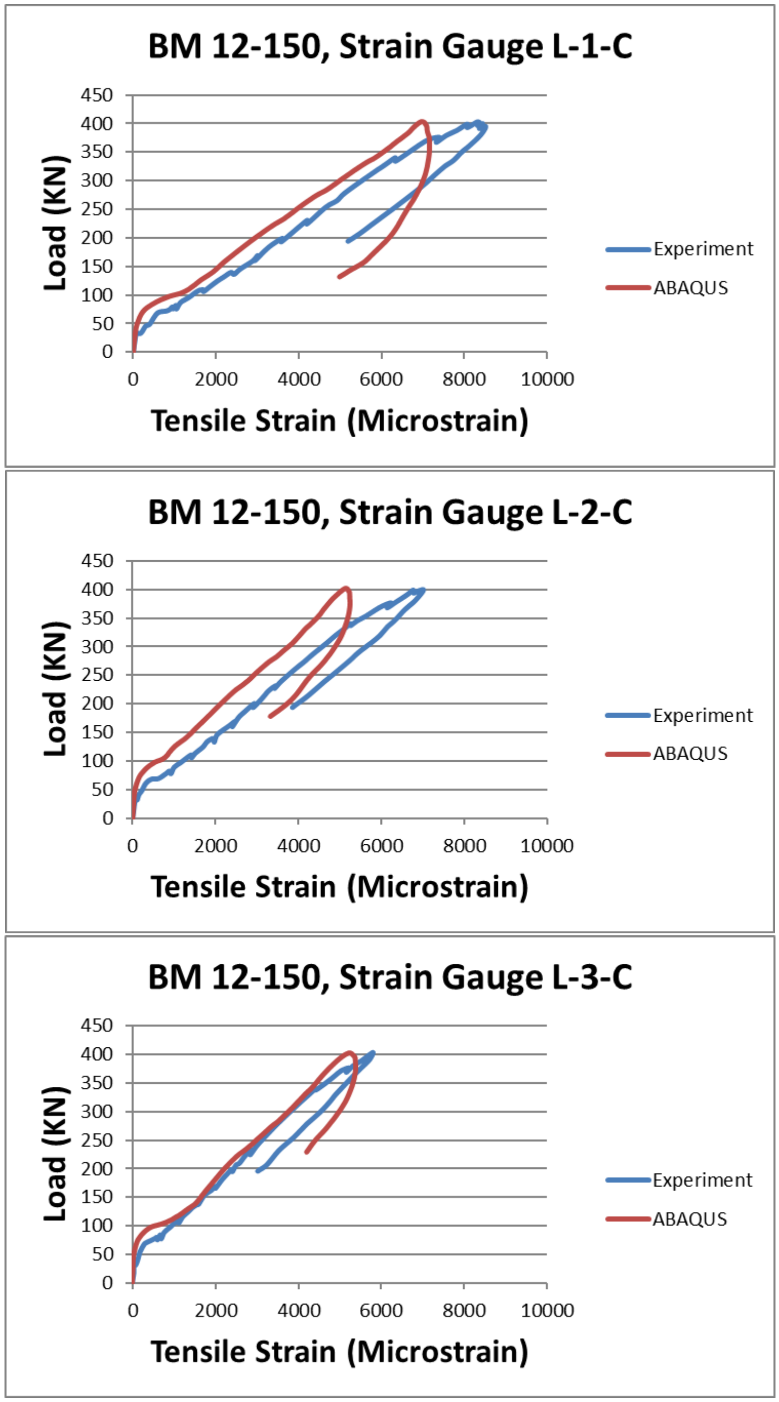


Figure 5.9: Longitudinal Reinforcement Strains - BM 12-150

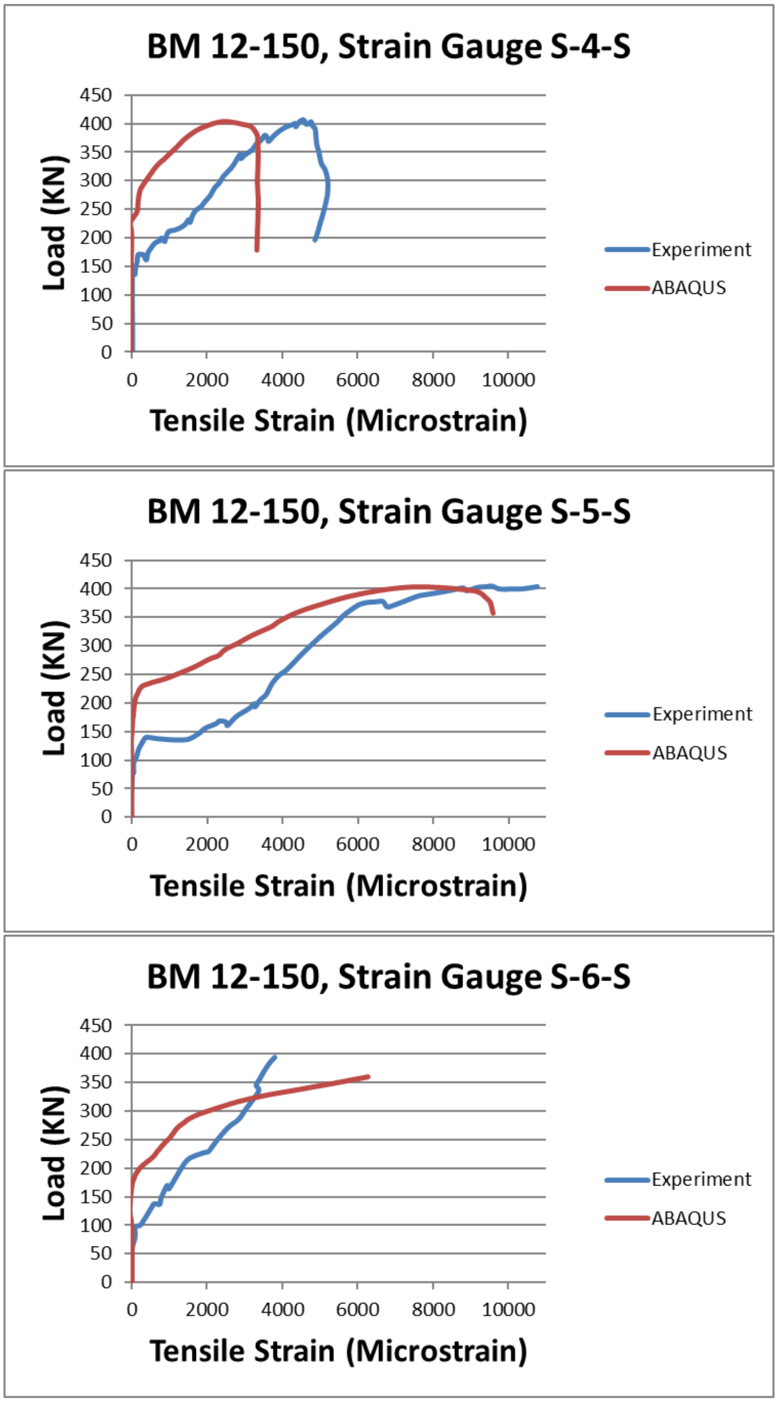


Figure 5.10: Transverse Reinforcement Strains - BM 12-150

Figure 5.9 compares the experimentally obtained strains for strain gauges L-1-C, L-2-C, and L-3-C to the values obtained from the ABAQUS model. Like the results for BM 12-INF, the modelled strains in the longitudinal reinforcement correlate strongly to those observed in the experiment.

In addition to the longitudinal reinforcement, the strains in the stirrups were compared to experimental values. Figure 5.10 suggests a good correlation between the model data and experiment as the two curves follow the same trend. However, the curve for strain gauges S-4-S shows the model under-predicting the strains at maximum load. In Krall's experiment, BM 12-150 failed by the crushing of a diagonal strut from the load application point to the support. The failure crack crossed stirrups S-6-S and S-5-S, resulting in larger strains compared to S-4-S. The load-deflection and moment-deflection responses, in addition to the crack patterns, were then observed for slenderness ratios 1.5 through 12.5.

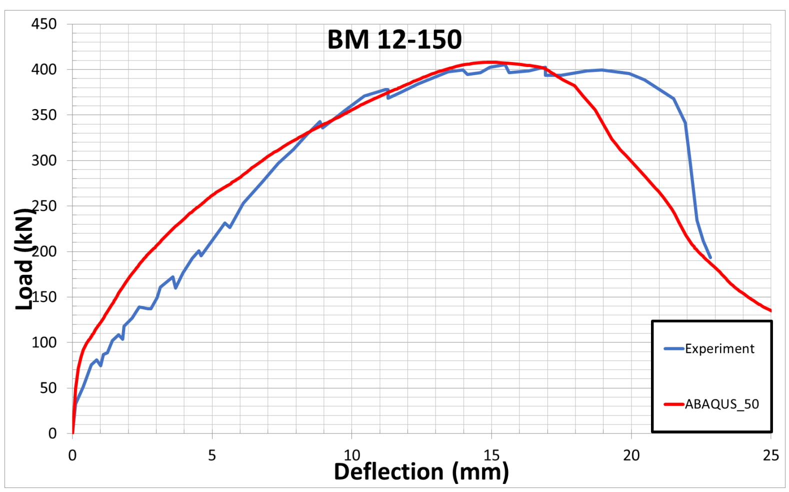


Figure 5.11: ABAQUS Load-Deflection Data vs Experiment for BM 12-150, a/d = 2.5, 50° Dilation

The load-deflection responses plotted in Figure 5.11 demonstrate the use of the 50° dilation model to capture the confining effects of the stirrups, as the model and experimental peak loads are almost identical. The 50° model was therefore recommended and used to study slenderness for BM 12-150.

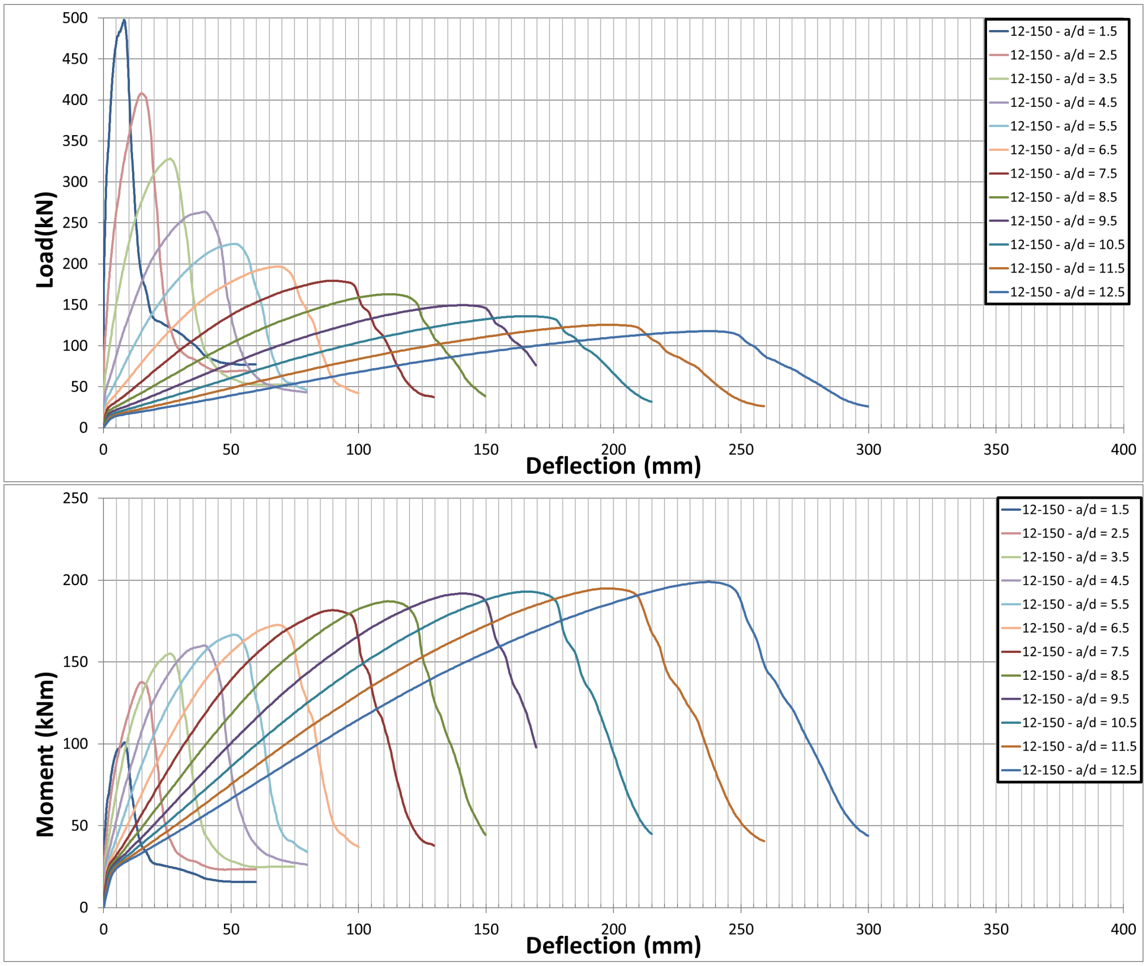


Figure 5.12: Influence of Slenderness Ratio for BM 12-150, 50° Dilation

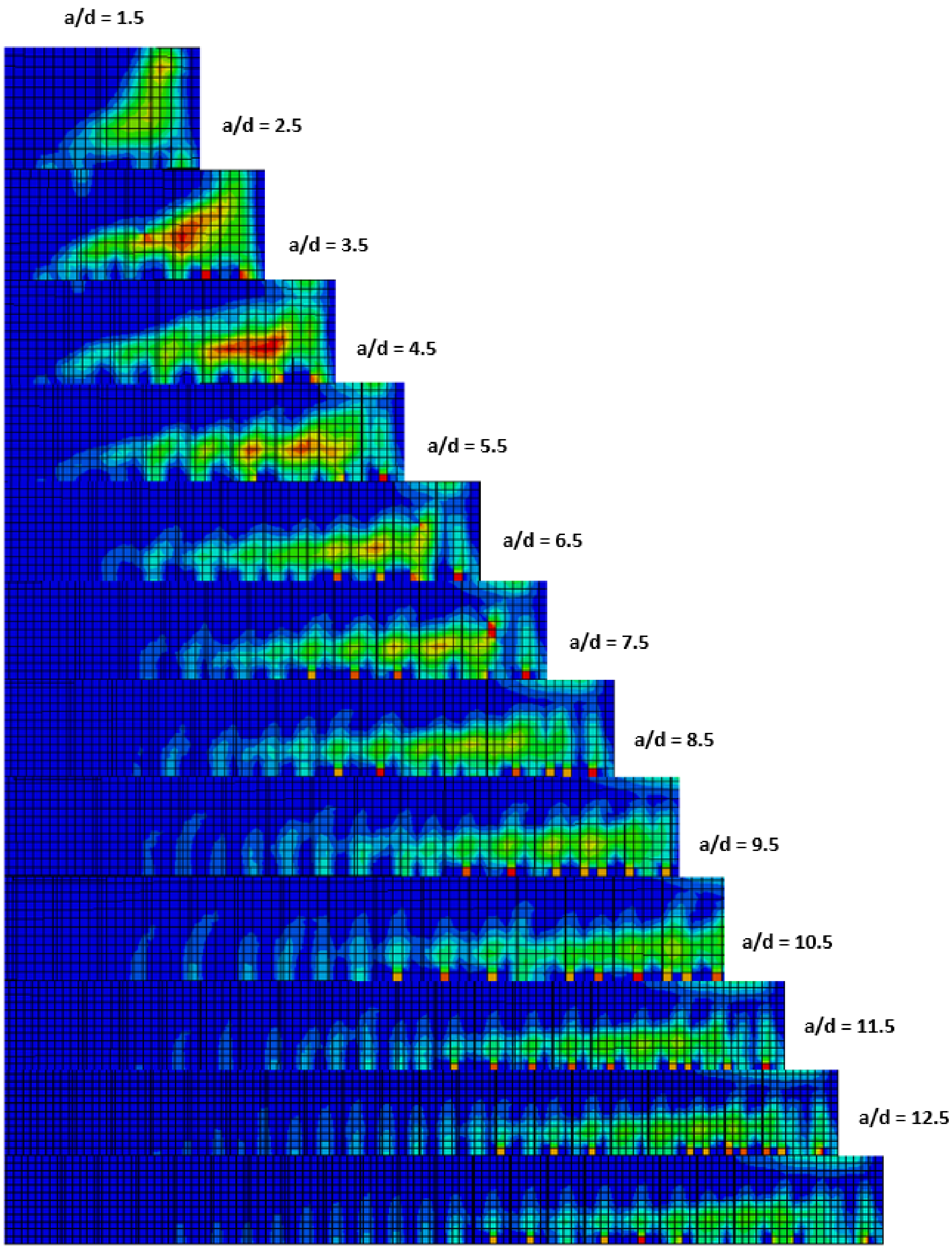


Figure 5.13: Influence of Slenderness Ratio for BM 12-150 - Crack Patterns, 50° Dilation

The moment-deflection response shown in Figure 5.12 displays plateauing failure moments, suggesting a transition towards flexural failure. The crack patterns illustrated in Figure 5.13 show clear diagonal shear cracks extending from the load application point to the support for slenderness ratios 1.5 to 9.5. For slenderness ratios 9.5 to 12.5, the flexural cracks become distinct, with shear cracks no longer apparent. Clear diagonal shear cracks propagating from the load application points down to the supports can be observed for slenderness ratios 1.5 through 10.5. Furthermore, the plateauing of the moment-deflection curves in Figure5.12 becomes more defined between slenderness ratios 9.5 and 10.5, corroborating the conclusions drawn form the crack patterns. An analysis of the failure loads (compared to code predictions) was conducted to further investigate the observed behaviour.

Table 5.5 compares the ultimate loads obtained from ABAQUS for BM 12-150 with flexural strength predictions from the CSA and ACI flexure models.

Table 5.5: Comparison of Ultimate Loads to Flexure Models for BM 12-150

| $a/d$ | ABAQUS (50°, KN) | ABAQUS (50°, KNm) | CSA (Flexure, KNm) | CSA (Flexure, KN) | ACI (Flexure, KNm) | ACI (Flexure, KN) |
|---|---|---|---|---|---|---|
| 1.5 | 498 | 101 | 147 | 725 | 130 | 643 |
| 2.5 | 385 | 130 | 147 | 435 | 130 | 386 |
| 3.5 | 328 | 155 | 147 | 311 | 130 | 276 |
| 4.5 | 263 | 160 | 147 | 242 | 130 | 214 |
| 5.5 | 224 | 166 | 147 | 198 | 130 | 175 |
| 6.5 | 197 | 173 | 147 | 167 | 130 | 148 |
| 7.5 | 179 | 181 | 147 | 145 | 130 | 129 |
| 8.5 | 163 | 187 | 147 | 128 | 130 | 114 |
| 9.5 | 150 | 192 | 147 | 114 | 130 | 102 |
| 10.5 | 136 | 193 | 147 | 104 | 130 | 92 |
| 11.5 | 126 | 196 | 147 | 95 | 130 | 84 |
| 12.5 | 118 | 199 | 147 | 87 | 130 | 77 |

Similarly, Table 5.6 compares the ultimate loads obtained from ABAQUS for BM 12-150 with shear strength predictions from the CSA and ACI shear models. The CSA models predict that flexural failure will begin to govern at a slenderness ratio of 7.5, as the predicted shear capacity (151 KN) begins to overtake the ultimate load based on flexural capacity (145 KN). The ACI models however predict flexural failure to begin governing at a slenderness ratio of 4.5, with predicted shear and flexural capacities of 245 KN and 214 KN respectively. The CSA and ACI models show a larger discrepancy with the model results than for BM 12-INF, a result consistent with observations from Chapter 4. This trend exemplifies the difficulty faced by both the CSA and ACI models in predicting the stirrup contribution to the shear capacity of FRP reinforced beams. While the change in moment capacity for slenderness ratios 9.5 through 12.5 is small enough to suggest flexural failure, an extension to higher slenderness ratios was conducted to confirm the results. Like BM 12-INF, the extension to higher slenderness ratios for beams with stirrups was only conducted for BM 12-150.

Table 5.6: Comparison of Ultimate Loads to Shear Models for BM 12-150

| $a/d$ | ABAQUS (50°, KN) | CSA (Shear, KN) | ACI (Shear, KN) |
|---|---|---|---|
| 1.5 | 498 | 266 | 245 |
| 2.5 | 385 | 242 | 245 |
| 3.5 | 328 | 211 | 245 |
| 4.5 | 263 | 190 | 245 |
| 5.5 | 224 | 174 | 245 |
| 6.5 | 197 | 161 | 245 |
| 7.5 | 179 | 151 | 245 |
| 8.5 | 163 | 142 | 245 |
| 9.5 | 150 | 139 | 245 |
| 10.5 | 136 | 139 | 245 |
| 11.5 | 126 | 139 | 245 |
| 12.5 | 118 | 139 | 245 |

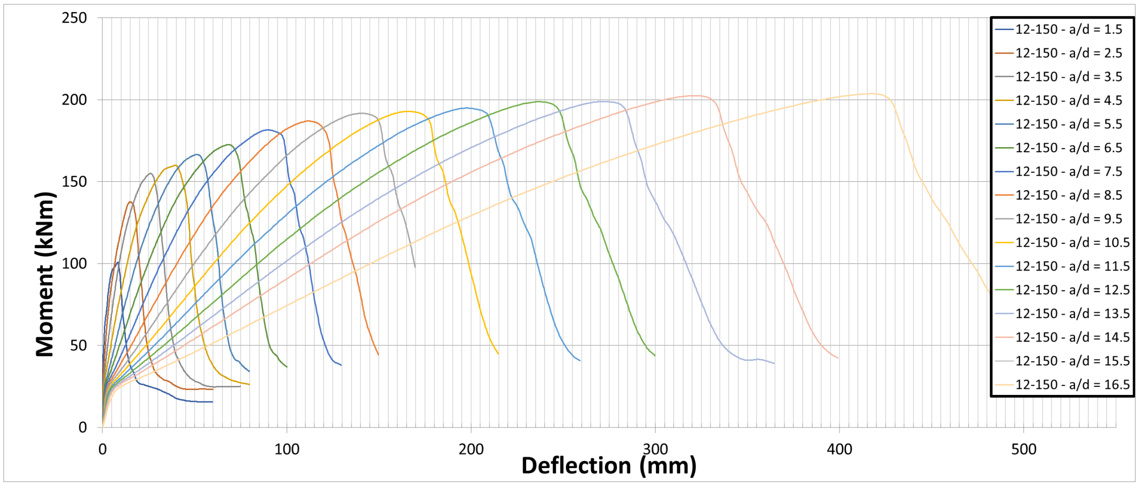


Figure 5.14: Influence of Slenderness Ratio on Flexural Failure of BM 12-150, 50° Dilation

Table 5.7: Comparison of Ultimate Loads to Prediction Models for BM 12-150

| $a/d$ | ABAQUS (50°, KN) | ABAQUS (50°, KNm) | CSA Flexure (KN) | CSA Shear (KN) | ACI Flexure (KN) | ACI Shear (KN) |
|---|---|---|---|---|---|---|
| 6.5 | 197 | 173 | 167 | 161 | 148 | 245 |
| 7.5 | 179 | 181 | 145 | 151 | 129 | 245 |
| 8.5 | 163 | 187 | 128 | 142 | 114 | 245 |
| 9.5 | 150 | 192 | 114 | 139 | 102 | 245 |
| 10.5 | 136 | 193 | 104 | 139 | 92 | 245 |
| 11.5 | 126 | 196 | 95 | 139 | 84 | 245 |
| 12.5 | 118 | 199 | 87 | 139 | 77 | 245 |
| 13.5 | 109 | 199 | 81 | 139 | 71 | 245 |

The moment capacities shown in Figure 5.14 display the expected plateau for slenderness ratios higher than 12.5. Furthermore, Table 5.7 shows identical failure moments for slenderness ratios 12.5 and 13.5, suggesting flexure to be the governing mode of failure. The percent change in moment capacities for slenderness ratios greater than 9.5 is consistently less than 2%, suggesting a/d = 9.5 to be the moment where the failure mode changes. This result is in accordance with the trends observed in the crack patterns, as well as the expectation that BM 12-150 fails in flexure prior to BM 12-INF; the shear capacity of the latter is much higher due to the stirrups. The fact that GFRP reinforced beams fail at higher slenderness ratios to steel reinforced beams is reasonable as GFRP bars exhibit stronger tensile properties than steel bars.

## 5.2 Comparison of ACI and CSA Strength Predictions to ABAQUS Results

### 5.2.1 Influence of Longitudinal Reinforcement Ratio

Tables 5.8, 5.9, and 5.10 present the model results and code predictions for BM 12-INF, BM 16-INF, and BM 25-INF. The variable of interest in this study is the longitudinal reinforcement ratio. The longitudinal ratios for BM 12-INF, BM 16-INF, and BM 25-INF are 2.51%, 2.23%, and 1.82% respectively. Chapter 4 demonstrated the efficacy of the CSA shear model in predicting the capacity for beams without transverse reinforcement, and will be used as a benchmark for assessing the robustness of the ABAQUS model under the varied parameter.

Table 5.8: Comparison of Ultimate Loads for BM 12-INF

| $a/d$ | ABAQUS (30°, KN) | ABAQUS (50°, KN) | CSA (Flexure, KN) | ACI (Flexure, KN) | CSA (Shear, KN) | ACI (Shear, KN) |
|---|---|---|---|---|---|---|
| 1.5 | 261 | 339 | 724 | 653 | 167 | 82 |
| 2.5 | 182 | 220 | 435 | 392 | 155 | 82 |
| 3.5 | 139 | 190 | 311 | 280 | 131 | 82 |
| 4.5 | 117 | 162 | 242 | 218 | 115 | 82 |
| 5.5 | 95 | 148 | 198 | 178 | 105 | 82 |
| 6.5 | 88 | 137 | 167 | 151 | 96 | 82 |
| 7.5 | 81 | 123 | 145 | 131 | 90 | 82 |
| 8.5 | 76 | 118 | 128 | 115 | 84 | 82 |
| 9.5 | 71 | 109 | 114 | 103 | 83 | 82 |
| 10.5 | 68 | 102 | 104 | 93 | 83 | 82 |
| 11.5 | 67 | 96 | 95 | 85 | 83 | 82 |
| 12.5 | 63 | 90 | 87 | 78 | 83 | 82 |

Table 5.9: Comparison of Ultimate Loads for BM 16-INF

| $a/d$ | ABAQUS (30°, KN) | ABAQUS (50°, KN) | CSA (Flexure, KN) | ACI (Flexure, KN) | CSA (Shear, KN) | ACI (Shear, KN) |
|---|---|---|---|---|---|---|
| 1.5 | 248 | 304 | 696 | 628 | 164 | 78 |
| 2.5 | 142 | 210 | 417 | 377 | 147 | 78 |
| 3.5 | 132 | 188 | 298 | 269 | 125 | 78 |
| 4.5 | 110 | 161 | 232 | 209 | 110 | 78 |
| 5.5 | 93 | 141 | 190 | 171 | 99 | 78 |
| 6.5 | 85 | 133 | 161 | 145 | 91 | 78 |
| 7.5 | 79 | 122 | 139 | 126 | 85 | 78 |
| 8.5 | 75 | 114 | 123 | 111 | 82 | 78 |
| 9.5 | 69 | 107 | 110 | 99 | 82 | 78 |
| 10.5 | 72 | 106 | 99 | 90 | 82 | 78 |
| 11.5 | 67 | 96 | 91 | 82 | 82 | 78 |
| 12.5 | 64 | 90 | 83 | 75 | 82 | 78 |

Table 5.10: Comparison of Ultimate Loads for BM 25-INF

| $a/d$ | ABAQUS (30°, KN) | ABAQUS (50°, KN) | CSA (Flexure, KN) | ACI (Flexure, KN) | CSA (Shear, KN) | ACI (Shear, KN) |
|---|---|---|---|---|---|---|
| 1.5 | 272 | 286 | 647 | 587 | 161 | 71 |
| 2.5 | 152 | 220 | 388 | 352 | 136 | 71 |
| 3.5 | 123 | 178 | 277 | 251 | 115 | 71 |
| 4.5 | 98 | 153 | 216 | 196 | 101 | 71 |
| 5.5 | 87 | 134 | 176 | 160 | 91 | 71 |
| 6.5 | 85 | 129 | 149 | 135 | 84 | 71 |
| 7.5 | 78 | 113 | 129 | 117 | 80 | 71 |
| 8.5 | 71 | 118 | 114 | 104 | 80 | 71 |
| 9.5 | 64 | 109 | 102 | 93 | 80 | 71 |
| 10.5 | 73 | 100 | 92 | 84 | 80 | 71 |
| 11.5 | 70 | 100 | 84 | 77 | 80 | 71 |
| 12.5 | 69 | 93 | 78 | 70 | 80 | 71 |

The failure loads (ABAQUS) shown in Tables 5.8, 5.9, and 5.10 for the 30° model match closely for beams with slenderness ratios greater than 2.5. The larger difference in predicted capacity for slenderness ratios lower than 2.5 can be attributed to the model's inability to adequately capture arch action in very deep beams.

The CSA models predict flexural failure to start occurring at a slenderness ratio of 12.5 for beams BM 16-INF and 25-INF, while the CSA predictions in section 5.1 showed that BM 12-INF begins to experience flexure governed failure at a slenderness ratio of 13.5. The CSA predicted shear capacities agree strongly with the 30° model failure loads for the studied reinforcement ratios, suggesting robustness of the ABAQUS model under varying longitudinal reinforcement ratios.

The ACI model does not consider the slenderness of a beam when calculating shear capacity, but rather offers a conservative approach to ensure safety. However, the ACI models' prediction that flexural failure will begin to govern at a slenderness ratio of 12.5 for all three beams agrees with the predictions made by the CSA.

### 5.2.2 Influence of Stirrup Spacing

Tables 5.11, and 5.12 present the model results and code predictions for BM 25-150, and BM 25-220. The variable of interest in this study is the spacing of the transverse reinforcement. The key points to note in this analysis are that the flexural capacity of the beams should not be affected by the presence of stirrups (under flexure governed failure), and that the spacing of the stirrups influences the confinement of the concrete (and thus the shear capacity). The 50° model results will be considered in this analysis as Chapter 4 validated the use of 50° dilation concrete to model beams with transverse reinforcement.

Table 5.11: Comparison of Ultimate Loads for BM 25-150

| $a/d$ | ABAQUS (30°, KN) | ABAQUS (50°, KN) | CSA (Flexure, KN) | ACI (Flexure, KN) | CSA (Shear, KN) | ACI (Shear, KN) |
|---|---|---|---|---|---|---|
| 1.5 | 276 | 371 | 647 | 572 | 244 | 234 |
| 2.5 | 236 | 342 | 388 | 343 | 208 | 234 |
| 3.5 | 192 | 278 | 277 | 245 | 180 | 234 |
| 4.5 | 169 | 231 | 216 | 191 | 161 | 234 |
| 5.5 | 137 | 201 | 176 | 156 | 147 | 234 |
| 6.5 | 126 | 182 | 149 | 132 | 138 | 234 |
| 7.5 | 121 | 162 | 129 | 114 | 134 | 234 |
| 8.5 | 114 | 149 | 114 | 101 | 134 | 234 |
| 9.5 | 102 | 135 | 102 | 90 | 134 | 234 |
| 10.5 | 95 | 127 | 92 | 82 | 134 | 234 |
| 11.5 | 87 | 117 | 84 | 75 | 134 | 234 |
| 12.5 | 84 | 109 | 78 | 69 | 134 | 234 |

Table 5.12: Comparison of Ultimate Loads for BM 25-220

| $a/d$ | ABAQUS (30°, KN) | ABAQUS (50°, KN) | CSA (Flexure, KN) | ACI (Flexure, KN) | CSA (Shear, KN) | ACI (Shear, KN) |
|---|---|---|---|---|---|---|
| 1.5 | 276 | 336 | 647 | 572 | 221 | 182 |
| 2.5 | 216 | 294 | 388 | 343 | 189 | 182 |
| 3.5 | 184 | 258 | 277 | 245 | 163 | 182 |
| 4.5 | 161 | 216 | 216 | 191 | 146 | 182 |
| 5.5 | 140 | 198 | 176 | 156 | 133 | 182 |
| 6.5 | 128 | 165 | 149 | 132 | 123 | 182 |
| 7.5 | 118 | 159 | 129 | 114 | 117 | 182 |
| 8.5 | 113 | 143 | 114 | 101 | 117 | 182 |
| 9.5 | 100 | 132 | 102 | 90 | 117 | 182 |
| 10.5 | 92 | 123 | 92 | 82 | 117 | 182 |
| 11.5 | 89 | 112 | 84 | 75 | 117 | 182 |
| 12.5 | 85 | 106 | 78 | 69 | 117 | 182 |

The effects of stirrup spacing will be discussed in the context of shear failure. It is therefore pertinent to assess the domain of slenderness ratios in which shear failure is predicted to occur. The 50° ABAQUS model predicts flexural failure to begin governing at a slenderness ratio of 10.5, while the CSA and ACI models predict ratios of 8.5 and 5.5 respectively. Furthermore, Chapter 4 determined that the CSA and ACI predictions for the shear capacity of beams with transverse reinforcement were low when compared to experimental data, but matched closely for beams without transverse reinforcement.

Since both the CSA and ACI are empirically derived, confinement is inherently taken into account in the calculation of the shear capacity of beams. The inclusion is further demonstrated in Tables 5.11, and 5.12, as the predicted shear capacities for both the CSA and ACI models are higher for BM 25-150 than BM 25-220. The larger shear capacities predicted by the models agree with expected behaviour, as the concrete is more confined (and therefore stiffer) in BM 25-150. However, the extent of which confinement is considered in the models requires further investigation, as the predicted shear capacity of both the CSA and ACI models is much lower than the ABAQUS model results.

To further investigate the effects of confinement modelling in the CSA shear strength prediction model, the ABAQUS failure loads for the BM 16-(s)YYY series were plotted against the CSA predictions.

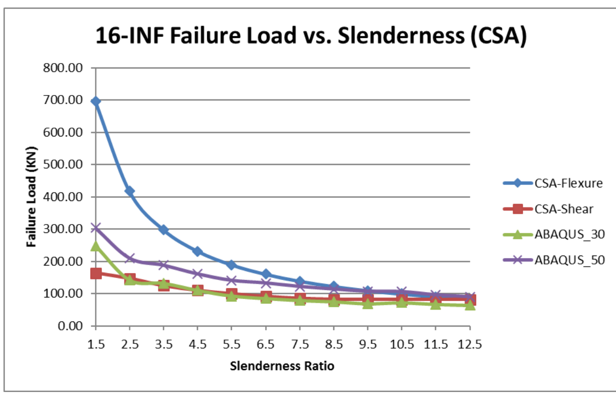


(a)

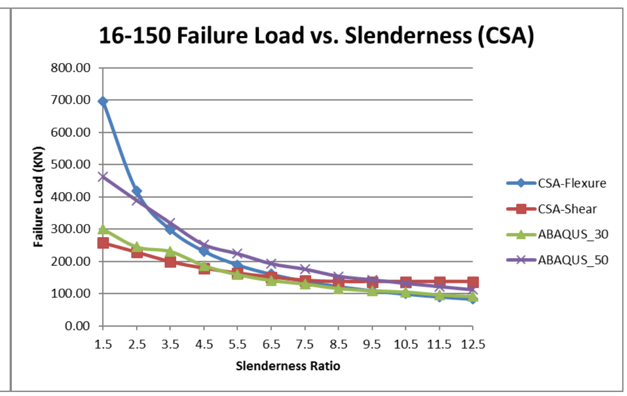


(b)

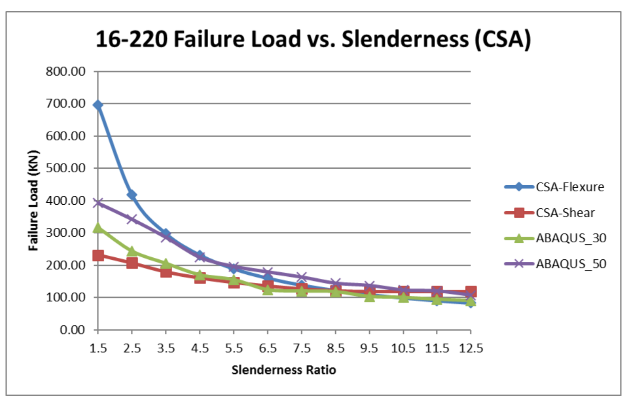


(c)

Figure 5.15: Comparison of ABAQUS Failure Loads and Strength Predictions from CSA against Slenderness Ratios for BM 16-(s)YYY series

Figure 5.15 shows the plots of predicted failure loads versus slenderness ratio for the ABAQUS and CSA models. In all cases, the beams failed in shear prior to a slenderness ratio of 12.5, indicating that the shear models are of primary interest in the investigation. All plots in Figure 5.15 show almost identical curves for the 30° ABAQUS model and CSA shear model. This pattern is expected for BM 16-INF, where the use of 30° dilation concrete to model beams without stirrups was validated. Since the CSA shear model curves match almost identically with the 30° ABAQUS model, one can infer that the CSA model does not adequately account for the confining effects of the stirrups. The expected behaviour would be for the CSA model to closely match the 50° ABAQUS model, where confining effects are considered. To further substantiate this claim, the equations used by the CSA to predict the stirrup contribution to the overall shear capacity are revisited.

The stirrup contribution to the shear capacity is defined by the CSA as

$$V_{sF} = \frac{0.4\phi_F A_{Fv} f_{Fu} d_v}{s} cot\theta,$$

where

$$\theta = 30^\circ + 7000\epsilon_l,$$

and

$$\epsilon_l = \frac{\frac{M_f}{d_v} + (V_f - V_p) + 0.5N_f - A_p f_{po}}{2(E_F A_F + E_p A_p)} \geq 0$$

The strain term $\epsilon_l$ does not contain a term indicating a modification to concrete strength, nor a term that suggests inclusion of confining effects. Furthermore, the only variable in the calculation of $V_{sF}$ that suggests inclusion of confining effects is the stirrup spacing. However, the analysis of the results from Tables 5.11, and 5.12 deemed that modification was insufficient to capture the increased strength provided by the stirrups.

Further investigation into an optimized shear design equation proposed by Shahnewaz et al. [63] yielded a similar conclusion. Shahnewaz et al. proposed that the inclusion of the concrete compressive strength to the design equations sufficed to model the increased strength provided by the stirrups. They utilized a similar genetic optimization algorithm to the one used by Nehdi et al. [53] and yielded that multiplying the stirrup contribution by a factor on the order of $\sqrt{f_c'}$ sufficed to account for the difference. Further research is recommended to study the confining effects of the stirrups on the shear capacity of FRP reinforced beams, as it seems to be an emerging cause for the under-prediction observed in the CSA and ACI prediction methods.

# Chapter 6

# Conclusions and Final Recommendations

This thesis introduced the reader to the work done by Stoner [66] to model the beams tested by Krall [43] in ABAQUS. The calibrated models were then evaluated against experimental data from literature. The validated models were then used in a parametric study to investigate the effects of slenderness on GFRP reinforced beams; the beams tested by Krall were modelled for slenderness ratios ranging from 1.5 to 12.5.

Furthermore, current strength prediction methods for FRP reinforced beams were evaluated against a database of tested beams from literature. The methods evaluated include the provisions set forth by the CSA S806-12, the ACI440.1R-15, the JSCE, the ISIS Canada Manual No. 3, and the methods used by Nehdi et al. [53].

## 6.1 Current Strength Prediction Methods

All the beams that were considered while comparing the different strength prediction methods failed were relatively deep, and thus failed in shear. The following conclusions therefore address the shear strength prediction methods of the evaluated models.

- **CSA S806-12**: The model displays robustness to changes in longitudinal reinforcement ratios, as well as varying concrete strengths. The strength predictions match closely for beams without stirrups, but tend to under-predict the capacity for beams with shear reinforcement. Furthermore, the accuracy of the model tends to decrease for beams with larger sections. Further research is recommended to investigate the effects of section size, as well as the stirrup contribution to the calculated shear capacity.

- **ACI440.1R-15**: The ACI presents a conservative approach to predicting the shear capacity of FRP reinforced beams. The effects of slenderness are not considered in the model, displaying a varying degree of accuracy in shear prediction. While the predicted shear capacity does not change with slenderness, the model always provides a conservative estimate. Furthermore, this thesis recommends an investigation into the stirrup contribution to the predicted shear strength, as the accuracy of the model decreases for beams with transverse reinforcement.

- **JSCE**: The JSCE present an overall robust model for predicting the shear capacity of beams without shear reinforcement. The predicted capacities match very closely with experimental results, slightly under-predicting failure in all cases. The model however faces difficulty for beams with shear reinforcement, as the predicted capacity is much lower than the experimental values. Further research into the effects of stirrups on the predicted shear capacity is recommended.

- **ISIS Canada Manual No. 3**: Like the JSCE and CSA models, the ISIS Canada shear strength predictions match closely for all beams without transverse reinforcement, but tend to under-predict the capacity by a larger margin for beams with stirrups. Further research is recommended to determine the stirrup contribution to predicted shear capacity.

- **Nehdi et al.**: The genetic algorithm used by Nehdi et al. matches closely with experimentally obtained values, over-predicting the capacity by a small margin for beams without shear reinforcement. The results for beams with stirrups show that the model considers a fixed approach when accounting for the confining effects of the stirrups. The model becomes more accurate as the stirrup spacing decreases, suggesting that the considered influence of confinement is not spacing dependent. Further research into the confining effects of the stirrups is recommended for future iterations.

## 6.2 Validation of ABAQUS Models

The ABAQUS models proposed by Stoner were evaluated against a series of 8 beams tested by Johnson and Sheikh [39]. The influence of dilation angle was investigated to confirm the suggestions made by Stoner.

The load-deflection responses generated by ABAQUS were consistent across all specimens, with the concrete for beams without stirrups being best represented using a dilation angle of 30°. The 50° model over-predicted the peak load for all beams without stirrups. For beams with stirrups, the 30° model consistently under-predicted failure, with the results matching most closely in the 50° model.

The results for beams with stirrups, primarily specimens JSC32-40B and JSC32-50B exemplified the model's inability to accurately represent behaviour past the first failure point. The two specimens exhibited flexural crushing, followed by an increase in stirrups strains, ultimately leading to rupture and shear failure. The model determined the load at flexural crushing to be the peak load, not accounting for the increase leading up to the stirrup rupture. Further research is recommended to model behaviour when multiple points of failure are to be considered. A possible technique to investigate is the omission of the crushed elements, allowing ABAQUS to model the response past that point.

## 6.3 Parametric Study

A study on the effects of slenderness was conducted in ABAQUS, using the validated models from Chapter 4. The goal of the investigation was to observe the behaviour of GFRP reinforced beams at higher slenderness ratios, as well as comparing the collected data against current strength prediction methods. The beams included in this study are those tested by Krall [43], tested at higher slenderness ratios. The conclusions are as follows:

- **Beams without stirrups**: The moment-deflection curves for beams without stirrups show a difference in peak values even at higher slenderness ratios (a/d >8.5), with the change plateauing at higher ratios. The CSA S806-12 models predicted that the beams did not fail in flexure for slenderness ratios $\leq$ 12.5 , corroborating the results from the moment-deflection curves and crack patterns from ABAQUS;

the peak moments were never identical, suggesting shear failure. The investigation was extended to higher slenderness ratios to observe flexural failure; the slenderness ratio at which the governing failure mode changed for BM 12-INF was 16.5.

- **Beams with stirrups**: The CSA S806-12 models predicted the switch from shear failure to flexural failure to occur at a slenderness ratio of 7.5 for BM 12-150. This change in failure mode is not observed in the model response prior to a slenderness ratio of 9.5. The study was extended to higher slenderness ratios to confirm the switch to flexural failure; the failure moments confirmed the switch to occur at a/d = 9.5. Due to the shear reinforcement present, observing flexural failure of BM 12-150 in beams less slender than BM 12-INF is expected. Physical tests are recommended for future research to confirm the accuracy of the model responses.

- **CSA S806-12 Shear Strength Prediction**: The CSA S806-12 model was shown to under-predict the shear capacity for beams with transverse reinforcement. A comparison with the results from ABAQUS yielded that the confinement of concrete induced by the stirrups was not adequately modelled by the CSA equations. Further research is required to confirm the results; however, a proposed alternative by Shahnewaz et al. [63] suggested that the inclusion of the compressive strength of concrete to the equations yielded more accurate results.

# References

[1] ACI Committee 440 (2003). Guide for the Design and Construction of Concrete Reinforced with FRP Bars, (ACI 440.1R-03), American Concrete Institute, Detroit, Michigan.

[2] ACI Committee 440 (2006). Guide for the Design and Construction of Structural Concrete Reinforced with FRP Bars, (ACI 440.1R-06), American Concrete Institute, Detroit, Michigan.

[3] ACI Committee 440 (2015). Guide for the Design and Construction of Structural Concrete Reinforced with FRP Bars, (ACI 440.1R-15), American Concrete Institute, Detroit, Michigan.

[4] Ahmed, E. A., El-Salakawy, E. F., Benmokrane, B., "Performance Evaluation of Glass Fiber-Reinforced Polymer Shear Reinforcement for Concrete Beams", ACI Structural Journal, 107(1), (January/February) 2010a, pp 53-62.

[5] Alkhrdaji, T., Wideman, M., Belarbi, A., & Nanni, A. (2001, October). Shear strength of GFRP RC beams and slabs. In Proceedings of the international conference, composites in construction-CCC (Vol. 2001, pp. 409-414).

[6] Almusallam, T., Al-Salloum, Y., Alsayed, S., and Amjad, A. (1997). Behaviour of Concrete Beams Doubly Reinforced by FRP bars. Proceedings of the Third International Symposium on Non-Metallic (FRP) Reinforcement for Concrete Structures (FRPRCS-3), Pages 471-478.

[7] Ametrano, D. (2011). Bond Characteristics of Glass Fibre Reinforced Polymer Bars Embedded in High Performance and Ultra-High Performance Concrete. Master's Thesis, Ryerson University.

[8] Ashour, A. F. (2006). Flexural and shear capacities of concrete beams reinforced with GFRP bars. Construction and Building Materials, 20(10), 1005-1015.

[9] Bai, J. (2013). Advanced fibre-reinforced polymer composites for structural applications. Woodhead Publishing, Oxford.

[10] Barris, C., Torres, L., Turon, A., Baena, M., & Catalan, A. (2009). An experimental study of the flexural behaviour of GFRP RC beams and comparison with prediction models. Composite Structures, 91(3), 286-295.

[11] Bentz, E. C., Massam, L., & Collins, M. P. (2010). Shear strength of large concrete members with FRP reinforcement. Journal of Composites for Construction, 14(6), 637-646.

[12] Bischoff, P. H., & Paixao, R. (2004). Tension stiffening and cracking of concrete reinforced with glass fiber reinforced polymer (GFRP) bars. Canadian Journal of Civil Engineering, 31(4), 579-588.

[13] Canadian Composite Structures, Inc. Structural Pultrusion Process, Retrieved January 19, 2017. http://www.canadiancomposites.com/pultrusionprocess.aspx

[14] Canadian Standards Association (2012). Design and Construction of Building Structures with Fibre-Reinforced Polymers, (CAN/CSA S806-12), Canadian Standards Association, Mississauga, Ontario.

[15] Chaallal, O., & Benmokrane, B. (1993). Physical and mechanical performance of an innovative glass-fiber-reinforced plastic rod for concrete and grouted anchorages. Canadian Journal of Civil Engineering, 20(2), 254-268.

[16] Chen, W. F. and Han, D. J. (1988). Plasticity for Structural Engineers. Springer-Verlag, New York.

[17] Collins, M. P. and Mitchell, D. (1991). Material Properties: Prestressed Concrete Structures. Prentice-Hall, New Jersey.

[18] Dassault Systemes Simulia (DSS) (2012). ABAQUS [6.12]. Providence, RI, USA.

[19] De Domenico, D., Pisano, A. A., & Fuschi, P. (2014). A FE-based limit analysis approach for concrete elements reinforced with FRP bars. Composite Structures, 107, 594-603.

[20] Duranovic, N., Pilakoutas, K., & Waldron, P. (1997, October). Tests on concrete beams reinforced with glass fibre reinforced plastic bars. In Proceedings of the third international symposium on non-metallic (FRP) reinforcement for concrete structures (FRPRCS-3) (Vol. 2, pp. 479-86).

[21] Ehsani, M. R., Saadatmanesh, H., & Tao, S. (1995). Bond of hooked glass fiber reinforced plastic (GFRP) reinforcing bars to concrete. ACI Materials Journal, 92(4), 391-400.

[22] Farghaly, A. S., & Benmokrane, B. (2013). Shear behavior of FRP-reinforced concrete deep beams without web reinforcement. Journal of Composites for Construction, 17(6), 04013015.

[23] Ferreira, A. J. M., Camanho, P. P., Marques, A. T., & Fernandes, A. A. (2001). Modelling of concrete beams reinforced with FRP re-bars. Composite structures, 53(1), 107-116.

[24] Fico, R., Prota, A., & Manfredi, G. (2008). Assessment of Eurocode-like design equations for the shear capacity of FRP RC members. Composites Part B: Engineering, 39(5), 792-806.

[25] Gardiner, G. (2009). The Making of Glass Fiber, Retrieved 20 January, 2017. http://www.compositesworld.com/articles/the-making-of-glass-fiber

[26] Grace, N. F., Soliman, A. K., Abdel-Sayed, G., & Saleh, K. R. (1998). Behavior and ductility of simple and continuous FRP reinforced beams. Journal of Composites for Construction, 2(4), 186-194.

[27] Gromicko, Nick, and Kenton Shepard (2013).The History of Concrete, Retrieved 9 February, 2017. http://www.nachi.org/history-of-concrete.htm

[28] Gross, S. P., Yost, J. R., Dinehart, D. W., Svensen, E., and Liu, N. (2003). Shear Strength of Normal and High Strength Concrete Beams Reinforced with GFRP Reinforcing Bars. Proc. of the Int. Conference on High Performance Materials in Bridges, ASCE, 426-437.

[29] Habeeb, M. N., & Ashour, A. F. (2008). Flexural behavior of continuous GFRP reinforced concrete beams. Journal of Composites for Construction, 12(2), 115-124.

[30] Hebei Maple Fiberglass Industry Co. Ltd. (2013). FRP/GRP Pipe Filament Winding Machine Working Process, Retrieved 19 January, 2017. http://www.frpmachining.com/faqs/frpgrp-pipe-filament-winding-machine

[31] Hollaway, L. C. (2009). Polymer composites in construction: a brief history. Proceedings of the Institution of Civil Engineers-Engineering and Computational Mechanics, 162(3), 107-118.

[32] Imjai, T., Guadagnini, M., & Pilakoutas, K. (2007). Mechanical performance of curved FRP rebars-Part I: Experimental study. In Asia-Pacific Conference on FRP in Structures (pp. 333-338). International Institute for FRP in Construction, Kingston, ON, Canada.

[33] Imjai, T., Guadagnini, M., & Pilakoutas, K. (2007). Mechanical performance of curved FRP rebars-Part II: Analytical study. In Proceedings of the First Asia-Pacific Conference on FRP in Structures, APFIS 2007, by the International Institute for FRP in Construction (IIFC) (pp. 339-344).

[34] International Federation for Structural Concrete (2007). FRP Reinforcement in RC Structures - Bulletin 40, Laussanne, Switzerland.

[35] ISIS Educational Committee (2003). ISIS Educational Module 2: An Introduction to FRP Composites for Construction. ISIS Canada, Intelligent Sensing for Innovative Structures, A Canadian Network of Centres of Excellence, University of Manitoba, Winnipeg, Manitoba, Canada.

[36] ISIS Educational Committee (2006). ISIS Educational Module 8: Durability of FRP Com- posites for Construction. ISIS Canada, Intelligent Sensing for Innovative Struc-

tures, A Canadian Network of Centres of Excellence, University of Manitoba, Winnipeg, Manitoba, Canada.

[37] ISIS Canada (2007). Reinforcing Concrete Structures with Fibre Reinforced Polymers -Design Manual No. 3. ISIS Canada, Intelligent Sensing for Innovative Structures, A Network of Centres of Excellence, University of Manitoba, Winnipeg, Manitoba, Canada.

[38] Jankowiak, T., & Lodygowski, T. (2005). Identification of parameters of concrete damage plasticity constitutive model. Foundations of civil and environmental engineering, 6(1), 53-69.

[39] Johnson, D. T., & Sheikh, S. A. (2016). Experimental Investigation of Glass Fiber-Reinforced Polymer-Reinforced Normal-Strength Concrete Beams. ACI Structural Journal, 113(6), 1165.

[40] Japan Society of Civil Engineers (1997). Recommendation for Design and Construction of Concrete Structures Using Continuous Fibre Reinforcing Materials. Concrete Engineering Series, (23).

[41] Kara, I. F., & Ashour, A. F. (2012). Flexural performance of FRP reinforced concrete beams. Composite Structures, 94(5), 1616-1625.

[42] Kobayashi, K. and Fujisaki, T. (1995). Compressive Behavior of FRP Reinforcement in Nonprestressed Concrete Members. Proceedings of the Second International Symposium on Nonmetallic (FRP) Reinforcement for Concrete Structures (FRPRCS-2), Pages 267-274.

[43] Krall, M. (2014). Tests on Concrete Beams with GFRP Flexural and Shear Reinforcements & Analysis Method for Indeterminate Strut-And-Tie Models with Brittle Reinforcements. Masters' Thesis, University of Waterloo.

[44] MacGregor, J. and Wight, J. (2005). Reinforced Concrete: Mechanics and Design. Pearson Prentice Hall, Upper Saddle River, New Jersey, 4th edition.

[45] Machial, R., Alam, M. S., & Rteil, A. (2012). Revisiting the shear design equations for concrete beams reinforced with FRP rebar and stirrup. Materials and structures, 45(11), 1593-1612.

[46] Malm, R. (2006). Shear cracks in concrete structures subjected to in-plane stresses (Doctoral dissertation, KTH).

[47] Malm, R. (2009). Predicting shear type crack initiation and growth in concrete with non-linear finite element method (Doctoral dissertation, KTH).

[48] Matta, F., El-Sayed, A. K., Nanni, A., & Benmokrane, B. (2013). Size effect on concrete shear strength in beams reinforced with fiber-reinforced polymer bars. ACI Structural Journal, 110(4), 617.

[49] Morphy, R., Shehata, E., & Rizkalla, S. (1997, October). Bent effect on strength of CFRP stirrups. In Proceedings of the Third International Symposium on Non-Metallic (FRP) Reinforcement for Concrete Structures (Vol. 2, pp. 19-26).

[50] Nagasaka, T., Fukuyama, H., Tanigaki, M., "Shear Performance of Concrete Beams Reinforced with FRP Stirrups", Special Publication of the ACI, 138, (September) 1993, pp 789-812.

[51] Nakamura, H., Higai, T., "Evaluation of Shear Strength of Concrete Beams Reinforced with FRP", (English Translation) Concrete Library International of Japanese Society of Civil Engineers (JSCE), 26, (December) 1995, pp 111-123.

[52] Nakamura, E., Watanabe, H., & Koga, H. (2006, October). Shear resisting mechanism in RC beams with fractured stirrups. In Proceedings of the 22nd US-Japan Bridge Engineering Workshop (S. 50-60).

[53] Nehdi, M., Chabib, H. E., and Said, A. A. (2007). Proposed Shear Design Equations for FRP-Reinforced Concrete Beams Based on Genetic Algorithms Approach. Journal of in Civil Engineering, 19(12):1033-1042.

[54] Newhook, J., Ghali, A., & Tadros, G. (2002). Concrete flexural members reinforced with fiber reinforced polymer: design for cracking and deformability. Canadian Journal of Civil Engineering, 29(1), 125-134.

[55] Newhook, J., and Svecova, D. (2006). Reinforcing Concrete Structures with Fibre-Reinforced Polymers. Winnipeg: ISIS Canada Corporation.

[56] Nour, A., Massicotte, B., Yildiz, E., & Koval, V. (2007). Finite element modeling of concrete structures reinforced with internal and external fibre-reinforced polymers. Canadian Journal of Civil Engineering, 34(3), 340-354.

[57] Nuplex Industries Ltd. (2014). Hand Lay-Up, Retrieved 19 January, 2017. http://www.nuplex.com/composites/processes/hand-lay-up

[58] Pecce, M., Manfredi, G., & Cosenza, E. (2000). Experimental response and code Models of GFRP RC beams in bending. Journal of Composites for Construction, 4(4), 182-190.

[59] Rafi, M. M., Nadjai, A., & Ali, F. (2007). Analytical modeling of concrete beams reinforced with carbon FRP bars. Journal of Composite Materials, 41(22), 2675-2690.

[60] Rafi, M. M., Nadjai, A., & Ali, F. (2008). Finite element modeling of carbon fiber-reinforced polymer reinforced concrete beams under elevated temperatures. ACI Structural Journal, 105(6), 701.

[61] Rasheed, H. A., Nayal, R., & Melhem, H. (2004). Response prediction of concrete beams reinforced with FRP bars. Composite Structures, 65(2), 193-204.

[62] Razaqpur, A. G., Isgor, B. O., Greenaway, S., & Selley, A. (2004). Concrete contribution to the shear resistance of fiber reinforced polymer reinforced concrete members. Journal of Composites for Construction, 8(5), 452-460.

[63] Shahnewaz, M., Machial, R., Alam, M. S., & Rteil, A. (2016). Optimized shear design equation for slender concrete beams reinforced with FRP bars and stirrups using Genetic Algorithm and reliability analysis. Engineering Structures, 107, 151-165.

[64] Shehata, E., Morphy, R., & Rizkalla, S. (1999). FRP for shear reinforcement in concrete structures. J]. Ph. D. dissertation submitted to the department of Civil Engineering at the University of Manitoba, Winnipeg, Manitoba, Canada, 237-239.

[65] Shehata, E., Morphy, R., & Rizkalla, S. (2000). Fibre reinforced polymer shear reinforcement for concrete members: behaviour and design guidelines. Canadian Journal of Civil Engineering, 27(5), 859-872.

[66] Stoner, J. (2015). Finite Element Modelling of GFRP Reinforced Concrete Beams. Masters' Thesis, University of Waterloo.

[67] Swenson, A., and Chang, P.C. (2014). Building Construction, Retrieved 27 January, 2017. https://www.britannica.com/biography/Francois-Coignet

[68] Theriault, M., & Benmokrane, B. (1998). Effects of FRP reinforcement ratio and concrete strength on flexural behavior of concrete beams. Journal of composites for construction, 2(1), 7-16.

[69] Tottori, S., & Wakui, H. (1993). Shear capacity of RC and PC beams using FRP reinforcement. Special Publication, 138, 615-632.

[70] Ueda, T., Sato, Y., Kakuta, Y., Imamura, A., & Kanematsu, H. (1995, August). Failure criteria for FRP rods subjected to a combination of tensile and shear forces. In RILEM PROCEEDINGS (pp. 26-26). CHAPMAN & HALL.

[71] Vijay, P. V., Kumar, S. V., & GangaRao, H. V. S. (1996). Shear and ductility behavior of concrete beams reinforced with GFRP rebars. In PROCEEDINGS OF THE 2ND INTERNATIONAL CONFERENCE ON ADVANCED COMPOSITE MATERIALS IN BRIDGES AND STRUCTURES, ACMBS-II, MONTREAL 1996.

[72] Wegian, F. M., & Abdalla, H. A. (2005). Shear capacity of concrete beams reinforced with fiber reinforced polymers. Composite Structures, 71(1), 130-138.

[73] Yost, J. R., Gross, S. P., & Dinehart, D. W. (2001). Shear strength of normal strength concrete beams reinforced with deformed GFRP bars. Journal of composites for construction, 5(4), 268-275.

[74] Zhang, Y. X., & Lin, X. (2013). Nonlinear finite element analyses of steel/FRP-reinforced concrete beams by using a novel composite beam element. Advances in Structural Engineering, 16(2), 339-352.

[75] Zhao, W., Maruyama, K., & Suzuki, H. (1995, August). Shear behavior of concrete beams reinforced by FRP rods as longitudinal and shear reinforcement. In RILEM PROCEEDINGS (pp. 352-352). CHAPMAN & HALL.

[76] Zhao, W. (1999). Crack and Deformation Behavior of FRP Reinforced Concrete Structures. PhD Thesis, University of Sheffield, Sheffield, UK.

# Appendices

# Appendix A

# Software Developed for Analysis

This Appendix collates all the software that was developed to compute strength predictions and automate FEM analyses. The MATLAB codes written to calculate code values are presented first, and are followed by the Python code written to automate the FEM analyses.

# Flexural Strength Prediction

## CSA S806-12

```
function [Mr] = CSA_flexural(fc,Ef,Af,f_fu,d,b_w,a_d)

L = a_d*d*2/1000; % Beam length, based on a/d and 3 point bend
    specimen *CHANGE IF NOT 3 POINT BENDING*

Phi_c = 1;
Phi_f = 1;
epsilon_t = -3.5E-03; % for over-reinforced beams (max concrete
     strain)
epsilon_ult = 3.5E-03; % Concrete crushing strain
epsilon_c = 2.5E-03; % epsilon'c from Hognestad parabola
alpha1 = 0.85-(0.0015*fc); % Stress block parameter alpha1

if alpha1 < 0.67 % Limit on alpha1
    alpha1 = 0.67;
end

beta1 = 0.97-(0.0025*fc); % Stress block parameter beta1

if beta1 < 0.67 % Limit on beta1
    beta1 = 0.67;
end
```

```
f_f_estimate  = 995; % Initial guess for strength of FRP bar (
    iterative procedure)
Ff = 800; % Initial guess for stress due to FRP
while abs(Ff-f_f_estimate)>0.1 % find correct stress in FRP
    Tf = Phi_f*Af*f_f_estimate; % Tensile force

    c = Tf/(alpha1*Phi_c*fc*b_w*beta1); % Calculate stress
        block parameter c

    epsilon_f = epsilon_t*((c-d)/c); %Using similar triangles
        for strain to find strain in FRP

    Ff = epsilon_f*Ef; % Calculate stress due to FRP

    f_f_estimate=((2*Ff)+f_f_estimate)/3; % Update estimated
        strength of FRP, trapezoidal
end

if Ff<f_fu % under-reinforced if stress in FRP < ultimate
    Mr=(Phi_f*Af*Ff*(d-(beta1*c/2)))*10^-6; % Calculate
        flexural strength
else %over-reinforced, iterative procedure
    epsilon_f = epsilon_ult; % Set strain = ultimate
    Ff = f_fu; % Set stress in FRP = ultimate
```

```
    epsilon_t_estimate = -3E-03; % Initialize guess for estimated strain in FRP
    epsilon_t = 50; % Initialize guess for actual strain in FRP

    while abs(epsilon_t_estimate-epsilon_t)>1E-05 % Loop until guess matches calculated value
        beta1 = (4-(epsilon_t_estimate/epsilon_c))/(6-(2*epsilon_t_estimate/epsilon_c)); % Stress block parameter beta1
        alpha1 = ((epsilon_t_estimate/epsilon_c) - (((epsilon_t_estimate/epsilon_c)^2)/3))/beta1; % Stress block parameter beta1
        c = Phi_f*Af*f_fu/(alpha1*Phi_c*fc*b_w*beta1); % Stress block parameter c
        epsilon_t = epsilon_ult*(c/(c-d)); % Calculate strain
        if abs(epsilon_t_estimate-epsilon_t)>1E-05 % If estimated strain =/= calculated strain, set calculated strain as new estimate
            epsilon_t_estimate = epsilon_t_estimate-1E-05;
        end
    end
    Mr = (Phi_f*Af*f_fu*(d-(beta1*c/2)))*10^-6; % Calculate flexural strength
end
```

```
P = 4*Mr/L % Load P based on flexural capacity and 3 point bend test. *CHANGE IF NOT 3 POINT BENDING*
end
```

The input parameters are:

- fc: The compressive strength of the concrete used.
- Ef: The modulus of elasticity of the longitudinal reinforcing bars.
- Af: The total area of longitudinal reinforcement used..
- f_fu: The tensile strength of the longitudinal reinforcing bars.
- d: The distance from the extreme compression fibre to the centroid of the longitudinal tension force.
- b_w: The width of the beam.
- a_d: The slenderness ratio (shear span to effective depth).

## ACI440.1R-15

```
function [Mr] = ACI_flexural(num_bars,fc,beta1,Ef,A_bar,d,b_w,a_d)

CE = 0.8; % no environmental effects => reduction factor =0.8
f_fu = 1000*CE; % Adjusted strength
epsilon_cu = 0.003; % From ACI440 document, max concrete strain

Af = A_bar*num_bars; % Calculate total bar area

L = a_d*d*2/1000; % Beam length, based on a/d and 3 point bend specimen *CHANGE IF NOT 3 POINT BENDING*

p_f = Af/(b_w*d); % Calculate flexural reinforcement ratio
p_b = 0.85*beta1*(fc/f_fu)*((Ef*epsilon_cu)/((Ef*epsilon_cu) + f_fu)); % Calculate rho balanced

if (p_f/p_b) >= 1.4 % Compression-Controlled Section, flexural ratio > 1.4* rho balanced
%     phi = 0.65;
    phi = 1; % Set safety factors to 1
    Ff = sqrt((((Ef*epsilon_cu)^2)/4)+((0.85*beta1*fc/p_f)*Ef*epsilon_cu))-(0.5*Ef*epsilon_cu); % Stress in GFRP at ultimate
    if Ff>f_fu  % Limit on stress in GFRP
```

```
            Ff = f_fu;
        end

        a = Af*Ff/(0.85*fc*b_w); % Stress block parameter a
        Mr = (Af*Ff*(d-(a/2)))*phi*10^-6; % Flexural strength
            calculation
        %PHI_Mr = phi*Mr; % When safety factors included

    else % Tension-Controlled Section
    %     phi = 0.55;
        phi = 1;
        Ff = f_fu; % Stress in GFRP at ultimate
        epsilon_fu = Ff/Ef;
        c = (epsilon_cu/(epsilon_cu+epsilon_fu))*d; % Calculate
            stress block parameter c
        Mr = (Af*f_fu*(d-(beta1*c/2)))*phi*10^-6; % Flexural
            strength calculation
       % PHI_Mr = phi*Mr; % When safety factors included
    end
    P = 4*Mr/L % Load P based on flexural capacity and 3 point bend
        test. *CHANGE IF NOT 3 POINT BENDING*
    end
```

The input parameters are:

- num_bars: The number of longitudinal reinforcing bars used.

- fc: The compressive strength of the concrete used.
- beta1: Whitney stress block parameter.
- Ef: The modulus of elasticity of the longitudinal reinforcing bars.
- A_bar: The cross-sectional area of a single longitudinal reinforcing bar.
- d: The distance from the extreme compression fibre to the centroid of the longitudinal tension force.
- b_w: The width of the beam.
- a_d: The slenderness ratio (shear span to effective depth).

## Shear Strength Prediction

### CSA S806-12

```
function [Vr] = CSA_Shear(num_bars,fc,f_fu,Astirr,h,rho_f,Ef,
    A_bar,s,d,b_w,a_d)

% Phi_f = 0.75;
Phi_f = 1; % Set safety factors to 1
% Phi_c = 0.65;
Phi_c = 1; % Set safety factors to 1
if f_fu>0.005*Ef % Clause 8.4.4.9 CSA806
    f_fu = 0.005*Ef;
end

Af = A_bar*num_bars; % Calculate total bar area

dv = max(0.72*h,0.9*d); %Design shear depth
V_sf = 0; % Initialize stirrup shear variable
Vr=200000; % Initialize total shear capacity variable
load = 1; % Initialize applied load (P) variable
L = a_d*d*2/1000; % Beam length, based on a/d and 3 point bend
    specimen *CHANGE IF NOT 3 POINT BENDING*
while abs((2*Vr)-load)>10^-1 % Loop until applied load matches
    load based on shear capacity *CHANGE IF NOT 3 POINT BENDING*
```

```
moment = (load*L/4); % Max moment on speciment due to load P. *CHANGE IF NOT 3 POINT BENDING*
if moment<(load*dv/2000)
    moment = load*dv/2000; % Minimum moment set by code
end
if s~=0 % For beams with stirrups
    epsilon_l = (((moment*10^6)/dv)+((load*10^3)/2))/(2*Ef*Af) % Epsilon_x used for theta calculation (same as for general shear)
    theta = 30 + (7000*epsilon_l);
    if theta > 60 % Limit on theta
        theta = 60;
    end
    if theta < 30 % Limit on theta
        theta = 30;
    end
    V_sf = (0.4*Astirr*f_fu*Phi_f*dv)/(s*tan(theta*pi/180)); % Equation 8-22, CSA806, Clause 8.4.4.9, shear strength due to transverse reinforcement
end

Kr = 1 + ((Ef*rho_f)^(1/3)); % Kr factor for concrete shear strength contribution

```

```
Km = sqrt(1/a_d); % Kr factor for concrete shear strength
    contribution

if Km > 1 % Limit on Km
    Km = 1;
end

Vc = 0.05*Phi_c*Km*Kr*(fc^(1/3))*b_w*dv; % Concrete
    contribution to shear

Ka = 2.5/a_d; % Ka factor to account for arch effect
if Ka> 2.5
    Ka = 2.5;
end
if Ka< 1 % Limit on Km
    Ka = 1;
end
Vc = Vc*Ka; % Apply Ka factor to account for arch effect
if Vc > (0.22*Phi_c*sqrt(fc)*b_w*dv) % Upper limit on Vc
    Vc = (0.22*Phi_c*sqrt(fc)*b_w*dv);
end
if Vc < (0.11*Phi_c*sqrt(fc)*b_w*dv) % Lower limit on Vc
    Vc = (0.11*Phi_c*sqrt(fc)*b_w*dv);
end

```

```
    Vr = Vc + V_sf; % Total shear capacity
    if Vr > (0.22*Phi_c*fc*b_w*dv) % Limit on total shear capacity
        Vr = (0.22*Phi_c*fc*b_w*dv);
    end
    load = load +0.001; % Iterate over load (concentrated load P)
    Vr = Vr/1000;
end
P = 2*Vr  % Concentrated load based on shear, and 3 point bending test set up (*CHANGE IF TEST SET UP NOT 3 POINT BENDING*)
end
```

The input parameters are:

- num_bars: The number of longitudinal reinforcing bars used.
- fc: The compressive strength of the concrete used.
- f_fu: The tensile strength of the longitudinal reinforcing bars.
- Astirr: Cross-sectional area of two legs of transverse reinforcement.
- h: Height of the beam.
- rho_f: The longitudinal reinforcement ratio.
- Ef: The modulus of elasticity of the longitudinal reinforcing bars.

- A_bar: The cross-sectional area of a single longitudinal reinforcing bar.
- s: The stirrup spacing (zero if no stirrups).
- d: The distance from the extreme compression fibre to the centroid of the longitudinal tension force.
- b_w: The width of the beam.
- a_d: The slenderness ratio (shear span to effective depth).

## ACI440.1R-15

```
function [Vr] = ACI_Shear(fc,Astirr,f_fb,rho_f,Ef,Efv,Ec,s,d,b_w)

% Phi_f = 0.75;
Phi_f = 1; % Set safety factors to 1
% Phi_c = 0.65;
Phi_c = 1; % Set safety factors to 1

V_sf = 0; % Initialize stirrup shear variable

if s~=0 % For beams with stirrups
    f_fv = 0.004*Efv; % Equation 8.2d, Section 8 (ACI440)
    if f_fv>f_fb
        f_fv = f_fb; % Find ultimate design strength of FRP bars
    end
    V_sf = (Astirr*f_fv*d)/s; % Equation 8.2c, ACI440, shear strength due to transverse reinforcement
end

nf = Ef/Ec; % Ratio of Elastic moduli of FRP to concrete

k = sqrt((2*rho_f*nf)+(rho_f*nf)^2)-(rho_f*nf); % Calculate k factor for use in concrete shear contribution
```

```

Vc = (2/5)*sqrt(fc)*b_w*k*d; % Concrete contribution to shear
V_sf
Vr = Vc+V_sf; % Total shear capacity
Vr = Vr/1000;
P = 2*Vr  % Concentrated load based on shear, and 3 point bending test set up (*CHANGE IF TEST SET UP NOT 3 POINT BENDING*)
end
```

The input parameters are:

- fc: The compressive strength of the concrete used.
- Astirr: Cross-sectional area of two legs of transverse reinforcement.
- f_fb: The tensile strength at the bend of the transverse reinforcement.
- rho_f: The longitudinal reinforcement ratio.
- Ef: The modulus of elasticity of the longitudinal reinforcing bars.
- Efv: The modulus of elasticity of the transverse reinforcement.
- Ec: The modulus of elasticity of the concrete.
- s: The stirrup spacing (zero if no stirrups).
- d: The distance from the extreme compression fibre to the centroid of the longitudinal tension force.

- b_w: The width of the beam.

### Nehdi et al., 2007

```
function [Vr] = Nehdi_Shear(fc,rho_f,rho_v,f_fu,Ef,d,b_w,a_d)

Es = 200000; % Modulus of Elasticity for Steel

L = a_d*d*2/1000; % Beam length, based on a/d and 3 point bend specimen *CHANGE IF NOT 3 POINT BENDING*

if a_d > 2.5 % Slenderness ratio > 2.5
    Vc = 2.1 * ((fc*rho_f*Ef/(a_d*Es))^0.23) * b_w * d; % Concrete contribution to shear strength
end

if a_d <= 2.5 % Slenderness ratio <= 2.5
    Vc = 2.1 * ((fc*rho_f*Ef/(a_d*Es))^(0.23)) * b_w * d * (2.5/a_d); % Concrete contribution to shear strength
end

Vf = 0.74 * ((rho_v * f_fu)^0.51)*b_w*d; % Transverse reinforcement contribution to shear strength
Vf
Vr = Vc + Vf;
Vr = Vr/1000;
P = 2*Vr  % Concentrated load based on shear, and 3 point bending test set up (*CHANGE IF TEST SET UP NOT 3 POINT
```

```
    BENDING*)
end
```

The input parameters are:

- fc: The compressive strength of the concrete used.
- rho_f: The longitudinal reinforcement ratio.
- rho_v: The transverse reinforcement ratio.
- f_fu: The tensile strength of the longitudinal reinforcing bars.
- Ef: The modulus of elasticity of the longitudinal reinforcing bars.
- d: The distance from the extreme compression fibre to the centroid of the longitudinal tension force.
- b_w: The width of the beam.
- a_d: The slenderness ratio (shear span to effective depth).

## Japan Society of Civil Engineers

```
function [Vr] = JSCE_Shear(fc,f_fu,h,rho_f,rho_v,Ef,Efv,Astirr,s,d_b,r_b,d,b_w)

Es = 200000; % Modulus of Elasticity for Steel

gamma_c = 1; % Set safety factors to 1

f_cd = fc/gamma_c; % Adjusted concrete strength
gamma_b = 1; % Set safety factor to 1 (usually 1.15)
Vf = 0; % Initialize variable for transverse reinforcement contribution to shear strength
if s~=0 % For beams with stirrups
    fmcd = f_cd * ((h/300)^(-1/10)); % Concrete strength, adjusted for shear
    gamma_mfb = 1; % Bent portion of bar safety factor (usually 1.3) set to 1
    f_bend = ((0.05*r_b/d_b) + 0.3)*(f_fu/gamma_mfb); % Strength of stirrup at bend calculation
    if f_bend > f_fu % Set limit on bemd strength of stirrup
        f_bend = f_fu;
    end
    epsilon_fv = 0.0001*(fmcd*rho_f*Ef/(rho_v*Efv))^0.5; % Find strain in transverse reinforcement
```

```
    if epsilon_fv > (f_bend/Efv) % Set limit on strain in transverse reinforcement
        epsilon_fv = f_bend/Efv;
    end
    jd = d/1.15;
    alpha_s = 90; % Angle between shear reinforcement and beam axis
    Vf = (Astirr*Efv*epsilon_fv*(sind(alpha_s)+cosd(alpha_s))/s)*jd/gamma_b; % Transverse reinforcement contribution to shear strength
end

f_vcd = 0.2*(f_cd^(1/3)); % Adjustment to concrete strength factor

if f_vcd > 0.72 % Set limit on concrete strength factor
    f_vcd = 0.72;
end

beta_d = (1000/d)^0.25; % Beta_d factor for concrete contribution to shear strength

if beta_d >= 1.5 % Set limit on beta_d
    beta_d = 1.5;
end
```

```

beta_p = (100*rho_f*Ef/Es)^(1/3); % Beta_p factor for concrete contribution to shear strength

if beta_p >= 1.5 % Set limit on beta_p
    beta_p = 1.5;
end

beta_n = 1; % For members with no axial force

Vc = beta_d*beta_p*beta_n*f_vcd*b_w*d/gamma_b; % Concrete contribution to shear strength
Vf
Vr = Vc + Vf; % Total shear capacity
Vr = Vr/1000;
P = 2*Vr  % Concentrated load based on shear, and 3 point bending test set up (*CHANGE IF TEST SET UP NOT 3 POINT BENDING*)
end
```

The input parameters are:

- fc: The compressive strength of the concrete used.
- f_fu: The tensile strength of the longitudinal reinforcing bars.
- h: The height of the beam.

- rho_f: The longitudinal reinforcement ratio.
- rho_v: The transverse reinforcement ratio.
- Ef: The modulus of elasticity of the longitudinal reinforcing bars.
- Efv: The modulus of elasticity of the transverse reinforcement.
- Astirr: Cross-sectional area of two legs of transverse reinforcement.
- s: The stirrup spacing (zero if no stirrups).
- d_b: The diameter of a single transverse reinforcing bar.
- r_b: The bend radius of a single transverse reinforcing bar.
- d: The distance from the extreme compression fibre to the centroid of the longitudinal tension force.
- b_w: The width of the beam.

## Intelligent Sensing for Innovative Structures (ISIS) Canada Manual No.3

```
function [Vr] = ISIS_Canada_Shear(num_bars,fc,f_fu,Ef,Astirr,s,d_b,A_bar,r_b,d,b_w,a_d)

dv = 0.9*d; % effective shear depth

Af = A_bar*num_bars; % Calculate total bar area

Es = 200000; % Modulus of Elasticity for Steel

lambda = 1; % Normal density concrete
PHI_c = 1; % Set safety factors to 1
PHI_f = 1; % Set safety factors to 1

if d <= 300
    V_cf = 0.2*lambda*PHI_c*sqrt(fc)*b_w*d*sqrt(Ef/Es); % Concrete contribution to shear capacity for depth <= 300mm
else
    V_cf = (260/(1000+d))*lambda*PHI_c*sqrt(fc)*b_w*d*sqrt(Ef/Es); % Concrete contribution to shear capacity for depth > 300mm
```

```
    V_min = 0.1*lambda*PHI_c*sqrt(fc)*b_w*d*sqrt(Ef/Es); % Minimum limit on concrete contribution to shear capacity (only for d >300mm)
    if V_cf < V_min
        V_cf = V_min;
    end
end

V_f = 0; % Initialize stirrup contribution to shear capacity
Vr=200000; % Initialize total shear capacity variable
load = 1; % Initialize applied load (P) variable
L = a_d*d*2/1000; % Beam length, based on a/d and 3 point bend specimen *CHANGE IF NOT 3 POINT BENDING*


if s~=0 % For beams with stirrups
    while abs((2*Vr)-load)>10^-1 % Loop until applied load matches load based on shear capacity *CHANGE IF NOT 3 POINT BENDING*
            moment = (load*L/4); % Max moment on speciment due to load P. *CHANGE IF NOT 3 POINT BENDING*
            epsilon_l = (((moment*10^6)/dv)+((load*10^3)/2))/(2*Ef*Af); % Epsilon_x used for theta calculation (same as for general shear)
            theta = 30 + (7000*epsilon_l);
```

```
            if theta > 60 % Limit on theta
                theta = 60;
            end
            if theta < 30 % Limit on theta
                theta = 30;
            end
            f_fv = ((0.05*(r_b/d_b))+0.3)*f_fu/1.5; % Calculate effective tensile capacity of stirrups, based on bend radius and bar diameter
            V_f = PHI_f*Astirr*f_fv*dv*cotd(theta)/s; % Stirrup contribution to shear capacity
            Vr = V_cf + V_f; % Total shear capacity
            Vr = Vr/1000;
            load = load +0.001; % Iterate over load (concentrated load P)
    end
end

V_f
Vr = V_cf + V_f; % Total shear capacity
Vr = Vr/1000;
P = 2*Vr  % Concentrated load based on shear, and 3 point bending test set up (*CHANGE IF TEST SET UP NOT 3 POINT BENDING*)
end
```

The input parameters are:

- num_bars: The number of longitudinal reinforcing bars used.
- fc: The compressive strength of the concrete used.
- f_fu: The tensile strength of the longitudinal reinforcing bars.
- Ef: The modulus of elasticity of the longitudinal reinforcing bars.
- Astirr: Cross-sectional area of two legs of transverse reinforcement.
- s: The stirrup spacing (zero if no stirrups).
- d_b: The diameter of a single transverse reinforcing bar.
- A_bar: The cross-sectional area of a single longitudinal reinforcing bar.
- r_b: The bend radius of a single transverse reinforcing bar.
- d: The distance from the extreme compression fibre to the centroid of the longitudinal tension force.
- b_w: The width of the beam.
- a_d: The slenderness ratio (shear span to effective depth).

# Python Code for Automation

```
import numpy as np
import xlsxwriter
from abaqus import *
import section
import regionToolset
import displayGroupMdbToolset as dgm
import part
import material
import assembly
import step
import interaction
import load
import mesh
import optimization
import job
import sketch
import visualization
import xyPlot
import displayGroupOdbToolset as dgo
import connectorBehavior
import os
from part import *
from material import *
from assembly import *
```

```
from step import *
from interaction import *
from load import *
from mesh import *
from job import *
from sketch import *
from visualization import *
from connectorBehavior import *
from abaqusConstants import *
from regionToolset import Region
from multiprocessing import cpu_count
from visualization import openOdb
from abaqus import mdb
import csv                  # utilities to write a .CSV file
#from UgenKeyword import *   # utilities to write the UGENS parameters on the Job.inp file directly from CAE

for ad in [1.5,2.5,3.5,4.5,5.5,6.5,7.5,8.5,9.5,10.5,11.5,12.5]:

        for beamSelect in [0,1,2,3,4,5,6,7,8,9,10,11]:

                beams = ['12-INF','12-150','12-220','12-s230','16-INF','16-150','16-220','16-s230','25-INF','25-150','25-220','25-s230']

```

```
            depth = 270

            L = (ad*depth*2)/1000

            odbname = 'GFI09,conf015,BiLinRec,ft248,DA30,v20' # Change if DA = 50

            beamType = beams[beamSelect]

            path = 'C:\\Users\\USER1\\Desktop\\30 dilation parametric\\'  + beamType +'\\a-d = ' +str(ad) +'\\'
            myodbpath = path + odbname +'.odb'
            mbd_path = path + beamType

            os.chdir(path)

            File=openMdb(pathName=mbd_path)

            job = path + odbname +'.inp'
            mdb.jobs[odbname].writeInput(consistencyChecking=OFF)
            File.jobs[odbname].submit(consistencyChecking=OFF)
            File.jobs[odbname].waitForCompletion()
```

```
odb = openOdb(myodbpath)

step = odb.steps['ApplyLoad']

n = 1
m = 1

Force = [0,0,0,0,0,0,0,0,0]

for node_x in odb.rootAssembly.instances['BEAM-1'].nodeSets['REACTIONS'].nodes:
    session.XYDataFromHistory(name='Force-' + str(n), odb=odb,
        outputVariableName ='Reaction force: RF2 PI: BEAM-1 Node ' + str(node_x.label) + ' in NSET REACTIONS',
        steps=('ApplyLoad', ), )
    Force[n-1] = session.xyDataObjects['Force-' + str(n)]
    n=n+1

session.XYDataFromHistory(name='Displacement', odb=odb,
```

```
                outputVariableName='Spatial displacement: U2 PI: BEAM-1 Node ' + str(odb.rootAssembly.nodeSets['MIDSPAN'].nodes[0][0].label) + ' in NSET MIDSPAN',
                steps=('ApplyLoad', ), )
        Displacement = session.xyDataObjects['Displacement']

        n = n-1
        row = 0
        col = 0
        print n
        workbook = xlsxwriter.Workbook(path + beamType + '.xlsx')
        worksheet = workbook.add_worksheet()


        if n == 9:
                session.xyReportOptions.setValues(numDigits=9, numberFormat=ENGINEERING)
                session.writeXYReport(fileName=path+'load_displacement.DAT', appendMode=OFF, xyData=(Force[0],
```

```
                        Force[1], Force[2], Force[3], Force[4], Force[5], Force[6], Force[7], Force[8], Displacement))
        with open(path+'load_displacement.DAT') as f:
                array = np.genfromtxt(f)
                t,f0,f1,f2,f3,f4,f5,f6,f7,f8,d = array.T
        worksheet.write(0, 0, 'Reaction Force')
        worksheet.write(0, 1, 'Displacement')
        worksheet.write(0, 2, 'Moment')
        max_load = [0,0]
        for i in range(1,len(f1)-1):
                RF = (f0[i]+f1[i]+f2[i]+f3[i]+f4[i]+f5[i]+f6[i]+f7[i]+f8[i])/1000
                if RF>max_load[0]:
                        max_load = [RF,i-1]
                worksheet.write(i, 0, 2*RF)
                worksheet.write(i, 1, abs(d[i]))
                worksheet.write(i, 2, 2*RF*L/4)


```

```
        else:
                session.xyReportOptions.setValues(numDigits=9, numberFormat=ENGINEERING)
                session.writeXYReport(fileName=path+'load_displacement.DAT', appendMode=OFF, xyData=(Force[0],
                        Force[1], Force[2], Force[3], Force[4], Force[5], Force[6], Force[7], Displacement))
                with open(path+'load_displacement.DAT') as f:
                        array = np.genfromtxt(f)
                        t,f0,f1,f2,f3,f4,f5,f6,f7,d = array.T
                worksheet.write(0, 0, 'Reaction Force')
                worksheet.write(0, 1, 'Displacement')
                worksheet.write(0, 2, 'Moment')
                max_load = [0,0]
                for i in range(1,len(f1)-1):
                        RF = (f0[i]+f1[i]+f2[i]+f3[i]+f4[i]+f5[i]+f6[i]+f7[i])/1000
                        if RF>max_load[0]:
                                max_load = [RF,i-1]
                        worksheet.write(i, 0, 2*RF)
```

```
                        worksheet.write(i, 1, abs(d[i])
                          )
                        worksheet.write(i, 2, 2*RF*L/4)


        o1 = session.openOdb(name=myodbpath)
        session.viewports['Viewport: 1'].setValues(
          displayedObject=o1)
        session.viewports['Viewport: 1'].odbDisplay.
          setPrimaryVariable(
              variableLabel='PEMAG', outputPosition=
                INTEGRATION_POINT, )
        session.viewports['Viewport: 1'].odbDisplay.
          display.setValues(
              plotState=CONTOURS_ON_DEF)
        session.viewports['Viewport: 1'].odbDisplay.
          display.setValues(plotState=(
              CONTOURS_ON_UNDEF, ))
        session.viewports['Viewport: 1'].view.setValues
          (cameraPosition=(7844, 88.418,
1928.04), cameraUpVector=(0, 1, 0))
        session.viewports['Viewport: 1'].view.fitView()
        session.viewports[session.currentViewportName].
          odbDisplay.setFrame(
```

```
                            step='ApplyLoad', frame=
                                max_load[1])
        session.printToFile(
                fileName='C:/Users/USER1/Desktop/30
                    dilation parametric/' + beamType +'/a
                    -d = '+str(ad)+'/crack_pattern_' +
                    beamType,
                format=PNG, canvasObjects=(session.
                    viewports['Viewport: 1'], ))

        odb.save()
        odb.close()
        workbook.close()
```

# Appendix B

# Beam Drawings

This Appendix displays the detailed drawings of the beams used to calibrate ABAQUS to analyze FRP reinforced concrete beams. The beams were tested by Martin Krall [43]) and the drawings are taken from the thesis of Joseph Stoner [66]. All beams presented in this Appendix have a slenderness ratio of 2.5.

## BM 12-INF

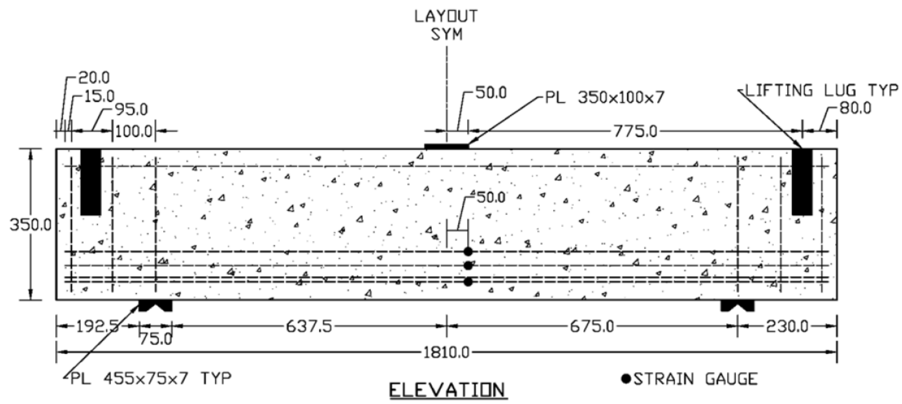


(a)

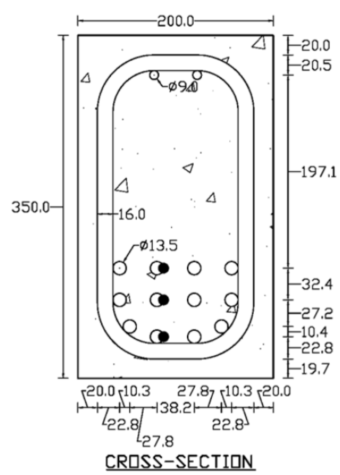


(b)

Figure B.1: Beam Details for BM 12-INF

## BM 12-150

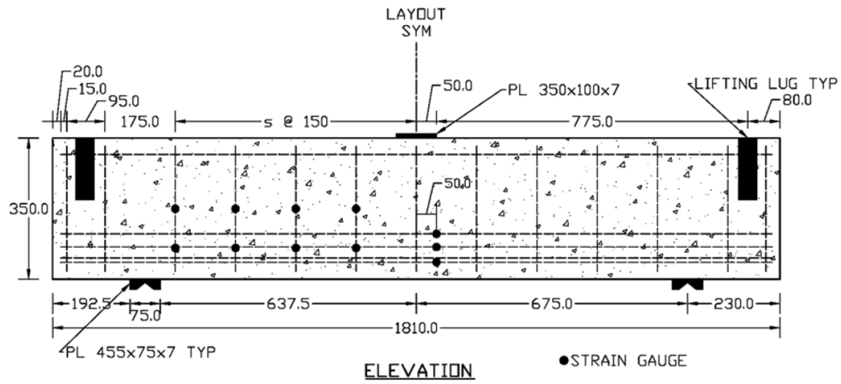


(a)

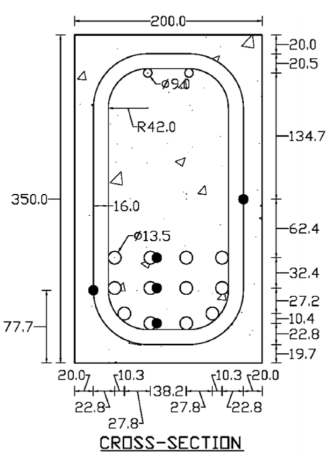


(b)

Figure B.2: Beam Details for BM 12-150

## BM 12-220

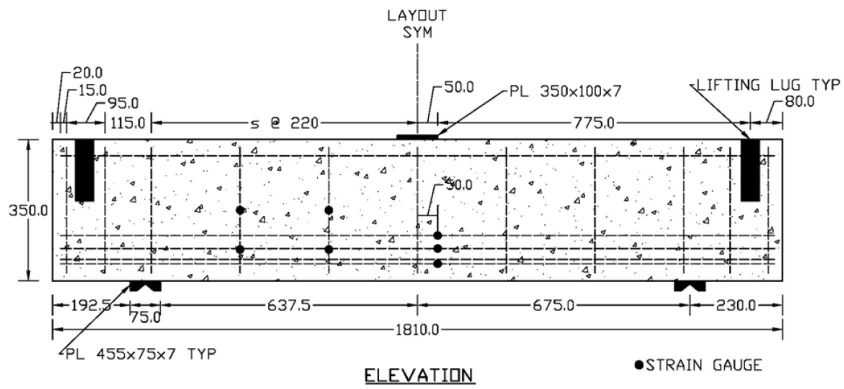


(a)

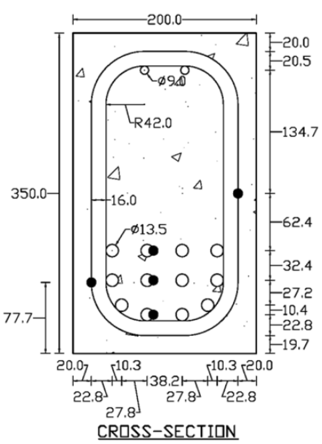


(b)

Figure B.3: Beam Details for BM 12-220

# BM 12-s230

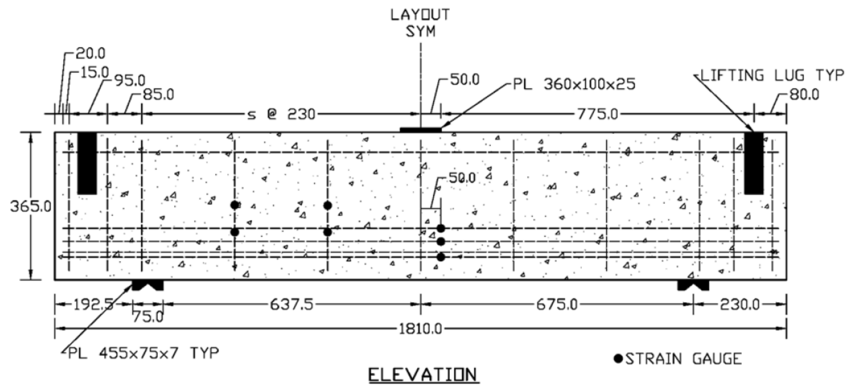


(a)

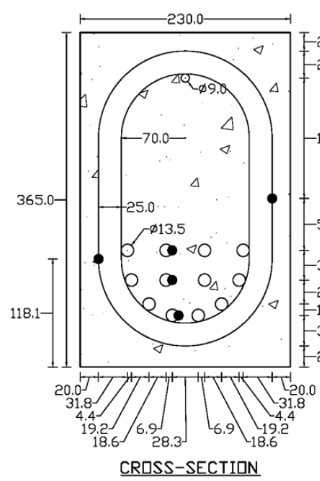


(b)

Figure B.4: Beam Details for BM 12-s230

# BM 16-INF

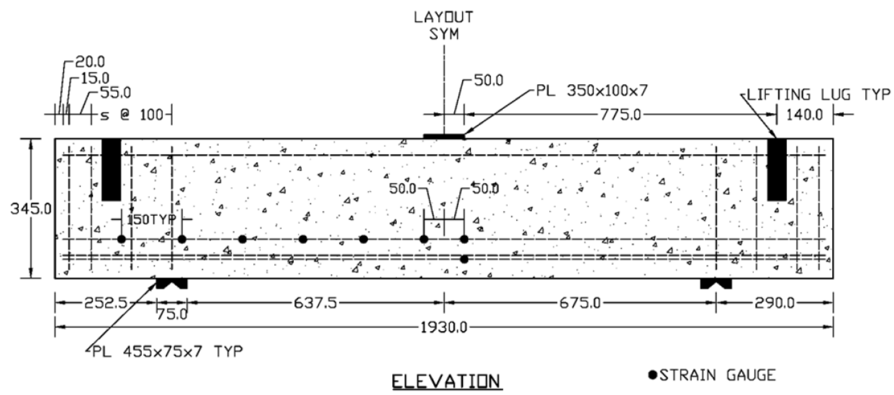


(a)

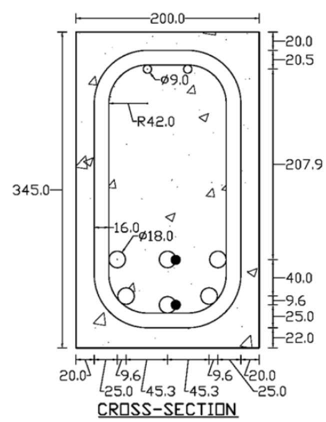


(b)

Figure B.5: Beam Details for BM 16-INF

# BM 16-150

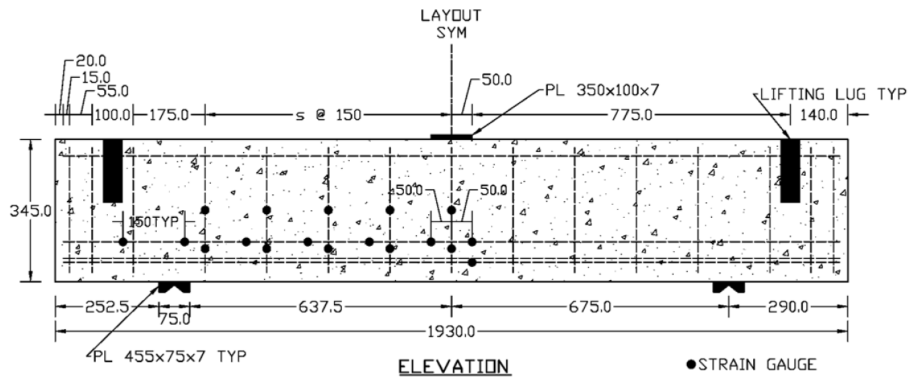


(a)

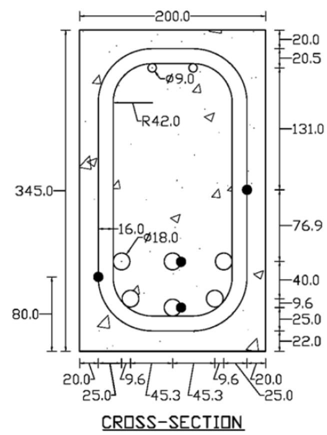


(b)

Figure B.6: Beam Details for BM 16-150

# BM 16-220

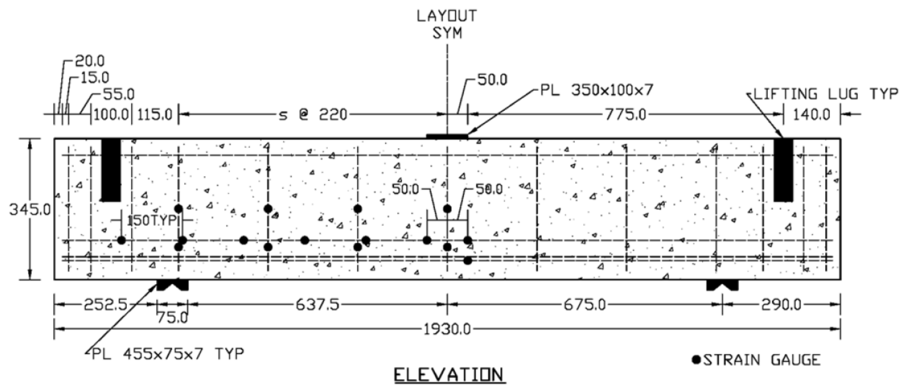


(a)

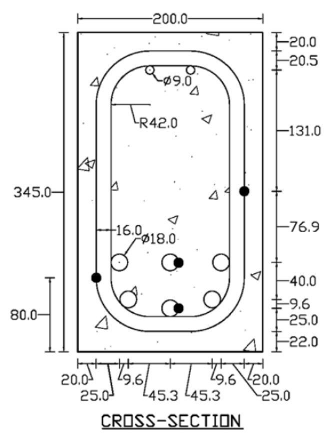


(b)

Figure B.7: Beam Details for BM 16-220

# BM 16-s230

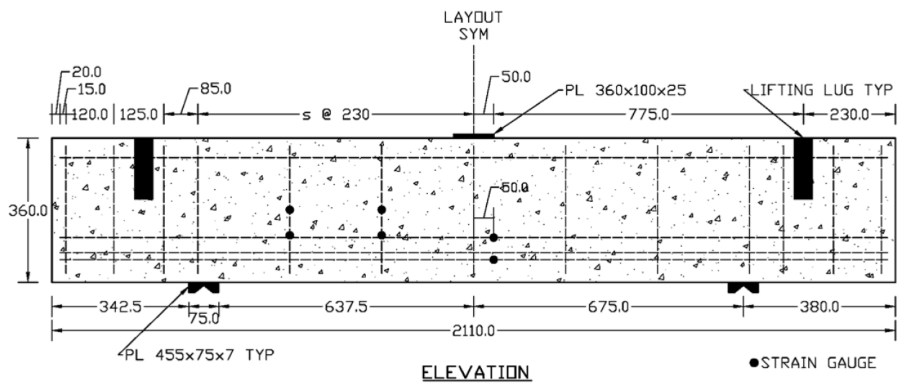


(a)

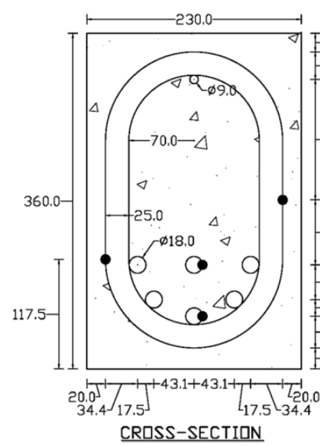


(b)

Figure B.8: Beam Details for BM 16-s230

# BM 25-INF

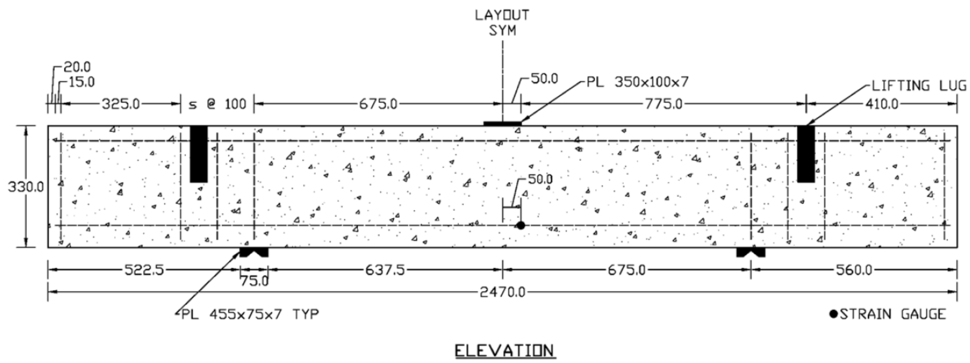


(a)

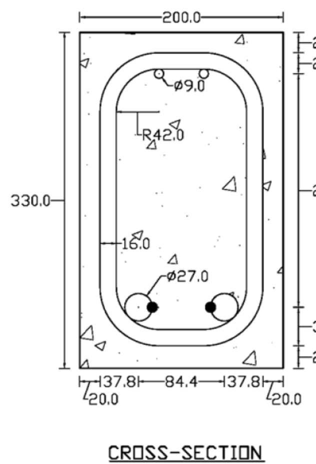


(b)

Figure B.9: Beam Details for BM 25-INF

# BM 25-150

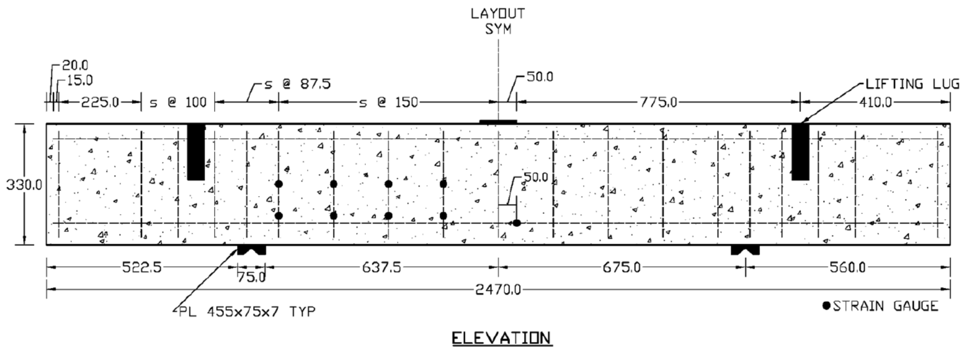


(a)

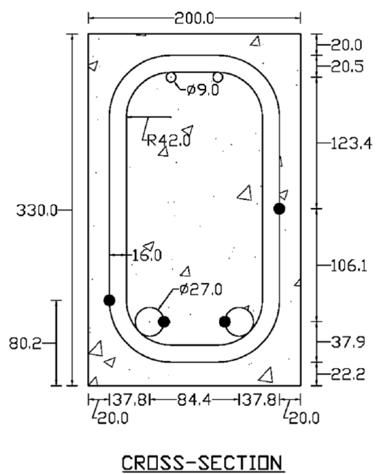


(b)

Figure B.10: Beam Details for BM 25-150

# BM 25-220

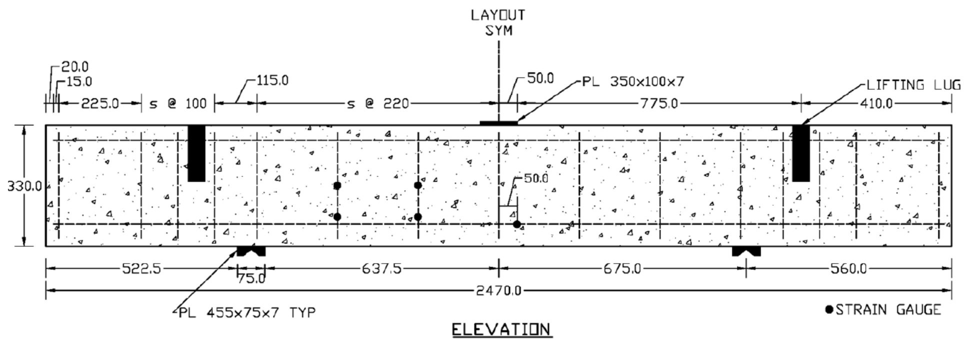


(a)

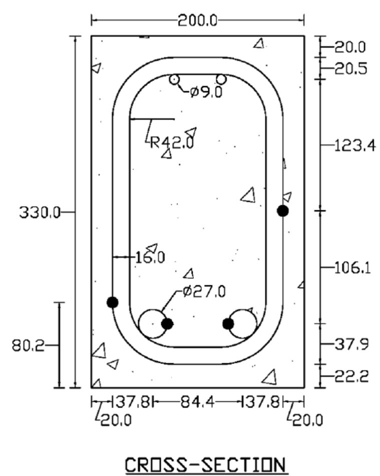


(b)

Figure B.11: Beam Details for BM 25-220

# BM 25-s230

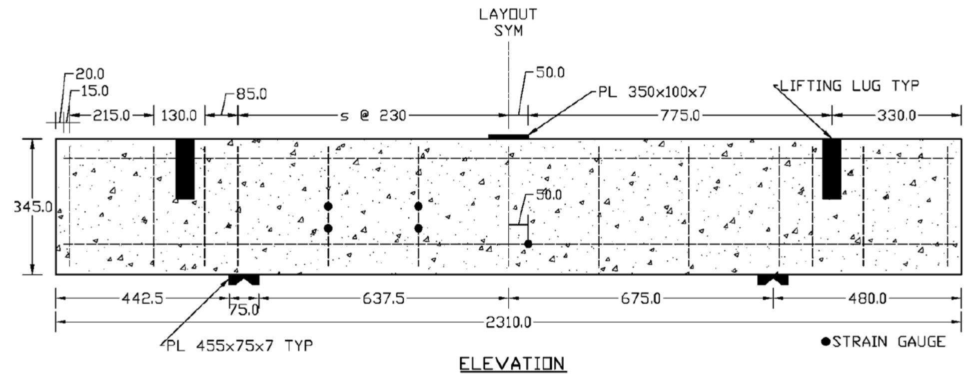


(a)

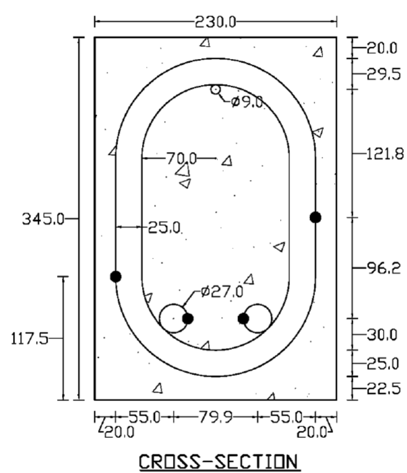


(b)

Figure B.12: Beam Details for BM 25-s230

# Appendix C

# Results for Beams without Stirrups

This Appendix presents the results of the parametric FEM analysis conducted on beams without stirrups. The results displayed are for slenderness ratios ranging from 1.5 to 12.5. Table C.1 summarizes the material properties used in these analyses.

Table C.1: Summary of ABAQUS Modelling Parameters Used

| **Concrete** | |
|---|---|
| Damage Model: | Concrete Damaged Plasticity (Tension, Compression) |
| Compression Model: | Modified Hognestad Parabola |
| Tension Model: | Bilinear Stress-Displacement |
| Fracture Energy ($G_f$): | 90 N/m |
| Dilation Angle: | 30°, 50° |
| $E_c$: | 37583 MPa |
| Poisson's Ratio ($\nu$): | 0.2 |
| $\sigma_{bo}/\sigma_{co}$: | 1.16 |
| Eccentricity ($\epsilon$): | 0.1 |
| $K_c$: | 2/3 |
| Viscosity ($\mu$): | 0.0001 |
| Element Type: | C3D8R |
| Element Size: | 30 mm |
| **Longitudinal Reinforcement** | |
| $E_f$: | 63500 MPa |
| Poisson's Ratio ($\nu$): | 0.3 |
| Element Type: | T3D2 |
| Element Size: | 30 mm |

# BM 12-INF

## 30° Dilation Angle

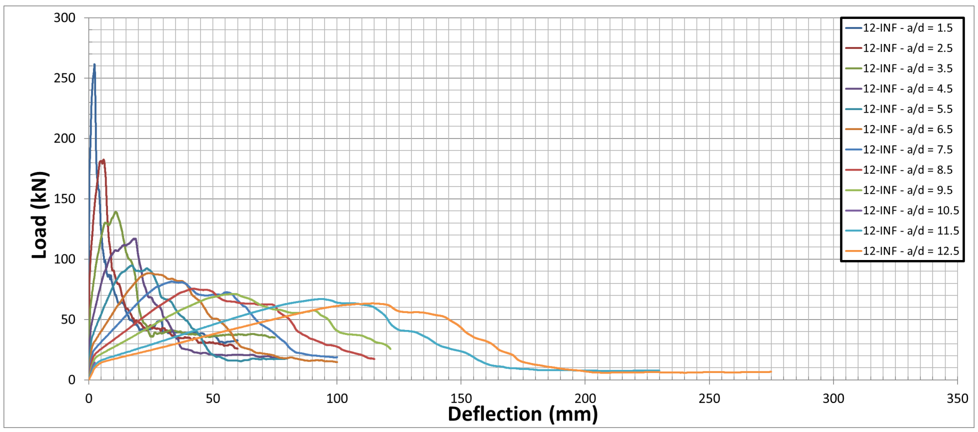


Figure C.1: Mid-Span Load-Deflection Curves for BM 12-INF Series, 30° Dilation

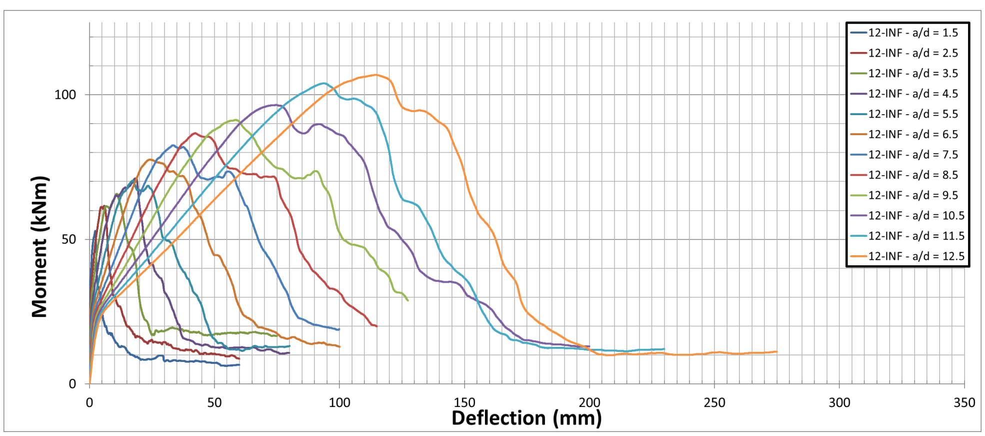


Figure C.2: Mid-Span Moment-Deflection Curves for BM 12-INF Series, 30° Dilation

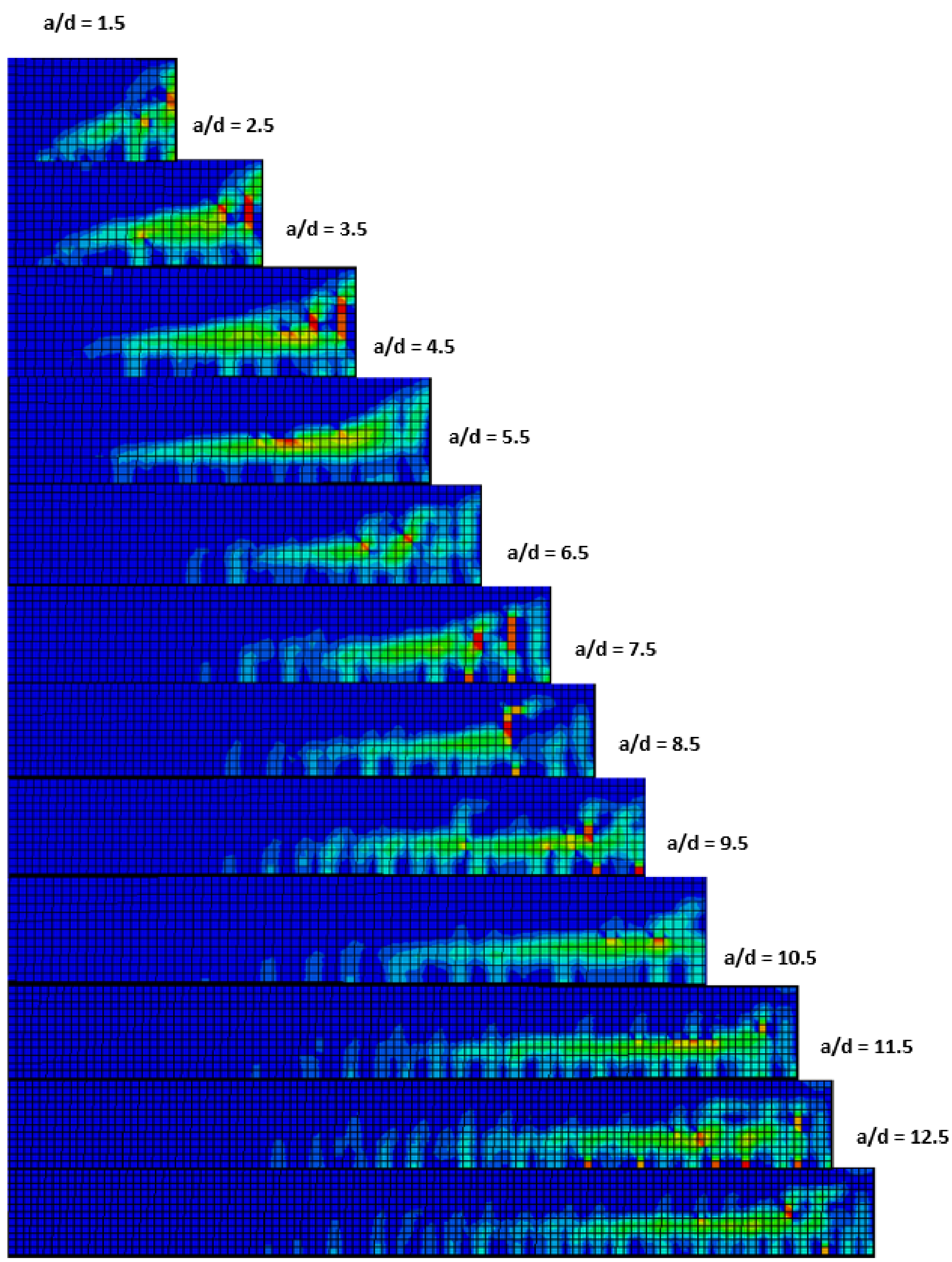


Figure C.3: Crack Patterns at Failure for BM 12-INF Series, 30° Dilation

Table C.2: Comparison of Ultimate Loads for BM 12-INF

| $a/d$ | ABAQUS (30°, KN) | CSA (Flexure, KN) | ACI (Flexure, KN) |
|---|---|---|---|
| 1.5 | 261 | 724 | 653 |
| 2.5 | 182 | 435 | 392 |
| 3.5 | 139 | 311 | 280 |
| 4.5 | 117 | 242 | 218 |
| 5.5 | 95 | 198 | 178 |
| 6.5 | 88 | 167 | 151 |
| 7.5 | 81 | 145 | 131 |
| 8.5 | 76 | 128 | 115 |
| 9.5 | 71 | 114 | 103 |
| 10.5 | 68 | 104 | 93 |
| 11.5 | 67 | 95 | 85 |
| 12.5 | 63 | 87 | 78 |

Table C.3: Comparison of Ultimate Loads for BM 12-INF

| $a/d$ | ABAQUS (30°, KN) | CSA (Shear, KN) | ACI (Shear, KN) | JSCE (Shear, KN) | Nehdi (2007) (Shear, KN) | ISIS Canada (Shear, KN) |
|---|---|---|---|---|---|---|
| 1.5 | 261 | 167 | 82 | 100 | 287 | 91 |
| 2.5 | 182 | 155 | 82 | 100 | 153 | 91 |
| 3.5 | 139 | 131 | 82 | 100 | 142 | 91 |
| 4.5 | 117 | 115 | 82 | 100 | 134 | 91 |
| 5.5 | 95 | 105 | 82 | 100 | 128 | 91 |
| 6.5 | 88 | 96 | 82 | 100 | 123 | 91 |
| 7.5 | 81 | 90 | 82 | 100 | 119 | 91 |
| 8.5 | 76 | 84 | 82 | 100 | 115 | 91 |
| 9.5 | 71 | 83 | 82 | 100 | 112 | 91 |
| 10.5 | 68 | 83 | 82 | 100 | 110 | 91 |
| 11.5 | 67 | 83 | 82 | 100 | 108 | 91 |
| 12.5 | 63 | 83 | 82 | 100 | 106 | 91 |

## 50° Dilation Angle

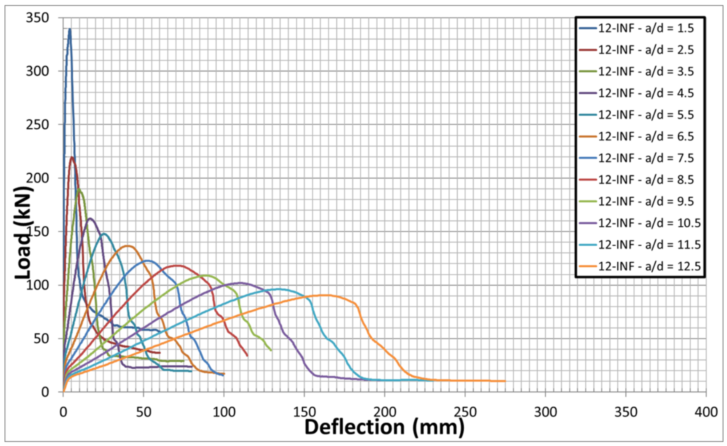


Figure C.4: Mid-Span Load-Deflection Curves for BM 12-INF Series, 50° Dilation

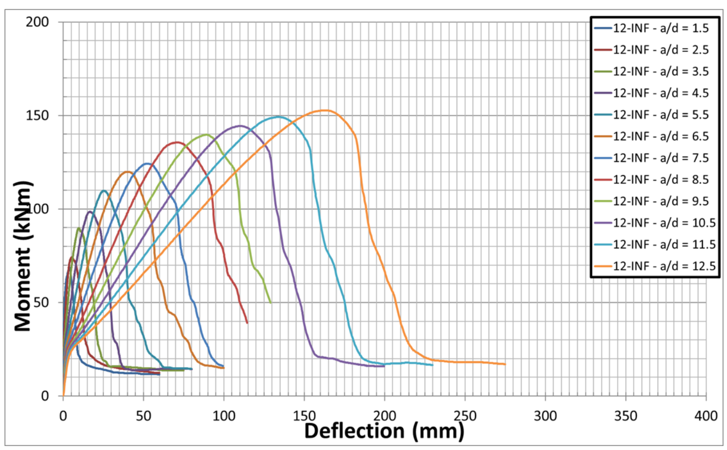


Figure C.5: Mid-Span Moment-Deflection Curves for BM 12-INF Series, 50° Dilation

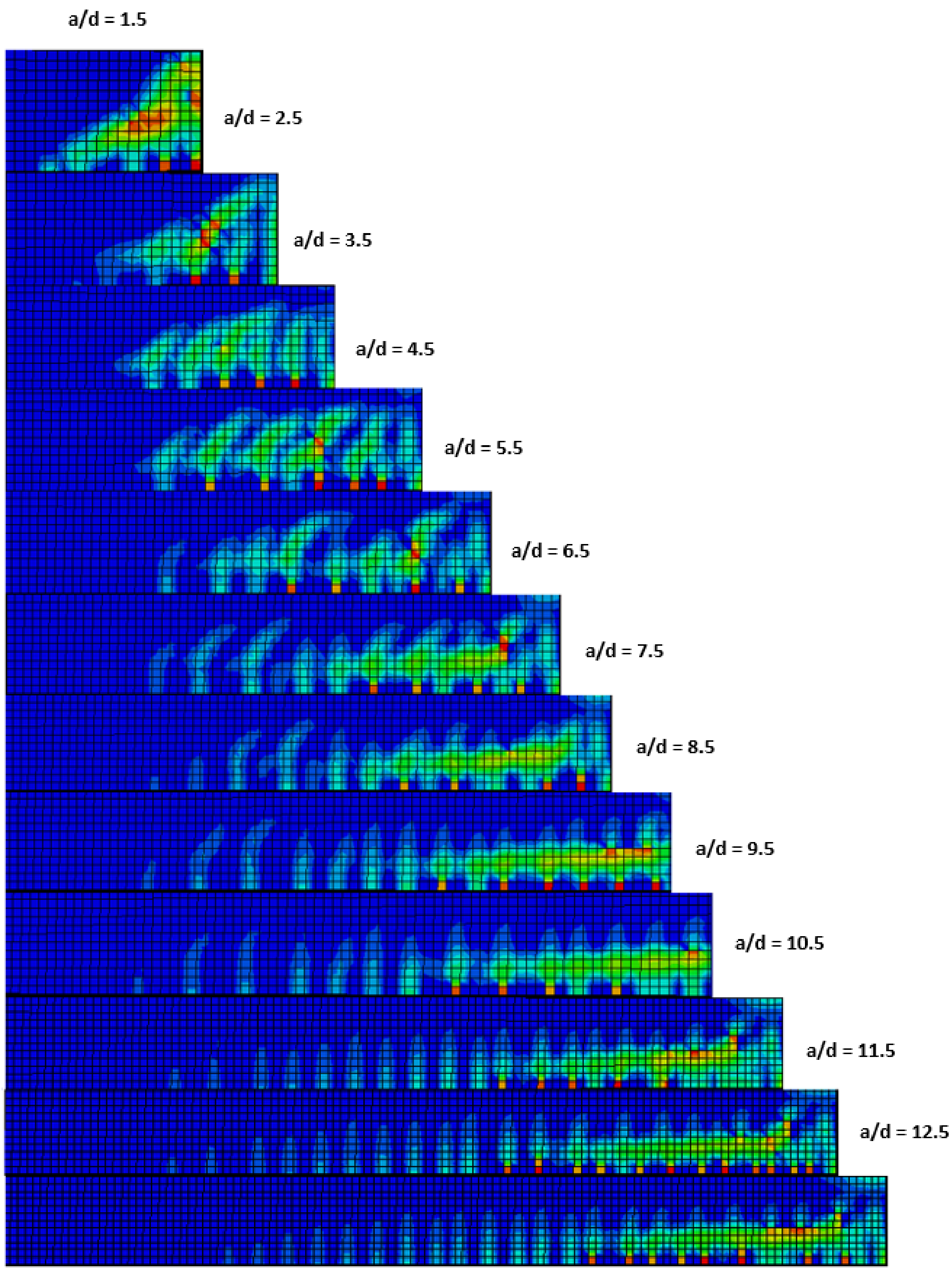


Figure C.6: Crack Patterns at Failure for BM 12-INF Series, 50° Dilation

Table C.4: Comparison of Ultimate Loads for BM 12-INF

| $a/d$ | ABAQUS (50°, KN) | CSA (Flexure, KN) | ACI (Flexure, KN) |
|---|---|---|---|
| 1.5 | 339 | 724 | 653 |
| 2.5 | 220 | 435 | 392 |
| 3.5 | 190 | 311 | 280 |
| 4.5 | 162 | 242 | 218 |
| 5.5 | 148 | 198 | 178 |
| 6.5 | 137 | 167 | 151 |
| 7.5 | 123 | 145 | 131 |
| 8.5 | 118 | 128 | 115 |
| 9.5 | 109 | 114 | 103 |
| 10.5 | 102 | 104 | 93 |
| 11.5 | 96 | 95 | 85 |
| 12.5 | 90 | 87 | 78 |

Table C.5: Comparison of Ultimate Loads for BM 12-INF

| $a/d$ | ABAQUS (50°, KN) | CSA (Shear, KN) | ACI (Shear, KN) | JSCE (Shear, KN) | Nehdi (2007) (Shear, KN) | ISIS Canada (Shear, KN) |
|---|---|---|---|---|---|---|
| 1.5 | 339 | 167 | 82 | 100 | 287 | 91 |
| 2.5 | 220 | 155 | 82 | 100 | 153 | 91 |
| 3.5 | 190 | 131 | 82 | 100 | 142 | 91 |
| 4.5 | 162 | 115 | 82 | 100 | 134 | 91 |
| 5.5 | 148 | 105 | 82 | 100 | 128 | 91 |
| 6.5 | 137 | 96 | 82 | 100 | 123 | 91 |
| 7.5 | 123 | 90 | 82 | 100 | 119 | 91 |
| 8.5 | 118 | 84 | 82 | 100 | 115 | 91 |
| 9.5 | 109 | 83 | 82 | 100 | 112 | 91 |
| 10.5 | 102 | 83 | 82 | 100 | 110 | 91 |
| 11.5 | 96 | 83 | 82 | 100 | 108 | 91 |
| 12.5 | 90 | 83 | 82 | 100 | 106 | 91 |

# BM 16-INF

## 30° Dilation Angle

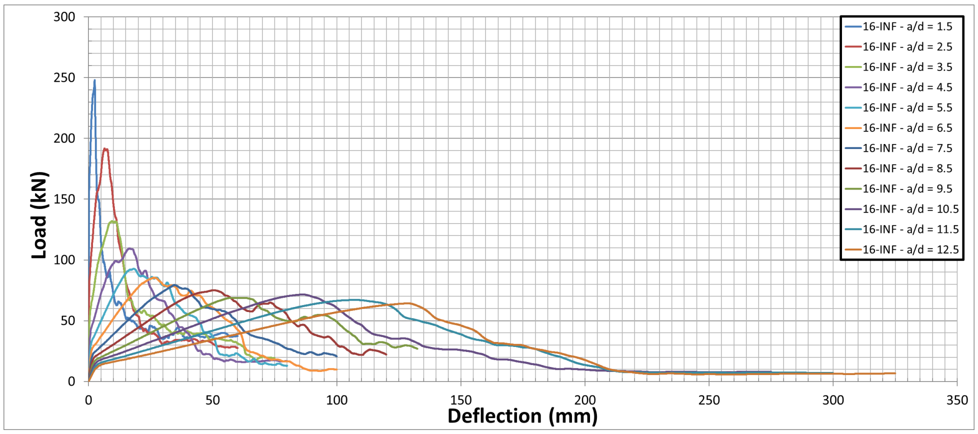


Figure C.7: Mid-Span Load-Deflection Curves for BM 16-INF Series, 30° Dilation

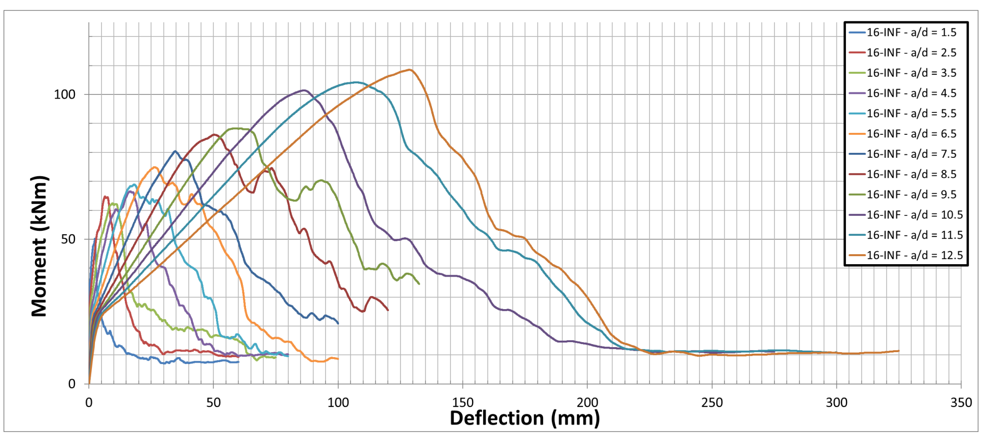


Figure C.8: Mid-Span Moment-Deflection Curves for BM 16-INF Series, 30° Dilation

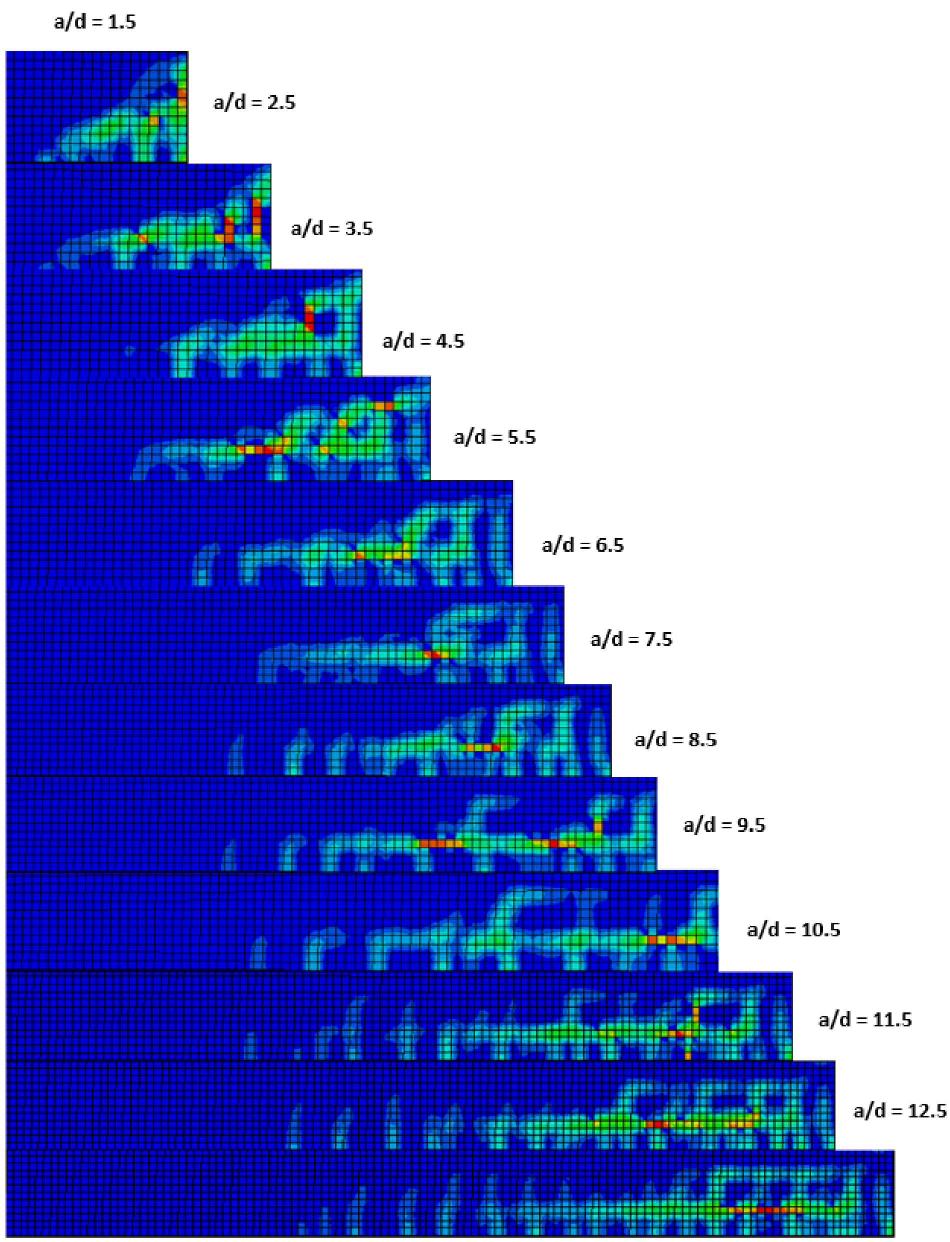


Figure C.9: Crack Patterns at Failure for BM 16-INF Series, 30° Dilation

Table C.6: Comparison of Ultimate Loads for BM 16-INF

| $a/d$ | ABAQUS (30°, KN) | CSA (Flexure, KN) | ACI (Flexure, KN) |
|---|---|---|---|
| 1.5 | 248 | 696 | 628 |
| 2.5 | 142 | 417 | 377 |
| 3.5 | 132 | 298 | 269 |
| 4.5 | 110 | 232 | 209 |
| 5.5 | 93 | 190 | 171 |
| 6.5 | 85 | 161 | 145 |
| 7.5 | 79 | 139 | 126 |
| 8.5 | 75 | 123 | 111 |
| 9.5 | 69 | 110 | 99 |
| 10.5 | 72 | 99 | 90 |
| 11.5 | 67 | 91 | 82 |
| 12.5 | 64 | 83 | 75 |

Table C.7: Comparison of Ultimate Loads for BM 16-INF

| $a/d$ | ABAQUS (30°, KN) | CSA (Shear, KN) | ACI (Shear, KN) | JSCE (Shear, KN) | Nehdi (2007) (Shear, KN) | ISIS Canada (Shear, KN) |
|---|---|---|---|---|---|---|
| 1.5 | 248 | 164 | 78 | 96 | 279 | 91 |
| 2.5 | 142 | 147 | 78 | 96 | 149 | 91 |
| 3.5 | 132 | 125 | 78 | 96 | 138 | 91 |
| 4.5 | 110 | 110 | 78 | 96 | 130 | 91 |
| 5.5 | 93 | 99 | 78 | 96 | 124 | 91 |
| 6.5 | 85 | 91 | 78 | 96 | 119 | 91 |
| 7.5 | 79 | 85 | 78 | 96 | 116 | 91 |
| 8.5 | 75 | 82 | 78 | 96 | 112 | 91 |
| 9.5 | 69 | 82 | 78 | 96 | 109 | 91 |
| 10.5 | 72 | 82 | 78 | 96 | 107 | 91 |
| 11.5 | 67 | 82 | 78 | 96 | 105 | 91 |
| 12.5 | 64 | 82 | 78 | 96 | 103 | 91 |

## 50° Dilation Angle

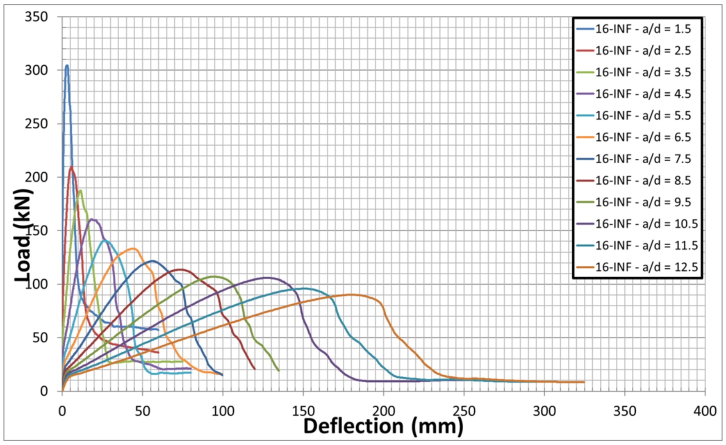


Figure C.10: Mid-Span Load-Deflection Curves for BM 16-INF Series, 50° Dilation

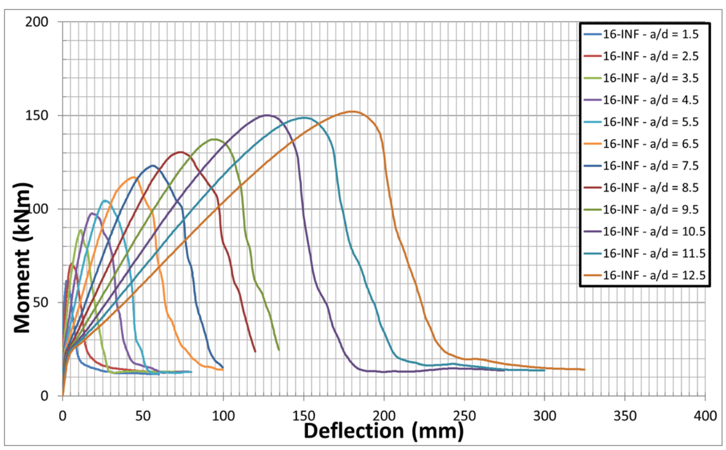


Figure C.11: Mid-Span Moment-Deflection Curves for BM 16-INF Series, 50° Dilation

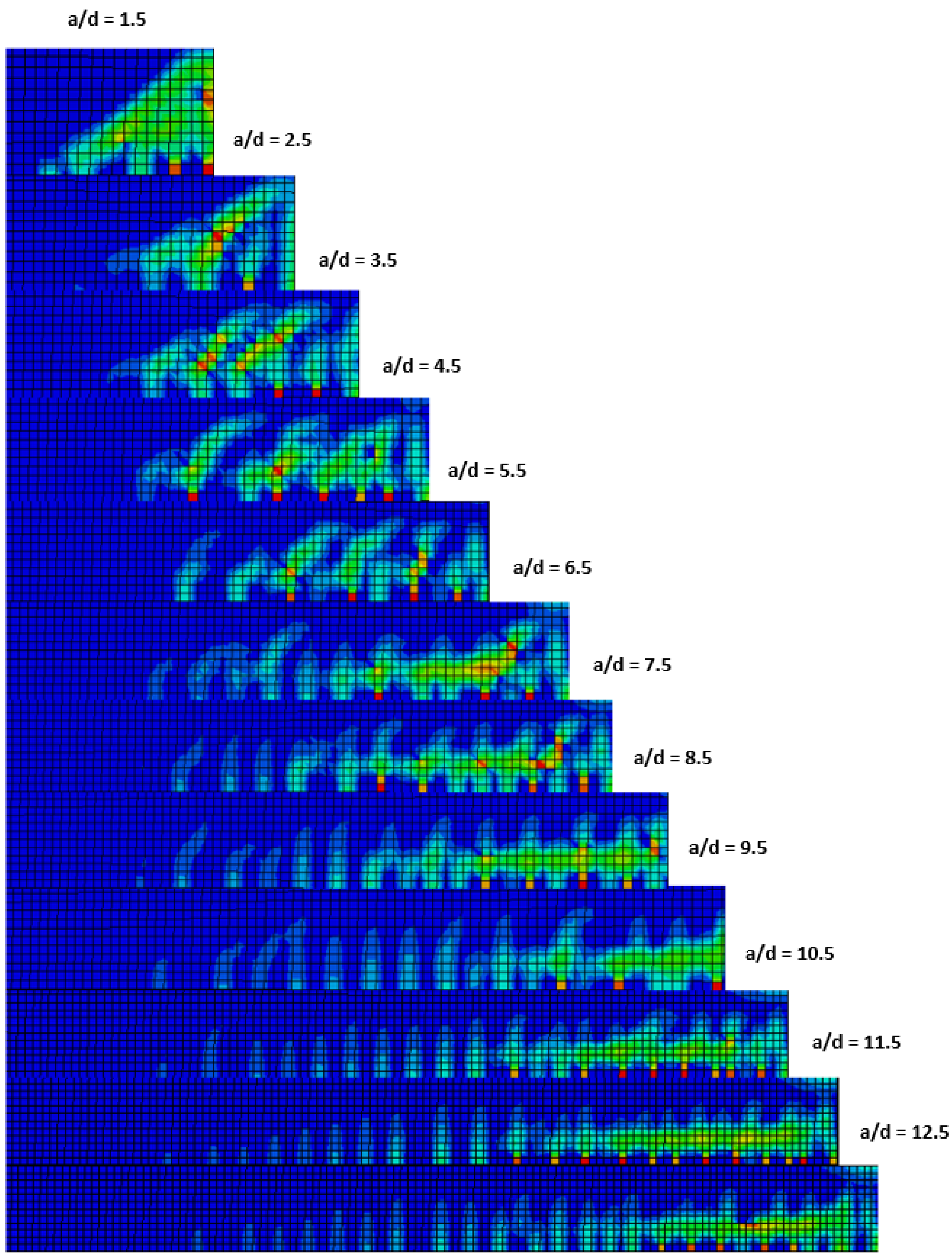


Figure C.12: Crack Patterns at Failure for BM 16-INF Series, 50° Dilation

Table C.8: Comparison of Ultimate Loads for BM 16-INF

| $a/d$ | ABAQUS (50°, KN) | CSA (Flexure, KN) | ACI (Flexure, KN) |
|---|---|---|---|
| 1.5 | 304 | 696 | 628 |
| 2.5 | 210 | 417 | 377 |
| 3.5 | 188 | 298 | 269 |
| 4.5 | 161 | 232 | 209 |
| 5.5 | 141 | 190 | 171 |
| 6.5 | 133 | 161 | 145 |
| 7.5 | 122 | 139 | 126 |
| 8.5 | 114 | 123 | 111 |
| 9.5 | 107 | 110 | 99 |
| 10.5 | 106 | 99 | 90 |
| 11.5 | 96 | 91 | 82 |
| 12.5 | 90 | 83 | 75 |

Table C.9: Comparison of Ultimate Loads for BM 16-INF

| $a/d$ | ABAQUS (50°, KN) | CSA (Shear, KN) | ACI (Shear, KN) | JSCE (Shear, KN) | Nehdi (2007) (Shear, KN) | ISIS Canada (Shear, KN) |
|---|---|---|---|---|---|---|
| 1.5 | 304 | 164 | 78 | 96 | 279 | 91 |
| 2.5 | 210 | 147 | 78 | 96 | 149 | 91 |
| 3.5 | 188 | 125 | 78 | 96 | 138 | 91 |
| 4.5 | 161 | 110 | 78 | 96 | 130 | 91 |
| 5.5 | 141 | 99 | 78 | 96 | 124 | 91 |
| 6.5 | 133 | 91 | 78 | 96 | 119 | 91 |
| 7.5 | 122 | 85 | 78 | 96 | 116 | 91 |
| 8.5 | 114 | 82 | 78 | 96 | 112 | 91 |
| 9.5 | 107 | 82 | 78 | 96 | 109 | 91 |
| 10.5 | 106 | 82 | 78 | 96 | 107 | 91 |
| 11.5 | 96 | 82 | 78 | 96 | 105 | 91 |
| 12.5 | 90 | 82 | 78 | 96 | 103 | 91 |

# BM 25-INF

## 30° Dilation Angle

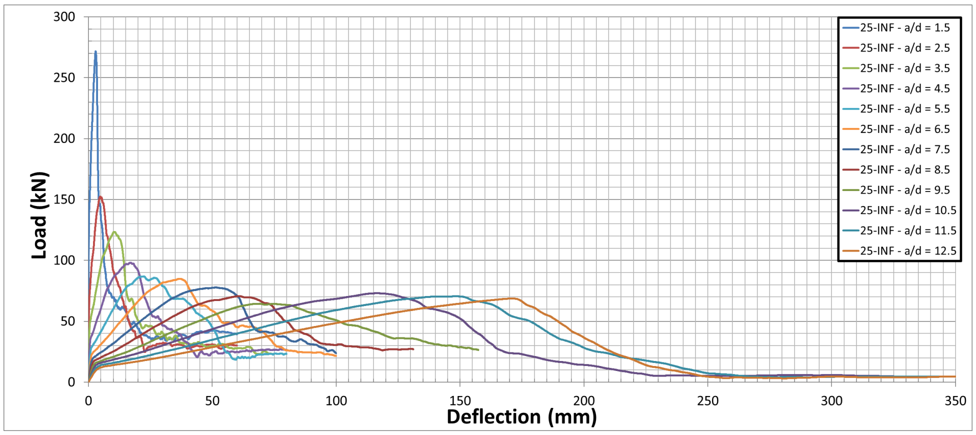


Figure C.13: Mid-Span Load-Deflection Curves for BM 25-INF Series, 30° Dilation

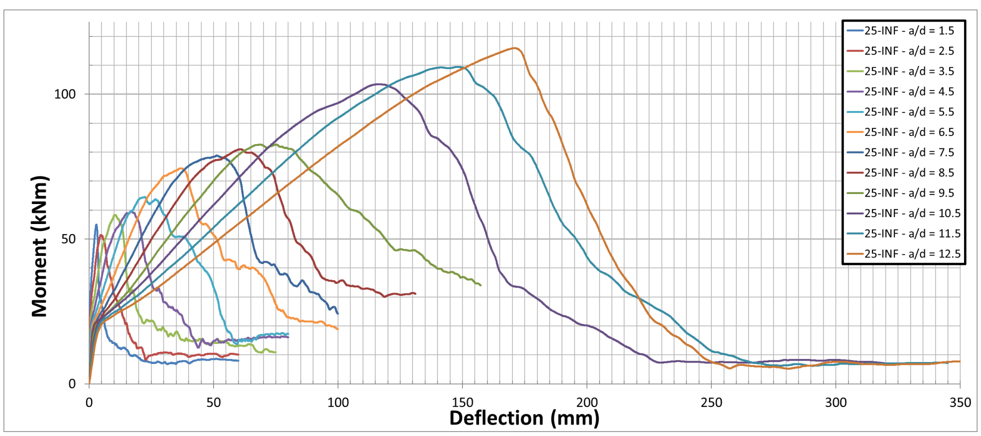


Figure C.14: Mid-Span Moment-Deflection Curves for BM 25-INF Series, 30° Dilation

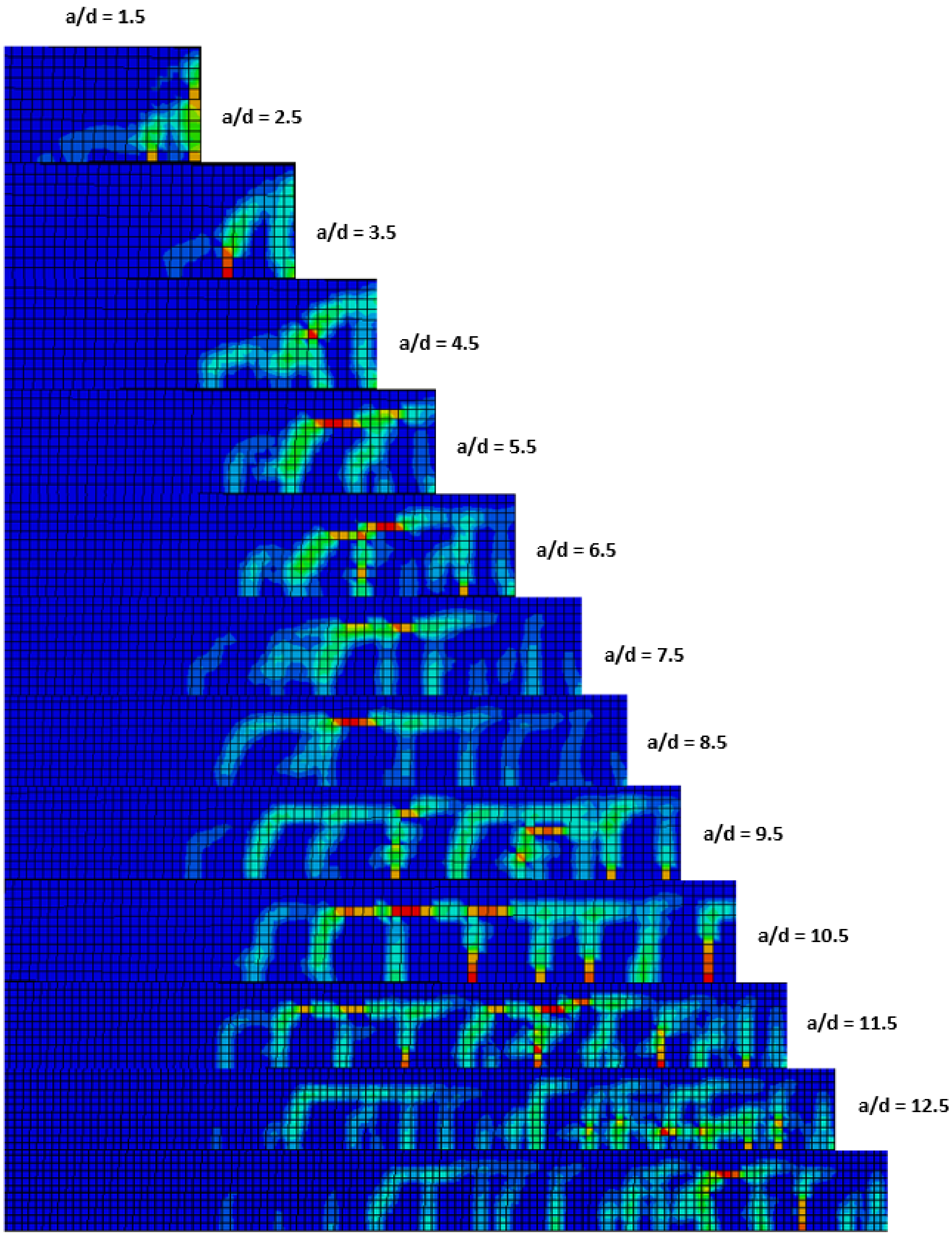


Figure C.15: Crack Patterns at Failure for BM 25-INF Series, 30° Dilation

Table C.10: Comparison of Ultimate Loads for BM 25-INF

| $a/d$ | ABAQUS (30°, KN) | CSA (Flexure, KN) | ACI (Flexure, KN) |
|---|---|---|---|
| 1.5 | 272 | 647 | 587 |
| 2.5 | 152 | 388 | 352 |
| 3.5 | 123 | 277 | 251 |
| 4.5 | 98 | 216 | 196 |
| 5.5 | 87 | 176 | 160 |
| 6.5 | 85 | 149 | 135 |
| 7.5 | 78 | 129 | 117 |
| 8.5 | 71 | 114 | 104 |
| 9.5 | 64 | 102 | 93 |
| 10.5 | 73 | 92 | 84 |
| 11.5 | 70 | 84 | 77 |
| 12.5 | 69 | 78 | 70 |

Table C.11: Comparison of Ultimate Loads for BM 25-INF

| $a/d$ | ABAQUS (30°, KN) | CSA (Shear, KN) | ACI (Shear, KN) | JSCE (Shear, KN) | Nehdi (2007) (Shear, KN) | ISIS Canada (Shear, KN) |
|---|---|---|---|---|---|---|
| 1.5 | 272 | 161 | 71 | 90 | 266 | 91 |
| 2.5 | 152 | 136 | 71 | 90 | 142 | 91 |
| 3.5 | 123 | 115 | 71 | 90 | 131 | 91 |
| 4.5 | 98 | 101 | 71 | 90 | 124 | 91 |
| 5.5 | 87 | 91 | 71 | 90 | 118 | 91 |
| 6.5 | 85 | 84 | 71 | 90 | 114 | 91 |
| 7.5 | 78 | 80 | 71 | 90 | 110 | 91 |
| 8.5 | 71 | 80 | 71 | 90 | 107 | 91 |
| 9.5 | 64 | 80 | 71 | 90 | 104 | 91 |
| 10.5 | 73 | 80 | 71 | 90 | 102 | 91 |
| 11.5 | 70 | 80 | 71 | 90 | 100 | 91 |
| 12.5 | 69 | 80 | 71 | 90 | 98 | 91 |

## 50° Dilation Angle

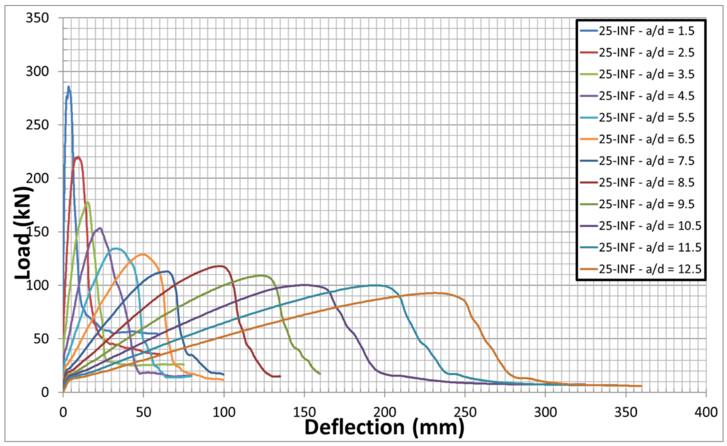


Figure C.16: Mid-Span Load-Deflection Curves for BM 25-INF Series, 50° Dilation

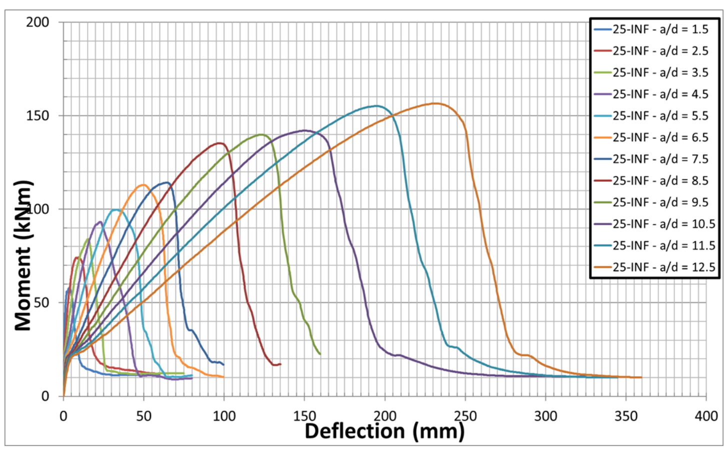


Figure C.17: Mid-Span Moment-Deflection Curves for BM 25-INF Series, 50° Dilation

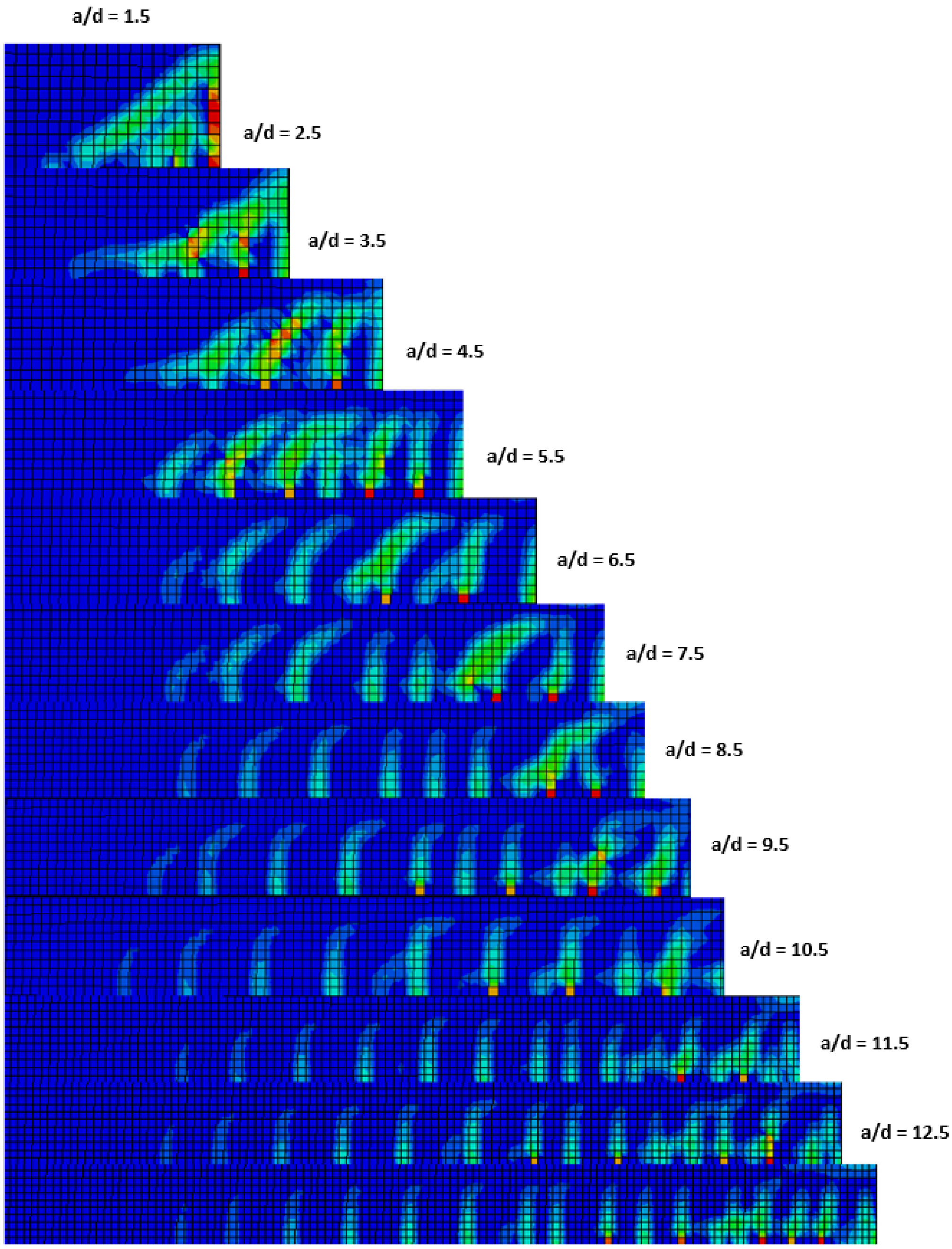


Figure C.18: Crack Patterns at Failure for BM 25-INF Series, 50° Dilation

Table C.12: Comparison of Ultimate Loads for BM 25-INF

| $a/d$ | ABAQUS (50°, KN) | CSA (Flexure, KN) | ACI (Flexure, KN) |
|---|---|---|---|
| 1.5 | 286 | 647 | 587 |
| 2.5 | 220 | 388 | 352 |
| 3.5 | 178 | 277 | 251 |
| 4.5 | 153 | 216 | 196 |
| 5.5 | 134 | 176 | 160 |
| 6.5 | 129 | 149 | 135 |
| 7.5 | 113 | 129 | 117 |
| 8.5 | 118 | 114 | 104 |
| 9.5 | 109 | 102 | 93 |
| 10.5 | 100 | 92 | 84 |
| 11.5 | 100 | 84 | 77 |
| 12.5 | 93 | 78 | 70 |

Table C.13: Comparison of Ultimate Loads for BM 25-INF

| $a/d$ | ABAQUS (50°, KN) | CSA (Shear, KN) | ACI (Shear, KN) | JSCE (Shear, KN) | Nehdi (2007) (Shear, KN) | ISIS Canada (Shear, KN) |
|---|---|---|---|---|---|---|
| 1.5 | 286 | 161 | 71 | 90 | 266 | 91 |
| 2.5 | 220 | 136 | 71 | 90 | 142 | 91 |
| 3.5 | 178 | 115 | 71 | 90 | 131 | 91 |
| 4.5 | 153 | 101 | 71 | 90 | 124 | 91 |
| 5.5 | 134 | 91 | 71 | 90 | 118 | 91 |
| 6.5 | 129 | 84 | 71 | 90 | 114 | 91 |
| 7.5 | 113 | 80 | 71 | 90 | 110 | 91 |
| 8.5 | 118 | 80 | 71 | 90 | 107 | 91 |
| 9.5 | 109 | 80 | 71 | 90 | 104 | 91 |
| 10.5 | 100 | 80 | 71 | 90 | 102 | 91 |
| 11.5 | 100 | 80 | 71 | 90 | 100 | 91 |
| 12.5 | 93 | 80 | 71 | 90 | 98 | 91 |

# Appendix D

# Results for Beams with Stirrups

This Appendix presents the results of the parametric FEM analysis conducted on beams with stirrups. The results displayed are for slenderness ratios ranging from 1.5 to 12.5. Table D.1 summarizes the material properties used in these analyses.

Table D.1: Summary of ABAQUS Modelling Parameters Used

| **Concrete** | |
|---|---|
| Damage Model: | Concrete Damaged Plasticity (Tension, Compression) |
| Compression Model: | Modified Hognestad Parabola |
| Tension Model: | Bilinear Stress-Displacement |
| Fracture Energy ($G_f$): | 90 N/m |
| Dilation Angle: | 30°, 50° |
| $E_c$: | 37583 MPa |
| Poisson's Ratio ($\nu$): | 0.2 |
| $\sigma_{bo}/\sigma_{co}$: | 1.16 |
| Eccentricity ($\epsilon$): | 0.1 |
| $K_c$: | 2/3 |
| Viscosity ($\mu$): | 0.0001 |
| Element Type: | C3D8R |
| Element Size: | 30 mm |
| **Longitudinal Reinforcement** | |
| $E_f$: | 63500 MPa |
| Poisson's Ratio ($\nu$): | 0.3 |
| Element Type: | T3D2 |
| Element Size: | 30 mm |
| **Transverse Reinforcement** | |
| $E_{f,v}$: | 50000 MPa |
| Poisson's Ratio ($\nu$): | 0.3 |
| Element Type: | M3D4R |
| Element Size: | 30 mm |

# BM 12-150

## 30° Dilation Angle

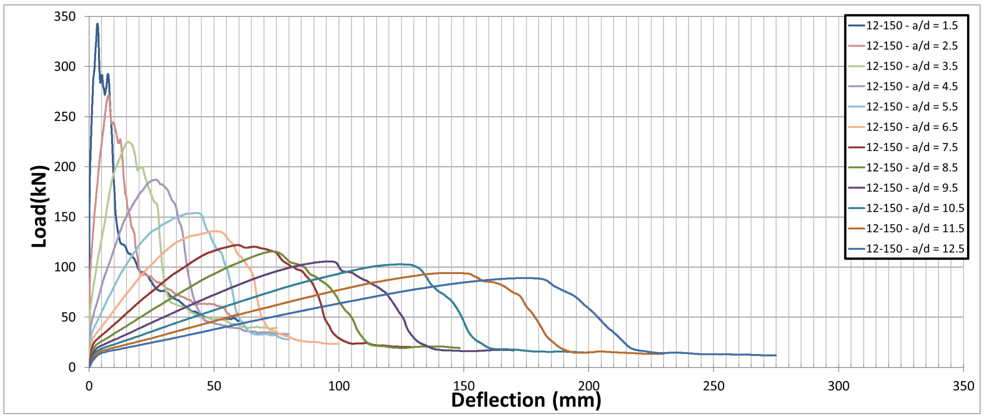


Figure D.1: Mid-Span Load-Deflection Curves for BM 12-150 Series, 30° Dilation

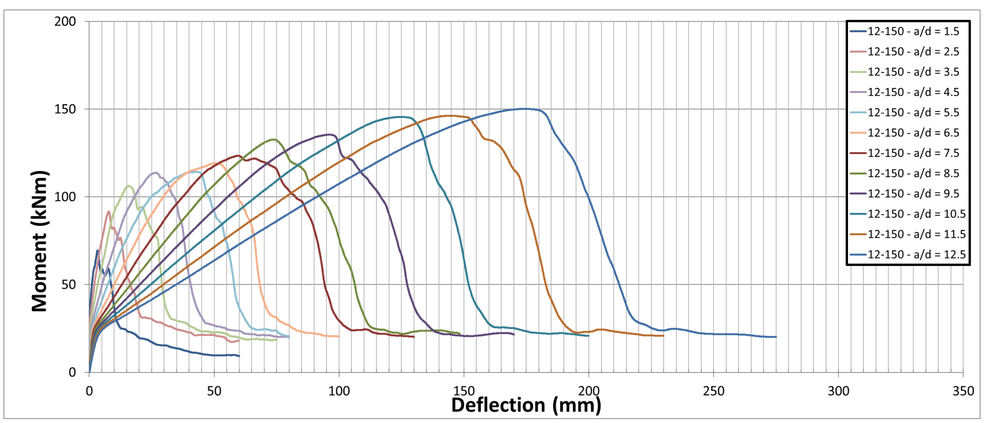


Figure D.2: Mid-Span Moment-Deflection Curves for BM 12-150 Series, 30° Dilation

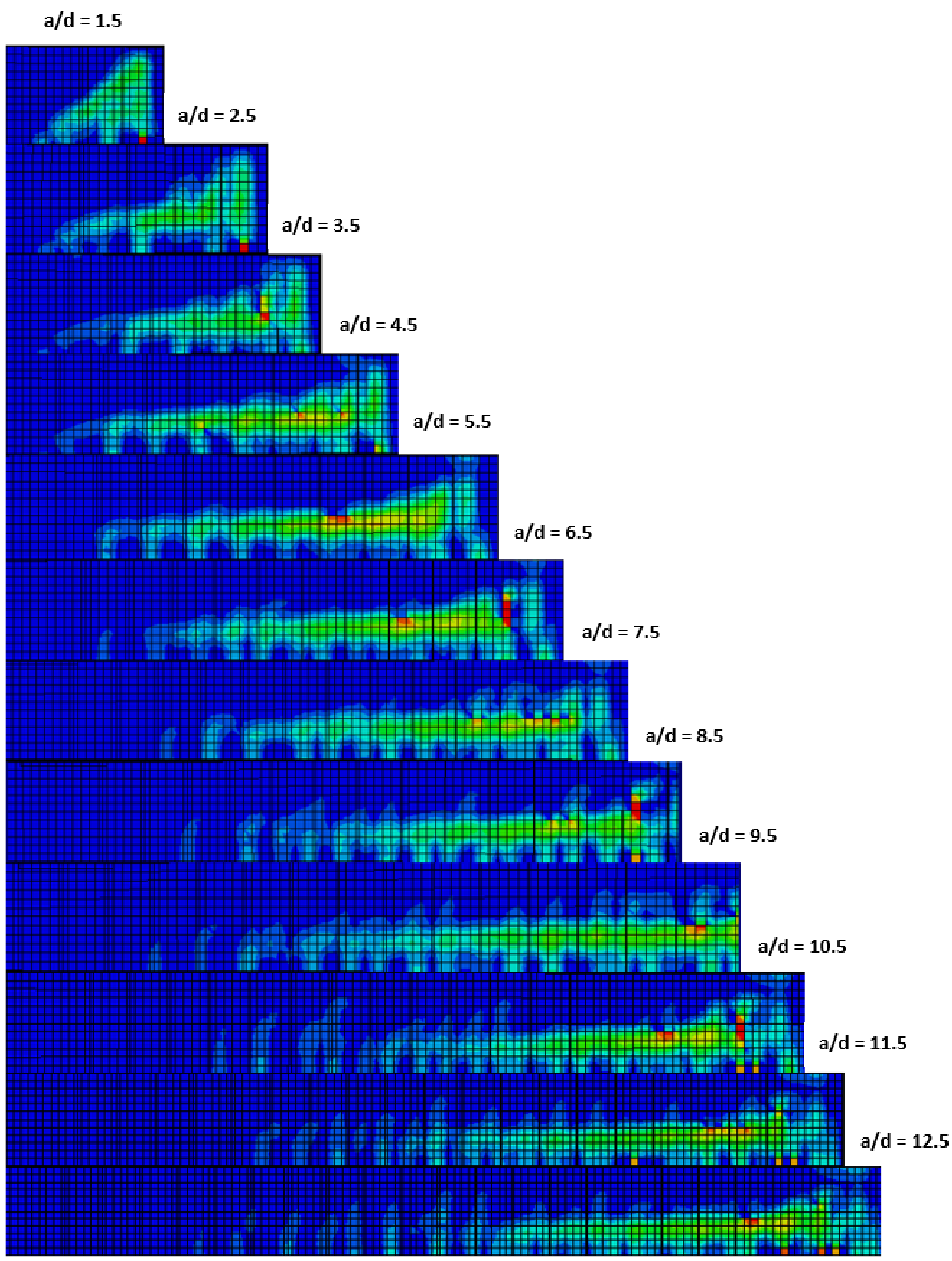


Figure D.3: Crack Patterns at Failure for BM 12-150 Series, 30° Dilation

Table D.2: Comparison of Ultimate Loads for BM 12-150

| $a/d$ | ABAQUS (30°, KN) | CSA (Flexure, KN) | ACI (Flexure, KN) |
|---|---|---|---|
| 1.5 | 343 | 725 | 643 |
| 2.5 | 271 | 435 | 386 |
| 3.5 | 225 | 311 | 276 |
| 4.5 | 187 | 242 | 214 |
| 5.5 | 154 | 198 | 175 |
| 6.5 | 136 | 167 | 148 |
| 7.5 | 122 | 145 | 129 |
| 8.5 | 116 | 128 | 114 |
| 9.5 | 106 | 114 | 102 |
| 10.5 | 103 | 104 | 92 |
| 11.5 | 94 | 95 | 84 |
| 12.5 | 89 | 87 | 77 |

Table D.3: Comparison of Ultimate Loads for BM 12-150

| $a/d$ | ABAQUS (30°, KN) | CSA (Shear, KN) | ACI (Shear, KN) | JSCE (Shear, KN) | Nehdi (2007) (Shear, KN) | ISIS Canada (Shear, KN) |
|---|---|---|---|---|---|---|
| 1.5 | 343 | 266 | 245 | 154 | 510 | 309 |
| 2.5 | 271 | 242 | 245 | 154 | 376 | 277 |
| 3.5 | 225 | 211 | 245 | 154 | 365 | 253 |
| 4.5 | 187 | 190 | 245 | 154 | 357 | 234 |
| 5.5 | 154 | 174 | 245 | 154 | 351 | 225 |
| 6.5 | 136 | 161 | 245 | 154 | 346 | 225 |
| 7.5 | 122 | 151 | 245 | 154 | 342 | 225 |
| 8.5 | 116 | 142 | 245 | 154 | 339 | 225 |
| 9.5 | 106 | 139 | 245 | 154 | 336 | 225 |
| 10.5 | 103 | 139 | 245 | 154 | 333 | 225 |
| 11.5 | 94 | 139 | 245 | 154 | 331 | 225 |
| 12.5 | 89 | 139 | 245 | 154 | 329 | 225 |

## 50° Dilation Angle

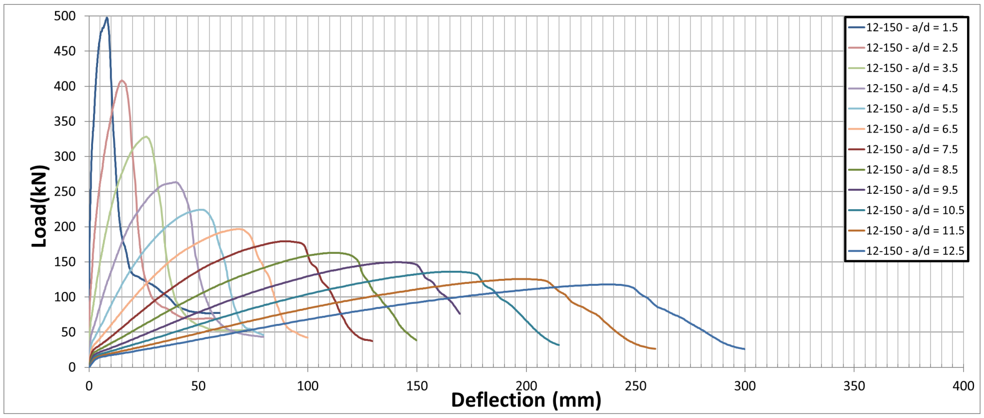


Figure D.4: Mid-Span Load-Deflection Curves for BM 12-150 Series, 50° Dilation

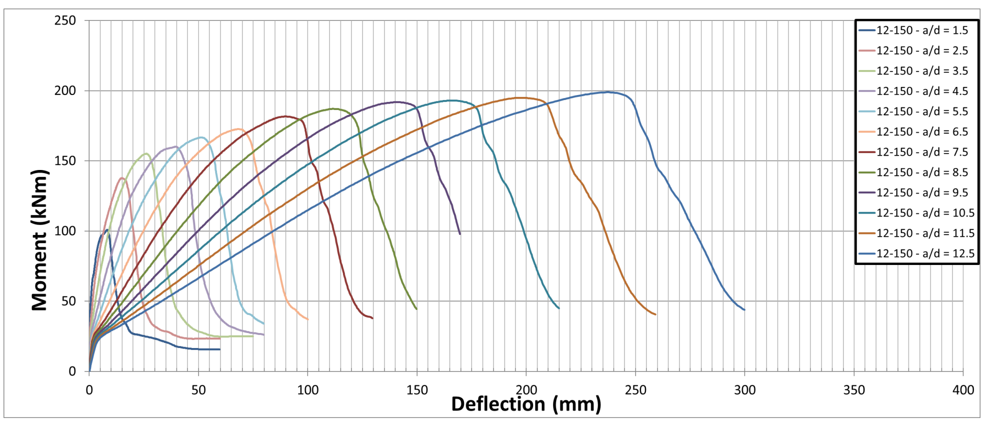


Figure D.5: Mid-Span Moment-Deflection Curves for BM 12-150 Series, 50° Dilation

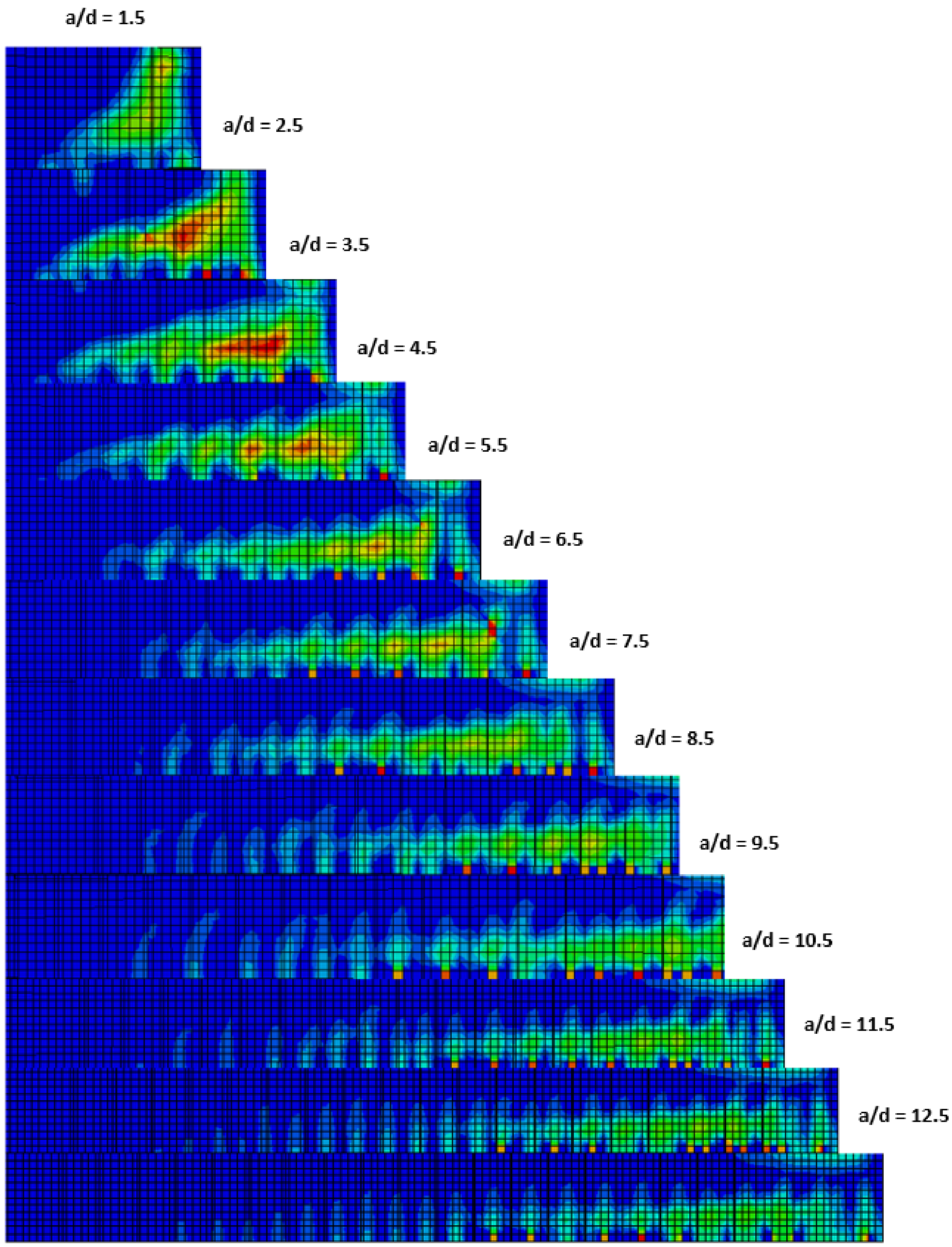


Figure D.6: Crack Patterns at Failure for BM 12-150 Series, 50° Dilation

Table D.4: Comparison of Ultimate Loads for BM 12-150

| $a/d$ | ABAQUS (50°, KN) | CSA (Flexure, KN) | ACI (Flexure, KN) |
|---|---|---|---|
| 1.5 | 498 | 725 | 643 |
| 2.5 | 385 | 435 | 386 |
| 3.5 | 328 | 311 | 276 |
| 4.5 | 263 | 242 | 214 |
| 5.5 | 224 | 198 | 175 |
| 6.5 | 197 | 167 | 148 |
| 7.5 | 179 | 145 | 129 |
| 8.5 | 163 | 128 | 114 |
| 9.5 | 150 | 114 | 102 |
| 10.5 | 136 | 104 | 92 |
| 11.5 | 126 | 95 | 84 |
| 12.5 | 118 | 87 | 77 |

Table D.5: Comparison of Ultimate Loads for BM 12-150

| $a/d$ | ABAQUS (50°, KN) | CSA (Shear, KN) | ACI (Shear, KN) | JSCE (Shear, KN) | Nehdi (2007) (Shear, KN) | ISIS Canada (Shear, KN) |
|---|---|---|---|---|---|---|
| 1.5 | 498 | 266 | 245 | 154 | 510 | 309 |
| 2.5 | 385 | 242 | 245 | 154 | 376 | 277 |
| 3.5 | 328 | 211 | 245 | 154 | 365 | 253 |
| 4.5 | 263 | 190 | 245 | 154 | 357 | 234 |
| 5.5 | 224 | 174 | 245 | 154 | 351 | 225 |
| 6.5 | 197 | 161 | 245 | 154 | 346 | 225 |
| 7.5 | 179 | 151 | 245 | 154 | 342 | 225 |
| 8.5 | 163 | 142 | 245 | 154 | 339 | 225 |
| 9.5 | 150 | 139 | 245 | 154 | 336 | 225 |
| 10.5 | 136 | 139 | 245 | 154 | 333 | 225 |
| 11.5 | 126 | 139 | 245 | 154 | 331 | 225 |
| 12.5 | 118 | 139 | 245 | 154 | 329 | 225 |

# BM 12-220

## 30° Dilation Angle

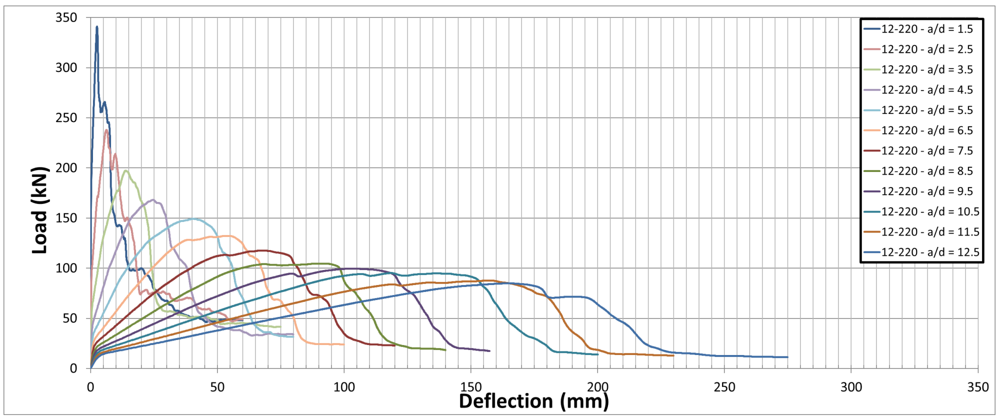


Figure D.7: Mid-Span Load-Deflection Curves for BM 12-220 Series, 30° Dilation

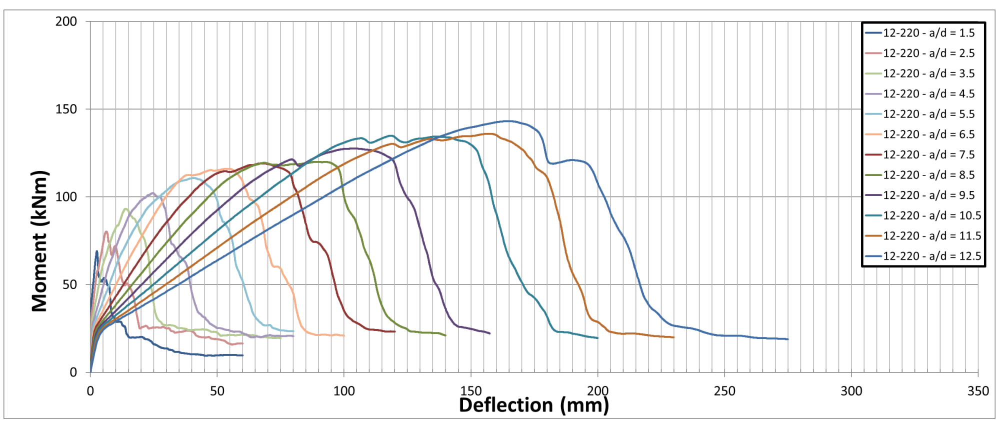


Figure D.8: Mid-Span Moment-Deflection Curves for BM 12-220 Series, 30° Dilation

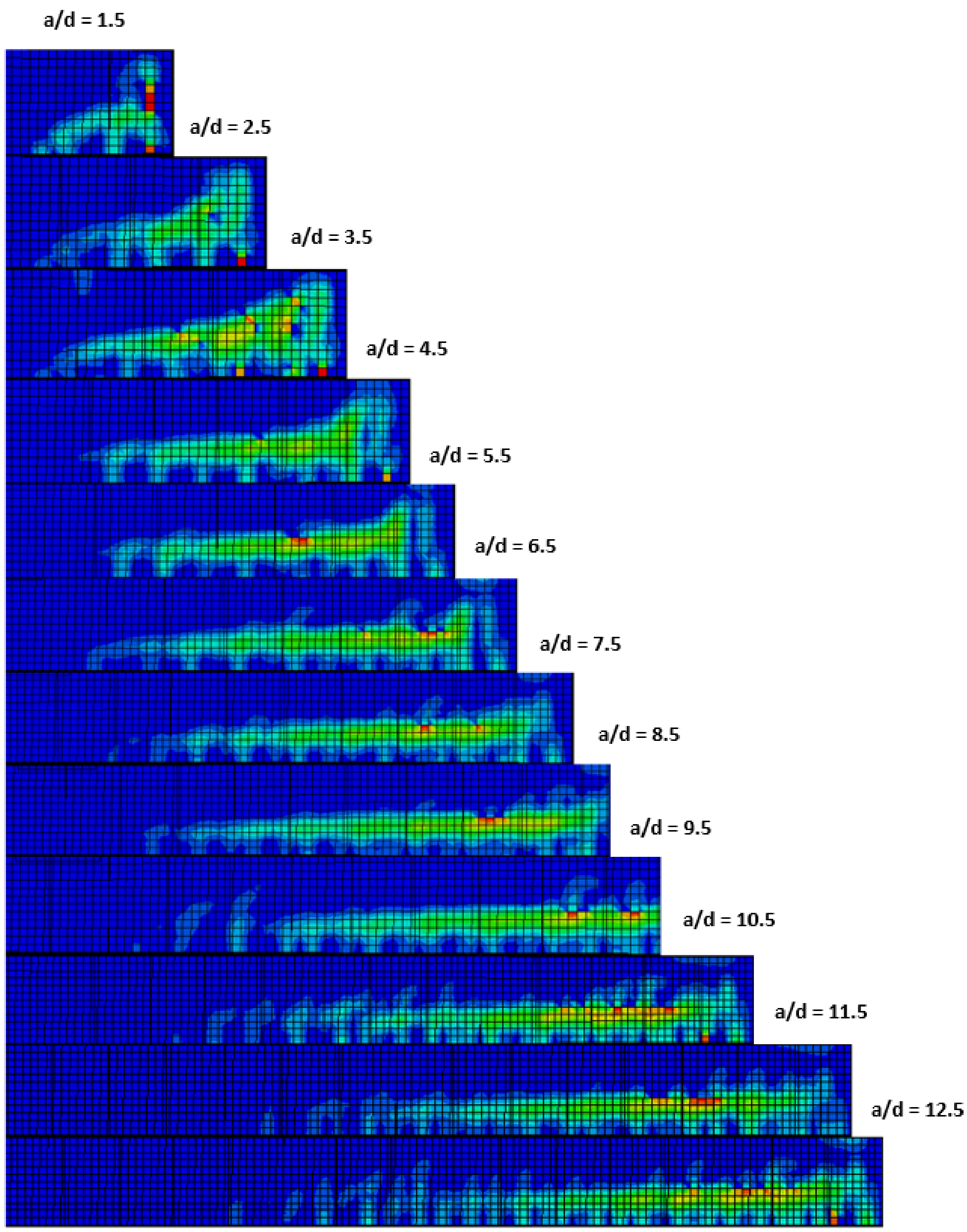


Figure D.9: Crack Patterns at Failure for BM 12-220 Series, 30° Dilation

Table D.6: Comparison of Ultimate Loads for BM 12-220 (KN)

| $a/d$ | ABAQUS (30°, KN) | CSA (Flexure, KN) | ACI (Flexure, KN) |
|---|---|---|---|
| 1.5 | 341 | 724 | 643 |
| 2.5 | 238 | 435 | 386 |
| 3.5 | 197 | 311 | 276 |
| 4.5 | 168 | 242 | 214 |
| 5.5 | 149 | 198 | 175 |
| 6.5 | 132 | 167 | 148 |
| 7.5 | 118 | 145 | 129 |
| 8.5 | 105 | 128 | 114 |
| 9.5 | 99 | 114 | 102 |
| 10.5 | 95 | 104 | 92 |
| 11.5 | 88 | 95 | 84 |
| 12.5 | 85 | 87 | 77 |

Table D.7: Comparison of Ultimate Loads for BM 12-220

| $a/d$ | ABAQUS (30°, KN) | CSA (Shear, KN) | ACI (Shear, KN) | JSCE (Shear, KN) | Nehdi (2007) (Shear, KN) | ISIS Canada (Shear, KN) |
|---|---|---|---|---|---|---|
| 1.5 | 341 | 238 | 193 | 145 | 470 | 309 |
| 2.5 | 238 | 218 | 193 | 145 | 336 | 277 |
| 3.5 | 197 | 190 | 193 | 145 | 325 | 253 |
| 4.5 | 168 | 170 | 193 | 145 | 317 | 234 |
| 5.5 | 149 | 156 | 193 | 145 | 311 | 225 |
| 6.5 | 132 | 145 | 193 | 145 | 306 | 225 |
| 7.5 | 118 | 136 | 193 | 145 | 302 | 225 |
| 8.5 | 105 | 128 | 193 | 145 | 299 | 225 |
| 9.5 | 99 | 124 | 193 | 145 | 296 | 225 |
| 10.5 | 95 | 121 | 193 | 145 | 293 | 225 |
| 11.5 | 88 | 121 | 193 | 145 | 291 | 225 |
| 12.5 | 85 | 121 | 193 | 145 | 289 | 225 |

## 50° Dilation Angle

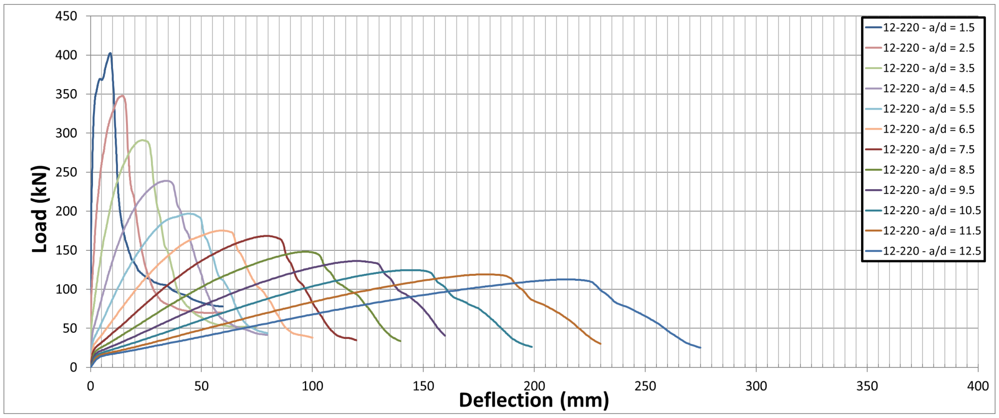


Figure D.10: Mid-Span Load-Deflection Curves for BM 12-220 Series, 50° Dilation

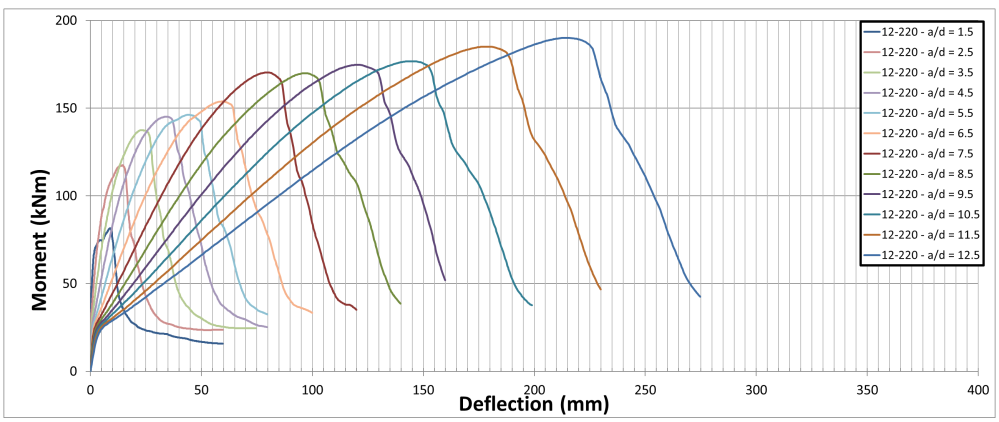


Figure D.11: Mid-Span Moment-Deflection Curves for BM 12-220 Series, 50° Dilation

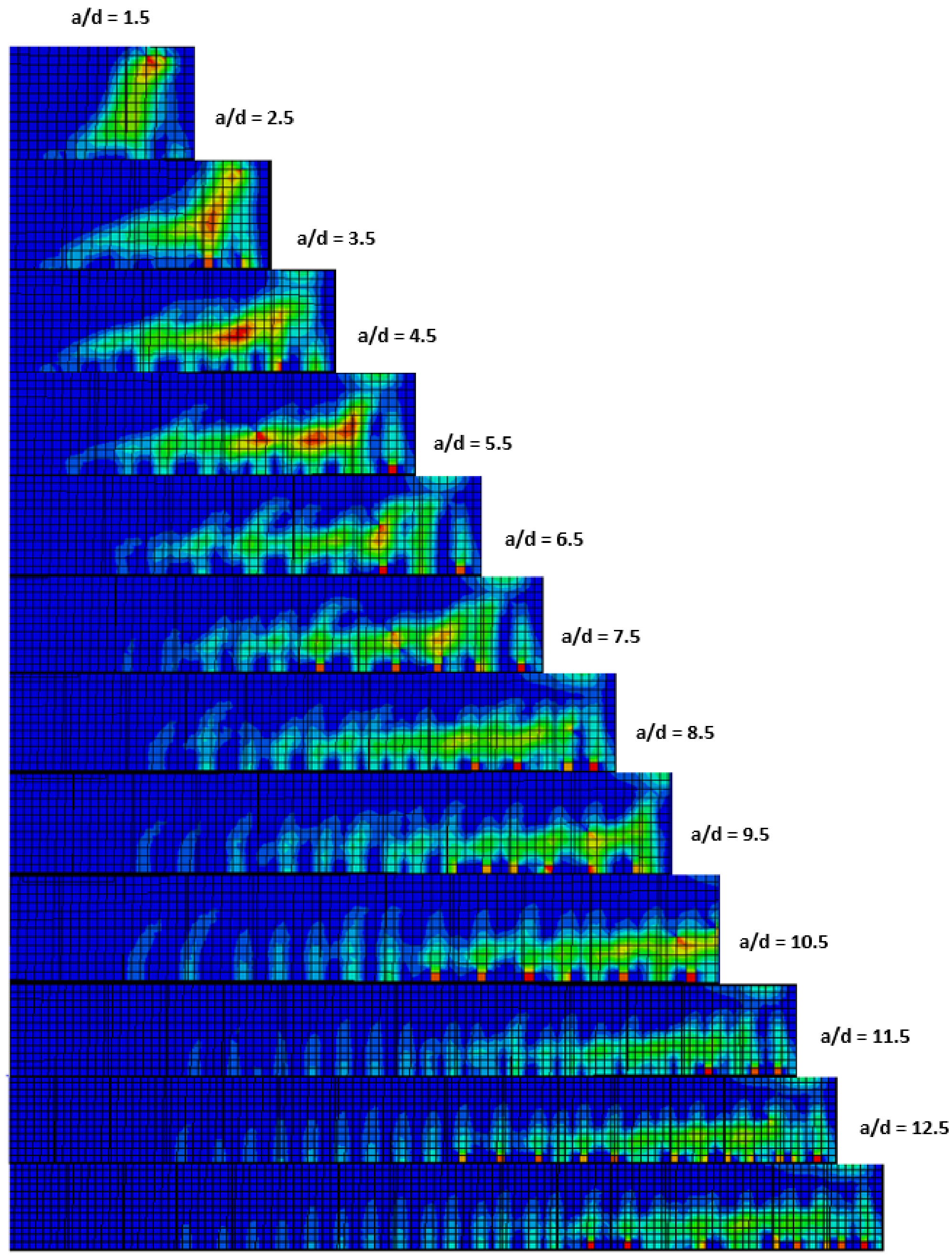


Figure D.12: Crack Patterns at Failure for BM 12-220 Series, 50° Dilation

Table D.8: Comparison of Ultimate Loads for BM 12-220

| $a/d$ | ABAQUS (50°, KN) | CSA (Flexure, KN) | ACI (Flexure, KN) |
|---|---|---|---|
| 1.5 | 403 | 724 | 643 |
| 2.5 | 332 | 435 | 386 |
| 3.5 | 291 | 311 | 276 |
| 4.5 | 239 | 242 | 214 |
| 5.5 | 197 | 198 | 175 |
| 6.5 | 175 | 167 | 148 |
| 7.5 | 168 | 145 | 129 |
| 8.5 | 148 | 128 | 114 |
| 9.5 | 136 | 114 | 102 |
| 10.5 | 125 | 104 | 92 |
| 11.5 | 119 | 95 | 84 |
| 12.5 | 113 | 87 | 77 |

Table D.9: Comparison of Ultimate Loads for BM 12-220

| $a/d$ | ABAQUS (50°, KN) | CSA (Shear, KN) | ACI (Shear, KN) | JSCE (Shear, KN) | Nehdi (2007) (Shear, KN) | ISIS Canada (Shear, KN) |
|---|---|---|---|---|---|---|
| 1.5 | 403 | 238 | 193 | 145 | 470 | 309 |
| 2.5 | 332 | 218 | 193 | 145 | 336 | 277 |
| 3.5 | 291 | 190 | 193 | 145 | 325 | 253 |
| 4.5 | 239 | 170 | 193 | 145 | 317 | 234 |
| 5.5 | 197 | 156 | 193 | 145 | 311 | 225 |
| 6.5 | 175 | 145 | 193 | 145 | 306 | 225 |
| 7.5 | 168 | 136 | 193 | 145 | 302 | 225 |
| 8.5 | 148 | 128 | 193 | 145 | 299 | 225 |
| 9.5 | 136 | 124 | 193 | 145 | 296 | 225 |
| 10.5 | 125 | 121 | 193 | 145 | 293 | 225 |
| 11.5 | 119 | 121 | 193 | 145 | 291 | 225 |
| 12.5 | 113 | 121 | 193 | 145 | 289 | 225 |

# BM 12-s230

## 30° Dilation Angle

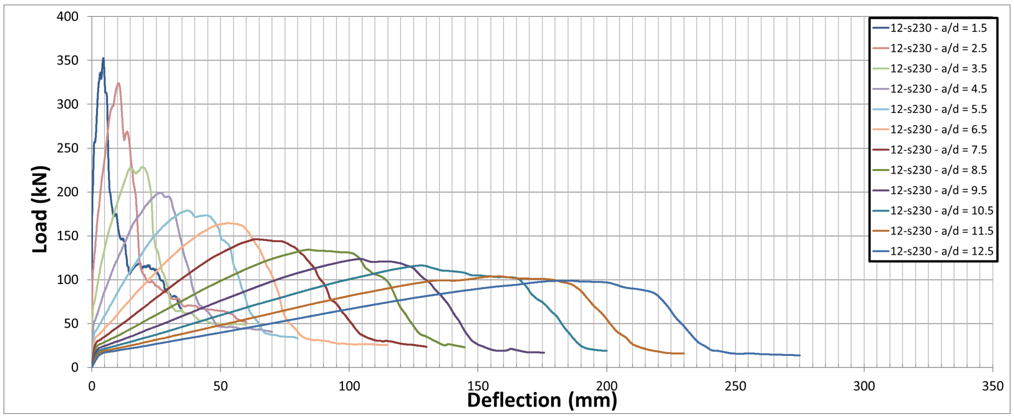


Figure D.13: Mid-Span Load-Deflection Curves for BM 12-s230 Series, 30° Dilation

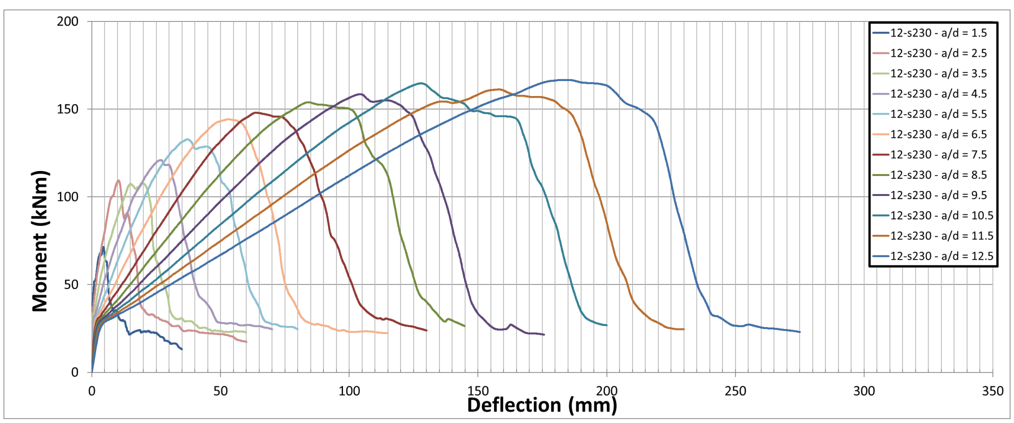


Figure D.14: Mid-Span Moment-Deflection Curves for BM 12-s230 Series, 30° Dilation

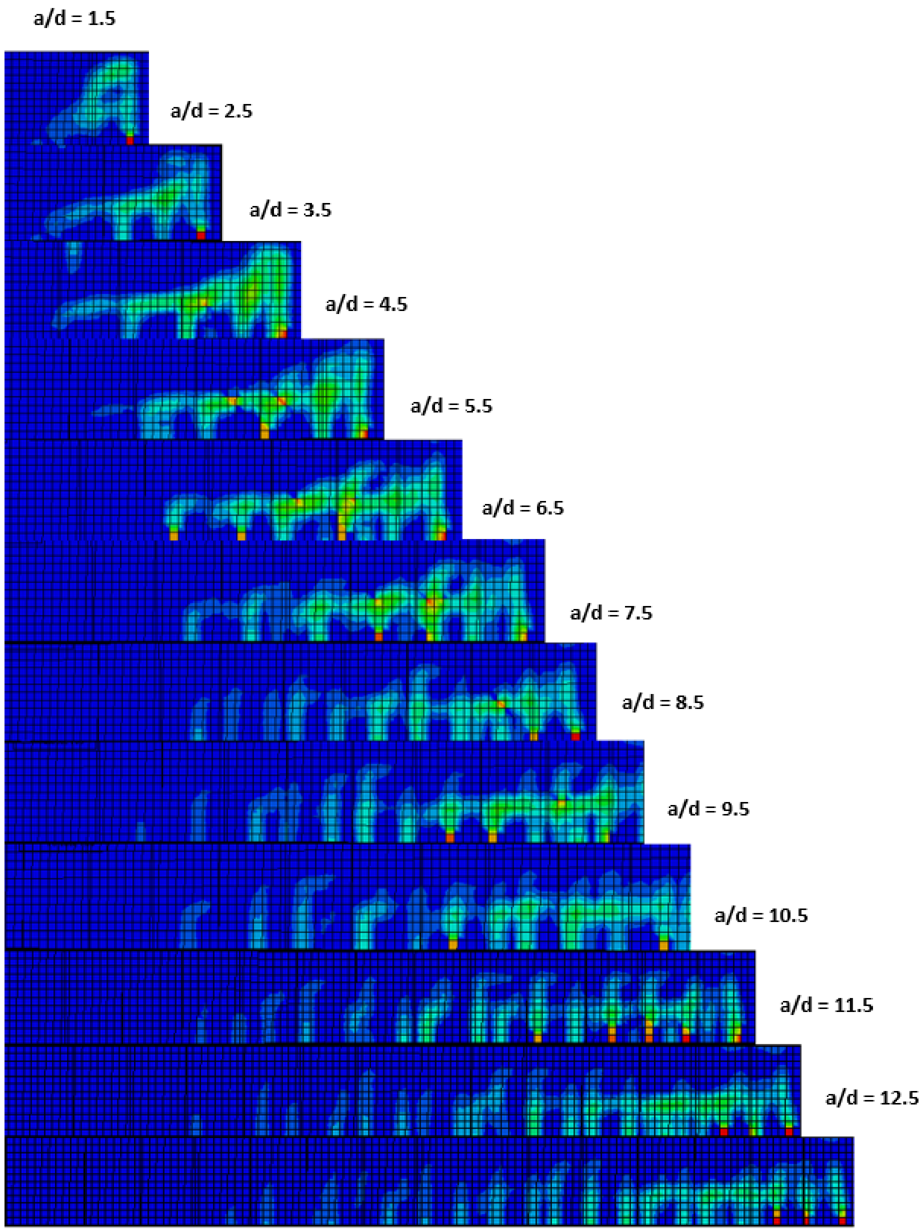


Figure D.15: Crack Patterns at Failure for BM 12-s230 Series, 30° Dilation

Table D.10: Comparison of Ultimate Loads for BM 12-s230

| $a/d$ | ABAQUS (30°, KN) | CSA (Flexure, KN) | ACI (Flexure, KN) |
|---|---|---|---|
| 1.5 | 352 | 794 | 703 |
| 2.5 | 324 | 476 | 422 |
| 3.5 | 229 | 340 | 301 |
| 4.5 | 199 | 265 | 234 |
| 5.5 | 179 | 216 | 192 |
| 6.5 | 164 | 183 | 162 |
| 7.5 | 146 | 159 | 141 |
| 8.5 | 134 | 140 | 124 |
| 9.5 | 124 | 125 | 111 |
| 10.5 | 116 | 113 | 100 |
| 11.5 | 104 | 104 | 92 |
| 12.5 | 99 | 95 | 84 |

Table D.11: Comparison of Ultimate Loads for BM 12-s230

| $a/d$ | ABAQUS (30°, KN) | CSA (Shear, KN) | ACI (Shear, KN) | JSCE (Shear, KN) | Nehdi (2007) (Shear, KN) | ISIS Canada (Shear, KN) |
|---|---|---|---|---|---|---|
| 1.5 | 352 | 361 | 383 | 183 | 644 | 423 |
| 2.5 | 324 | 316 | 383 | 183 | 495 | 366 |
| 3.5 | 229 | 275 | 383 | 183 | 483 | 348 |
| 4.5 | 199 | 246 | 383 | 183 | 474 | 348 |
| 5.5 | 179 | 225 | 383 | 183 | 467 | 348 |
| 6.5 | 164 | 216 | 383 | 183 | 462 | 348 |
| 7.5 | 146 | 208 | 383 | 183 | 457 | 348 |
| 8.5 | 134 | 205 | 383 | 183 | 453 | 348 |
| 9.5 | 124 | 205 | 383 | 183 | 450 | 348 |
| 10.5 | 116 | 205 | 383 | 183 | 447 | 348 |
| 11.5 | 104 | 205 | 383 | 183 | 445 | 348 |
| 12.5 | 99 | 205 | 383 | 183 | 443 | 348 |

## 50° Dilation Angle

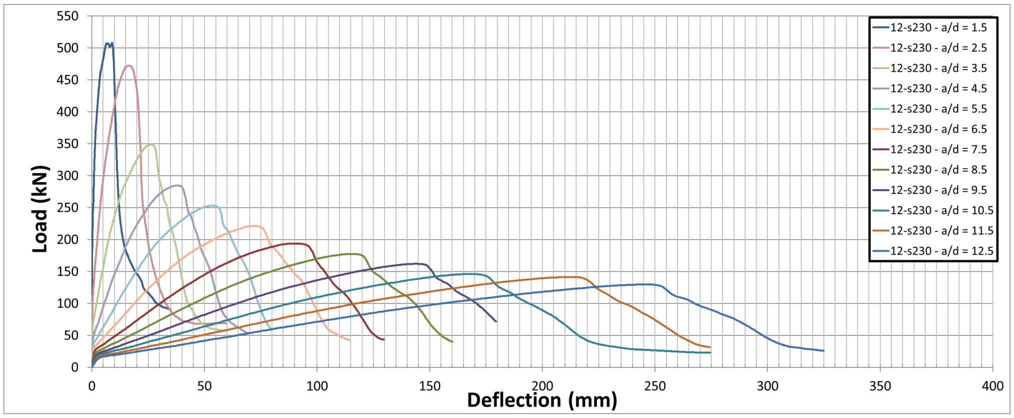


Figure D.16: Mid-Span Load-Deflection Curves for BM 12-s230 Series, 50° Dilation

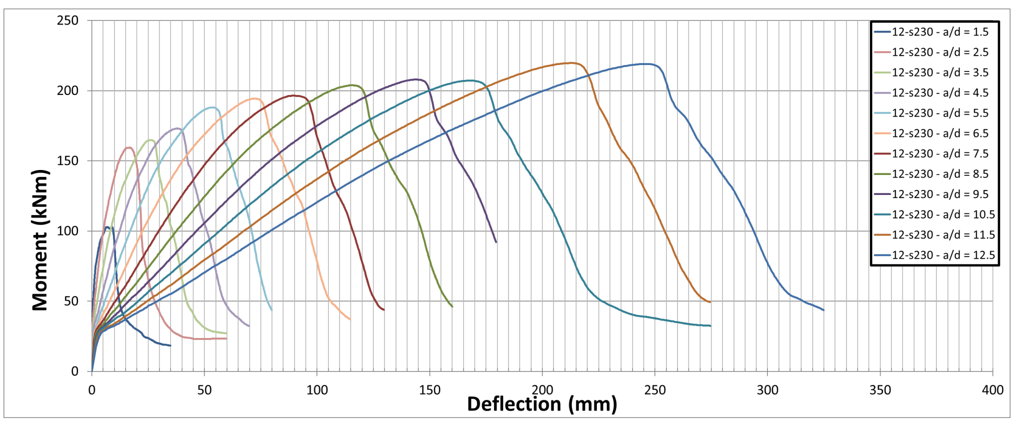


Figure D.17: Mid-Span Moment-Deflection Curves for BM 12-s230 Series, 50° Dilation

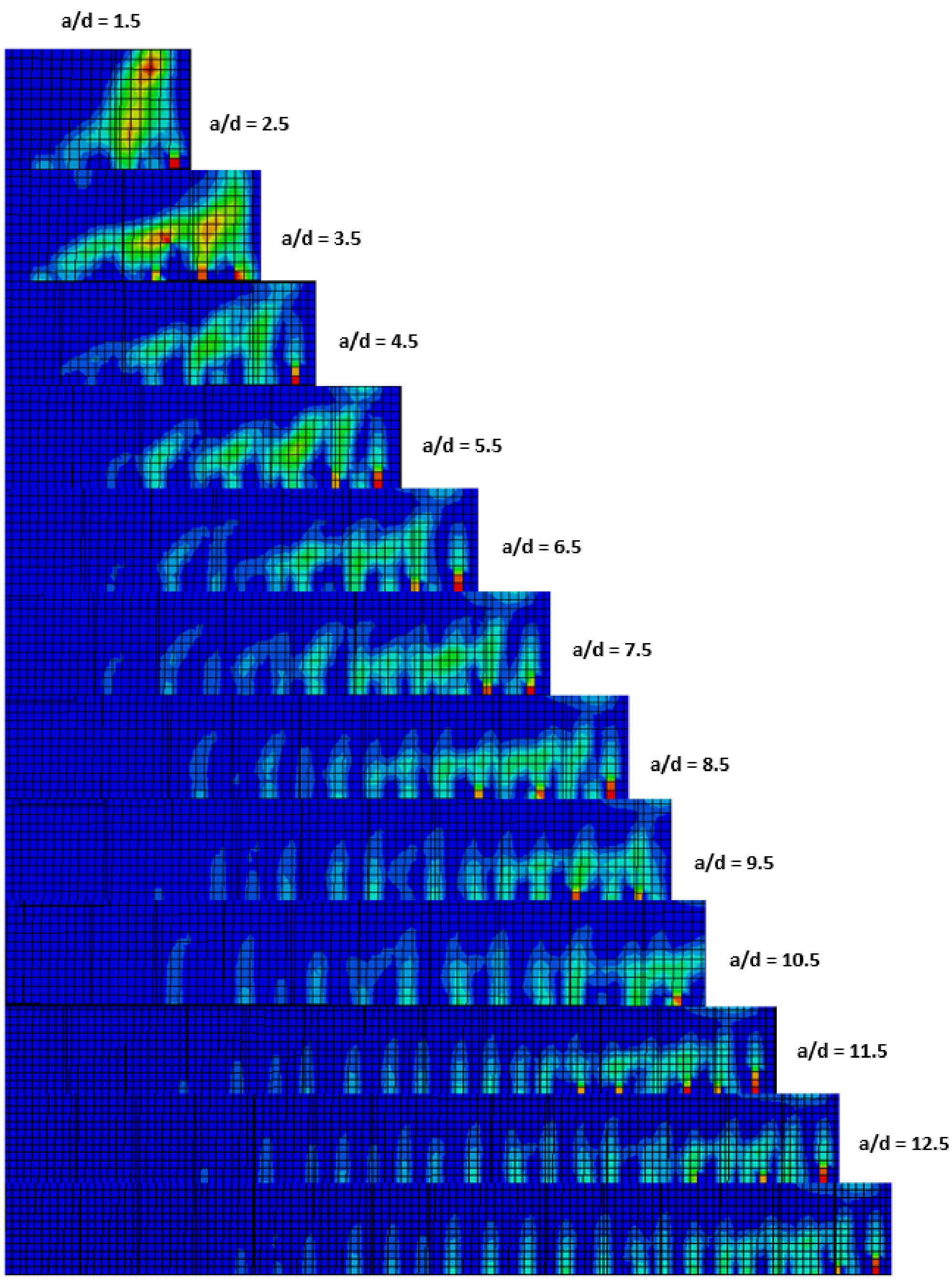


Figure D.18: Crack Patterns at Failure for BM 12-s230 Series, 50° Dilation

Table D.12: Comparison of Ultimate Loads for BM 12-s230

| $a/d$ | ABAQUS (50°, KN) | CSA (Flexure, KN) | ACI (Flexure, KN) |
|---|---|---|---|
| 1.5 | 508 | 794 | 703 |
| 2.5 | 472 | 476 | 422 |
| 3.5 | 349 | 340 | 301 |
| 4.5 | 285 | 265 | 234 |
| 5.5 | 253 | 216 | 192 |
| 6.5 | 221 | 183 | 162 |
| 7.5 | 194 | 159 | 141 |
| 8.5 | 178 | 140 | 124 |
| 9.5 | 162 | 125 | 111 |
| 10.5 | 146 | 113 | 100 |
| 11.5 | 141 | 104 | 92 |
| 12.5 | 130 | 95 | 84 |

Table D.13: Comparison of Ultimate Loads for BM 12-s230

| $a/d$ | ABAQUS (50°, KN) | CSA (Shear, KN) | ACI (Shear, KN) | JSCE (Shear, KN) | Nehdi (2007) (Shear, KN) | ISIS Canada (Shear, KN) |
|---|---|---|---|---|---|---|
| 1.5 | 508 | 361 | 383 | 183 | 644 | 423 |
| 2.5 | 72 | 316 | 383 | 183 | 495 | 366 |
| 3.5 | 349 | 275 | 383 | 183 | 483 | 348 |
| 4.5 | 285 | 246 | 383 | 183 | 474 | 348 |
| 5.5 | 253 | 225 | 383 | 183 | 467 | 348 |
| 6.5 | 221 | 216 | 383 | 183 | 462 | 348 |
| 7.5 | 194 | 208 | 383 | 183 | 457 | 348 |
| 8.5 | 178 | 205 | 383 | 183 | 453 | 348 |
| 9.5 | 162 | 205 | 383 | 183 | 450 | 348 |
| 10.5 | 146 | 205 | 383 | 183 | 447 | 348 |
| 11.5 | 141 | 205 | 383 | 183 | 445 | 348 |
| 12.5 | 130 | 205 | 383 | 183 | 443 | 348 |

# BM 16-150

## 30° Dilation Angle

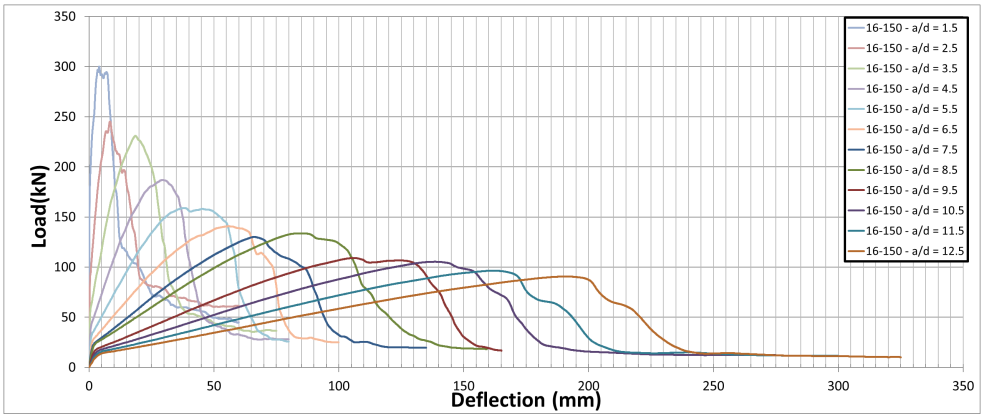


Figure D.19: Mid-Span Load-Deflection Curves for BM 16-150 Series, 30° Dilation

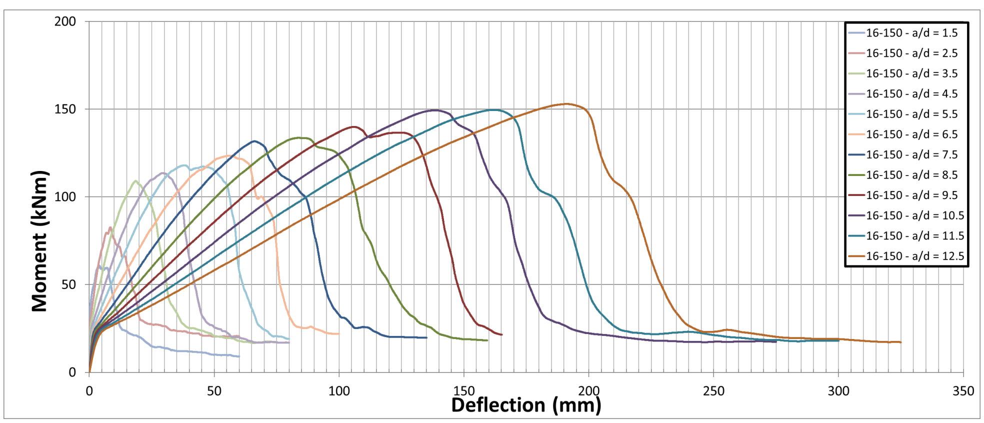


Figure D.20: Mid-Span Moment-Deflection Curves for BM 16-150 Series, 30° Dilation

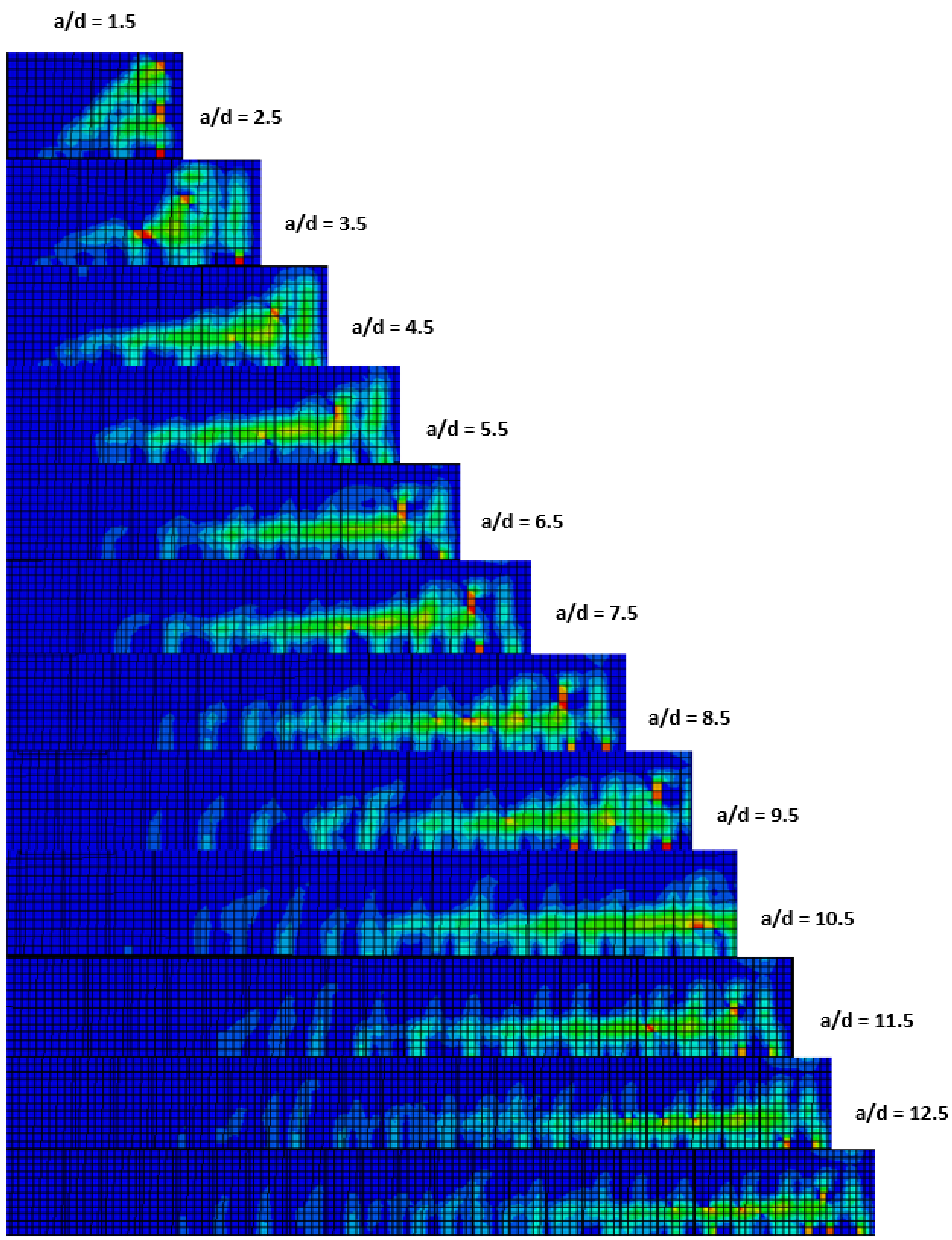


Figure D.21: Crack Patterns at Failure for BM 16-150 Series, 30° Dilation

Table D.14: Comparison of Ultimate Loads for BM 16-150

| $a/d$ | ABAQUS (30°, KN) | CSA (Flexure, KN) | ACI (Flexure, KN) |
|---|---|---|---|
| 1.5 | 300 | 696 | 617 |
| 2.5 | 245 | 417 | 370 |
| 3.5 | 231 | 298 | 264 |
| 4.5 | 187 | 232 | 206 |
| 5.5 | 159 | 190 | 168 |
| 6.5 | 141 | 161 | 142 |
| 7.5 | 130 | 139 | 123 |
| 8.5 | 116 | 123 | 109 |
| 9.5 | 109 | 110 | 97 |
| 10.5 | 105 | 99 | 88 |
| 11.5 | 96 | 91 | 80 |
| 12.5 | 91 | 83 | 74 |

Table D.15: Comparison of Ultimate Loads for BM 16-150

| $a/d$ | ABAQUS (30°, KN) | CSA (Shear, KN) | ACI (Shear, KN) | JSCE (Shear, KN) | Nehdi (2007) (Shear, KN) | ISIS Canada (Shear, KN) |
|---|---|---|---|---|---|---|
| 1.5 | 300 | 258 | 240 | 147 | 502 | 299 |
| 2.5 | 245 | 229 | 240 | 147 | 372 | 266 |
| 3.5 | 231 | 199 | 240 | 147 | 361 | 242 |
| 4.5 | 187 | 179 | 240 | 147 | 353 | 225 |
| 5.5 | 159 | 163 | 240 | 147 | 347 | 225 |
| 6.5 | 141 | 151 | 240 | 147 | 343 | 225 |
| 7.5 | 130 | 141 | 240 | 147 | 339 | 225 |
| 8.5 | 116 | 137 | 240 | 147 | 336 | 225 |
| 9.5 | 109 | 137 | 240 | 147 | 333 | 225 |
| 10.5 | 105 | 137 | 240 | 147 | 330 | 225 |
| 11.5 | 96 | 137 | 240 | 147 | 328 | 225 |
| 12.5 | 91 | 137 | 240 | 147 | 326 | 225 |

## 50° Dilation Angle

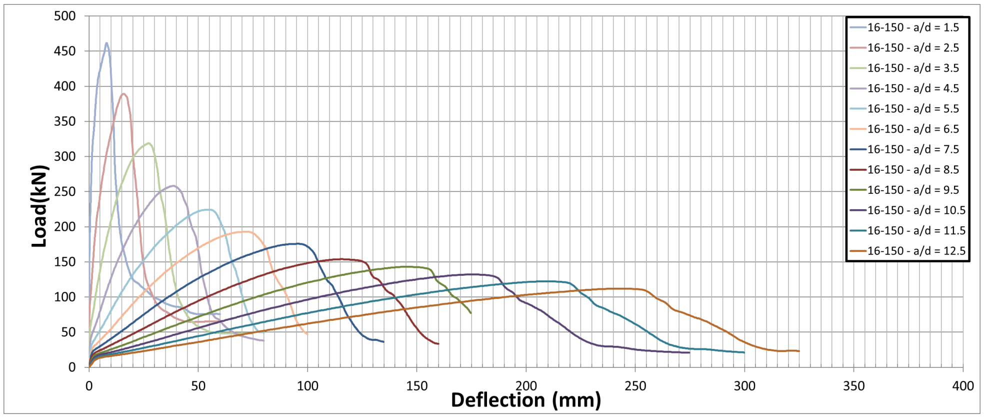


Figure D.22: Mid-Span Load-Deflection Curves for BM 16-150 Series, 50° Dilation

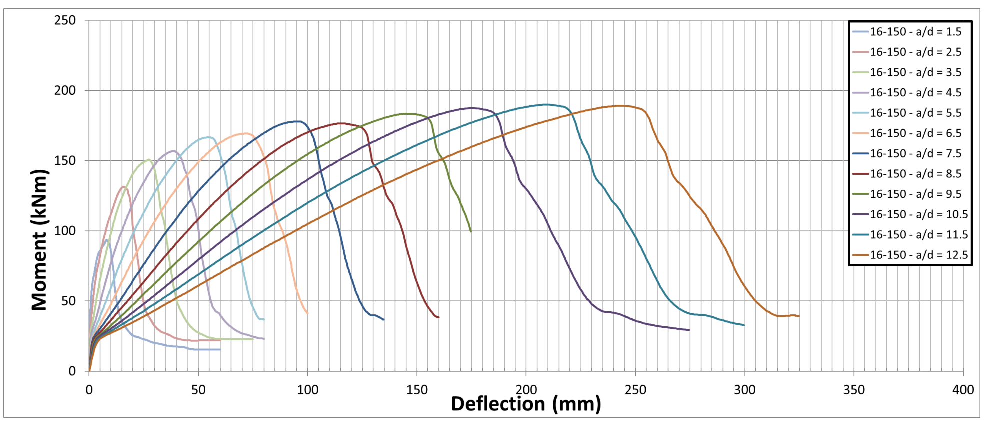


Figure D.23: Mid-Span Moment-Deflection Curves for BM 16-150 Series, 50° Dilation

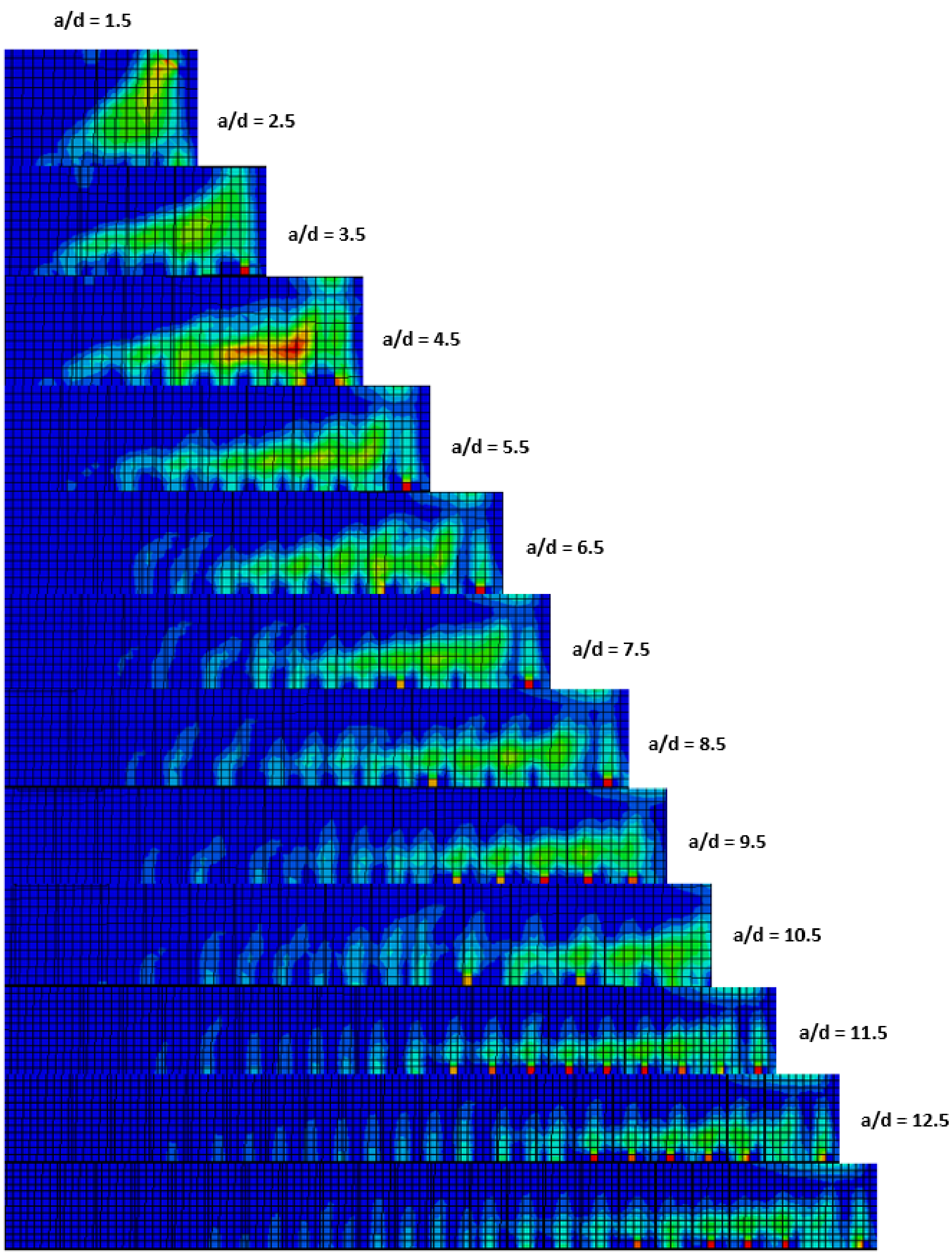


Figure D.24: Crack Patterns at Failure for BM 16-150 Series, 50° Dilation

Table D.16: Comparison of Ultimate Loads for BM 16-150

| $a/d$ | ABAQUS (50°, KN) | CSA (Flexure, KN) | ACI (Flexure, KN) |
|---|---|---|---|
| 1.5 | 462 | 696 | 617 |
| 2.5 | 389 | 417 | 370 |
| 3.5 | 319 | 298 | 264 |
| 4.5 | 252 | 232 | 206 |
| 5.5 | 224 | 190 | 168 |
| 6.5 | 193 | 161 | 142 |
| 7.5 | 176 | 139 | 123 |
| 8.5 | 154 | 123 | 109 |
| 9.5 | 143 | 110 | 97 |
| 10.5 | 132 | 99 | 88 |
| 11.5 | 122 | 91 | 80 |
| 12.5 | 112 | 83 | 74 |

Table D.17: Comparison of Ultimate Loads for BM 16-150

| $a/d$ | ABAQUS (50°, KN) | CSA (Shear, KN) | ACI (Shear, KN) | JSCE (Shear, KN) | Nehdi (2007) (Shear, KN) | ISIS Canada (Shear, KN) |
|---|---|---|---|---|---|---|
| 1.5 | 462 | 258 | 240 | 147 | 502 | 299 |
| 2.5 | 389 | 229 | 240 | 147 | 372 | 266 |
| 3.5 | 319 | 199 | 240 | 147 | 361 | 242 |
| 4.5 | 252 | 179 | 240 | 147 | 353 | 225 |
| 5.5 | 224 | 163 | 240 | 147 | 347 | 225 |
| 6.5 | 193 | 151 | 240 | 147 | 343 | 225 |
| 7.5 | 176 | 141 | 240 | 147 | 339 | 225 |
| 8.5 | 154 | 137 | 240 | 147 | 336 | 225 |
| 9.5 | 143 | 137 | 240 | 147 | 333 | 225 |
| 10.5 | 132 | 137 | 240 | 147 | 330 | 225 |
| 11.5 | 122 | 137 | 240 | 147 | 328 | 225 |
| 12.5 | 112 | 137 | 240 | 147 | 326 | 225 |

# BM 16-220

## 30° Dilation Angle

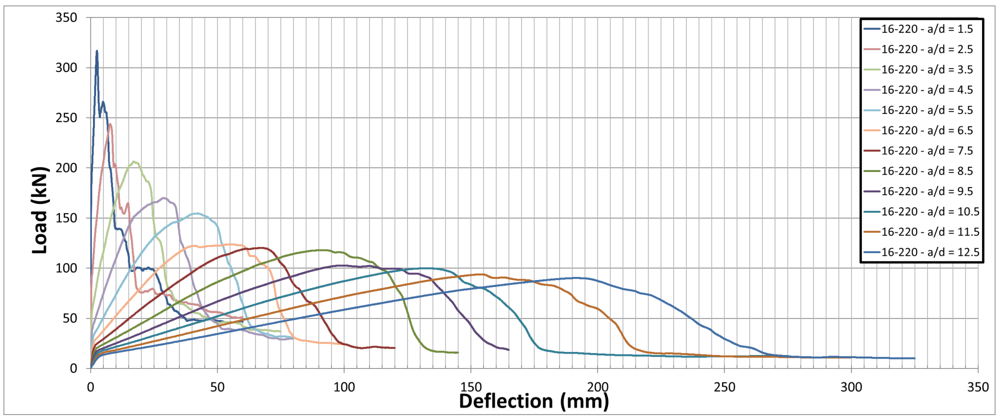


Figure D.25: Mid-Span Load-Deflection Curves for BM 16-220 Series, 30° Dilation

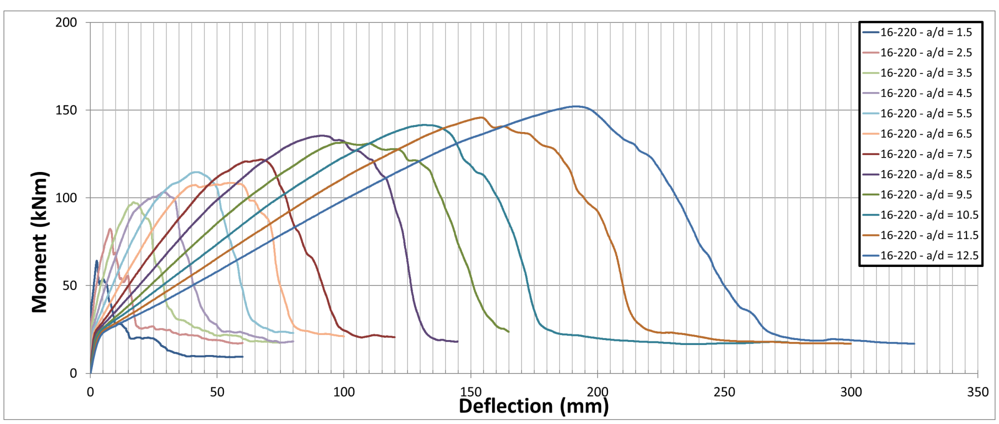


Figure D.26: Mid-Span Moment-Deflection Curves for BM 16-220 Series, 30° Dilation

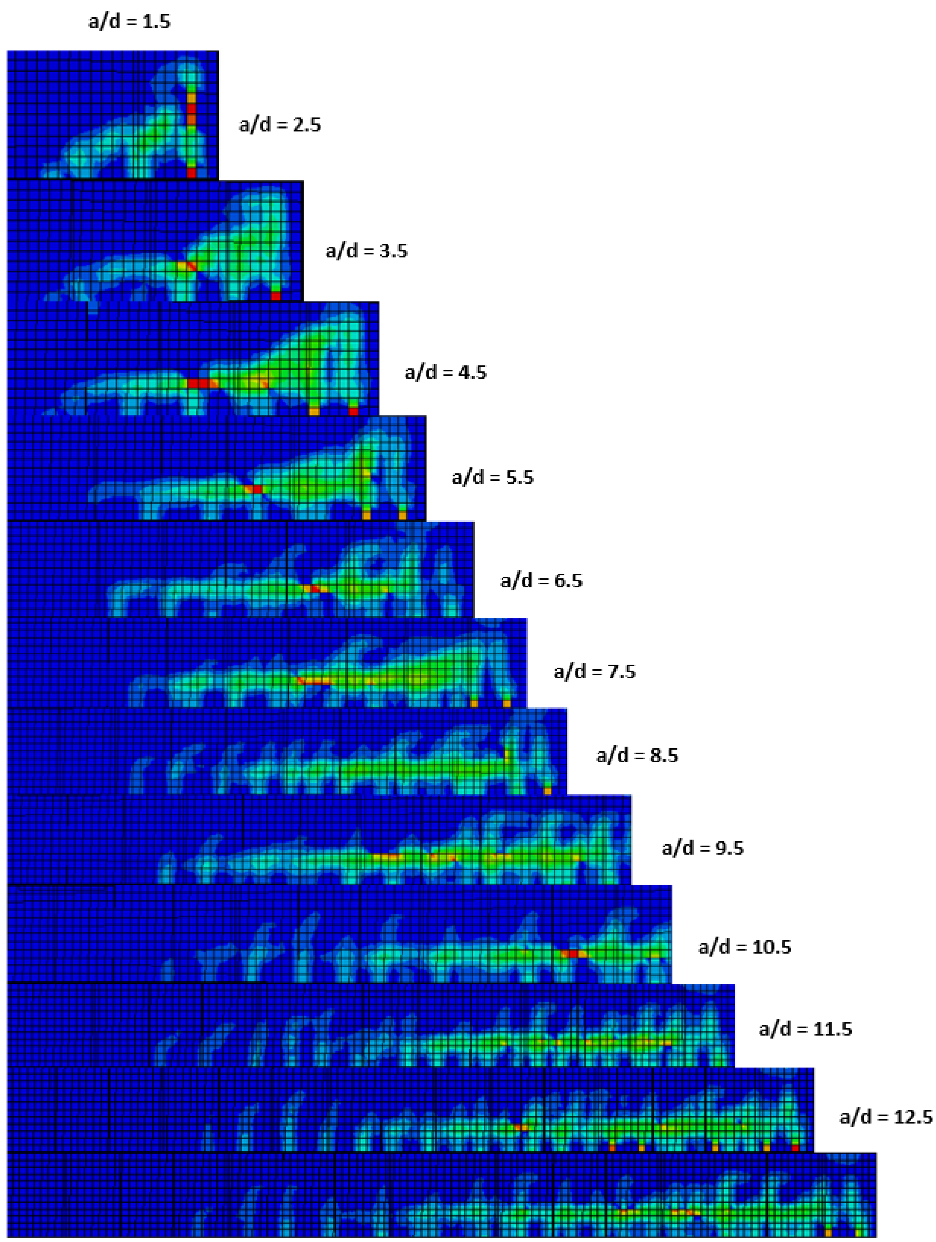


Figure D.27: Crack Patterns at Failure for BM 16-220 Series, 30° Dilation

Table D.18: Comparison of Ultimate Loads for BM 16-220

| $a/d$ | ABAQUS (30°, KN) | CSA (Flexure, KN) | ACI (Flexure, KN) |
|---|---|---|---|
| 1.5 | 317 | 696 | 617 |
| 2.5 | 244 | 417 | 370 |
| 3.5 | 206 | 298 | 264 |
| 4.5 | 170 | 232 | 206 |
| 5.5 | 155 | 190 | 168 |
| 6.5 | 124 | 161 | 142 |
| 7.5 | 120 | 139 | 123 |
| 8.5 | 118 | 123 | 109 |
| 9.5 | 103 | 110 | 97 |
| 10.5 | 100 | 99 | 88 |
| 11.5 | 94 | 91 | 80 |
| 12.5 | 90 | 83 | 74 |

Table D.19: Comparison of Ultimate Loads for BM 16-220

| $a/d$ | ABAQUS (30°, KN) | CSA (Shear, KN) | ACI (Shear, KN) | JSCE (Shear, KN) | Nehdi (2007) (Shear, KN) | ISIS Canada (Shear, KN) |
|---|---|---|---|---|---|---|
| 1.5 | 317 | 232 | 189 | 139 | 462 | 249 |
| 2.5 | 244 | 207 | 189 | 139 | 332 | 226 |
| 3.5 | 206 | 180 | 189 | 139 | 321 | 209 |
| 4.5 | 170 | 161 | 189 | 139 | 313 | 195 |
| 5.5 | 155 | 147 | 189 | 139 | 308 | 183 |
| 6.5 | 124 | 137 | 189 | 139 | 303 | 183 |
| 7.5 | 120 | 128 | 189 | 139 | 299 | 183 |
| 8.5 | 118 | 122 | 189 | 139 | 296 | 183 |
| 9.5 | 103 | 120 | 189 | 139 | 293 | 183 |
| 10.5 | 100 | 120 | 189 | 139 | 290 | 183 |
| 11.5 | 94 | 120 | 189 | 139 | 288 | 183 |
| 12.5 | 90 | 120 | 189 | 139 | 286 | 183 |

## 50° Dilation Angle

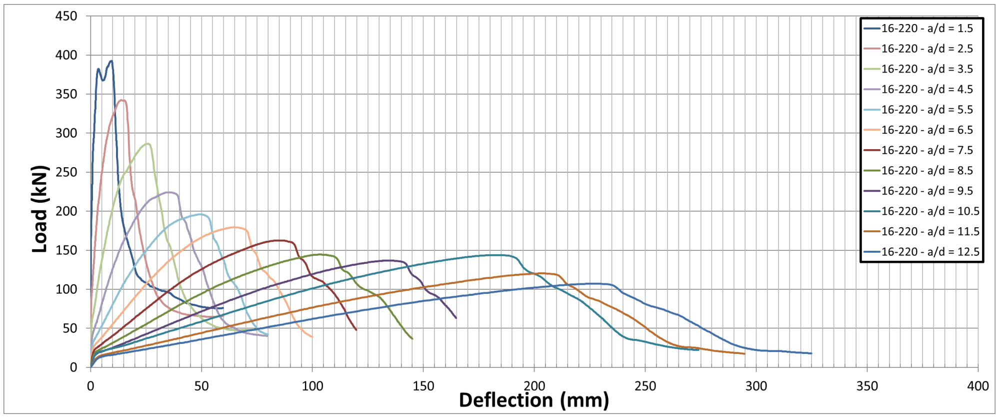


Figure D.28: Mid-Span Load-Deflection Curves for BM 16-220 Series, 50° Dilation

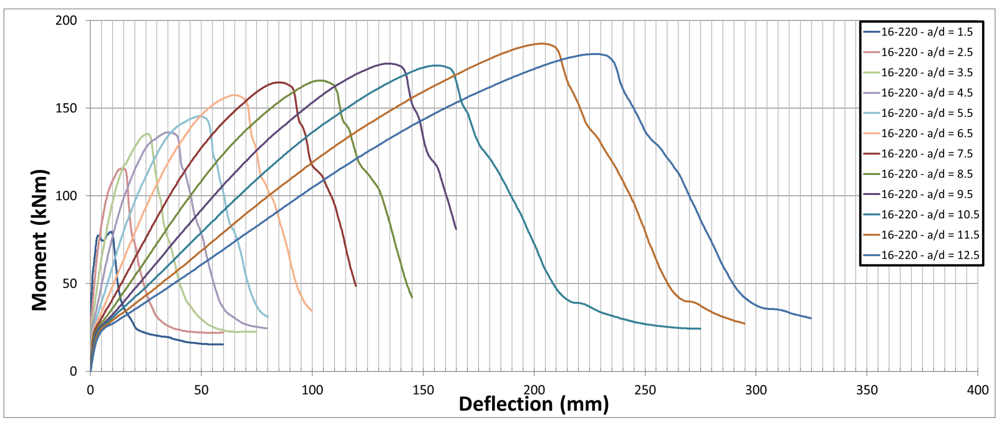


Figure D.29: Mid-Span Moment-Deflection Curves for BM 16-220 Series, 50° Dilation

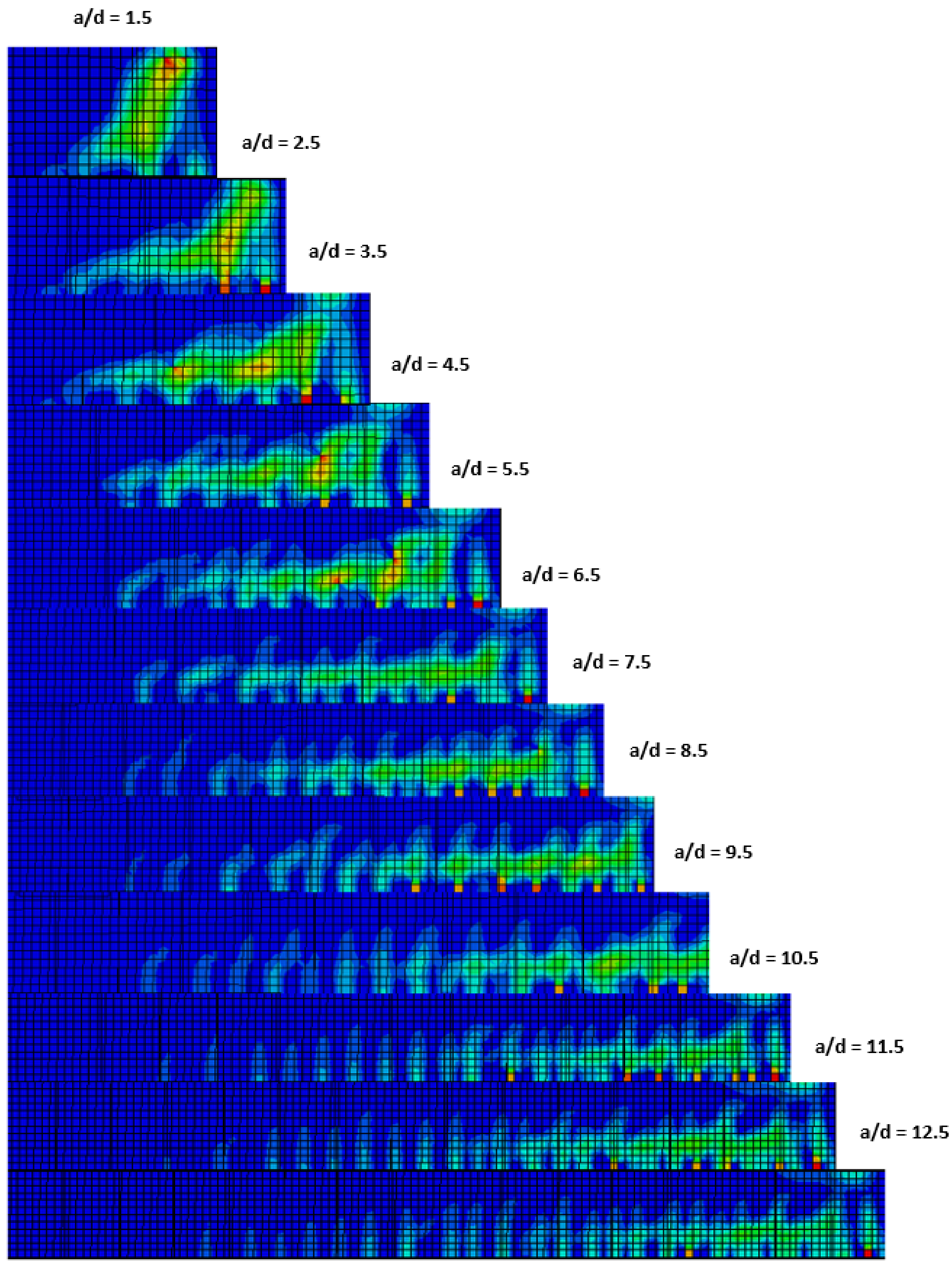


Figure D.30: Crack Patterns at Failure for BM 16-220 Series, 50° Dilation

Table D.20: Comparison of Ultimate Loads for BM 16-220

| $a/d$ | ABAQUS (50°, KN) | CSA (Flexure, KN) | ACI (Flexure, KN) |
|---|---|---|---|
| 1.5 | 392 | 696 | 617 |
| 2.5 | 342 | 417 | 370 |
| 3.5 | 286 | 298 | 264 |
| 4.5 | 224 | 232 | 206 |
| 5.5 | 196 | 190 | 168 |
| 6.5 | 179 | 161 | 142 |
| 7.5 | 163 | 139 | 123 |
| 8.5 | 144 | 123 | 109 |
| 9.5 | 137 | 110 | 97 |
| 10.5 | 123 | 99 | 88 |
| 11.5 | 120 | 91 | 80 |
| 12.5 | 107 | 83 | 74 |

Table D.21: Comparison of Ultimate Loads for BM 16-220

| $a/d$ | ABAQUS (50°, KN) | CSA (Shear, KN) | ACI (Shear, KN) | JSCE (Shear, KN) | Nehdi (2007) (Shear, KN) | ISIS Canada (Shear, KN) |
|---|---|---|---|---|---|---|
| 1.5 | 392 | 232 | 189 | 139 | 462 | 249 |
| 2.5 | 342 | 207 | 189 | 139 | 332 | 226 |
| 3.5 | 286 | 180 | 189 | 139 | 321 | 209 |
| 4.5 | 224 | 161 | 189 | 139 | 313 | 195 |
| 5.5 | 196 | 147 | 189 | 139 | 308 | 183 |
| 6.5 | 179 | 137 | 189 | 139 | 303 | 183 |
| 7.5 | 163 | 128 | 189 | 139 | 299 | 183 |
| 8.5 | 144 | 122 | 189 | 139 | 296 | 183 |
| 9.5 | 137 | 120 | 189 | 139 | 293 | 183 |
| 10.5 | 123 | 120 | 189 | 139 | 290 | 183 |
| 11.5 | 120 | 120 | 189 | 139 | 288 | 183 |
| 12.5 | 107 | 120 | 189 | 139 | 286 | 183 |

# BM 16-s230

## 30° Dilation Angle

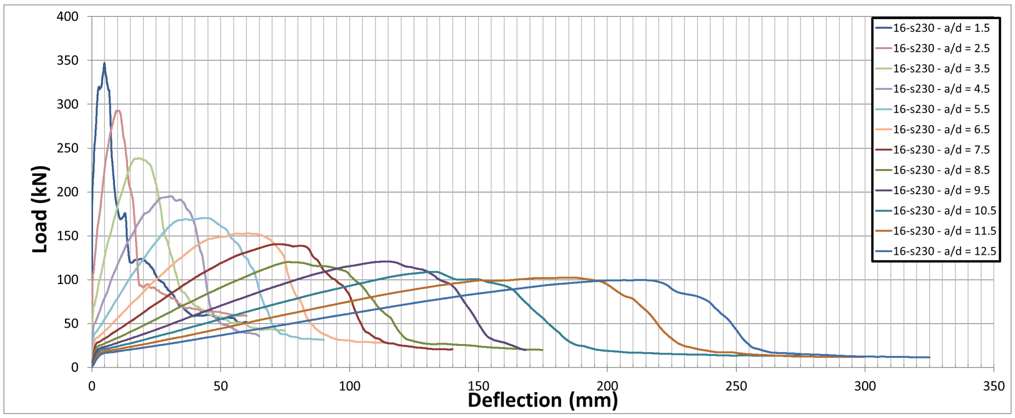


Figure D.31: Mid-Span Load-Deflection Curves for BM 16-s230 Series, 30° Dilation

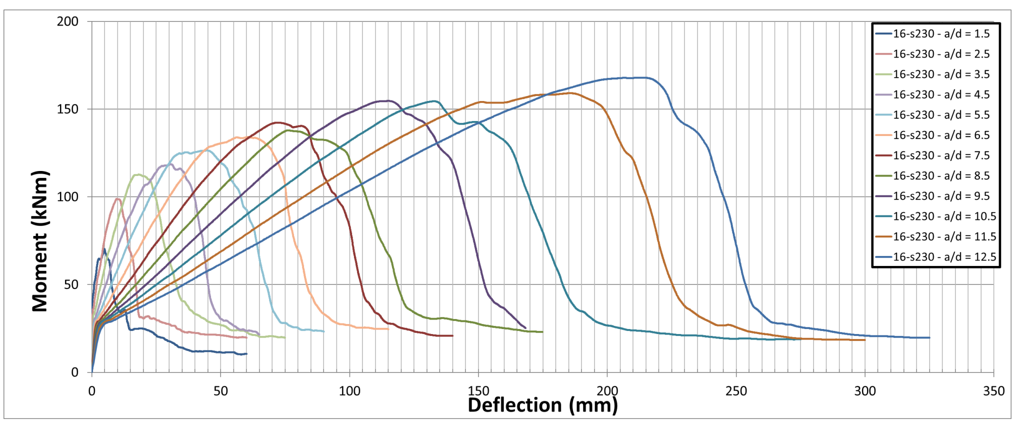


Figure D.32: Mid-Span Moment-Deflection Curves for BM 16-s230 Series, 30° Dilation

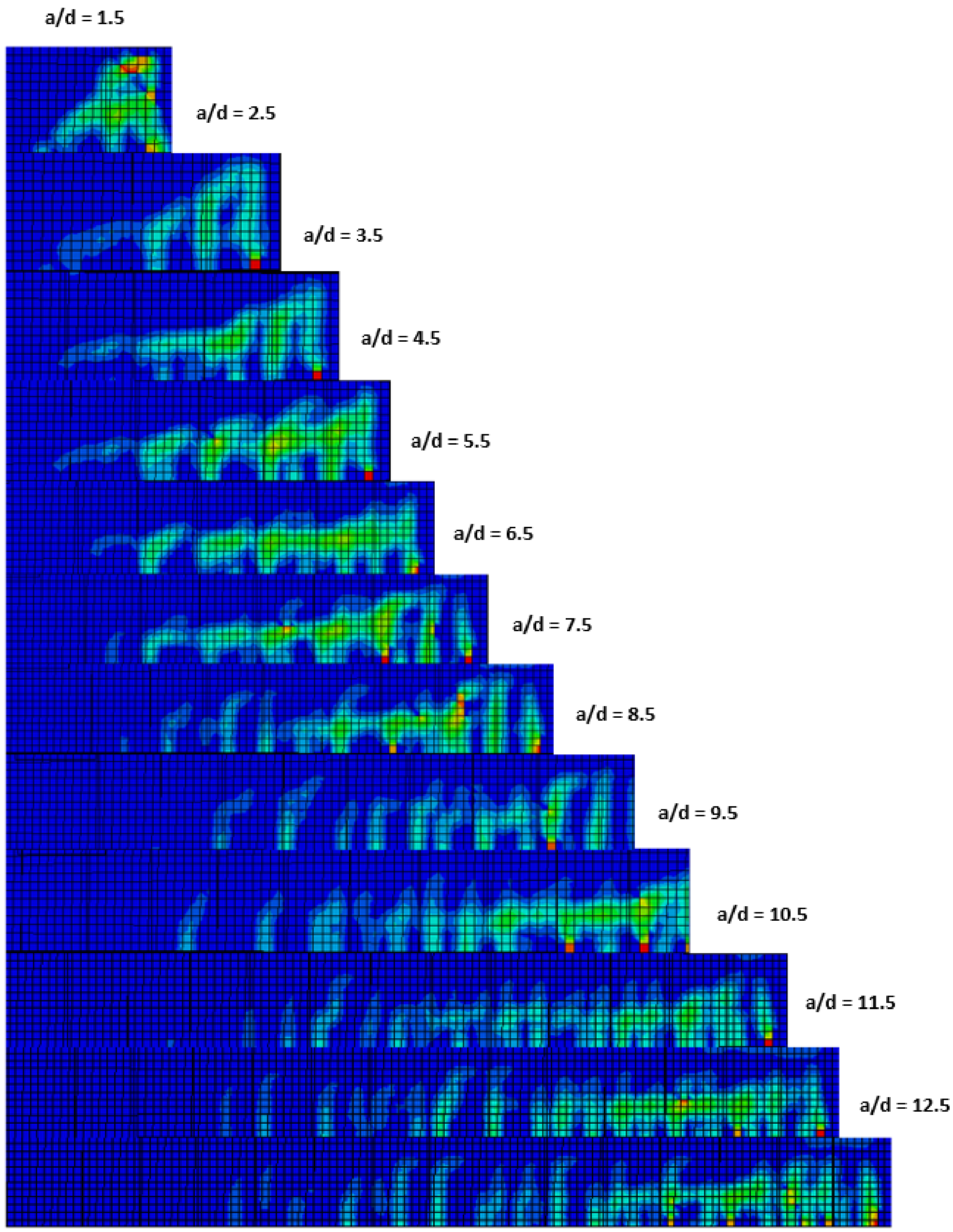


Figure D.33: Crack Patterns at Failure for BM 16-s230 Series, 30° Dilation

Table D.22: Comparison of Ultimate Loads for BM 16-s230

| $a/d$ | ABAQUS (30°, KN) | CSA (Flexure, KN) | ACI (Flexure, KN) |
|---|---|---|---|
| 1.5 | 347 | 762 | 674 |
| 2.5 | 293 | 457 | 404 |
| 3.5 | 239 | 326 | 289 |
| 4.5 | 195 | 254 | 225 |
| 5.5 | 170 | 208 | 184 |
| 6.5 | 153 | 176 | 155 |
| 7.5 | 141 | 152 | 135 |
| 8.5 | 120 | 134 | 119 |
| 9.5 | 121 | 120 | 106 |
| 10.5 | 109 | 109 | 96 |
| 11.5 | 102 | 99 | 88 |
| 12.5 | 100 | 91 | 81 |

Table D.23: Comparison of Ultimate Loads for BM 16-s230

| $a/d$ | ABAQUS (30°, KN) | CSA (Shear, KN) | ACI (Shear, KN) | JSCE (Shear, KN) | Nehdi (2007) (Shear, KN) | ISIS Canada (Shear, KN) |
|---|---|---|---|---|---|---|
| 1.5 | 347 | 347 | 379 | 174 | 636 | 404 |
| 2.5 | 293 | 298 | 379 | 174 | 491 | 348 |
| 3.5 | 239 | 258 | 379 | 174 | 478 | 348 |
| 4.5 | 195 | 230 | 379 | 174 | 470 | 348 |
| 5.5 | 170 | 218 | 379 | 174 | 463 | 348 |
| 6.5 | 153 | 209 | 379 | 174 | 458 | 348 |
| 7.5 | 141 | 202 | 379 | 174 | 454 | 348 |
| 8.5 | 120 | 202 | 379 | 174 | 450 | 348 |
| 9.5 | 121 | 202 | 379 | 174 | 447 | 348 |
| 10.5 | 109 | 202 | 379 | 174 | 444 | 348 |
| 11.5 | 102 | 202 | 379 | 174 | 442 | 348 |
| 12.5 | 100 | 202 | 379 | 174 | 439 | 348 |

## 50° Dilation Angle

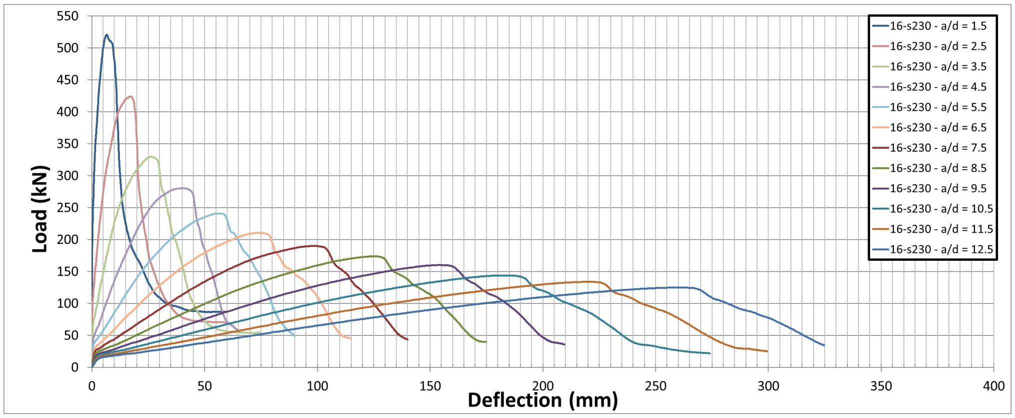


Figure D.34: Mid-Span Load-Deflection Curves for BM 16-s230 Series, 50° Dilation

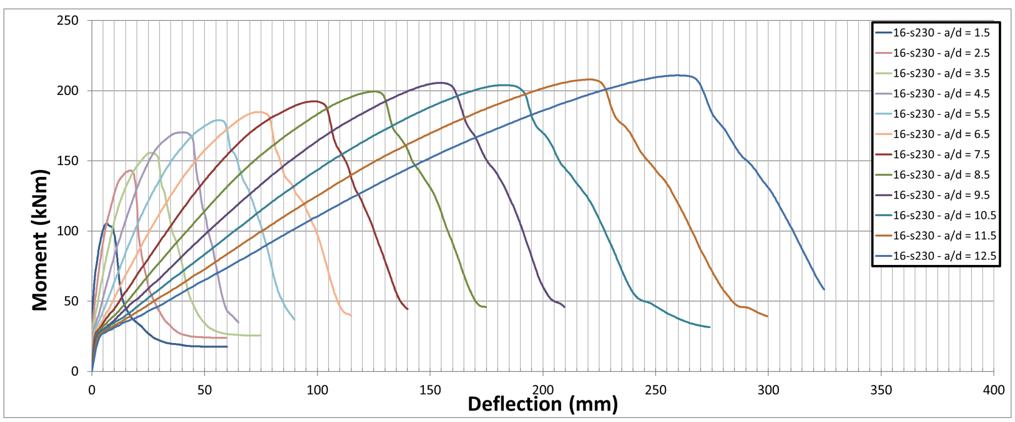


Figure D.35: Mid-Span Moment-Deflection Curves for BM 16-s230 Series, 50° Dilation

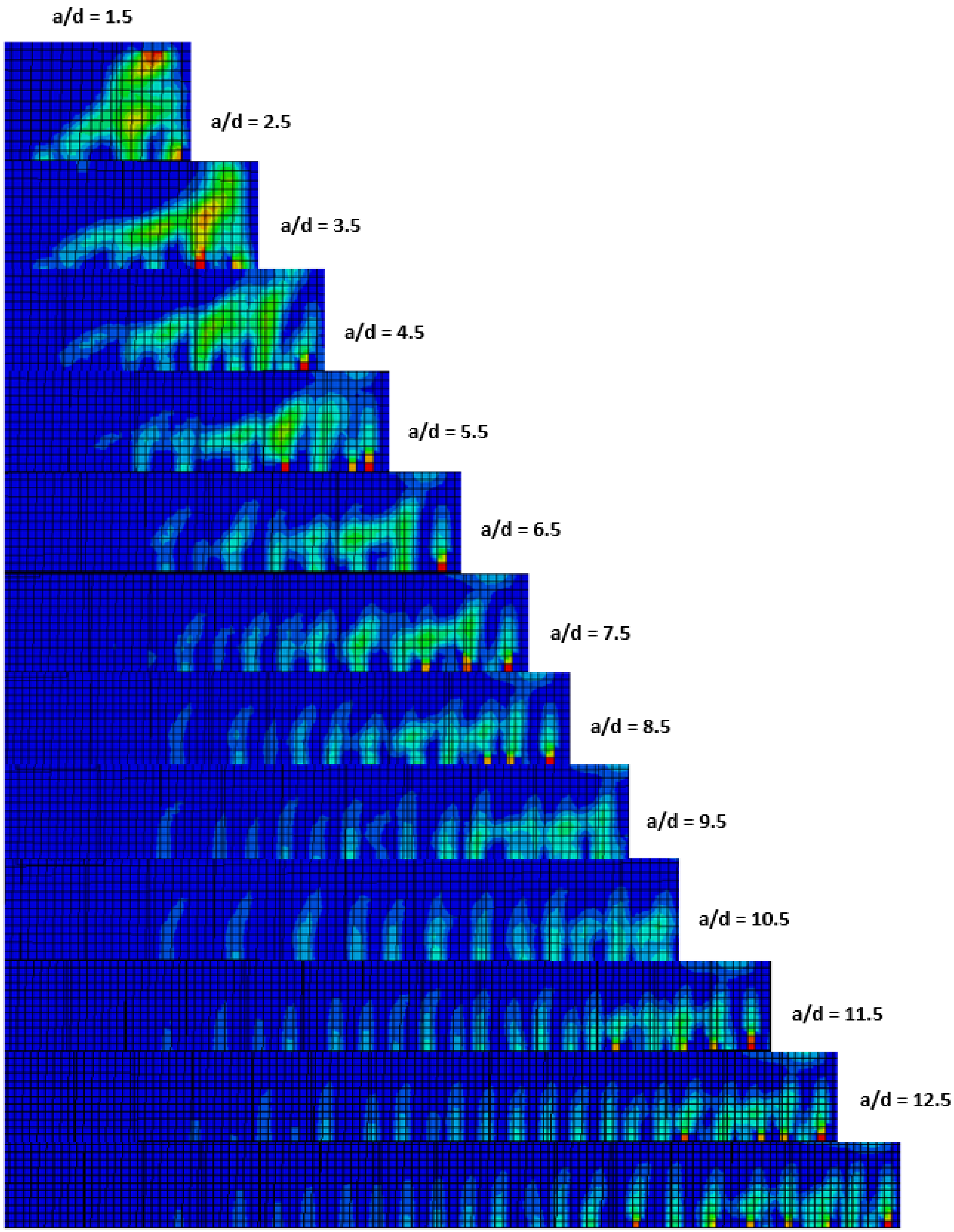


Figure D.36: Crack Patterns at Failure for BM 16-s230 Series, 50° Dilation

Table D.24: Comparison of Ultimate Loads for BM 16-s230

| $a/d$ | ABAQUS (50°, KN) | CSA (Flexure, KN) | ACI (Flexure, KN) |
|---|---|---|---|
| 1.5 | 521 | 762 | 674 |
| 2.5 | 424 | 457 | 404 |
| 3.5 | 330 | 326 | 289 |
| 4.5 | 280 | 254 | 225 |
| 5.5 | 241 | 208 | 184 |
| 6.5 | 211 | 176 | 155 |
| 7.5 | 190 | 152 | 135 |
| 8.5 | 174 | 134 | 119 |
| 9.5 | 160 | 120 | 106 |
| 10.5 | 144 | 109 | 96 |
| 11.5 | 134 | 99 | 88 |
| 12.5 | 125 | 91 | 81 |

Table D.25: Comparison of Ultimate Loads for BM 16-s230

| $a/d$ | ABAQUS (50°, KN) | CSA (Shear, KN) | ACI (Shear, KN) | JSCE (Shear, KN) | Nehdi (2007) (Shear, KN) | ISIS Canada (Shear, KN) |
|---|---|---|---|---|---|---|
| 1.5 | 521 | 347 | 379 | 174 | 636 | 404 |
| 2.5 | 424 | 298 | 379 | 174 | 491 | 348 |
| 3.5 | 330 | 258 | 379 | 174 | 478 | 348 |
| 4.5 | 280 | 230 | 379 | 174 | 470 | 348 |
| 5.5 | 241 | 218 | 379 | 174 | 463 | 348 |
| 6.5 | 211 | 209 | 379 | 174 | 458 | 348 |
| 7.5 | 190 | 202 | 379 | 174 | 454 | 348 |
| 8.5 | 174 | 202 | 379 | 174 | 450 | 348 |
| 9.5 | 160 | 202 | 379 | 174 | 447 | 348 |
| 10.5 | 144 | 202 | 379 | 174 | 444 | 348 |
| 11.5 | 134 | 202 | 379 | 174 | 442 | 348 |
| 12.5 | 125 | 202 | 379 | 174 | 439 | 348 |

# BM 25-150

## 30° Dilation Angle

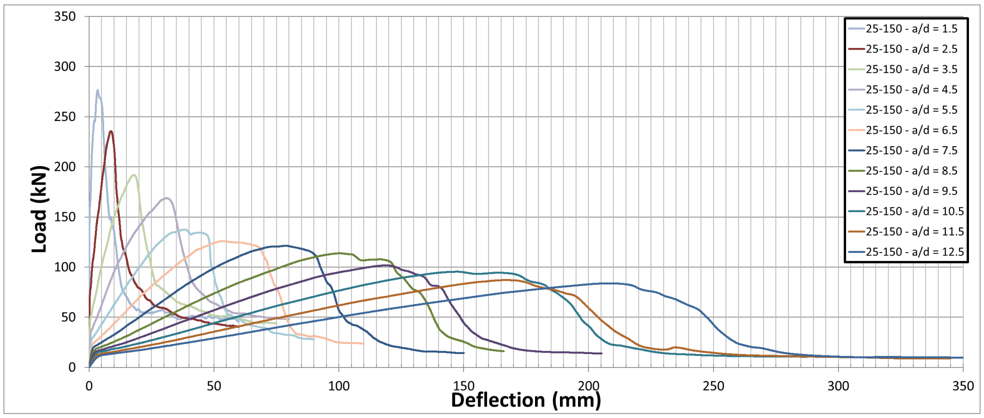


Figure D.37: Mid-Span Load-Deflection Curves for BM 25-150 Series, 30° Dilation

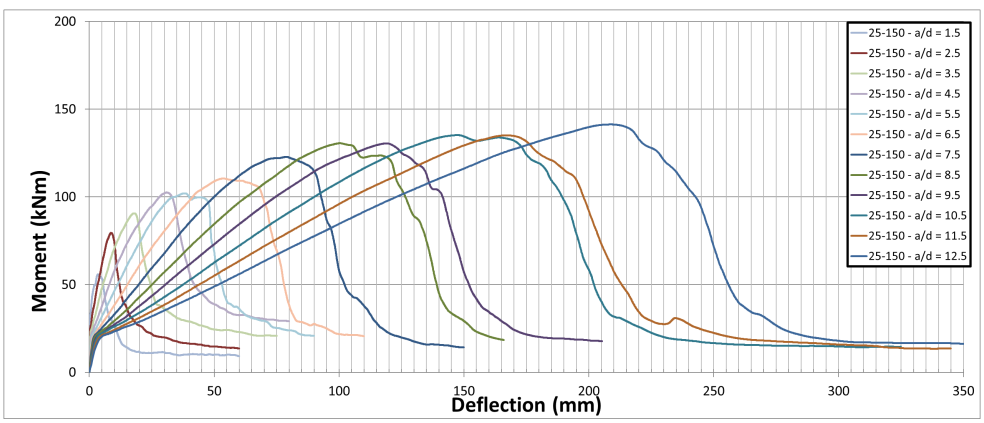


Figure D.38: Mid-Span Moment-Deflection Curves for BM 25-150 Series, 30° Dilation

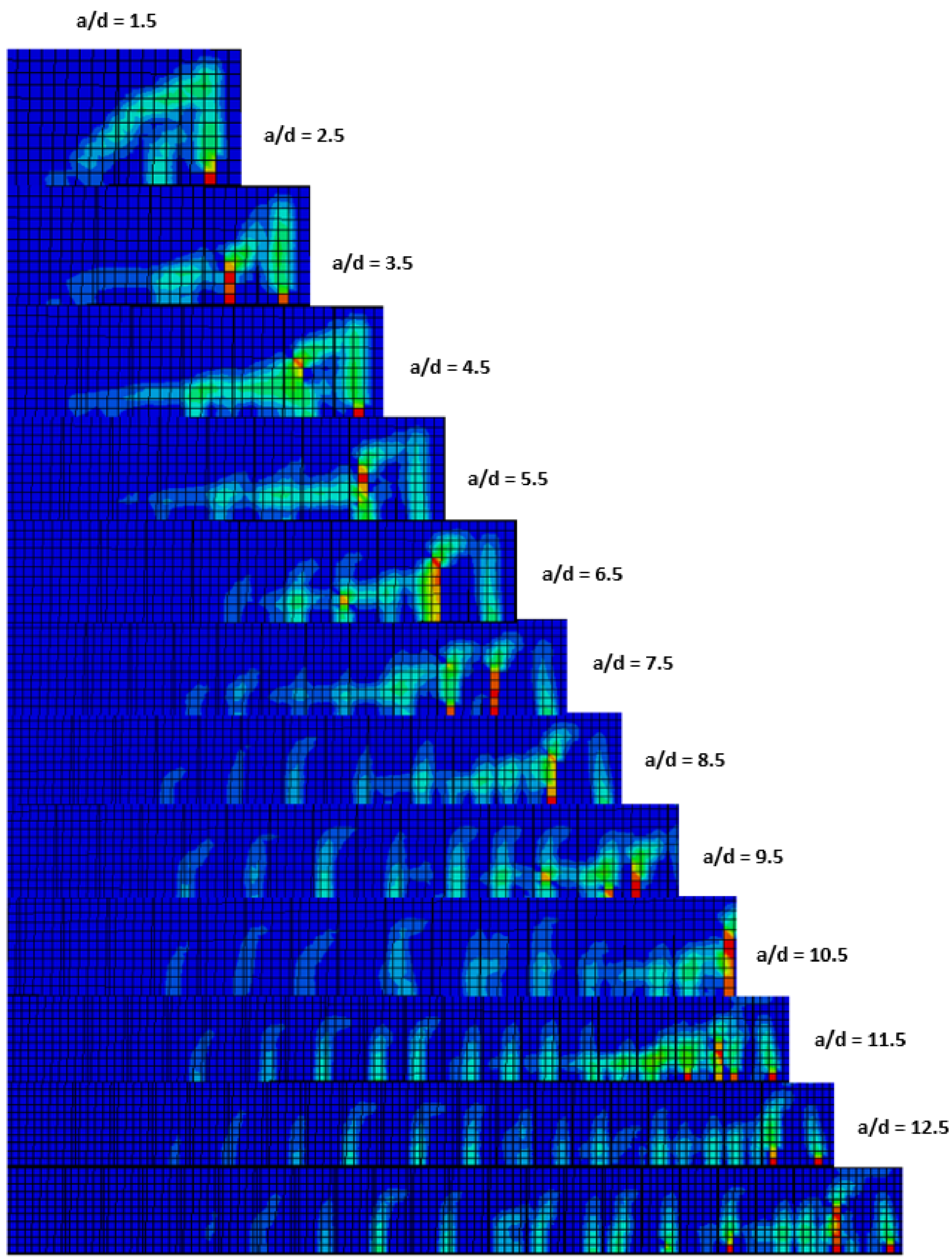


Figure D.39: Crack Patterns at Failure for BM 25-150 Series, 30° Dilation

Table D.26: Comparison of Ultimate Loads for BM 25-150

| $a/d$ | ABAQUS (30°, KN) | CSA (Flexure, KN) | ACI (Flexure, KN) |
|---|---|---|---|
| 1.5 | 276 | 647 | 572 |
| 2.5 | 236 | 388 | 343 |
| 3.5 | 192 | 277 | 245 |
| 4.5 | 169 | 216 | 191 |
| 5.5 | 137 | 176 | 156 |
| 6.5 | 126 | 149 | 132 |
| 7.5 | 121 | 129 | 114 |
| 8.5 | 114 | 114 | 101 |
| 9.5 | 102 | 102 | 90 |
| 10.5 | 95 | 92 | 82 |
| 11.5 | 87 | 84 | 75 |
| 12.5 | 84 | 78 | 69 |

Table D.27: Comparison of Ultimate Loads for BM 25-150

| $a/d$ | ABAQUS (30°, KN) | CSA (Shear, KN) | ACI (Shear, KN) | JSCE (Shear, KN) | Nehdi (2007) (Shear, KN) | ISIS Canada (Shear, KN) |
|---|---|---|---|---|---|---|
| 1.5 | 276 | 244 | 234 | 136 | 490 | 280 |
| 2.5 | 236 | 208 | 234 | 136 | 365 | 247 |
| 3.5 | 192 | 180 | 234 | 136 | 355 | 225 |
| 4.5 | 169 | 161 | 234 | 136 | 347 | 225 |
| 5.5 | 137 | 147 | 234 | 136 | 342 | 225 |
| 6.5 | 126 | 138 | 234 | 136 | 337 | 225 |
| 7.5 | 121 | 134 | 234 | 136 | 334 | 225 |
| 8.5 | 114 | 134 | 234 | 136 | 330 | 225 |
| 9.5 | 102 | 134 | 234 | 136 | 328 | 225 |
| 10.5 | 95 | 134 | 234 | 136 | 325 | 225 |
| 11.5 | 87 | 134 | 234 | 136 | 323 | 225 |
| 12.5 | 84 | 134 | 234 | 136 | 321 | 225 |

## 50° Dilation Angle

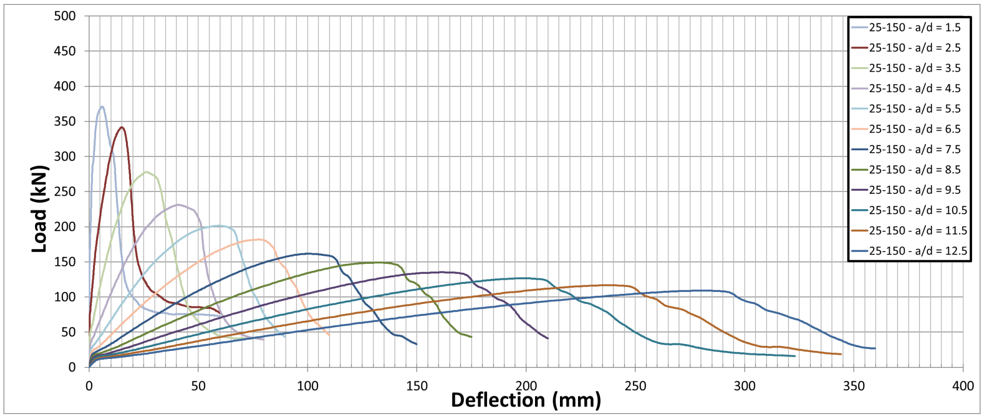


Figure D.40: Mid-Span Load-Deflection Curves for BM 25-150 Series, 50° Dilation

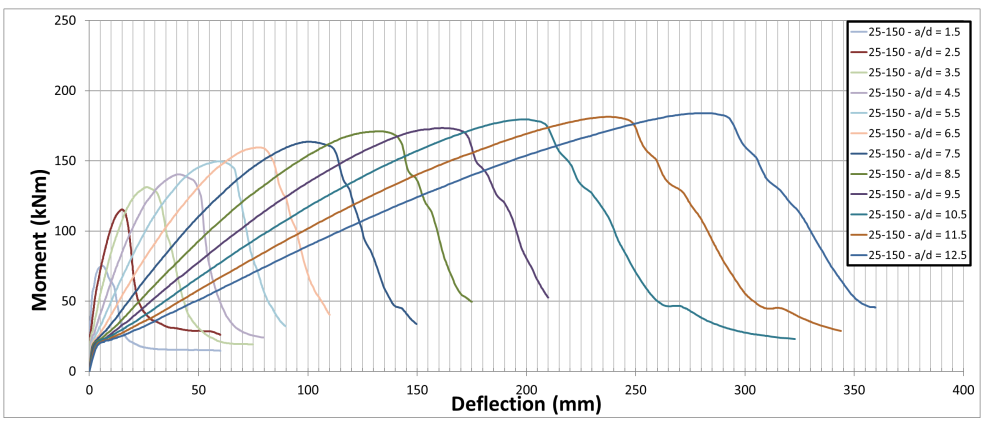


Figure D.41: Mid-Span Moment-Deflection Curves for BM 25-150 Series, 50° Dilation

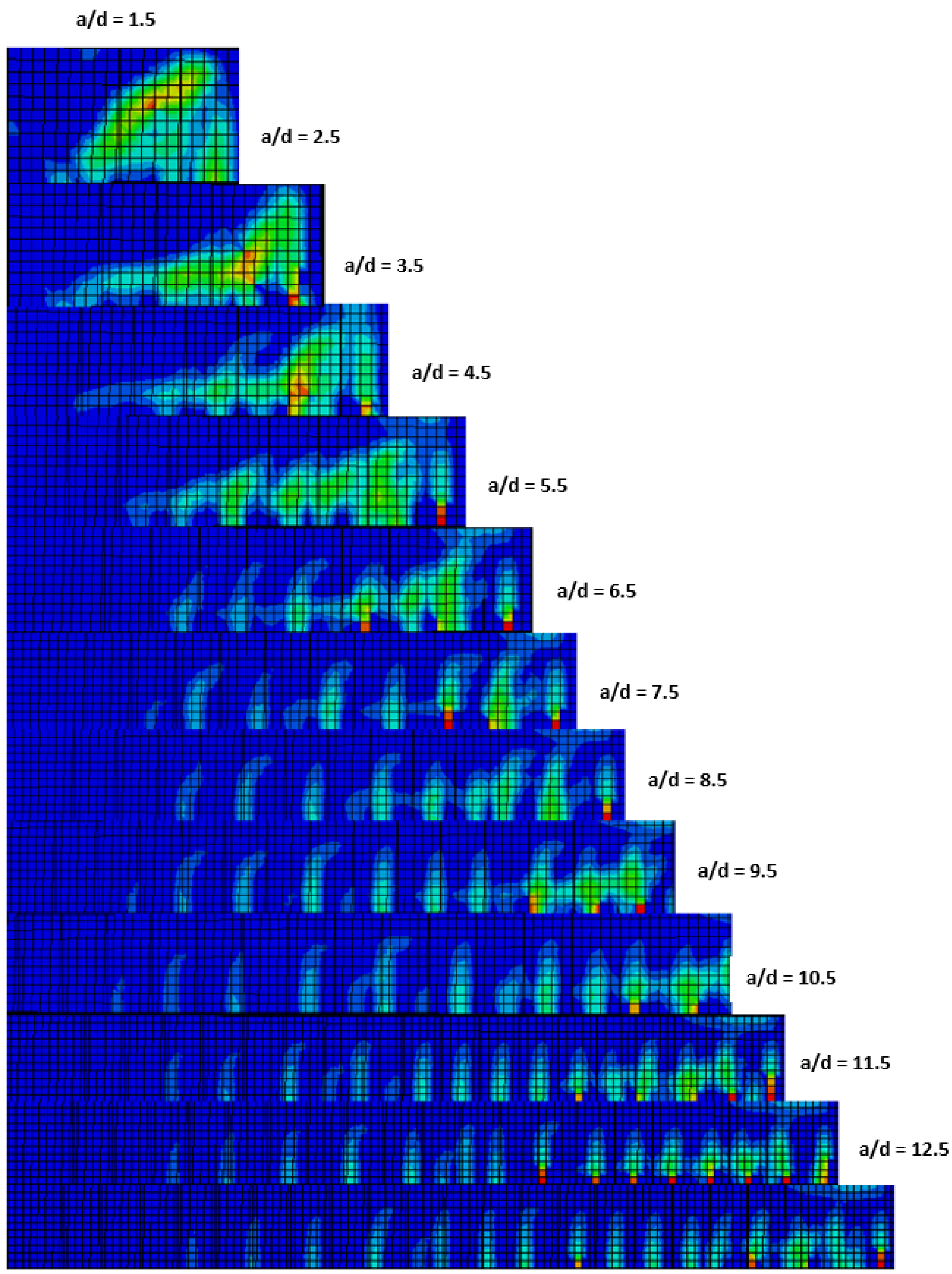


Figure D.42: Crack Patterns at Failure for BM 25-150 Series, 50° Dilation

Table D.28: Comparison of Ultimate Loads for BM 25-150

| $a/d$ | ABAQUS (50°, KN) | CSA (Flexure, KN) | ACI (Flexure, KN) |
|---|---|---|---|
| 1.5 | 371 | 647 | 572 |
| 2.5 | 342 | 388 | 343 |
| 3.5 | 278 | 277 | 245 |
| 4.5 | 231 | 216 | 191 |
| 5.5 | 201 | 176 | 156 |
| 6.5 | 182 | 149 | 132 |
| 7.5 | 162 | 129 | 114 |
| 8.5 | 149 | 114 | 101 |
| 9.5 | 135 | 102 | 90 |
| 10.5 | 127 | 92 | 82 |
| 11.5 | 117 | 84 | 75 |
| 12.5 | 109 | 78 | 69 |

Table D.29: Comparison of Ultimate Loads for BM 25-150

| $a/d$ | ABAQUS (50°, KN) | CSA (Shear, KN) | ACI (Shear, KN) | JSCE (Shear, KN) | Nehdi (2007) (Shear, KN) | ISIS Canada (Shear, KN) |
|---|---|---|---|---|---|---|
| 1.5 | 371 | 244 | 234 | 136 | 490 | 280 |
| 2.5 | 342 | 208 | 234 | 136 | 365 | 247 |
| 3.5 | 278 | 180 | 234 | 136 | 355 | 225 |
| 4.5 | 231 | 161 | 234 | 136 | 347 | 225 |
| 5.5 | 201 | 147 | 234 | 136 | 342 | 225 |
| 6.5 | 182 | 138 | 234 | 136 | 337 | 225 |
| 7.5 | 162 | 134 | 234 | 136 | 334 | 225 |
| 8.5 | 149 | 134 | 234 | 136 | 330 | 225 |
| 9.5 | 135 | 134 | 234 | 136 | 328 | 225 |
| 10.5 | 127 | 134 | 234 | 136 | 325 | 225 |
| 11.5 | 117 | 134 | 234 | 136 | 323 | 225 |
| 12.5 | 109 | 134 | 234 | 136 | 321 | 225 |

# BM 25-220

## 30° Dilation Angle

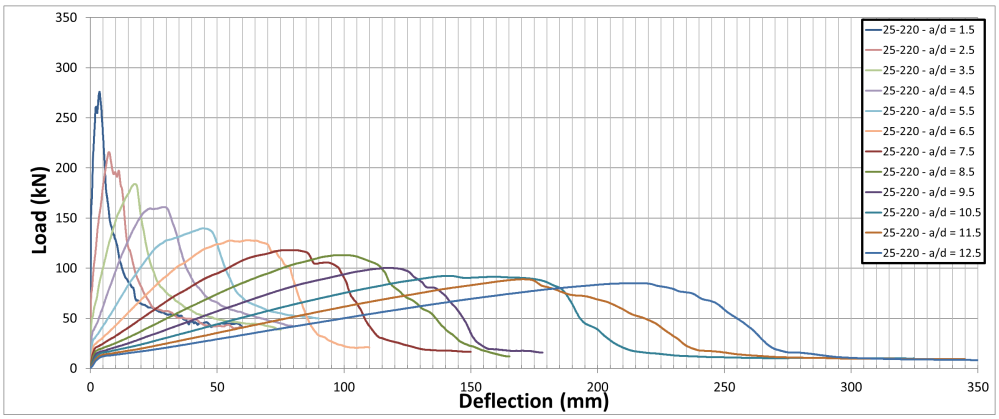


Figure D.43: Mid-Span Load-Deflection Curves for BM 25-220 Series, 30° Dilation

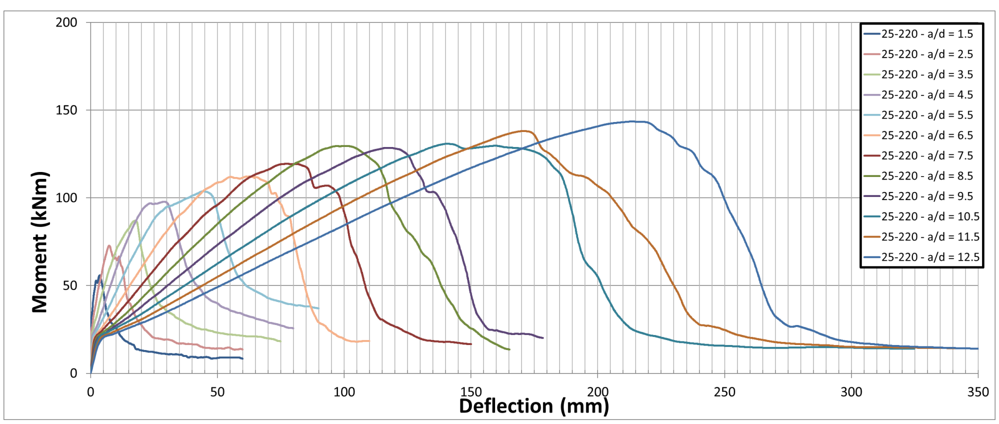


Figure D.44: Mid-Span Moment-Deflection Curves for BM 25-220 Series, 30° Dilation

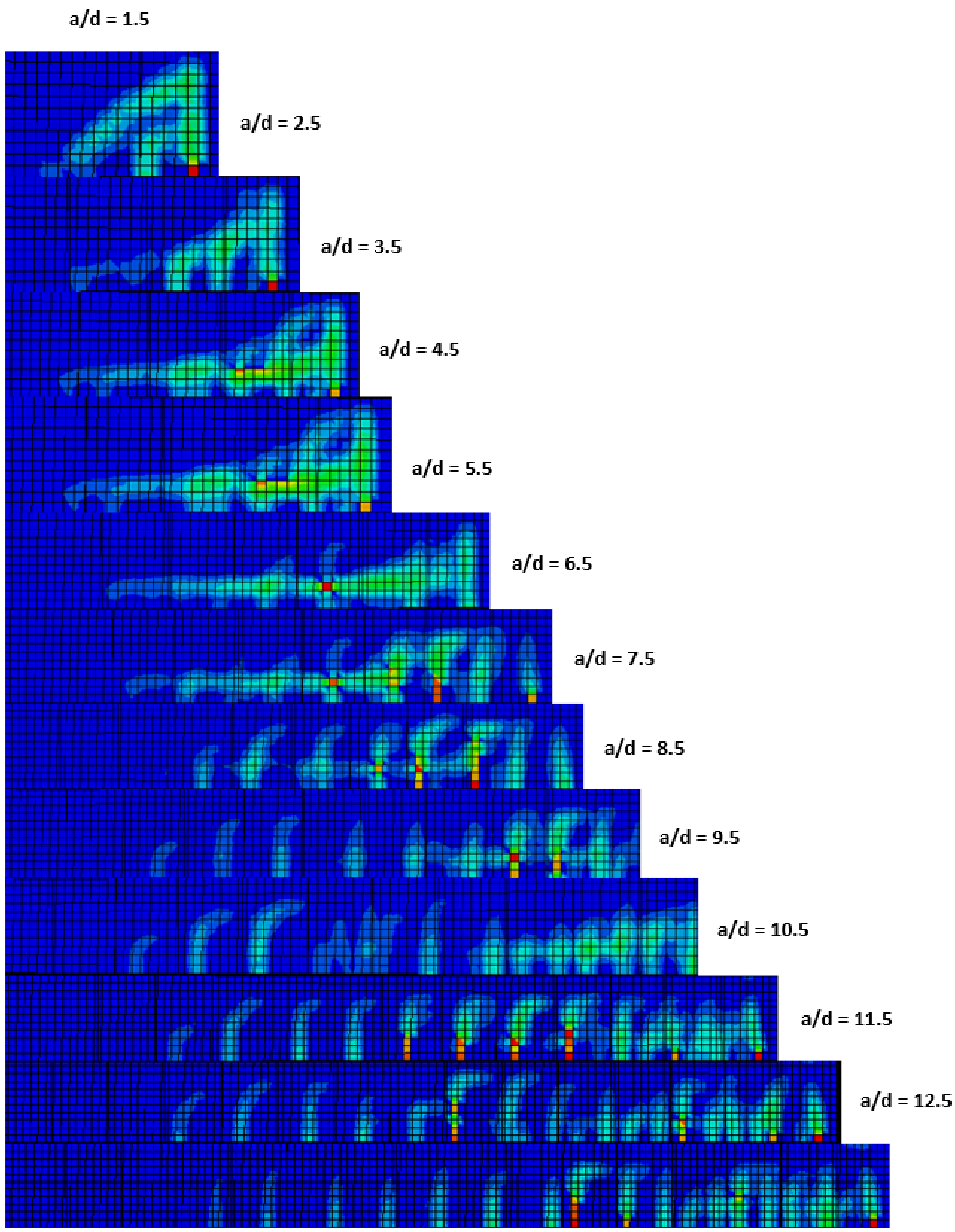


Figure D.45: Crack Patterns at Failure for BM 25-220 Series, 30° Dilation

Table D.30: Comparison of Ultimate Loads for BM 25-220

| $a/d$ | ABAQUS (30°, KN) | CSA (Flexure, KN) | ACI (Flexure, KN) |
|---|---|---|---|
| 1.5 | 276 | 647 | 572 |
| 2.5 | 216 | 388 | 343 |
| 3.5 | 184 | 277 | 245 |
| 4.5 | 161 | 216 | 191 |
| 5.5 | 140 | 176 | 156 |
| 6.5 | 128 | 149 | 132 |
| 7.5 | 118 | 129 | 114 |
| 8.5 | 113 | 114 | 101 |
| 9.5 | 100 | 102 | 90 |
| 10.5 | 92 | 92 | 82 |
| 11.5 | 89 | 84 | 75 |
| 12.5 | 85 | 78 | 69 |

Table D.31: Comparison of Ultimate Loads for BM 25-220

| $a/d$ | ABAQUS (30°, KN) | CSA (Shear, KN) | ACI (Shear, KN) | JSCE (Shear, KN) | Nehdi (2007) (Shear, KN) | ISIS Canada (Shear, KN) |
|---|---|---|---|---|---|---|
| 1.5 | 276 | 221 | 182 | 128 | 450 | 236 |
| 2.5 | 216 | 189 | 182 | 128 | 325 | 213 |
| 3.5 | 184 | 163 | 182 | 128 | 315 | 195 |
| 4.5 | 161 | 146 | 182 | 128 | 308 | 183 |
| 5.5 | 140 | 133 | 182 | 128 | 302 | 183 |
| 6.5 | 128 | 123 | 182 | 128 | 297 | 183 |
| 7.5 | 118 | 117 | 182 | 128 | 294 | 183 |
| 8.5 | 113 | 117 | 182 | 128 | 291 | 183 |
| 9.5 | 100 | 117 | 182 | 128 | 288 | 183 |
| 10.5 | 92 | 117 | 182 | 128 | 286 | 183 |
| 11.5 | 89 | 117 | 182 | 128 | 283 | 183 |
| 12.5 | 85 | 117 | 182 | 128 | 282 | 183 |

## 50° Dilation Angle

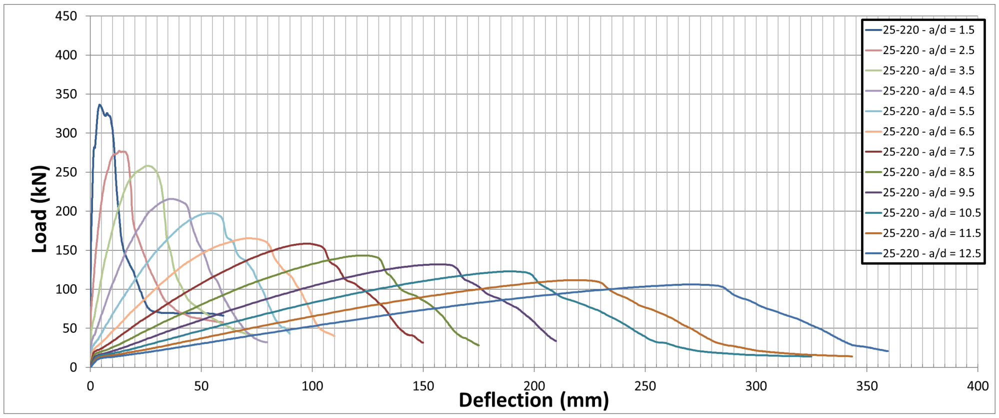


Figure D.46: Mid-Span Load-Deflection Curves for BM 25-220 Series, 50° Dilation

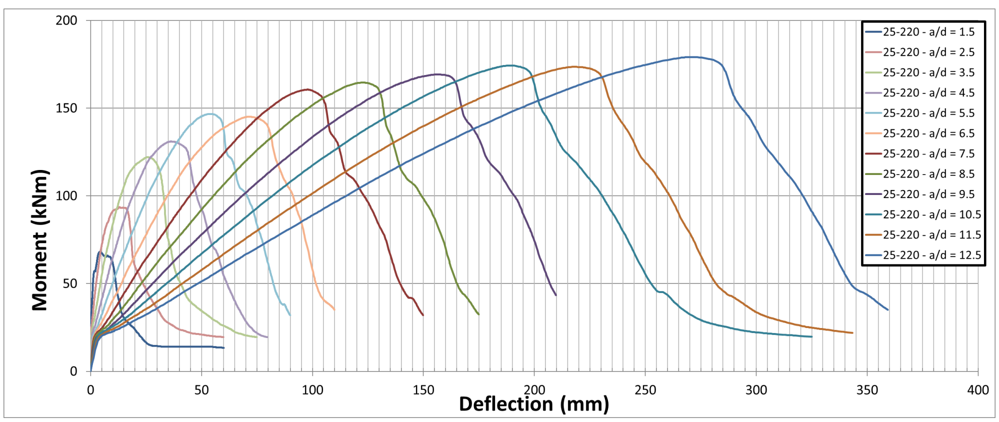


Figure D.47: Mid-Span Moment-Deflection Curves for BM 25-220 Series, 50° Dilation

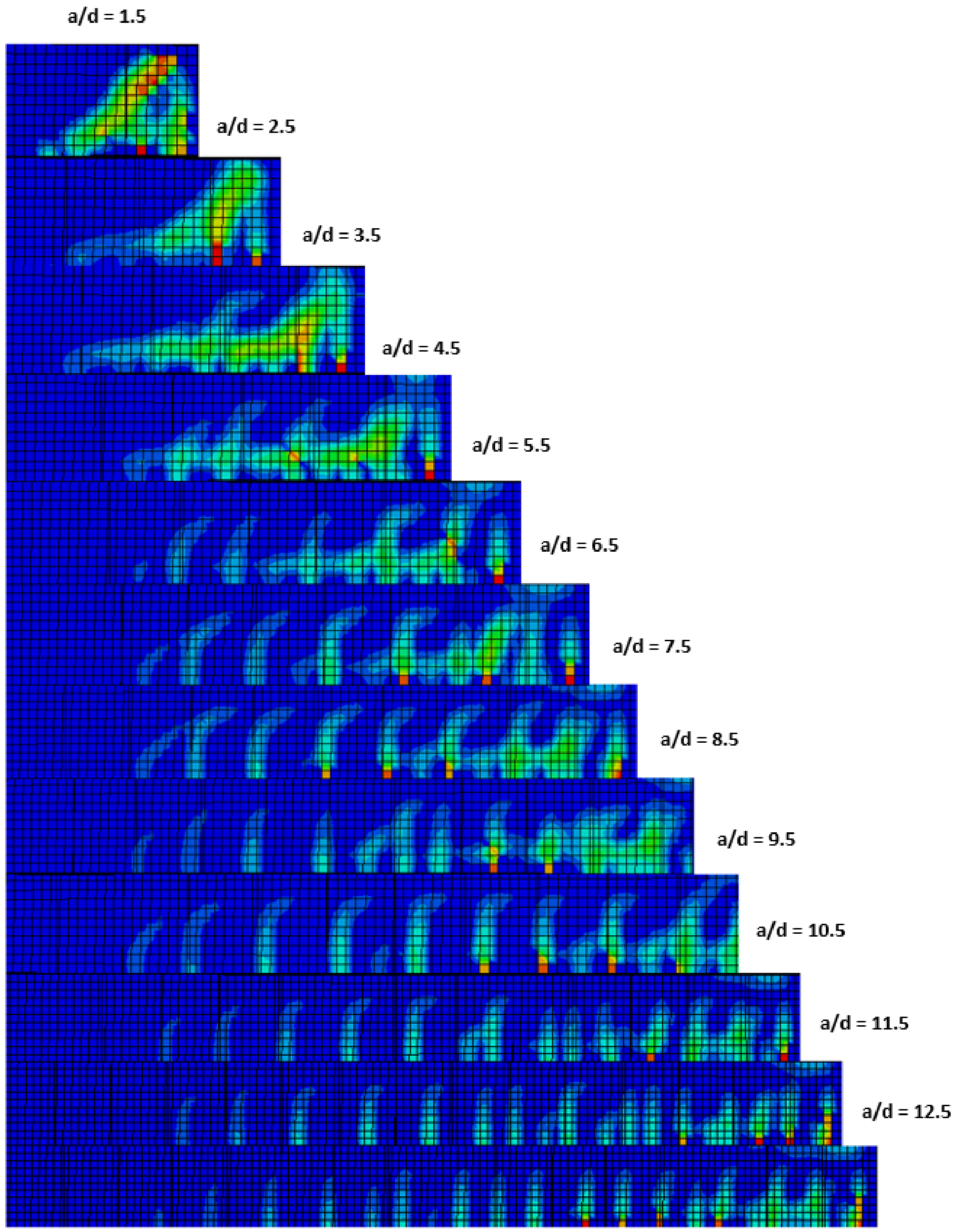


Figure D.48: Crack Patterns at Failure for BM 25-220 Series, 50° Dilation

Table D.32: Comparison of Ultimate Loads for BM 25-220

| $a/d$ | ABAQUS (50°, KN) | CSA (Flexure, KN) | ACI (Flexure, KN) |
|---|---|---|---|
| 1.5 | 336 | 647 | 572 |
| 2.5 | 294 | 388 | 343 |
| 3.5 | 258 | 277 | 245 |
| 4.5 | 216 | 216 | 191 |
| 5.5 | 198 | 176 | 156 |
| 6.5 | 165 | 149 | 132 |
| 7.5 | 159 | 129 | 114 |
| 8.5 | 143 | 114 | 101 |
| 9.5 | 132 | 102 | 90 |
| 10.5 | 123 | 92 | 82 |
| 11.5 | 112 | 84 | 75 |
| 12.5 | 106 | 78 | 69 |

Table D.33: Comparison of Ultimate Loads for BM 25-220

| $a/d$ | ABAQUS (50°, KN) | CSA (Shear, KN) | ACI (Shear, KN) | JSCE (Shear, KN) | Nehdi (2007) (Shear, KN) | ISIS Canada (Shear, KN) |
|---|---|---|---|---|---|---|
| 1.5 | 336 | 221 | 182 | 128 | 450 | 236 |
| 2.5 | 294 | 189 | 182 | 128 | 325 | 213 |
| 3.5 | 258 | 163 | 182 | 128 | 315 | 195 |
| 4.5 | 216 | 146 | 182 | 128 | 308 | 183 |
| 5.5 | 198 | 133 | 182 | 128 | 302 | 183 |
| 6.5 | 165 | 123 | 182 | 128 | 297 | 183 |
| 7.5 | 159 | 117 | 182 | 128 | 294 | 183 |
| 8.5 | 143 | 117 | 182 | 128 | 291 | 183 |
| 9.5 | 132 | 117 | 182 | 128 | 288 | 183 |
| 10.5 | 123 | 117 | 182 | 128 | 286 | 183 |
| 11.5 | 112 | 117 | 182 | 128 | 283 | 183 |
| 12.5 | 106 | 117 | 182 | 128 | 282 | 183 |

# BM 25-s230

## 30° Dilation Angle

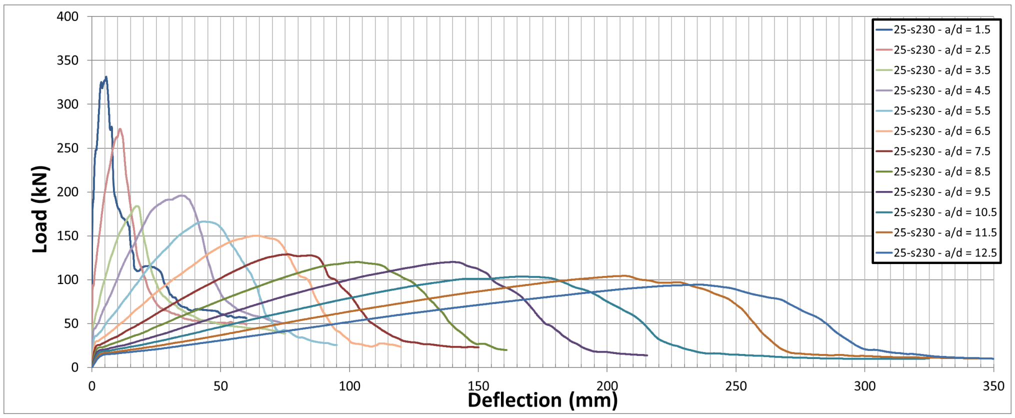


Figure D.49: Mid-Span Load-Deflection Curves for BM 25-s230 Series, 30° Dilation

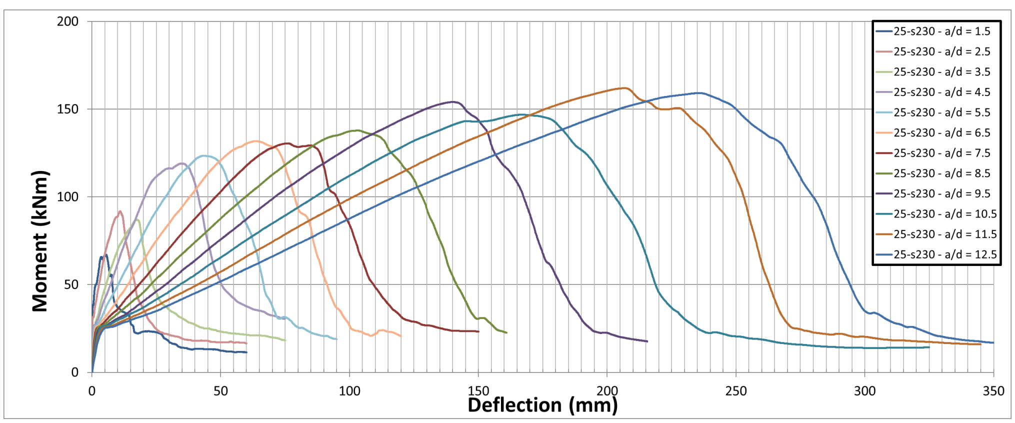


Figure D.50: Mid-Span Moment-Deflection Curves for BM 25-s230 Series, 30° Dilation

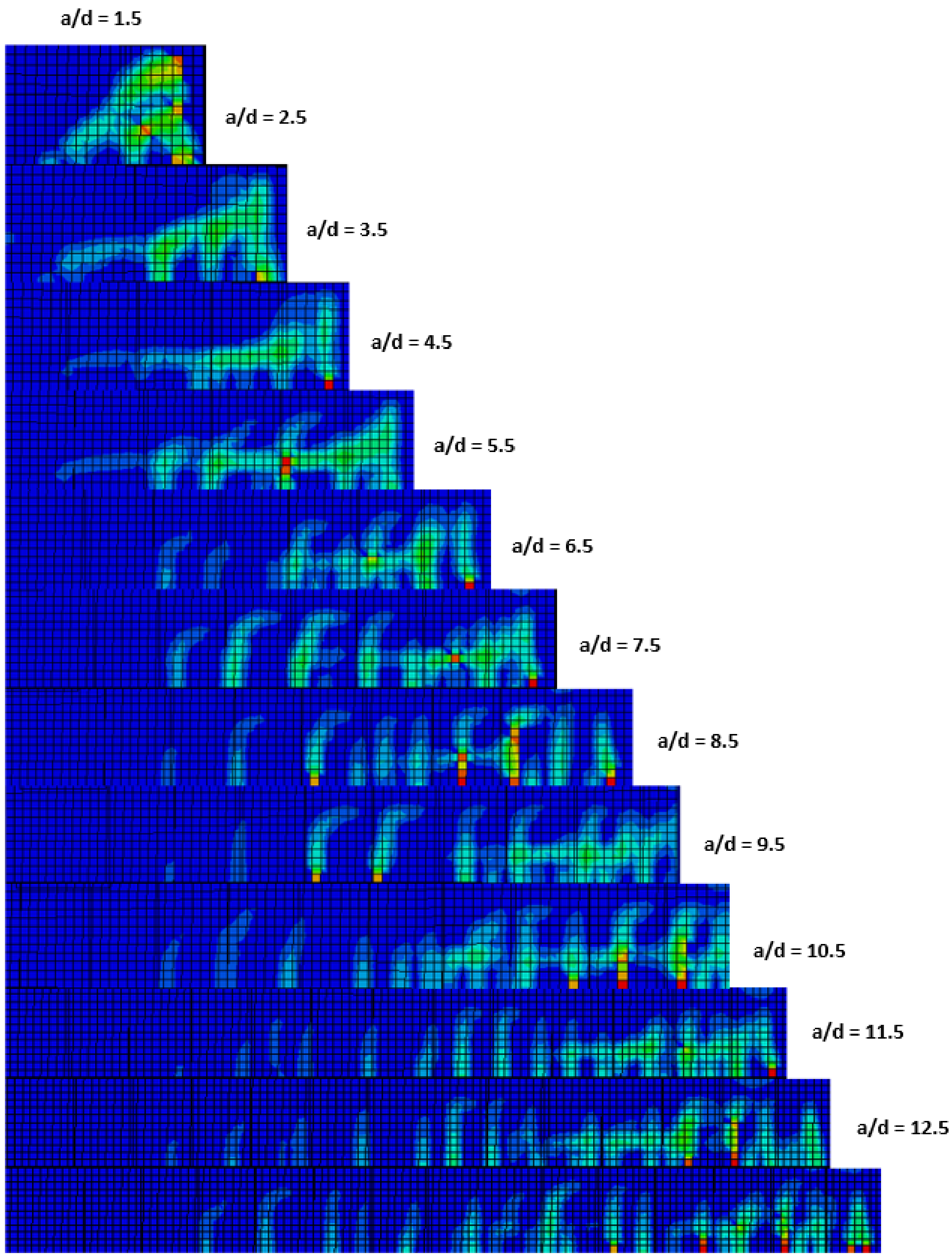


Figure D.51: Crack Patterns at Failure for BM 25-s230 Series, 30° Dilation

Table D.34: Comparison of Ultimate Loads for BM 25-s230

| $a/d$ | ABAQUS (30°, KN) | CSA (Flexure, KN) | ACI (Flexure, KN) |
|---|---|---|---|
| 1.5 | 331 | 707 | 623 |
| 2.5 | 272 | 424 | 374 |
| 3.5 | 223 | 303 | 267 |
| 4.5 | 196 | 236 | 208 |
| 5.5 | 166 | 193 | 170 |
| 6.5 | 150 | 163 | 144 |
| 7.5 | 129 | 141 | 125 |
| 8.5 | 120 | 125 | 110 |
| 9.5 | 120 | 112 | 98 |
| 10.5 | 104 | 101 | 89 |
| 11.5 | 104 | 92 | 84 |
| 12.5 | 94 | 85 | 75 |

Table D.35: Comparison of Ultimate Loads for BM 25-s230

| $a/d$ | ABAQUS (30°, KN) | CSA (Shear, KN) | ACI (Shear, KN) | JSCE (Shear, KN) | Nehdi (2007) (Shear, KN) | ISIS Canada (Shear, KN) |
|---|---|---|---|---|---|---|
| 1.5 | 331 | 317 | 372 | 161 | 621 | 371 |
| 2.5 | 272 | 263 | 372 | 161 | 483 | 348 |
| 3.5 | 223 | 228 | 372 | 161 | 471 | 348 |
| 4.5 | 196 | 213 | 372 | 161 | 463 | 348 |
| 5.5 | 166 | 202 | 372 | 161 | 457 | 348 |
| 6.5 | 150 | 194 | 372 | 161 | 452 | 348 |
| 7.5 | 129 | 194 | 372 | 161 | 448 | 348 |
| 8.5 | 120 | 194 | 372 | 161 | 444 | 348 |
| 9.5 | 120 | 194 | 372 | 161 | 441 | 348 |
| 10.5 | 104 | 194 | 372 | 161 | 439 | 348 |
| 11.5 | 104 | 194 | 372 | 161 | 436 | 348 |
| 12.5 | 94 | 194 | 372 | 161 | 434 | 348 |

## 50° Dilation Angle

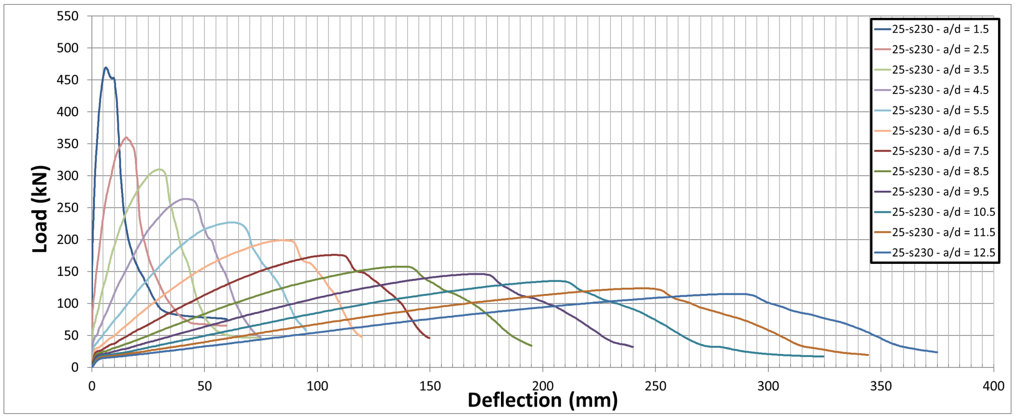


Figure D.52: Mid-Span Load-Deflection Curves for BM 25-s230 Series, 50° Dilation

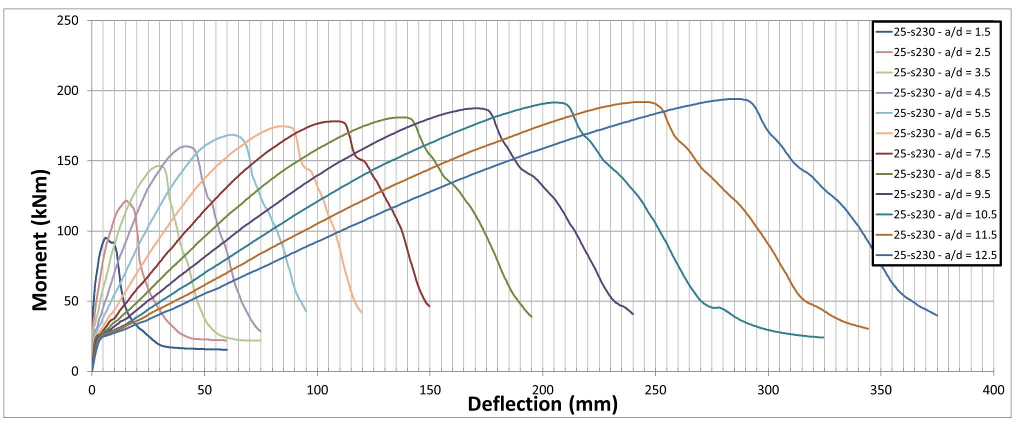


Figure D.53: Mid-Span Moment-Deflection Curves for BM 25-s230 Series, 50° Dilation

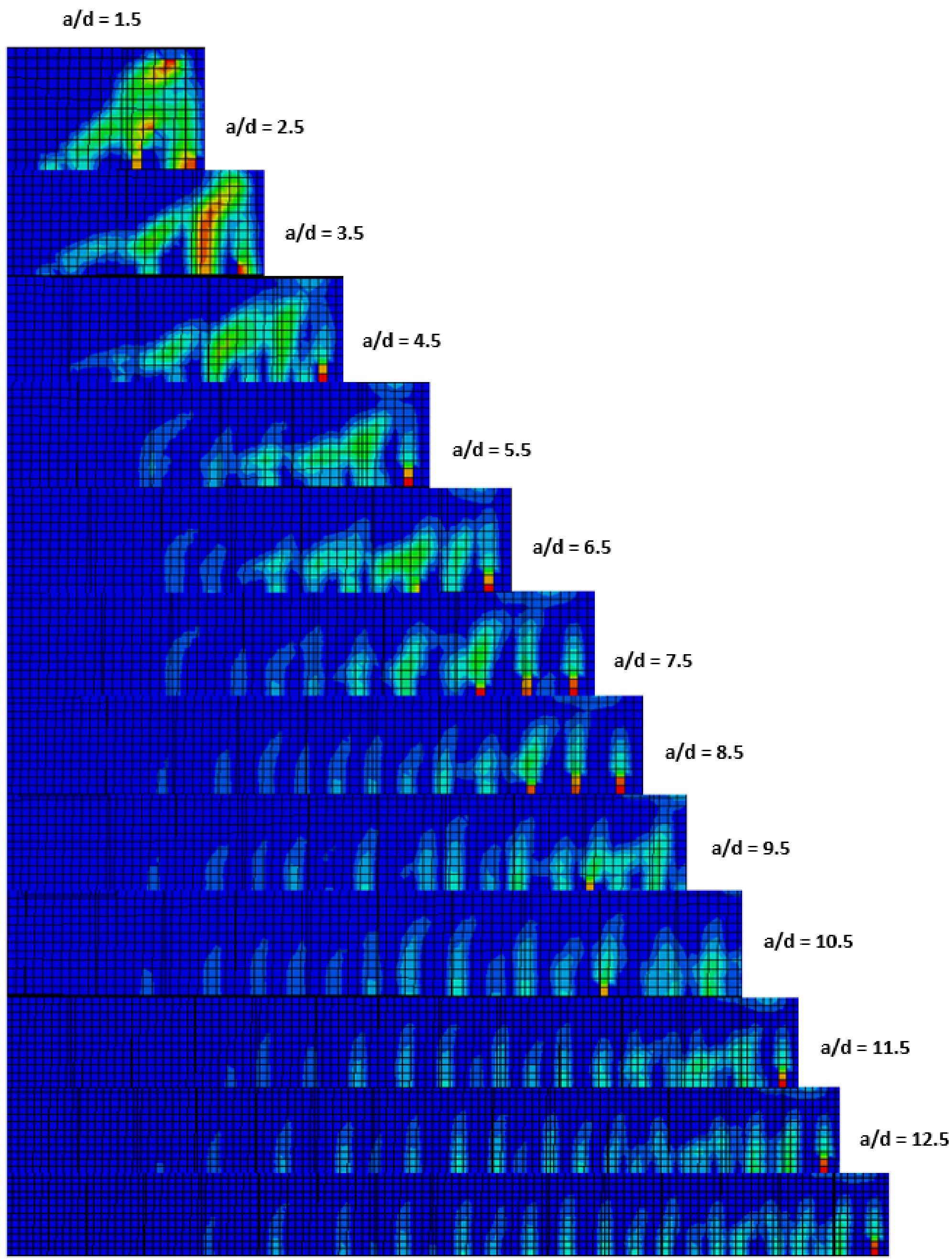


Figure D.54: Crack Patterns at Failure for BM 25-s230 Series, 50° Dilation

Table D.36: Comparison of Ultimate Loads for BM 25-s230

| $a/d$ | ABAQUS (50°, KN) | CSA (Flexure, KN) | ACI (Flexure, KN) |
|---|---|---|---|
| 1.5 | 469 | 707 | 623 |
| 2.5 | 360 | 424 | 374 |
| 3.5 | 310 | 303 | 267 |
| 4.5 | 264 | 236 | 208 |
| 5.5 | 227 | 193 | 170 |
| 6.5 | 199 | 163 | 144 |
| 7.5 | 176 | 141 | 125 |
| 8.5 | 158 | 125 | 110 |
| 9.5 | 146 | 112 | 98 |
| 10.5 | 135 | 101 | 89 |
| 11.5 | 124 | 92 | 84 |
| 12.5 | 115 | 85 | 75 |

Table D.37: Comparison of Ultimate Loads for BM 25-s230

| $a/d$ | ABAQUS (50°, KN) | CSA (Shear, KN) | ACI (Shear, KN) | JSCE (Shear, KN) | Nehdi (2007) (Shear, KN) | ISIS Canada (Shear, KN) |
|---|---|---|---|---|---|---|
| 1.5 | 469 | 317 | 372 | 161 | 621 | 371 |
| 2.5 | 360 | 263 | 372 | 161 | 483 | 348 |
| 3.5 | 310 | 228 | 372 | 161 | 471 | 348 |
| 4.5 | 264 | 213 | 372 | 161 | 463 | 348 |
| 5.5 | 227 | 202 | 372 | 161 | 457 | 348 |
| 6.5 | 199 | 194 | 372 | 161 | 452 | 348 |
| 7.5 | 176 | 194 | 372 | 161 | 448 | 348 |
| 8.5 | 158 | 194 | 372 | 161 | 444 | 348 |
| 9.5 | 146 | 194 | 372 | 161 | 441 | 348 |
| 10.5 | 135 | 194 | 372 | 161 | 439 | 348 |
| 11.5 | 124 | 194 | 372 | 161 | 436 | 348 |
| 12.5 | 115 | 194 | 372 | 161 | 434 | 348 |